

University of Nottingham
UK | CHINA | MALAYSIA

Applications of DTI and NODDI-MRI in Diabetes Mellitus and Multiple Sclerosis

A dissertation submitted in partial fulfilment of the requirements for the degree of Doctor of Philosophy of The University of Nottingham

Mental Health and Clinical Neurosciences Department at the School of Medicine and Queen's Medical Centre, University of Nottingham, UK

PhD. Supervisors

Prof. Rob Dineen

Dr Sieun Lee

Prof. Cris Constantinescu

Submitted by

Abdulmajeed Alotaibi

December 2022

Abstract

Type 2 diabetes (T2DM) and multiple sclerosis (MS) affect the central nervous system (CNS). Both diseases are major risk factors for brain damage and degeneration, challenging healthcare providers worldwide. Magnetic Resonance Imaging (MRI) can visualise brain structural abnormalities in patients with T2DM and MS, but conventional MRI cannot quantify microstructural changes. As a result, there has been a surge in interest in utilising imaging tools to quantify microstructural changes, such as advanced diffusion MRI models, to understand white matter abnormalities in MS and T2DM.

Diffusion tensor imaging (DTI) has been used to quantify microstructural abnormalities in T2DM and MS. Despite the sensitivity of DTI in detecting microstructural changes in white matter, DTI indices are influenced by fibre orientation dispersion, which may lead to the incomplete or erroneous characterisation of the microstructural changes occurring within a voxel. A biophysical diffusion model known as neurite orientation dispersion and density imaging (NODDI) has been proposed to overcome this DTI limitation.

My original contribution to knowledge is 1) a current systematic review of DTI studies that detected brain microstructural changes in diabetes; 2) a meta-analysis of NODDI studies in characterising white matter changes in MS; 3) optimising an up-to-date NODDI scanning protocol at the University of Nottingham; 4) using DTI/NODDI metrics derived from the UK Biobank to investigate brain white matter alterations in T2DM; 5) assessing the correlation between the altered DTI/NODDI metrics and metabolic profile in patients with T2DM.

I initially optimised the NODDI scanning protocol for this original PhD project. I tested four scanning protocols on a 3T Philips MRI scanner at Sir Peter Mansfield Imaging Centre (SPMIC). The research team agreed that Protocol #3 was the best choice. In parallel, I performed a systematic review to investigate the impact of diabetes on brain microstructure measured by DTI and correlated it with cognitive and metabolic tests. I reviewed 38 DTI

studies on both types of diabetes. This review showed that diabetes affects brain microstructure, suggesting its impact on cognitive abilities. I aimed to meta-analyse studies using NODDI metrics to detect the white matter neuroaxonal pathology in MS. The intracellular volume fraction in the white matter lesions and normal-appearing white matter were significantly reduced compared to healthy white matter, suggesting underlying damage or loss of neurites. After the COVID-19 pandemic halted my prospective patient study, I evaluated the microstructural impact of T2DM on brain white matter using DTI and NODDI metrics derived from UK Biobank. I evaluated the relationship between white matter alterations and disease duration/glycated haemoglobin (HbA1c). The study showed that T2DM was associated with subtle but global white matter microstructural changes, as indicated by the alterations of DTI and NODDI parameters. There were weak but statistically significant associations between altered DTI and NODDI parameters in participants with T2DM and glycaemic control/disease duration.

T2DM and MS were associated with white matter alterations detected by DTI and NODDI. Although the findings of this thesis demonstrated that DTI still has a potential value as a clinical biomarker in T2DM, NODDI could biophysically characterise white matter neuroaxonal pathology in T2DM and MS, which contributes to DTI parameters.

Impact Statement

Although it was difficult for me as a PhD student to mitigate the impact of Covid-19 on my mental health and research progress, I successfully produced original and novel research studies on brain microstructural alteration in T2DM using advanced diffusion imaging techniques. Using UK Biobank datasets, I evaluated the use of advanced quantitative diffusion methods (DTI and NODDI) in detecting white matter changes in T2DM. Also, my meta-analysis confirmed the ability of NODDI to detect reduced neurite density in MS.

My work has the potential to enhance the links between scientists in biomedical imaging and physicians. Also, it motivates further cooperation between these two communities to expand our understanding of T2DM and MS pathophysiology. A deep understanding of T2DM and MS pathology could benefit the entire society in the future by assisting in the development of successful therapeutic ways to delay or prevent brain illness in T2DM and MS. I presented my work to clinicians, academics, and researchers at national and international meetings (ISMRM, ASNR, ESNR, ASN, OHBM and ECTRISM). One of the thesis chapters was selected to receive the Oldendorf Award (best abstract submitted by a student, resident, or fellow in the category of CT, MRI, SPECT, or PET) and to be presented during the 44th virtual Annual Meeting of the American Society of Neuroimaging (ASN). I received another award from my current sponsor to recognise my academic achievements. Also, I was nominated as a research team member for the Tri Campus Award for my research progress and contribution to the postgraduate community at the University of Nottingham (clinical neurology research team). Furthermore, I published two systematic reviews in the Brain Sciences journal. According to Google Scholar, the first systematic review (Chapter 6) has been cited 7 times, and my second systematic review (Chapter 7) was cited 4 times. The original UK Biobank studies have been published as a preprint and as a merged-long paper.

In addition, I have co-authored two published systematic reviews and two original research studies in MS imaging; one study was recently accepted for publication.

Covid-19 Impact on PhD Progress

This PhD research was carried out as part of an ethically approved project funded by the University of Nottingham and Hospital Charity. This large project entitled "Spinal Imaging in Diabetic Neuropathy: Longitudinal Evaluation (SpINDLE) " was primarily investigated by Prof. Cris Constantinescu (my previous principal supervisor). Prof. Constantinescu, Prof. Dineen, Dr Lee, and I developed a research proposal to use novel diffusion imaging techniques to explore microstructural alterations in the brain of individuals with T2DM and MS. Fortunately, I was able to optimise the scanning methodology during the first year of my PhD with the help of our collaborators at Sir Peter Mansfield Imaging Centre (SPMIC).

Before upgrading to my PhD, the UK government declared the first lockdown in response to the spread of the Covid-19 pandemic across the country in March 2020. As a result, the University of Nottingham announced the closure of all campuses, including the facilities for this PhD project (clinical neurology offices/nursing stations and SPMIC). Unfortunately, all venues were closed for nearly two years. My supervisors and I agreed to prepare contingency plans and strategies to mitigate the risk of covid-19 impact on the research progress. First, I performed a comprehensive systematic review of diffusion imaging on brain microstructural alterations in diabetes. Second, I conducted a meta-analysis on NODDI to detect brain microstructural abnormalities in MS. Third, I attempted to collect brain datasets from our colleagues at the University College of London to reanalyse them differently. I sent many emails to the authors of relevant published studies; unfortunately, no responses have been received. Lastly, I applied to the UK Biobank to gain access to existing datasets and retrospectively answer the same research questions; this application was approved three months later. Following approval, the UK Biobank administration office

sought 2500 GBP in access fees, which I could not afford. Prof. Constantinescu, Prof. Dineen, and Prof. Auer met online in November 2020 and proposed accessing the UK Biobank data through Dr Stam Sotiropoulos. I developed a list of specified imaging and non-imaging data. I forwarded it to Dr Stam Sotiropoulos and Dr Ali-Reza Mohammadi-Nejad to retrieve the datasets for me. I could not retrieve data from MS patients due to limited access to the UK Biobank. Furthermore, there was no spinal cord imaging data in the UK Biobank yet. Therefore, my supervisors suggested excluding the investigation of the spinal cord and MS impact on the brain.

Publications

1. Journal papers

    - **Abdulmajeed Alotaibi***, Christopher Tench, Rebecca Stevenson, Ghadah Felmban, Amjad Altokhis, Ali Aldhebaib, Rob A. Dineen, and Cris S. Constantinescu. *Investigating Brain Microstructural Alterations in Type 1 and Type 2 Diabetes Using Diffusion Tensor Imaging: A Systematic Review*. Brain Sciences, 2021.
    - **Abdulmajeed Alotaibi***, Amjad Altokhis, Anna Podlasek, Ali Aldhebaib, Rob A. Dineen, and Cris S. Constantinescu. Investigating Microstructural Changes in White Matter in Multiple Sclerosis: A Systematic Review and Meta-Analysis of Neurite Orientation Dispersion and Density Imaging. Brain Sciences, 2021.
    - Amjad Altokhis*, **Abdulmajeed Alotaibi**, Ghadah A. Felmban, Cris S. Constantinescu, and Nikos Evangelou. *Iron Rims as an Imaging Biomarker in MS: A Systematic Mapping Review*. Diagnostics, 2020.
    - Amjad I. AlTokhis*, Abrar AlAmrani, **Abdulmajeed Alotaibi**, Anna Podlasek, and Cris S. Constantinescu. *Magnetic Resonance Imaging as a Prognostic Disability Markerin Clinically Isolated Syndrome and Multiple Sclerosis: A Systematic Review and Meta-Analysis*. Diagnostics, 2021.
    - Amjad Altokhis; Aimee Hibbert; Christopher Allen; Olivier Mougin; **Abdulmajeed Alotaibi**; Su Lim; Cris Constantinescu; Rasha Abdel-Fahim; Nikos Evangelou. *Longitudinal Clinical Study of Patients with Iron Rim Lesions in Multiple Sclerosis.*
    - Amjad Altokhis; Paul Morgan; **Abdulmajeed Alotaibi**; Radu Tanasescu, and Nikos Evangelou. *Predictors of long-term disability in multiple sclerosis patients using routine magnetic resonance imaging data: A 15-year retrospective study.* The Neuroradiology Journal, 2022.

2. Journal papers under peer reviewing (published as a preprint)

    - **Abdulmajeed Alotaibi**, Anna Podlasek, Amjad AlTokhis, Chris R. Tench, Ali-Reza Mohammadi-Nejad, Stamatios N. Sotiropoulos, Cris S. Constantinescu, Sieun Lee, Rob A. Dineen. *White Matter Microstructural Alteration in Type 2 Diabetes: A Combined UK Biobank Study of Diffusion Tensor Imaging and Neurite Orientation Dispersion and Density Imaging.*

Acknowledgements

The previous few years have been difficult for me, especially during the Covid-19 lockdowns. I am glad that I have made it to the end successfully. This is the best time to show my heartfelt gratitude to everyone who has helped me throughout my PhD years.

First and foremost, I would like to convey my heartfelt thanks to my supervisors, Prof. Rob Dineen, Prof. Cris Constantinescu, and Dr Sieun Lee, for their unconditional support, patience, and motivation during my PhD studies. Their guidance was valuable during the research work and the writing of this thesis. I could not have asked for greater supervisors and teachers for my PhD studies.

Besides my supervisors, I would like to express my gratitude to my thesis internal assessor: Prof. Susan Francis, for her insightful comments, encouragement and the challenging questions that prompted me to broaden my research and include multiple perspectives.

My sincere gratitude also goes to Dr Stam Sotiropoulos and Dr Ali-Reza Mohammadi-Nejad. They helped me access the UK Biobank and get the data used in my thesis. This PhD project would not be possible without their valuable support.

I am also grateful to my collaborators from the Division of Mental Health and Clinical Neurosciences at the University of Nottingham and my research team from the Radiologic Sciences department at King Saud bin Abdul-Aziz University for Health Sciences in Saudi Arabia.

Finally, I want to extend my thanks to my parents and siblings for their spiritual support throughout the writing of my thesis and my life in general.

TABLE OF CONTENTS

1. Introduction and Background (Word count: 915)..... 11

1.1. Background 11

2.1. Problem Statement 12

3.1. Aims and Objectives 12

4.1. Thesis Structure 13

2. White Matter Microstructure in Type 2 Diabetes and Multiple Sclerosis (Word count: 2052) ... 15

2.1. Brain and White Matter Microstructure 15

2.1.1. Axons 15
2.1.2. Glial cells 16
2.1.3. Myelin 16
2.1.4. Intracellular and Extracellular Spaces 16
2.1.5. Vascular System 17
2.1.6. White Matter Tracts 17

2.2. White Matter Impairment in Diabetes and Multiple Sclerosis 18

2.2.1. Diabetes Mellitus 18
2.2.2. Multiple Sclerosis 20
2.2.3. White Matter Pathology in T2DM and MS 21

3. Diffusion Magnetic Resonance Imaging (Word count: 8190) 24

3.1. Water Molecules Diffusion in the Brain 24

3.2. Water Molecules Diffusion in the Tissue Using MRI 25

3.2.1. Introduction to MRI 25
3.2.2. MRI Basic Principles 26
3.2.3. MRI System and Net Magnetization 27

3.3. MRI Image Formation 30

3.3.1. Slice Selection 30
3.3.2. Spatial Encoding (Phase and Frequency Encoding) 31
3.3.3. MRI Pulse Sequences 32
3.3.4. K-Space Filling Methods 35
3.3.5. Echo-Planar Imaging 36
3.3.6. Encoding MRI Diffusion Signals 37

3.4. Diffusion Imaging and White Matter Microstructure 39

3.4.1. Diffusion Tensor Imaging (DTI) 43
3.4.2. Neurite Orientation Dispersion and Density Imaging (NODDI) 48

4. Optimising the NODDI Scanning Protocol (Word count: 843) 61

4.1. Introduction 61

4.2. Methods and Materials 62

4.2.1. Subjects and Scanning Site 62
4.2.2. NODDI Protocols and Technical Characteristics 62
4.2.3. Data Processing and NODDI Fitting 63

4.3. Result and Discussion 64

4.4. Conclusion 68

5. Investigating Brain Microstructural Alterations in Type 1 and Type 2 Diabetes Using Diffusion Tensor Imaging: A Systematic Review (Word count: 7508) 69

5.1. Introduction 69

5.2. Materials and Methods 71
5.2.1. Data Sources and Search Strategy 72
5.2.2. Study Selection and Inclusion Criteria 72
5.2.3. Data Extraction and Management 73

5.3. Results 73
5.3.1. Overview of Reviewed DTI-T1DM Studies 74
5.3.2. Between-Group Differences: Microstructural Alterations in T1DM 78
5.3.3. Microstructural and Cognitive Abnormalities in T1DM 81
5.3.4. Microstructural Alterations and Metabolic Profile in T1DM 83
5.3.5. Overview of Reviewed DTI-T2DM Studies 85
5.3.6. Between-Group Differences: Microstructural Alterations in T2DM 89
5.3.7. Microstructural and Cognitive Abnormalities in T2DM 92
5.3.8. Microstructural Alterations and Metabolic Profile in T2DM 94

5.4. Discussion 96
5.4.1. T1DM Patients versus Healthy Controls 96
5.4.2. T2DM Patients versus Healthy Controls 98
5.4.3. Common Microstructural Alterations, Cognitive Deficits and Comorbidities 100
5.4.4. Multi-Shell Diffusion Imaging Models 102
5.4.5. Limitations 103
5.4.6. Future Directions 104

5.5. Conclusion 104

6. Investigating Microstructural Changes in White Matter in Multiple Sclerosis: A Systematic Review and Meta-Analysis of Neurite Orientation Dispersion and Density Imaging (Word count: 3344) 106

6.1. Introduction 106

6.2. Materials and Methods 108
6.2.1. Study Registration 108
6.2.2. Study Selection (Inclusion and Exclusion Criteria) 108
6.2.3. Sources, Search Strategy and Screening 109
6.2.4. Data Extraction and Collection 109
6.2.5. Outcome Measures 110
6.2.6. Statistical Analysis 110

6.3. Results 111
6.3.1. Included Studies and Sample Characteristics 111
6.3.2. NDI in White Matter Lesions (MS Subjects) vs Controls 113
6.3.3. NDI in NAWM (MS Subjects) vs Controls 114
6.3,4. ODI in MS White Matter Lesions (MS Subjects) vs Controls 115
6.3.5. ODI in NAWM (MS Subjects) vs Controls 116

6.4. Discussion 116

6.5. Conclusions 119

7. White Matter Microstructural Alteration in Type 2 Diabetes: A Combined UK Biobank Study of Diffusion Tensor Imaging and Neurite Orientation Dispersion and Density Imaging (Word count: 3428) 121

7.1. Introduction 121

7.2. Materials and Methods 124
7.2.1. UK Biobank Cohort 124
7.2.2. Clinical Characteristics and Sample Selection 124

7.2.3. Brain MRI Acquisition 125
7.2.4. Diffusion Image Processing 125
7.2.5. Confound Modelling in UK Biobank Brain Imaging 126
7.2.6. Statistical Analysis 127
7.3. Result 127
7.3.1. Clinical Characteristics 127
7.3.2. White Matter Intergroup Differences and Association with Metabolic Profile: Overview 128
7.3.3. DTI Intergroup White Matter Differences 128
7.3.4. NODDI Intergroup White Matter Differences 128
7.3.5. Diffusion Measures and Correlation with Metabolic Profile 131
7.4. Discussion 135
7.5. Conclusion 138
8. Discussion, Conclusion and Future Directions (Word count: 2369) 139
8.1. Summary of Major Findings 139
8.2. Characterising microstructural changes in DM using DTI 140
8.3. Characterising microstructural changes in T2DM and MS using NODDI 143
8.4. Thesis Limitations 145
8.5. Experimental Design 145
8.6. NODDI Model Assumption 146
8.5. Future Directions 146
8.6. Conclusion 147
Bibliography 148
Appendices 160

Chapter 1

1. Introduction and Background **(Word count: 805)**

This chapter discusses the scientific background and the aims of this thesis. Also, it provides an overview of the research problem and the thesis structure.

1.1. Background

T2DM and MS diseases are major risk factors for brain damage and degeneration, posing great challenges to healthcare globally. The prevalence of the T2DM and MS is increasing worldwide, causing a physical, cognitive, and financial burden for patients and societies. Both disorders cause different types of brain damage and have different effects on normal-appearing brain tissues. MS is a primary CNS disorder characterised by focal brain lesions[1]. On the other hand, T2DM is a systemic-metabolic disorder with secondary brain damage[2]. Also, it is clinically observed that T2DM coexisting with MS causes a higher degree of microstructural changes, more atrophy, and a worse course of MS. These microstructural changes, specifically in brain white matter, appear to be an early indicator of brain neurodegeneration, preceding volumetric losses and functional abnormalities[2,3].

Conventional MRI techniques have provided persuasive evidence and considerably expanded our understanding of brain damage in T2DM and MS, such as brain atrophy[2,4–6] that can be caused by microstructural degeneration in both disorders[7,8]. However, conventional MRI techniques cannot characterise microstructural damage in both diseases. White matter microstructural abnormalities have been investigated in MS using DTI[9–12]. The altered diffusion metrics of white matter in patients with MS matched some histological findings[13,14]. Similarly, DTI has also been used to investigate the white matter microstructural changes in T2DM[8]. DTI is sensitive to white matter microstructural changes, although it lacks specificity for tissue microstructure. When two crossing/kissing fibres are captured in the same voxel, interpreting DTI measures becomes very complex[15,16]. To overcome the

limitations of DTI, NODDI has been proposed as an alternative biophysical diffusion model, which theoretically enables the complete characterisation of white matter microstructure. NODDI employs a high-angular-resolution and multi-shell diffusion model that characterises brain tissue as a simplified mixture of three compartments (intracellular, extracellular, and cerebrospinal fluid (CSF) compartments) and separates signals from each compartment. NODDI parameters explicitly estimate the orientation dispersion and neurite density[17].

As NODDI has detected white matter alterations in a few neurodegenerative diseases[18], applying NODDI to investigate microstructural changes of white matter in T2DM and MS may help better understand white matter neurodegeneration[8]. Since MS and T2DM disorders may have similar effects on white matter connectivity, it would be interesting to see any differences in the extent of white matter damage, distribution, and diffusion parameters.

1.2. Problem Statement

T2DM and MS have been reported to cause white matter microstructural changes. These disease-related changes may cause brain atrophy and neurocognitive impairments, and the latter may lead to lower quality of life. Researchers have faced limitations in characterising microstructural white matter changes using standard DTI in brain voxels with crossing fibres or bending and fanning fibres. For this reason, I am interested in investigating the white matter changes in T2DM and MS using NODDI, and what is the add over conventional DTI?

Aims and Objectives

Pre-Covid-19 aims (interrupted due to the Covid-19 lockdowns).

- To explore the use of NODDI compared to DTI to quantify white matter microstructure in T2DM (by scanning patients at the University of Nottingham).
- To explore the use of NODDI compared to DTI to quantify white matter microstructure in MS (by scanning patients at the University of Nottingham).

- To evaluate the relationship between DTI/NODDI metrics and clinical assessments/metabolic profile (the clinical relevance).

Covid-19 aims (alternative aims to mitigate the Covid-19 impact on my PhD project):

- Systematically reviewing brain microstructural changes in diabetes using DTI.
- Meta-analysing studies used NODDI metrics to investigate white matter microstructural changes in MS.
- Exploring the use of NODDI compared to DTI to quantify white matter microstructure in T2DM using UK Biobank datasets.
- Evaluating the correlation between altered DTI/NODDI metrics and clinical assessments/metabolic profile using UK Biobank datasets.

1.3. Thesis Structure

This thesis is organised into three parts: **Part I** includes the introduction and background chapters, **Part II** consists of the original studies and results, and **Part II** includes the discussion and conclusion chapters.

Part I

Chapter 1 provides a broad context and description of the research problem, motivation, and the rationale of this thesis. Chapter 2 gives an overview of the brain anatomy, including the microstructural environment of white matter, and an overview of T2DM and MS and their microstructural impact on the white matter. In chapter 3, the basics of diffusion MRI and the principles behind it is given. This chapter is divided into three subchapters: First subchapter discusses the water diffusion inside the human brain. The second subchapter summarises the basic principles of MRI and how it enables measuring the water diffusion in brain microstructural tissues using diffusion techniques. The last subchapter covers how MRI models compute the information in brain microstructural tissues. The last chapter describes the UK Biobank project, datasets and the types of population recruited.

Part II

Chapter 4 describes the method and the result of optimising the scanning protocol of NODDI at SPMIC. Chapter 5 describes a comprehensive systematic review that provides evidence of the ability of DTI to image brain microstructural changes in diabetes and how these changes correlate with clinical and cognitive tests. Chapter 6 provides evidence for pre-covid-19 research question 2 through a meta-analysis of datasets from previous studies of white matter damage in MS. Chapter 7 addresses pre-covid-19 research questions 1 and 3 to investigate the white matter abnormalities in T2DM using DTI and NODDI metrics derived from the UK Biobank. Also, it assesses the relationship between metabolic profile and the detected white matter changes.

Part III

Chapter 8 discusses how the findings of the experiments reported in this thesis fit together to answer the research questions. Also, it discusses potential future directions, project limitations and conclusions.

Chapter 2

2. White Matter Microstructure in Type 2 Diabetes and Multiple Sclerosis **(Word count: 2070)**

In this chapter, the brain, including the microstructural environment of white matter, will be discussed (as the focus of this thesis). Also, an overview of T2DM and MS and their impact on the white matter will be presented.

2.1. Brain and White Matter Microstructure

The human brain can be described in three sections: brainstem, cerebellum, and cerebrum. The brainstem connects a greater part of the brain to the spinal cord and has roles in many vital functions, such as breathing control and cardiovascular system control. The cerebellum is placed inferior to the cerebrum occipital lobe, which is crucial in motor control and cognitive functions[19]. The brain's largest region is the cerebrum, separated into four main lobes: frontal, parietal, temporal, and occipital. The cerebral cortex, composed of folded grey matter, comprises many cell bodies of neurons and covers the two cerebral hemispheres[20].

White matter is located beneath the cortex and comprises densely packed axons that connect neurons in the cortical and subcortical grey matter[21]. The white appearance of white matter is caused by the electrical insulator (myelin) that coats the axons. It is formed by oligodendrocytes, nonneuronal cells that wrap up to 150 tightly squeezed cell membranes around axons[22]. In MR imaging, the white matter microstructure in a voxel comprises axons, myelin, glial cells, intra and extracellular spaces, and the vascular system.

2.2. Axons

In human white matter, up to 90% of the space is occupied by axons[21]. Axons are neuron projections ranging from less than a millimetre in intra-cortical neurons to over one meter in the sciatic nerve[23]. The axon is thinner than human hair, and its length varies depending on the neuron type - many are only ~ 0.1-10 μm[24,25].

Axon allows the travelling of electrical impulses from a neuron to other neurons. For one neuron to communicate with several others, an axon commonly develops side branches known as axon collaterals. Like tree roots, these collaterals branch into smaller extensions known as terminal branches. On the tip of each of these is a synaptic terminal. Synapses facilitate the communication between neurons, transferring the information between the axon terminals on one side and the dendrites or cell bodies on the other. The electrical signals travelling along the axon are transformed into chemical signals via the release of neurotransmitters and are then rapidly converted back into electricity as the information moves from one neuron to another[25].

2.3. Glial cells

Glial cells have three common subtypes: oligodendrocytes, astrocytes, and ependymal cells. These cells do not create electrical impulses or involve in any neuronal activities. However, recent research has discovered that astrocytes play an important role in altering synapses in the brain[26]. Astrocytes are responsible for preserving the neuronal working environment, particularly synapses. Oligodendrocytes produce myelin, and ependymal cells produce CSF[27].

2.4. Myelin

Oligodendrocytes form an insulating layer of myelin known as an internode. These myelin layers or sheaths comprise approximately 20% proteins and 80% lipids. Also, they produce an impermeable barrier and improve the conduction speed of action potentials[28,29]. Except for microscopic axons less than 1 μm in diameter, most axons are myelinated[28], and demyelination can occur due to numerous neurological disorders[30].

2.5. Intracellular and Extracellular Spaces

Extracellular space surrounds the brain cells (refers to the space outside the cells), which is made up of a fluid closely resembling CSF with the addition of extracellular molecules[31]. The

cell nucleus and cytoplasm, formed of cytosol (the majority of which is water) and cell organelles, make up the intracellular space[32]. The cell membrane restricts water diffusion, yet it is not entirely impermeable to water. Instead, water diffuses slowly across the lipid membrane and is actively carried across by water-specific membrane channel proteins[33].

2.6. Vascular System

The brain's vascular system consists of arteries, veins, and capillaries, which deliver oxygen, glucose, and other nutrients to the brain cells. Cerebral blood circulation is made up of arterial and draining venous circulations. The arterial system can then be divided into anterior and posterior cerebral circulations based on anatomical position and size. The macro-circulation is responsible for regional perfusion of the cerebrum. The microscopic exchange of oxygen and nutrient within the vasculature and the blood-brain barrier (BBB) is called microcirculation[34]. This cerebral blood circulation lacks orientational coherence[35], which could cause flowing blood to show displacements like diffusion but faster[36].

2.7. White Matter Tracts

According to their connectivity, white matter tracts are divided into three types. First, projection fibres connect the cortex to the deep grey matter, brainstem, cerebellum, spinal cord, or vice versa. Diffusion tractography can identify those projecting fibres, including corticospinal fibres, corticobulbar fibres, corticopontine fibres, thalamic radiations, and geniculocalcarine fibres (optic radiations). Second, association fibres connect multiple cortical regions within the same hemisphere. These fibres differ in size and length, the short fibres containing subcortical U fibres. However, the important long tracts are the cingulum, superior and inferior occipitofrontal fasciculi, uncinate fasciculus, superior longitudinal fasciculus (SLF), arcuate fasciculus, and inferior longitudinal fasciculus (occipitotemporal). Third, the commissural fibres that include the anterior commissure and the corpus callosum connect similar cortical regions in both hemispheres (Table 2.1)[37].

White matter tracts	Connection
Cingulum	It connects the cingulate gyrus to the entorhinal cortex
Fornix (FX)	It connects the hippocampus and the septal region to the hypothalamus
Superior longitudinal fasciculus (SLF)	SLF connects frontotemporal and frontoparietal regions
Inferior longitudinal fasciculus (ILF)	ILF connects ipsilateral temporal and occipital lobes
Superior fronto-occipital fasciculus (SFOF)	SFOF connects frontal lobe to ipsilateral parietal lobe
Inferior fronto-occipital fasciculus (IFOF)	IFOF connects the ipsilateral frontal and occipital, posterior parietal, and temporal lobes
Uncinate fasciculus (UF)	UF connects the frontal and temporal lobes
Thalamic radiations (TR)	TR connects lateral thalamic nuclei to cerebral cortex through the internal capsule
Corticofugal fibres (Descending projection fibres)	Motor cortex and cerebral peduncle through the internal capsule
Corpus callosum (CC)	CC connects corresponding cortical areas of both hemispheres
Anterior commissure (AC)	AC connects olfactory bulbs and nuclei, and amygdala

Table 2. 1. *White matter tracts and their connections*[37,38]*.*

2.8. White Matter Impairment in Diabetes and Multiple Sclerosis

2.8.1. Diabetes Mellitus

Diabetes Mellitus is a complex metabolic disorder associated with microvascular and macrovascular diseases. It is characterised by persistently elevated blood glucose levels (hyperglycemia) caused by insufficient insulin production or dysfunctional response to insulin[39–41]. The human body consists of millions of cells that require food for energy consumption. The digestion of carbohydrates in the diet is broken down in the digestive tract and absorbed in the small intestines into sugar. They are carried by the blood to organs or tissues for energy use or storage in the liver or muscles as glycogen; however, the produced sugar cannot be absorbed by cells without the assistance of insulin released by beta cells (β cells) in the pancreas. When sugar exits the bloodstream entering the cells, the blood sugar becomes lower. When blood sugar cannot enter the cells due to insulin deficiency, the blood sugar level rises, causing hyperglycemia[42].

For this reason, diabetes prevents the body from gaining energy from food in two ways. First, the inability of β cells to secrete insulin hormones leads to insufficient use of food

sugar for energy. Second, the pancreas produces insulin; however, specific body tissues do not take up insulin, causing insulin resistance and preventing the body from using sugar for energy.

T2DM is previously referred to as non-insulin-dependent diabetes, accounting for 90-95% of all diabetes[43]. In 2017, T2DM affected approximately 462 million people, or 6.28% of the global population, with a prevalence rate of 6059 cases per 100,000 people[44]. The incidence risk of T2DM is strongly associated with obesity, age, lack of physical activities, and sometimes ethnicity. T2DM is classified by the deficiency of β cell function and insulin resistance by target organs[45]. Patients do not notice the severity of the symptoms of T2DM at the early stages. Therefore, such patients are subject to an increased risk of vascular complications[43]. In patients younger than 25 years, T2DM is very challenging due to their complex phenotypes, which require intensive management to slow the progression of vascular complications. By contrast, patients 65 years or older require balanced control of comorbidities, hypoglycaemic risk and cognitive deficits[46].

Several complications are associated with T2DM, and they vary based on the duration of the disease development. Acute metabolic complications strongly correlate with mortality, including diabetic ketoacidosis, hyperglycaemia, and hypoglycaemia. The other types of complications are chronic and associated with long-term vascular abnormalities. These vascular abnormalities can result from blood glucose elevation in T2DM patients, which may damage blood vessels. These vascular complications are grouped under microvascular (small vessel damage) and macrovascular (large vessel damage). Microvascular abnormalities can affect several organs, such as the eyes, kidneys, and nerves. Also, these abnormalities involve changes in the cerebral microvasculature, causing functional and structural damage to the brain. On the other hand, macrovascular abnormalities cause heart and peripheral arterial diseases[47].

2.8.2. Multiple Sclerosis

MS is a chronic-autoimmune disease characterized by inflammation and demyelination that affect the CNS. MS destroys the axons by attacking the myelinated sheath covering the axons to variable degrees[48]. This inflammatory attack leads to white matter and grey matter lesions in the brain and spinal cord[3], involving different environmental and genetic factors. Several studies compared different populations and revealed different rates of prevalence and incidence based on geography and ethnicity. For instance, in Japan, the prevalence ranges from 2 per 100,000 to more than 100 per 100,000 in North America and Northern Europe[49].

The cause of MS is unknown yet, but it involves viruses, metabolism, and environmental factors, leading to an autoimmune disorder attacking the CNS. In MS, the disruption of the BBB, the leukocyte influx into the CNS, and demyelination that reduce the conductivity inside axons are all pathogenic features. MS begins as a relapsing-remitting disease that progresses to a progressive disease within a few years[50,51] (Fig. 2.1). In the MS disease, an autoreactive T-cell infiltration occurs across the BBB. Normally, regulatory T-cells (particularly CD4+CD25+) suppress autoreactive T-cells (faulty T-cells that wrongly react to the body rather than infections), but this process is interrupted in MS[52]. T-cell apoptosis is avoided by overexpressing a protein (ARRB1) that dampens the cellular response to stimuli[53]. As a result, the damaged tissues become inflamed.

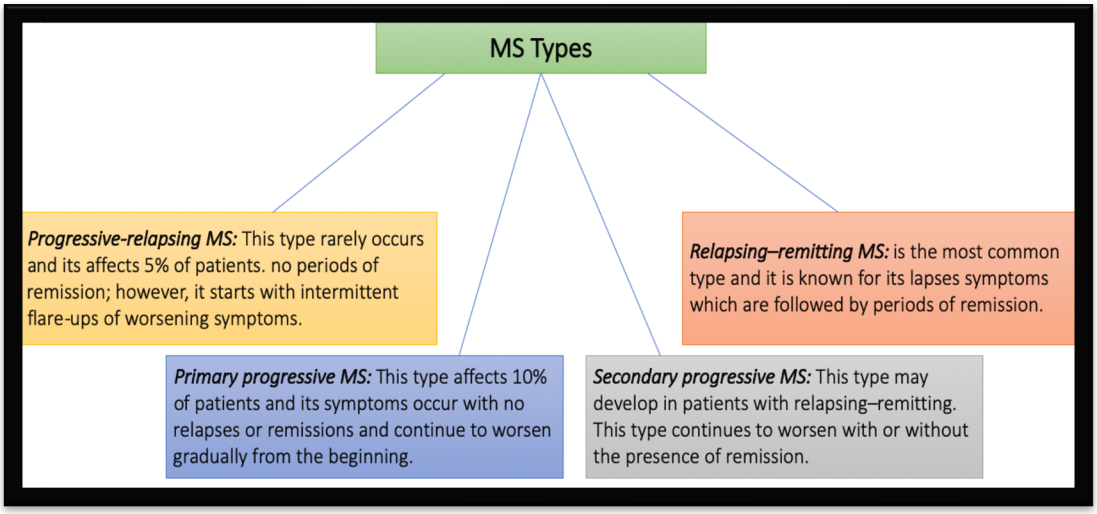


Figure 2. 1. *Demonstration of the types of MS*[48] *that have been traditionally grouped into four major types based on the course of the disease and an agreement made by neurologists. This classification has been refined recently into categories based on the clinical phenotype and disease activity*[51]*.*

MS is primarily a white matter disease in the early relapsing-remitting stage, marked by focal plaques of demyelination. Inflammation and BBB leaking in MS are related to active demyelination. Additional pathologies emerge as the disease progresses, including slow enlargement of pre-existing white matter lesions in the absence of BBB damage, extensive demyelination of cortical areas, and diffuse damage to the normal-appearing white matter (NAWM) and grey matter. Combined, these many forms of tissue damage result in substantial brain tissue loss and atrophy[54,55].

2.9. White Matter Pathology in T2DM and MS

There is substantial evidence that T2DM is directly associated with small cerebral vessel disorders. The prevalence of small cerebral vessels rises from 5% in adults aged 50 to about 100% in people aged 90[56], significantly contributing to the development of white matter abnormalities. Although white matter abnormalities are becoming more well-known, their aetiology remains unknown. Various studies have suggested that white matter abnormalities are caused by chronic hypoperfusion and several factors, including cerebral blood flow autoregulation, venous collagenases, reduced cerebrovascular responsiveness, and BBB disruption. Many scientific findings are being made to understand better the

mechanism of white matter abnormalities related to T2DM. Inflammatory response, oxidative stress, endothelial dysfunction, and other factors are all involved[57–59] (Fig. 2.2).

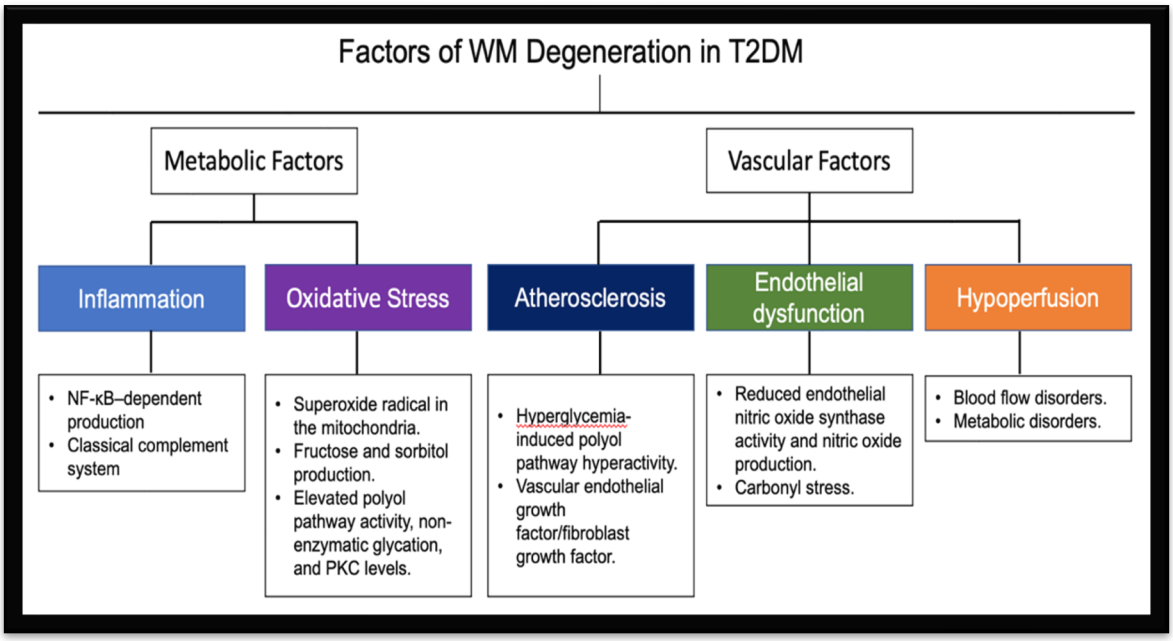


Figure 2. 2. *The mechanism for WM-related abnormalities in T2DM*[59].

Demyelination and neurodegeneration in MS are characterised by confluent plaques of demyelination in the white matter, axonal degeneration, and astrocytic gliosis[60]. Demyelination in the white matter causes neuronal damage via various suggested pathways, including microglia activation, persistent oxidative stress, and mitochondrial damage in axons[61]. As a result, demyelinated axons cannot conduct impulses at average velocity, which are more susceptible to Wallerian degeneration, trans-synaptic degeneration, and other neurodegenerative processes[62]. MS demyelination occurs in focal lesions in the white matter pathways and diffusely across NAWM. Several approaches have pathologically classified white matter lesions caused by MS. A staging scheme has been created to separate white matter lesions[63,64] (Table 2.2). Pathological profiles of white matter lesions in MS can also be used to characterise them, and there are four demyelination patterns of white matter lesions. Pattern I is characterised by infiltration of T cells, active demyelination, activation of microglia, and myelin-laden macrophages. However, there is no immunoglobulin (Ig) or complement

deposition. In this pattern of lesions, the demyelination process is characterised by simultaneously losing myelin proteins from injured myelin sheaths. Pattern II lesions, the most prevalent type, are identical to the pattern I lesions but contain Ig and complement deposition. Pattern III lesions have inflammatory cells, microglia, and macrophage activation but no Ig or complement deposition. There is obvious oligodendrocyte death with a loss of the peptide in myelin-associated glycoprotein (MAG). Pattern IV lesions are infrequent and are linked with non-apoptotic oligodendrocyte death in a rim of peri-plaque white matter[65].

WML Types and Stages	Biological Definition
Active WMLs	Hypercellular lesions with relatively preserved axons, a significant infiltration of lymphocytes, myelin-laden macrophages and major histocompatibility complex (MHC)-II+cells are equally distributed throughout the lesions.
Chronic active WMLs	Axonal preservation is also present, but myelin-laden macrophages accumulate at the edges of the lesions.
Inactive WMLs	Hypocellular lesions are characterised by a significant loss of axons, oligodendrocytes, astrogliosis, and minimal macrophage/microglia and lymphocyte infiltration seen in active WML.
Pre-active WMLs	Clusters of MHC-II+microglia characterise them without demyelination and the absence of lymphocytes.

Table 2. 2. *White matter lesions (WMLs) classification and staging system[65].*

Chapter 3

3. Diffusion Magnetic Resonance Imaging (Word count: 7520)

This chapter focuses on the foundations of diffusion MRI and its principles. It is divided into three subchapters: First subchapter discusses the water diffusion inside the human brain. The second subchapter summarises the basic principles of MRI and how it enables measuring the water diffusion in brain microstructural tissues using diffusion techniques. The last subchapter covers MRI diffusion models and image processing steps.

3.1. Water Molecules Diffusion in the Brain

Water diffusion or molecular water diffusion is the movement of water molecules within the human body when the temperature rises above 0 Kelvin[66]. This molecular water motion is also known as Brownian motion, which was discovered in 1827 by Robert Brown after observing the movement of pollen grains through a microscope[67]. Molecular diffusion of water can be used to explore the microstructure of an object non-invasively. The thermal energy of molecules in open space causes them to diffuse randomly in any direction. However, when molecules in an object come across barriers, their mobility slows down, and it is directional such that the molecular diffusion is less restricted in the direction parallel to the barriers than in the direction perpendicular to the barriers[68].

Grey matter, CSF, and white matter are the three tissue types that form the brain. The barriers to water diffusion in each tissue type are configured differently. As a result, different patterns of diffusion emerge in the displacement of water molecules across the brain. Since there are no barriers in CSF, water molecules can move freely in any direction. Thus, the diffusion of water in CSF is isotropic with higher diffusivity. Grey matter comprises cell bodies and dendrites, causing water diffusion to be isotropic. However, its diffusivity is lower than CSF due to barriers in cell membranes. White matter is a fibre tract area that consists primarily of myelinated axons. For this reason, water molecules in white matter have free

diffusion along the fibre tract but have more restricted diffusion in the direction perpendicular to the tract, resulting in an anisotropic diffusion (Fig. 3.1)[69].

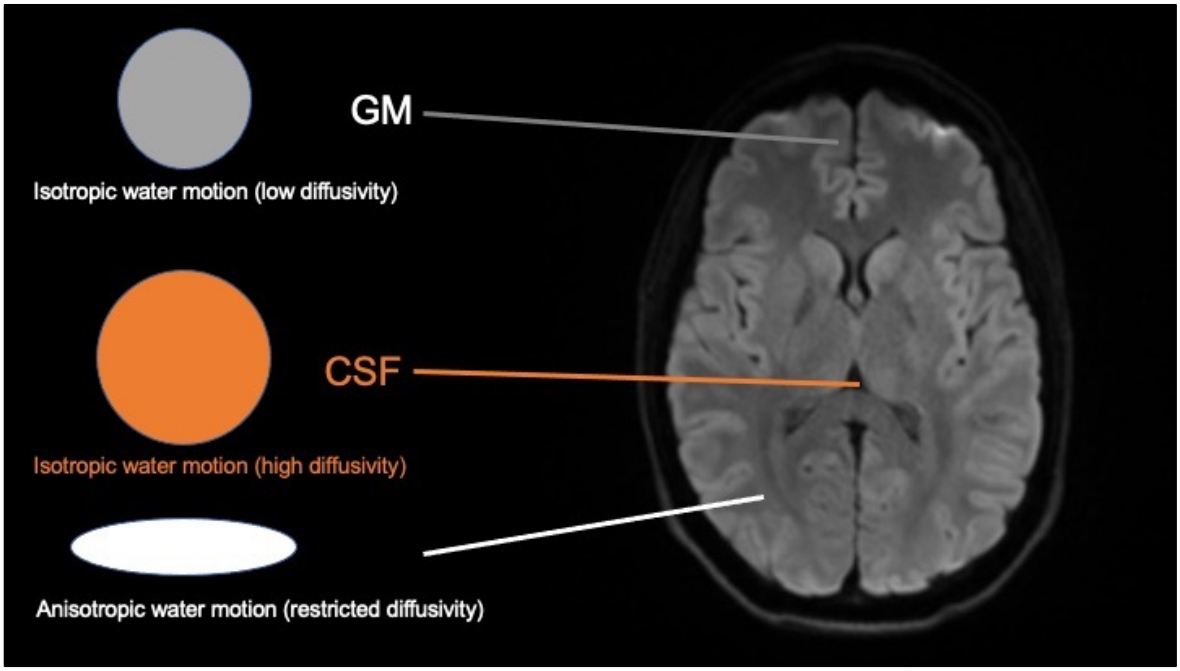


Figure 3. 1. *Water diffusion in white matter, grey matter (GM) and CSF and adapted from a previous work*[310]*.*

3.2. Water Molecules Diffusion in the Tissue Using MRI

3.2.1. Introduction to MRI

Nuclear Magnetic Resonance (NMR) is a quantum phenomenon that underpins MRI. This phenomenon relates to the absorption of proton energy. It was initially described in 1938 by Rabi et al.[70] when their research team conducted a study measuring the magnetic momentum of chemical elements. Bloch and Purcell further described NMR in materials in 1946[71]. The spatial encoding utilises magnetic gradients to allow MR imaging (MRI) systems to be successfully implemented by Lauterbur et al.[72]. His research team pioneered the translation of the physical phenomenon of NMR into the modern MRI system used in clinical practice and scientific research.

3.2.2. MRI Basic Principles

MRI is an imaging technology that measures the distributions of protons in biological samples using high magnetic fields and radiofrequency (RF) fields. Although the hydrogen nucleus is the most used, other nuclei, including those of sodium, carbon-13, and phosphorus, interact with strong magnetic fields. When these nuclei are in a random distribution in space, their magnetic moments tend to cancel each other, and the net magnetization vector becomes zero (Fig.3.2A). When the object is exposed to an external magnetic field ($\boldsymbol{B_0}$), the torque from the $\boldsymbol{B_0}$ causes the magnetic moments to precess and create a net magnetization. As a result, the nuclei start to orient either parallel or antiparallel to the $\boldsymbol{B_0}$ (Fig.3.2B)[67,73].

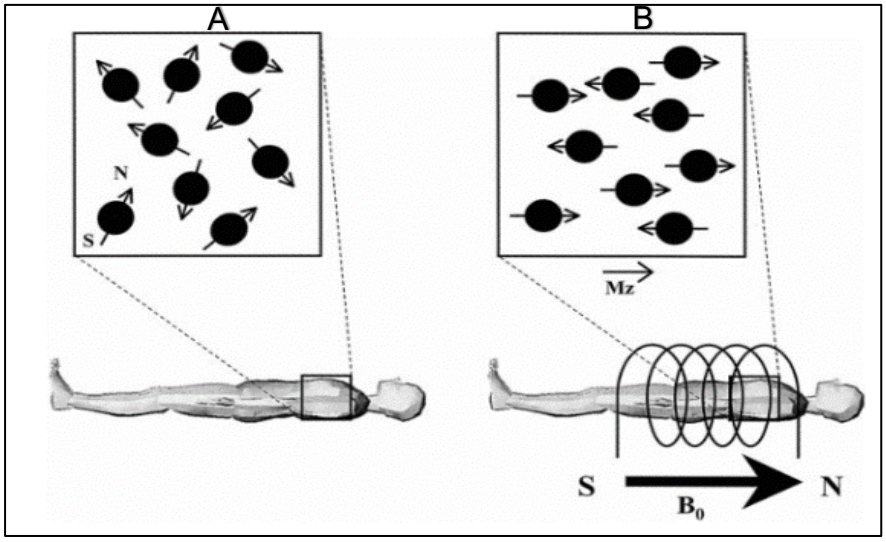


Figure 3. 2. *(A) When there is no magnetic field, the magnetic moments of the hydrogen nuclei are distributed randomly, resulting in a net magnetization of zero. (B) In the presence of a powerful external magnetic field, the nuclei move parallel or antiparallel to* $\boldsymbol{B_0}$*, with a few tending to be more parallel. As a result, a net magnetization vector M parallel to the external magnetic field is produced*[67]*.*

The magnetic moments of parallel and antiparallel hydrogen nuclei are equal but opposing and cancel each other out. However, there are always slightly more hydrogen nuclei parallel to $\boldsymbol{B_0}$, referred to as the ***NMV*** (net magnetisation vector) and denoted by the sign ***M***.

Nuclei with parallel alignment have the lowest energy, whereas nuclei with anti-parallel alignment have the highest energy. The nuclei do not align with the magnetic field but wobble or precess around the external field direction (Fig.3.3A)[67].

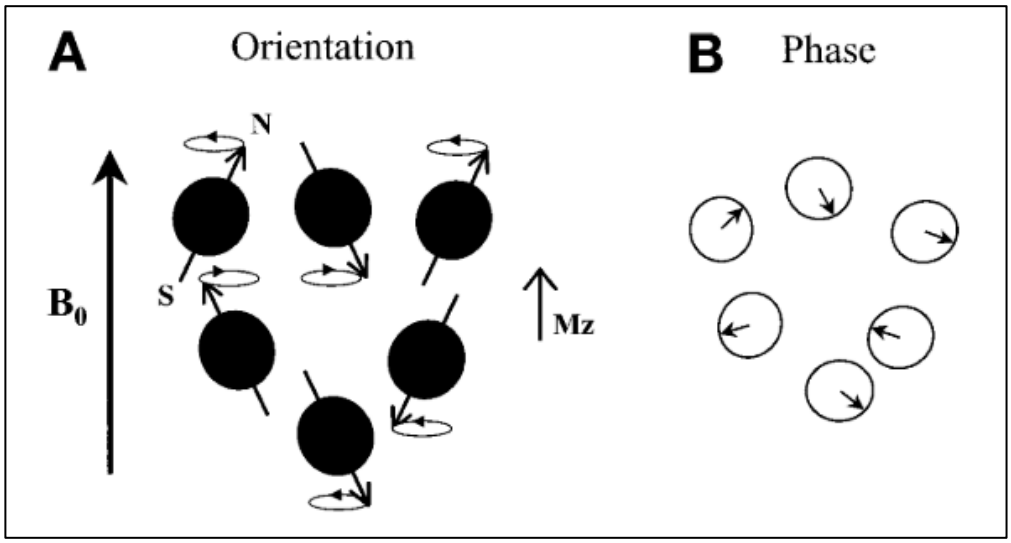


Figure 3. 3. *(A) The nuclei precess around the external field direction* ***B_0****, spinning around their axes. (B) The precession phase around the magnetic-field axis is different for every single nucleus*[67]*.*

The given Larmor equation determines the frequency of this precession:

$$\omega = \gamma B_0$$

Where ***ω*** refers to the Larmor frequency, ***B_0*** refers to the magnetic field strength, and ***γ*** refers to the gyromagnetic ratio of the nucleus (e.g., hydrogen = 42.576 MHz/Tesla). The Larmor frequency for hydrogen commonly used in commercial MRI scanners of 1.5 Tesla is 63.75 MHz. It is worth noting that the precession phase around the magnetic field axis differs for each nucleus (Fig.3.3B)[67].

3.2.3 MRI System and Net Magnetization

According to Faraday's law, when ***M*** is in a continuous precession around the direction of the magnetic field, this moving ***M*** creates an electromotive force in the coil. A radio frequency (RF) pulse with low amplitude or ***B_1*** produced by an RF electrical current in the coil with an

axis vertical to B_0 can rotate ***M*** (Fig.3.4). ***M*** is tilted from the z-axis toward the XY-axis (the transverse plan) by switching on B_1 field for a few milliseconds (Fig.3.5). B_1 application is known as the RF pulse. When B_1 is turned off, the tilted magnetization precesses around B_0, causing a free induction decay (FID) or NMR signal in the coil. The RF pulses can cause ***M*** to rotate by different angles known as flip angles (e.g., 45°, 90°, and 180°)[74]. Various RF pulses can be used to alter the moving direction of the nuclei: By applying a 90° rotation, RF excitation pulses rotate ***M*** from the z-axis to XY-axis. By applying 180°, the RF inverse pulse turns ***M*** from the XY-axis back towards the z-axis[75].

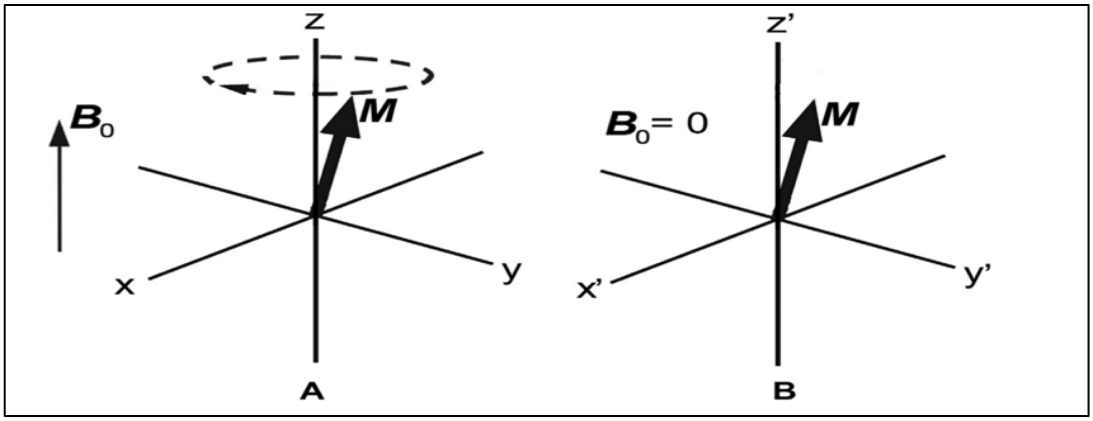


Figure 3. 4. *M visualisation in the laboratory (A) and a rotating coordinate system (B). In the spinning frame, the magnetization is static, as if B_0 were 0*[75].

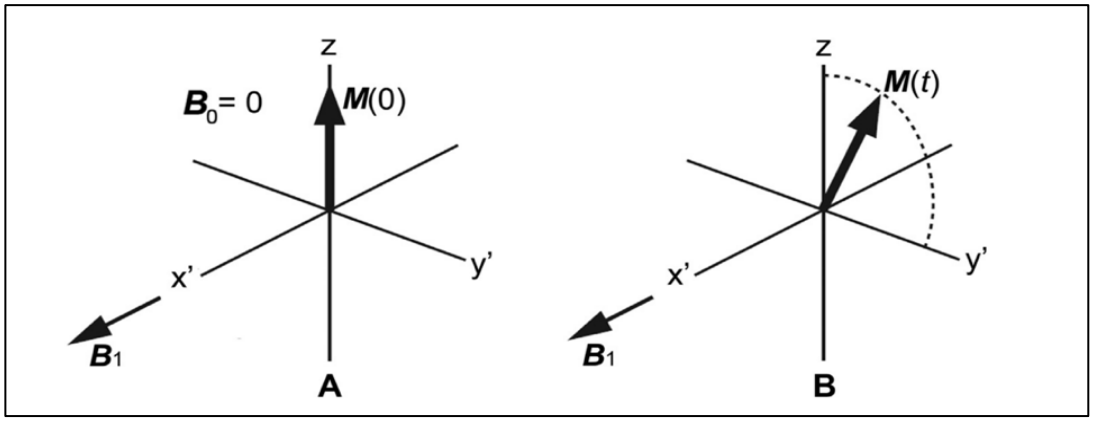


Figure 3. 5. *The influence of the RF pulses in the rotating frame. (A)* ***M*** *is rotated to the transverse plane (XY). (B) The amplitude of the RF pulse and its duration is determined by the angle of rotation*[75].

The MRI system manipulation of the net magnetization introduces two relaxations. The first is called longitudinal relaxation (spin-lattice relaxation) along $\boldsymbol{B_0}$ direction, and the second is known as transverse relaxation (spin-spin relaxation) at the transverse axis.

3.2.4. Spin-Lattice and Spin-Spin Relaxation

Due to the reduced number of spins parallel to the magnetic field following an RF pulse, ***M*** is no longer in equilibrium. ***M*** has a non-zero component in the axis vertical to the static magnetic field (the transverse plane). The magnetic moments interact with magnetic fields at the molecular level, causing an over-time decay of the precessing spins in the transverse plane. The spins of transverse ***M*** lose coherence (dephasing stage) due to such an interaction. The decay of ***M*** in the transverse axis is known as spin-spin relaxation, transverse relaxation or T2 relaxation (Fig.3.6A)[75].

Due to the inhomogeneous static magnetic field that produces the MR signal, the transverse ***M*** decays with a time constant shorter than T2. T2* represents the time constant for the MR signal to decay in MRI systems. Following the RF excitation pulse, the protons gradually begin to lose energy, and ***M*** begins to rotate back towards the z-axis. Also, the protons begin to recover to equilibrium at the z-axis. Longitudinal or spin-lattice relaxation is the term for this process (Fig.3.6B)[40,75].

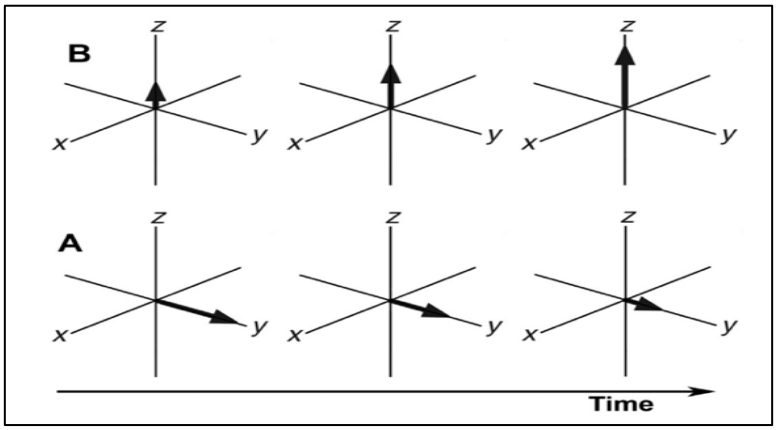


Figure 3. 6. *(A)Transvers relaxation; (B) Longitudinal relaxation of* ***M****. The transverse* ***M*** *decays to zero with the time constant (T2), while the longitudinal* ***M*** *recovers to equilibrium with the time constant (T1)*[54]*.*

3.3. MRI Image Formation

3.3.1. Slice Selection

The MRI system determines how much signal comes from each three-dimensional location (voxel) in the patient to produce an image. The simplest method is to locate a slice first, then the signal at each two-dimensional location (pixel) within it. This technique is known as spatial encoding and is carried out through the MRI gradient system. When the gradient coil is turned on, the magnetic field strength and the precessional frequency of hydrogen nuclei change in a linear fashion. As a result, the hydrogen nuclei situated along the gradient axis have a specific precessional frequency dependent on the gradient's amplitude and the nucleus's location along the gradient. A selected slice is excited by an RF excitation pulse that oscillates at the same frequency of hydrogen nuclei in this selected slice. As a result of this excitation, resonance develops in these nuclei. Due to the gradient presence and their different precessional frequencies, other nuclei along the gradient cannot resonate.

Three gradients perform slice selection during the RF excitation pulse (Fig.3.7). They are as follows: 1) The z gradient modifies the strength and frequency of the magnetic field along the z-axis, which chooses the axial images (from head to foot of the subject). 2) The x gradient changes the magnetic field strength and the precessional frequency along the x-

axis. This gradient makes it possible to choose sagittal images (from the left to right side of the subject). 3) The y gradient changes the magnetic field strength and precessional frequency along the y-axis to select coronal images (from the back to the front of the subject). 4) Oblique slices are selected by combining two or three gradients[76].

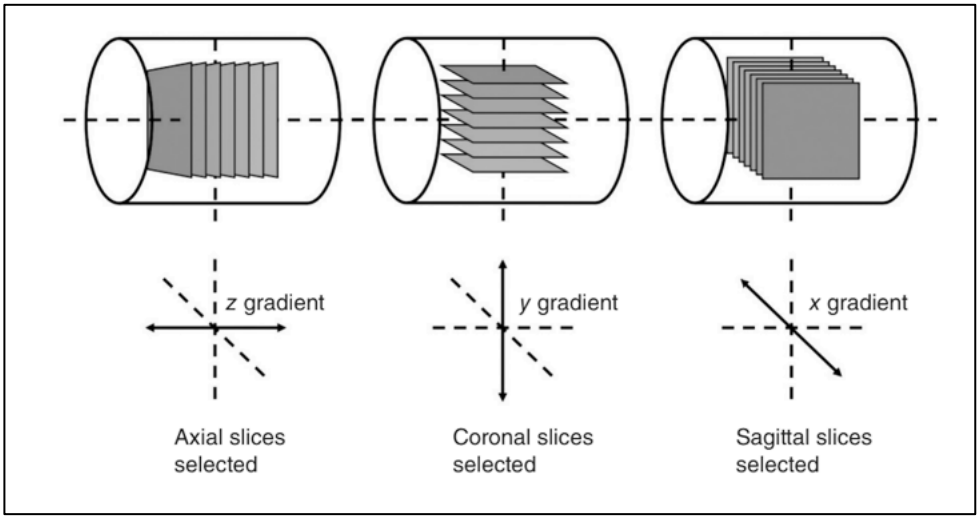


Figure 3. 7. *X, Y, and Z as slice selectors*[76].

3.3.2. Spatial Encoding (Phase and Frequency Encoding)

Combining phase and frequency encoding with pulsed gradients can effectively encode the positions of protons within a slice. The phase encoding uses a gradient that encodes the protons at non-identical positions with characteristic phases, while the frequency encoding has a similar approach to slice selection. Typically, the phase encoding gradient starts after turning off the RF excitation pulse between slice selection and frequency encoding (Fig.3.8A). At the same time, the frequency encoding gradient starts when the signal is measured (Fig.3.8B). By applying a gradient along one axis of the two-dimensional image, slices are phase-encoded along the shortest axis, while slices are frequency-encoded along the longest axis[76].

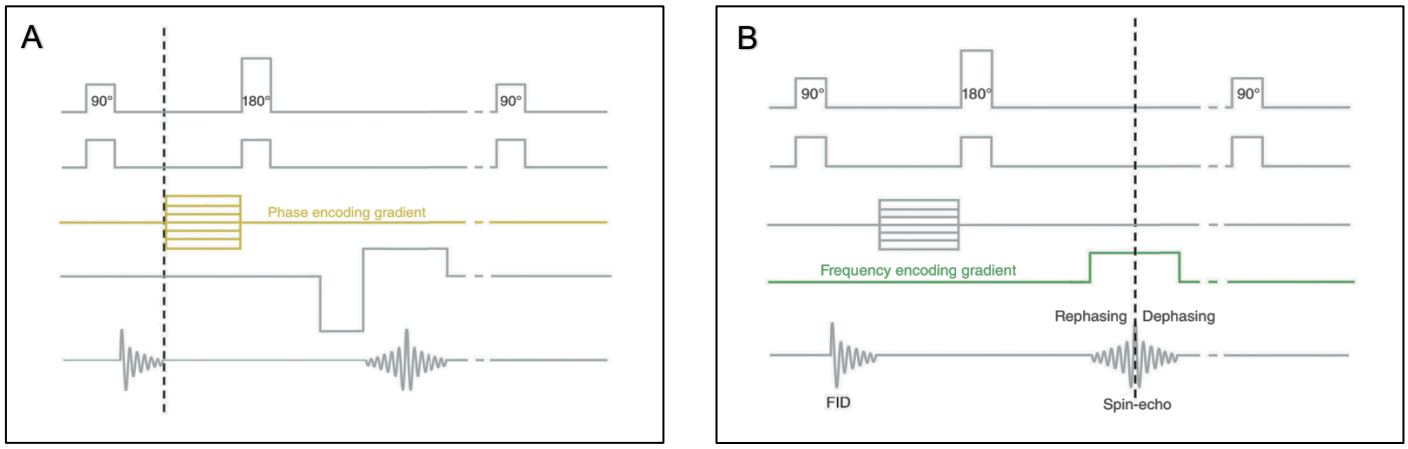


Figure 3. 8. *The phase-encoding (A) and the frequency-encoding gradients in a spin-echo pulse sequence (B)*[76].

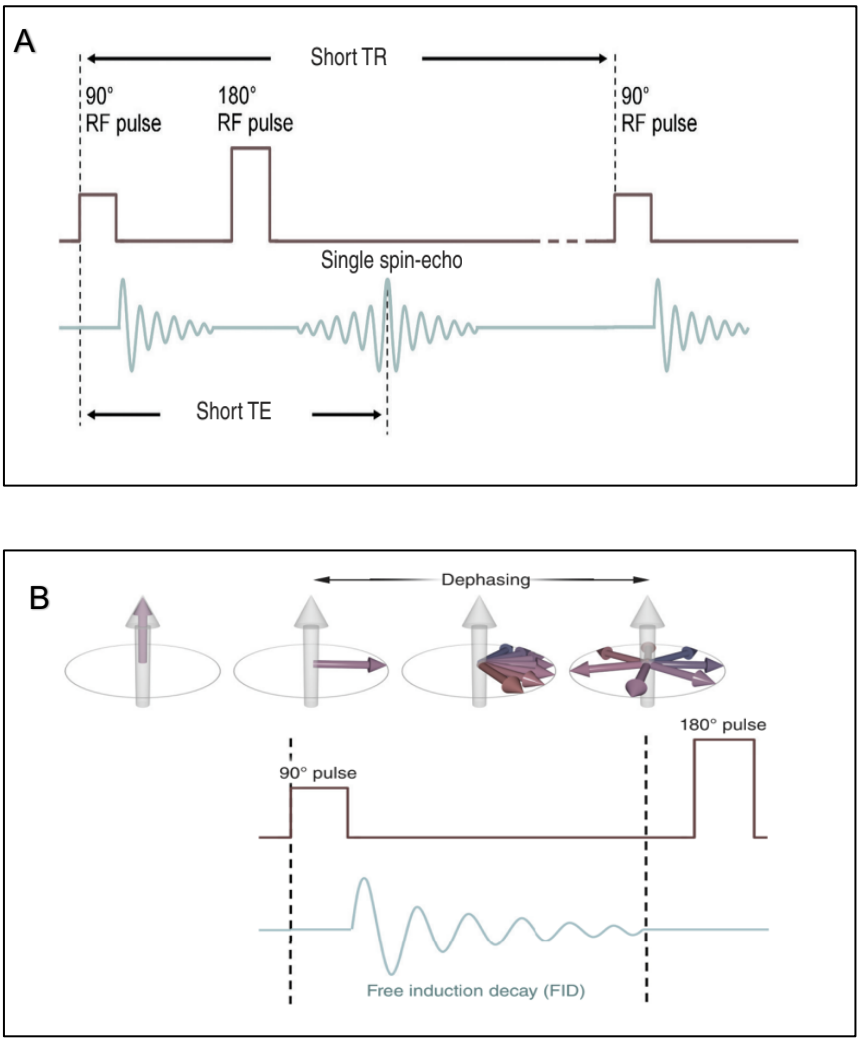
3.3.3. MRI Pulse Sequences

In MRI, a pulse sequence is a series of events that a computer program initiates, including RF pulses, gradient switching, and data acquisition. The role of the pulse sequence is to modify the magnetization to produce the desired signal and image contrast. The most important imaging parameters for manipulating an MRI pulse sequence are repetition time (TR), echo time (TE), field of view (FOV), matrix size, and k-space filling[77]. There are different types of MRI pulse sequences; this section focuses on the spin echo (SE) and pulsed gradient spin echo (PGSE) sequences.

3.3.3.1. Spin Echo (SE)

Erwin Hahn developed the spin echo in 1949 to determine the maximum signals and remove artefacts caused by the signal susceptibility and the magnetic field inhomogeneity. Hahn developed the spin-echo pulse sequence by combining the two 90º RF pulses. Combining the two RF pulses of spin echo recovers a portion of the signal by utilizing the second RF pulse[78]. Carr and Purcell improved the spin echo by combining one 90º RF pulse with one 180º RF pulse[79] (Fig.3.9A). RF rephasing distinguishes all spin-echo pulse sequences. A 90° RF excitation pulse is typically used in the spin-echo pulse sequence to flip ***M*** into the transverse plane entirely. ***M*** precesses in the transverse plane, producing a voltage in the

receiver coil. An FID happens when the 90° RF excitation pulse is turned off. Inhomogeneities cause T2* dephasing, and the signal decays to zero immediately in $\boldsymbol{B_0}$ field (Fig.3.9B). A second RF pulse is employed to adjust for this dephasing and rephasing of the magnetic moments of hydrogen nuclei. It is often known as the 180° RF rephasing pulse because of its magnitude (Fig.3.9C)[37,76].



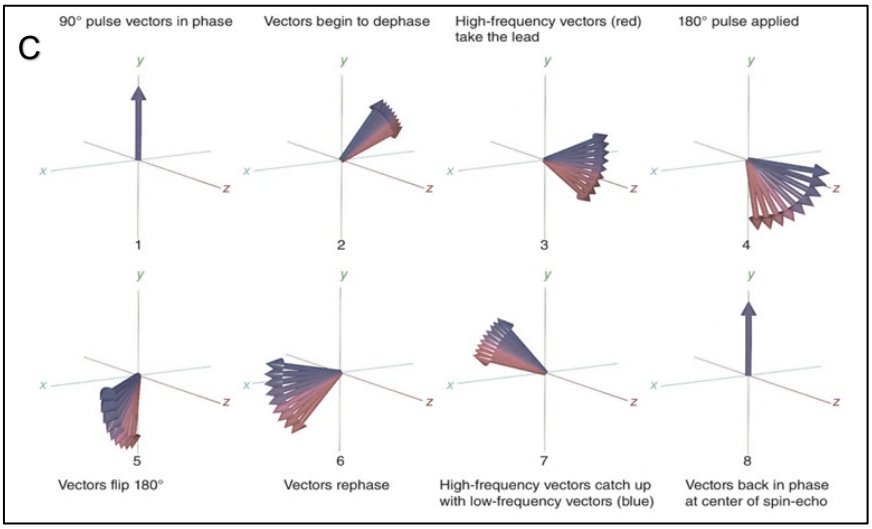


Figure 3. 9. *Conventional SE pulse sequence (A); T2* dephasing (B); 180º rephasing (C)* [55].

3.3.3.2. Pulsed Gradient Spin Echo (PGSE) Sequence

The pulsed gradient spin echo (PGSE) technique was developed by Edward Stejskal and John Tanner in the mid-1960s. This technique is the source of all modern diffusion-weighted sequences[80]. On either side of the 180° RF pulse, symmetric and strong diffusion-sensitizing gradients are applied (Fig.3.10). The pair of gradients has no effect on the phases of stationary spins because the second gradient lobe reverses any phase accumulation caused by the first gradient. On the other hand, the diffusing spins migrate to different places between the first and second lobes, losing phase and signal[81].

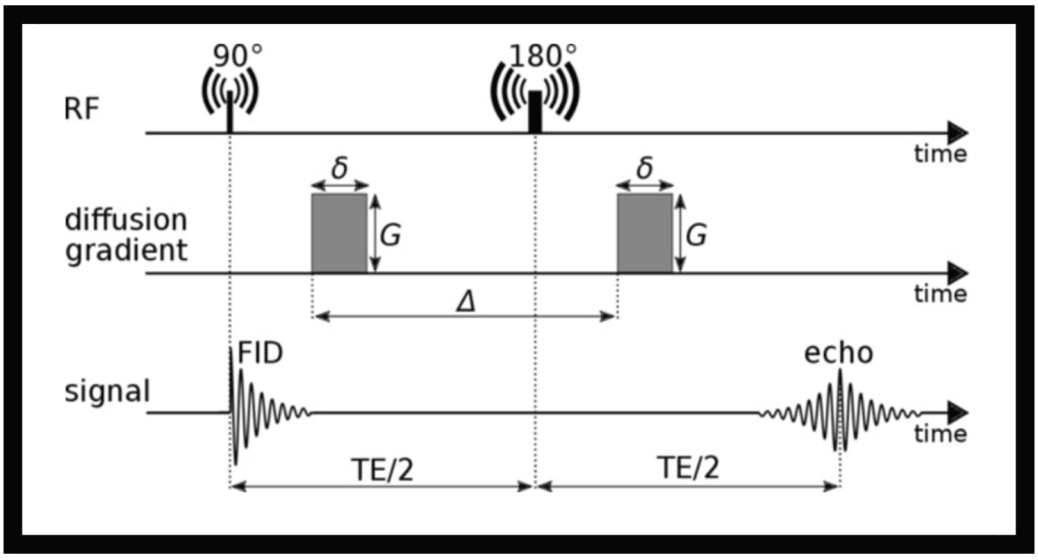


Figure 3. 10. *Schematic illustration of the PSGE*[311].

3.3.4. K-Space Filling Methods

The k-space represents and stores the spatial frequency of an object in two or three dimensions. The space covered by the phase and frequency encoding data defines the k-space[82]. To generate the final image, this stored data is subjected to a mathematical operation known as Fourier Transform (FT)[83]. A single slice corresponds to the real-time acquisition of a k-space plane. Each k-space point comprises phase, frequency (x and y coordinates), and the information of signal intensity (brightness). After the k-space acquisition, FT is applied to form the final image. Each pixel in the resulting image is the weighted sum of all the k-space points. Therefore, disruption of any k-space point results in final image distortion, determined by the frequency and phase-related data stored at that point. The centre of k-space stores contrasts information, whereas the periphery of k-space stores spatial resolution (Fig.3.11)[84].

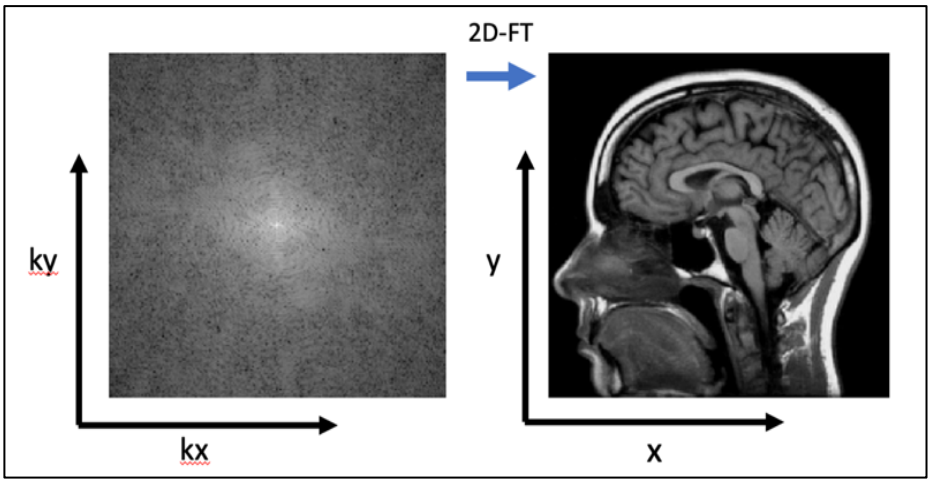


Figure 3. 11. *A depiction of data in 2D FT space (k-space) and reconstructed data in image space.*

The imaging data used to fill the k-space is obtained from the MR signal. The MR imaging signal is in a Fourier-like structure that is proper for sampling the k-space because gradients were used for phase and frequency encoding. The line-by-line Cartesian technique to fill the k-space has been the dominating method over the last 30 years (Fig. 3.12A). Each digitised echo in the Cartesian method fills a k-space line. Each k-space point has both

imaginary and real components due to the fact that the echo signal is recorded in quadrature. The values of the k-space on the left side of each row are acquired early, but those on the right side are acquired later. The centre of the echo where the large values are stored is in the middle of each row of the k-space[85].

In 2DFT imaging, each k-space row corresponds to the echo from every single application of the phase-encoding gradient. The rows in the centre of the k-space represent low-order phase-encoding steps, whereas the rows at the top and bottom represent higher-order phase-encodings. As the echo amplitudes are stronger at low-order phase-encoding steps, the k-space values will be higher towards the centre of the k-space[85]. Recently, additional k-space-filling methods have been introduced to fill the k-space faster, such as the spiral and radial trajectories (Fig.3.12B & C). These methods are becoming increasingly popular in clinical scanners[76,84,86].

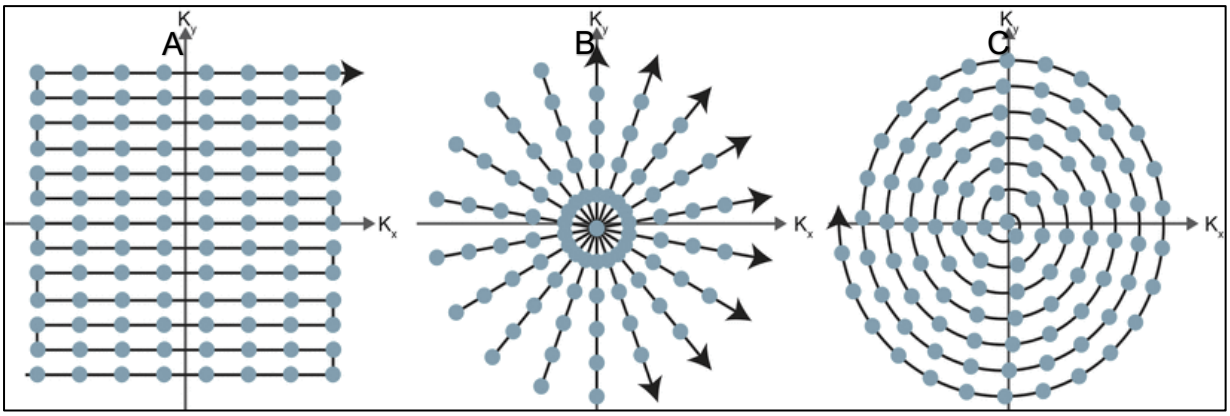


Figure 3. 12. *K-space filling methods. The cartesian sampling method (A), The radial method (B), and the spiral method (C)[86].*

3.3.5. Echo-Planar Imaging

Echo planar imaging (EPI) is a fast-imaging technique[87], introduced by Mansfield in 1977[88]. In EPI, several echoes of different phase encoding steps are recorded using rephasing gradients rather than the multiple 180^0 radiofrequency pulses and by a fast reversal of the readout gradient. This switching or reversal can also be accomplished sinusoidally. The EPI

method may employ gradient echoes entirely or a spin-echo in conjunction with a train of gradient echoes[87].

EPI fills the k-space line by line in a fast manner. As a result, the k-space is filled in a "zig-zag" fashion, causing the signal to move from the centre of the k-space to the left-bottom corner. Originally, the EPI referred to the sequence that recorded data from the entire k-space for a complete 2D plane following one RF-excitation pulse. Recently, the term has been modified to refer to any fast gradient-echo or spin-echo sequences in which k-space is filled with one or fewer RF excitation pulses. In modern MRI systems[85], the EPI is referred to as single-shot EPI and multi-shot EPI. EPI makes diffusion imaging more feasible as it collects the signal rapidly. Despite its advantages, EPI has limitations and produces MRI image artefacts[89].

3.3.6. Encoding MRI Diffusion Signals

In 1950, Hahn discovered the sensitivity of MRI to detect water diffusion when he detected a signal drop using the SE sequence[90] and reported that the diffusion coefficient could be measured. Four years later, Carr and Purcell[79] designed a new framework for measuring such phenomena using Hann's spin-echo sequence. They reported that the SE signal magnitude has a high sensitivity to capture molecular water diffusion.

Spins precess at Larmor frequency f_0 in the presence of a strong magnetic field B_0, where γ refers to the gyromagnetic ratio dependent on the nucleus:

$$f_0 = \gamma B_0 / (2\pi) \quad (1)$$

The precessing frequency of spins at location z1 is modified by applying a magnetic gradient pulse (Gz) along the z-axis, for example:

$$f_1 = (B_0 + G_z z_1)(\gamma / 2\pi) \quad (2)$$

If a first gradient is applied (referred to as the diffusion gradient diff1), all spins precess with various frequencies based on their locations. Different frequencies provide different phases simultaneously. Two spins i and j at different locations zi and zj will have phases φi, and φj is given by:

$$\begin{aligned}\phi_{i,diff1} &= 2\pi f_i \delta = \gamma(B_0 + G_{diff1} z_i)\delta \\ \phi_{j,diff1} &= 2\pi f_j \delta = \gamma(B_0 + G_{diff1} z_j)\delta\end{aligned} \quad (3)$$

When only gradient variation in relation to the $\boldsymbol{B_0}$ and the main frequency constant is considered, the phase expressions in (3) are reduced to:

$$\begin{aligned}\phi_{i,diff1} &= \gamma G_{diff1} z_i \delta \\ \phi_{j,diff1} &= \gamma G_{diff1} z_j \delta\end{aligned} \quad (4)$$

If both spins are stationary, a second gradient $\boldsymbol{diff_2}$ of the same time δ and magnitude as the first, $\boldsymbol{Gdiff_2 = Gdiff_1}$, but with the opposite polarity, generates the following phases:

$$\begin{aligned}\phi_{i,diff2} &= -\gamma G_{diff2} z_i \delta \\ \phi_{j,diff2} &= -\gamma G_{diff2} z_j \delta\end{aligned} \quad (5)$$

The phase difference between the two spins at the echo time cancels out. However, if one spin shifts due to the effects of diffusion, the rephasing effect of the second diffusion gradient is not exactly equal to the dephasing effect of the first diffusion gradient. For this reason, imperfect rephasing across the whole voxel results in decreased signal magnitude, as shown in Fig.3.13. The amount of motion between the application of the two diffusion gradients determines the signal loss; this is known as diffusion-weighting preparation. Before the imaging gradients, the "dephasing" and "rephasing" diffusion gradients are applied[91].

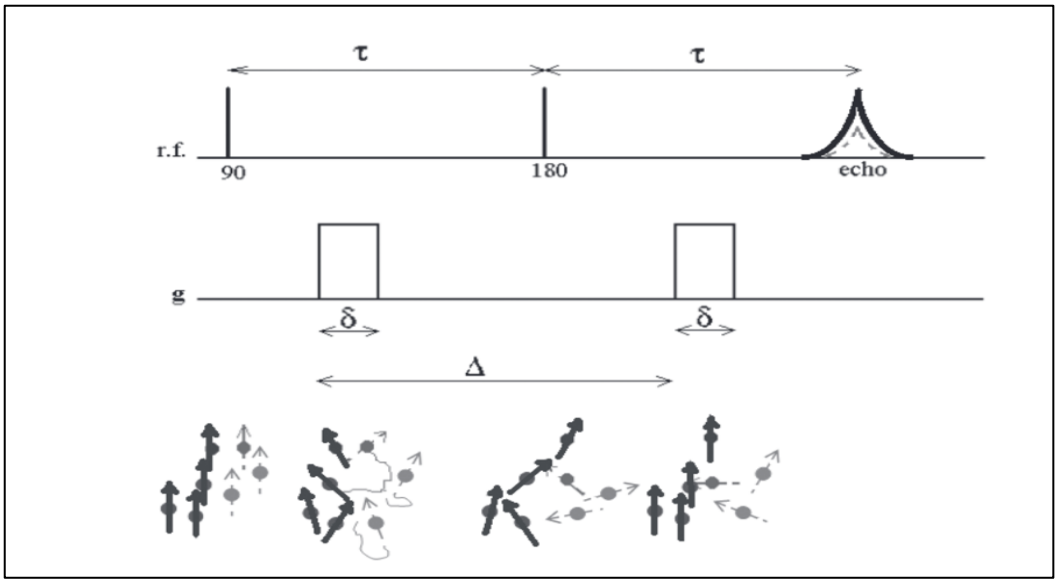


Figure 3. 13. *The first diffusion gradient dephases static spins (thick lines) according to their respective positions. A 180º pulse and a second diffusion gradient rephase those spins, resulting in an echo (thick lines). When the second diffusion gradient is applied, however, moving spins (interrupted lines) do not have the same position, so all spins are not completely in phase at the echo time, resulting in a reduced echo (interrupted line)*[91]*.*

By altering the magnitude of diffusion gradient *G*, the duration of application *d*, or the delay between the two diffusion gradients, diffusion weighting can be provided to the collected signal. The so-called "b-factor" is used to measure the degree of diffusion sensitization[91], which is given by:

$$b = (\gamma G \delta)^2 (\Delta - \delta/3) \quad (6)$$

3.4. Diffusion Imaging and White Matter Microstructure

The focus of microstructural imaging is to generate virtual histology, which involves mapping and estimating the histological characteristics of tissue using non-invasive imaging techniques such as MRI. Compared to traditional histology, virtual histology achieved by microstructural imaging has various advantages: 1) it is non-invasive, eliminating the need for biopsies and other tissue samples; 2) it helps avoid disruptions caused by tissue preparation and extraction; 3) it is non-destructive, allowing the repetition of measurements

for monitoring; 4) it has a large field of view, displaying an entire organ or body, as compared to the smaller samples typically used in histology; and 5) data acquisition is fast and accessible. Microstructural imaging is based on an imaging model that relates MRI signals to a microscopic architecture of tissues. The microstructural imaging approach obtains a set of images with varying sensitivities and fits a model in each voxel to a set of signals acquired from each corresponding voxel. The procedure generates a set of parameters in each image voxel, resulting in parametric maps of microscopic tissue properties. Due to its sensitivity to cellular architecture, diffusion MRI is an essential technique for microstructure imaging. This technique increases the sensitivity of the MR signal across diffusion durations ranging from milliseconds to one second (Fig.3.14)[92].

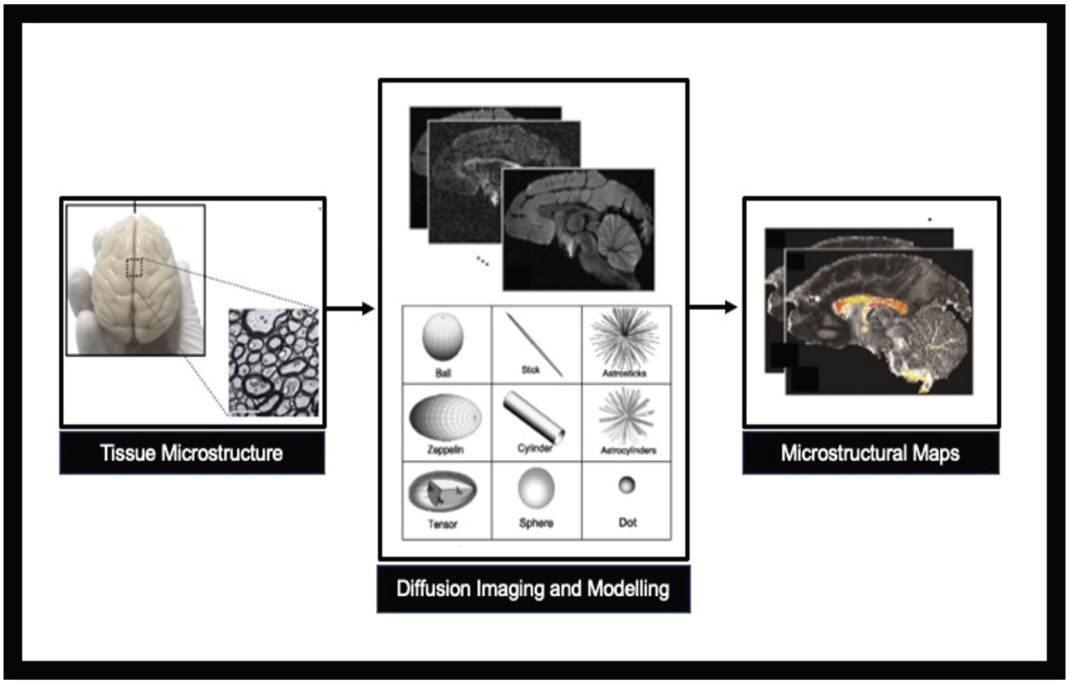


Figure 3. 14. *The basic concept of microstructural imaging using diffusion MRI. This figure is adapted from previous work*[68,92]*.*

Several diffusion MRI models have been introduced, falling into two categories: tissue and signal models. Tissue models explicitly depict the underlying tissue microstructure in each voxel using a multi-compartment approach[93–95]. The signal models focus on characterising the diffusion signal attenuation without explicitly specifying the underlying

tissue composition that gives rise to the signal[96–104]. Other approaches fall between these two categories and contain some tissue properties, such as the distribution of fibre orientations, but frequently describe the signal from individual fibres without modelling the fibre composition[105].

Apparent Diffusion Coefficient (ADC) is the simplest diffusion model that was used to generate the first diffusion MRI image of the human brain[106]. ADC models the signal and provides a global and statistical metric (ADC maps). ADC gives good contrast of tissues when the b-value (diffusion weightings and magnitude) is not high, and it has been widely and clinically used. On the other hand, the actual value of ADC is highly dependent on the diffusion gradient direction. Thus, ADC results do not seem to be comparable across studies[107].

DTI has been the most used MRI diffusion model over the past 25 years. DTI uses a tensor model to characterise the distribution of water[108,109], and it has been used in clinical and neuroimaging studies to assess the white matter microstructure[110]. DTI is sensitive to white matter microstructural changes in abnormal conditions, such as neurodegenerative diseases[111,112], brain tumours[113] and injuries[114]. However, DTI can assume a single Gaussian water diffusion and cannot provide additional information on complex white matter fibres[115]. For this reason, DTI indices may lack specificity to characterise tissue microstructure. For instance, fractional anisotropy (FA) is the main DTI parameter and can be influenced by myelination, the permeability of the axonal membrane, axonal orientation dispersion, and axonal packing density. As a result, alterations in FA could not be precisely linked to specific tissue properties. Alterations in Axial Diffusivity (AD) and Radial Diffusivity (RD) as additional DTI metrics are commonly sensitive to axonal abnormalities and demyelination[116]. AD and RD must be interpreted with caution and carefully linked to abnormal microstructural changes, as a change in one can cause changes in the other[117]. Furthermore, DTI may suffer

from the effects of partial volume, and its measures are vulnerable to free water contamination[118].

Recently, advanced MRI hardware has allowed MRI diffusion datasets with several gradient directions and higher b-values, providing richer information and a better understanding of tissue properties. For example, Diffusion Kurtosis Imaging (DKI)[119] is a diffusion model that represents diffusion signals and calculates the kurtosis (non-Gaussian water diffusion) and has been used to investigate ageing[120], epilepsy[121], and tumour[122]. Although DKI measures have been extended to identify non-gaussian diffusion of water molecules, its indices still lack tissue specificity compared to other diffusion models[68]. Diffusion tissue models demonstrate the diffusion-weighted signal as a mixture of signals given by various tissue compartments. In these compartments, water molecules are represented by basic geometric shapes, and each water molecule has a unique pattern of water diffusion.

Multi-compartment diffusion models have been developed to detect various properties of tissue microstructure, and they include: (1) axon diameter models such as CHARMED[123], AxCaliber[124], and ActiveAx[125]; (2) models that measure the density of axons or the volume fraction of intra-cellular compartments, such as CHARMED, NODDI[17], Bingham-NODDI[126], and Spherical Mean Technique (SMT)[127]; (3) the permeability - Karger model[128], apparent exchange rate imaging[129], and a machine learning-based model[130]; (4) the fibre orientation dispersion modelling in NODDI. Given the theoretical benefits of such models, more work on the practical translation of these multi-compartment models is urgently required. NODDI is the simplest of these models, requiring feasible clinical datasets. It is also one of the only validated multicompartment diffusion models using histology in human cerebral tissue[13]. As a result, NODDI is an excellent candidate for the clinical use of improved diffusion MRI techniques[68].

3.4.1. Diffusion Tensor Imaging (DTI)

3.4.1.1. Introduction to DTI

DTI model was developed to quantitatively describe the degree of anisotropy and structural orientation information. DTI method provided a straightforward way to model complicated neuroanatomical information with only six diffusion directions[131]. The concept of diffusion tensor imaging (DTI) is an extension of a scalar (isotropic) diffusion coefficient (e.g., the ADC) that includes different orientations (such as diffusion anisotropy)[109]. DTI is a quantitative technique for calculating diffusion tensor D, which defines the average water displacement profile and the white matter tract orientation in three dimensions. In practice, the diffusion tensor is an array of diffusion coefficients representing the diffusion in different orientations.

3.4.1.2. Mathematical Descriptions and Tensor Estimation of DTI

The diffusion tensor is typically an asymmetric 3 X 3 array with 6 distinct elements expressed in a Cartesian (x, y, z) coordinate system:

$$\mathbf{D} = \begin{bmatrix} D_{xx} & D_{xy} & D_{xz} \\ D_{yx} & D_{yy} & D_{yz} \\ D_{zx} & D_{zy} & D_{zz} \end{bmatrix} \quad (7)$$

Dxx, Dyy, and Dzz are the diffusion coefficients in the (x, y, z) orientations and refer to the coefficients of diffusion along the y, x, and z-axis. The tensor is calculated by solving a modified version of equation (numbers)[109] while considering adequate signal samples at various gradient directions. It is commonly computed by log-transforming the measured signal attenuation and applying linear regression[68,109]. The measured signal is relevant to the tensor elements as:

$$\ln\left(\frac{A(\mathbf{b})}{A(\mathbf{b}=\mathbf{0})}\right) = -\sum_{i=1}^{3}\sum_{j=1}^{3} b_{ij}D_{ij} \quad (8)$$

$$= -b_{xx}D_{xx} + 2b_{xy}D_{xy} + 2b_{xz}D_{xz} + b_{yy}D_{yy} + 2b_{yz}D_{yz} + b_{zz}D_{zz}$$

$$= -Trace(\mathbf{bD})$$

Since we only need to calculate 6 unique elements of the symmetric tensor, we may compute each element of the tensor as the gradient of the slope in a plot between A(b) and each b-value by measuring A(b=0) and A(b) and defining each b element. To compute each unique tensor element, we need at least 6 distinct measurements of A(b), one for each tensor direction (xx, xy, xz, yy, yz, zz), and one for the signal without any diffusion-induced attenuation A(b=0)[109]. The eigen-decomposition of the tensor yields descriptive terms such as principal diffusivities, which mostly correspond to the eigenvalues $\boldsymbol{\lambda_1}$, and principal diffusion directions, which correspond to the eigenvectors $\boldsymbol{v}$. These values may easily be utilised to define the local diffusion profile in relation to the anatomy and give insight into microstructure (Fig.3.15). Further descriptive terms can be derived from the eigenvalues and eigenvectors[109].

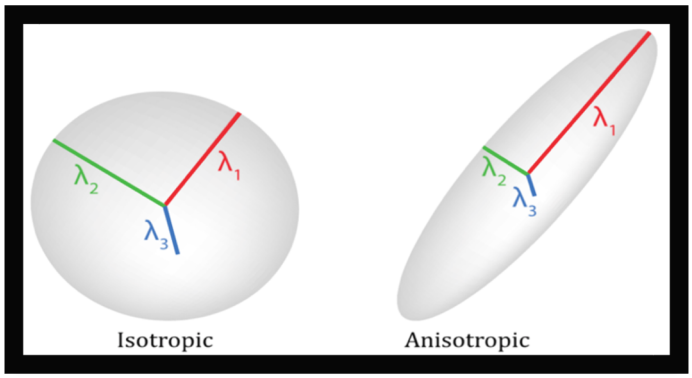


Figure 3. 15. *There are two archetypical diffusion tensor instances. The sample on the left shows an isotropic diffusion profile because the tensor has equal eigenvalues for each primary vector. An anisotropic diffusion profile is demonstrated on the right by diffusion in one direction*[132].

3.4.1.3. Computing DTI metrics

Diffusion-weighting by a couple of powerful gradient pulses introduces unique diffusion imaging parameters, including the b-value, orientations, and number of the least diffusion

images (b = 0 images). Most of the recent DTI studies used b-values in the range of 700–1000 s/mm^2, resulting in a 30–50% signal reduction if the average diffusivity of normal white matter is between 0.80 and 1.0 X 10^{-3} mm^2/s[131]. Several DTI metrics have been proposed, with the most utilised being fractional anisotropy (FA), mean diffusivity (MD), axial diffusivity (AD), and radial diffusivity (RD). The following equations illustrate how to construct these prominent DTI measures based on their eigenvalues [λ1, λ2, λ3] of the tensor.

$$FA = \sqrt{(\lambda_1 - \lambda_2)^2 + (\lambda_2 - \lambda_3)^2 + (\lambda_1 - \lambda_3)^2 / (\lambda_1^2 + \lambda_2^2 + \lambda_3^2)}$$
$$MD = 1/3\ (\lambda_1 + \lambda_2 + \lambda_3) \qquad (9)$$
$$AD = \lambda_1$$
$$RD = \lambda_1 + \lambda_2 / 2$$

The above equation indicates that FA represents the anisotropic diffusion in various directions. It has a 0-1 scale and is frequently used to measure the white matter tract integrity. MD represents the average diffusion magnitude in all directions measured. AD reflects the magnitude of water diffusion along with the tensor's major eigenvector $\boldsymbol{v^1}$, whereas RD indicates the average diffusion magnitude along the two eigenvectors ($\boldsymbol{v^2}$ and $\boldsymbol{v^3}$). In AD, we measure the value of $\boldsymbol{\lambda_1}$. In RD, the average of $\boldsymbol{\lambda_2}$ and $\boldsymbol{\lambda_3}$ is used. MD is the average of the three parameters [$\boldsymbol{\lambda_1, \lambda_2, \lambda_3}$]. Finally, FA quantifies the percentage of anisotropic diffusion by providing the relative difference between the biggest eigenvalue and the others (Fig.3.16)[132].

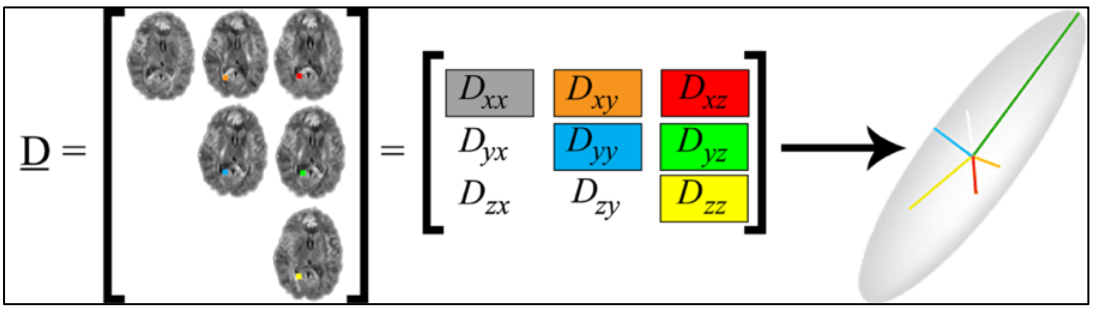


Figure 3. 16. *shows that once the water diffusion has been measured, the form of the tensors in each voxel may be quantified in various methods. Fractional anisotropy, mean diffusivity, axial diffusivity, and radial diffusivity are the most often utilised DTI measurements. These parameters are proportional to the tensor's three principal eigenvalues, which are labelled as λ1, λ2, and λ3*[132]*.*

When the value of each diffusivity measure is plotted in every voxel, scalar maps can be obtained. When examining the MD map, it is evident that the MD measure is particularly sensitive to CSF, which has high average diffusion values. In voxels with abundant CSF, MD is high, and thus the values are bright. While AD sensitivity to diffusion can be seen in the case of the longest eigenvalue. The large open cavities, such as lateral ventricles, have high levels of diffusion, resulting in high λ_1. RD shows the two shortest eigenvalues and demonstrates lower intensity in highly organised and dense structures, such as white matter tracts, and high values in regions containing CSF. Finally, FA shows the relative length of λ_1, particularly in comparison to λ_2 and λ_3. This results in selective higher intensities of white matter but not CSF[132] (Fig. 3.17).

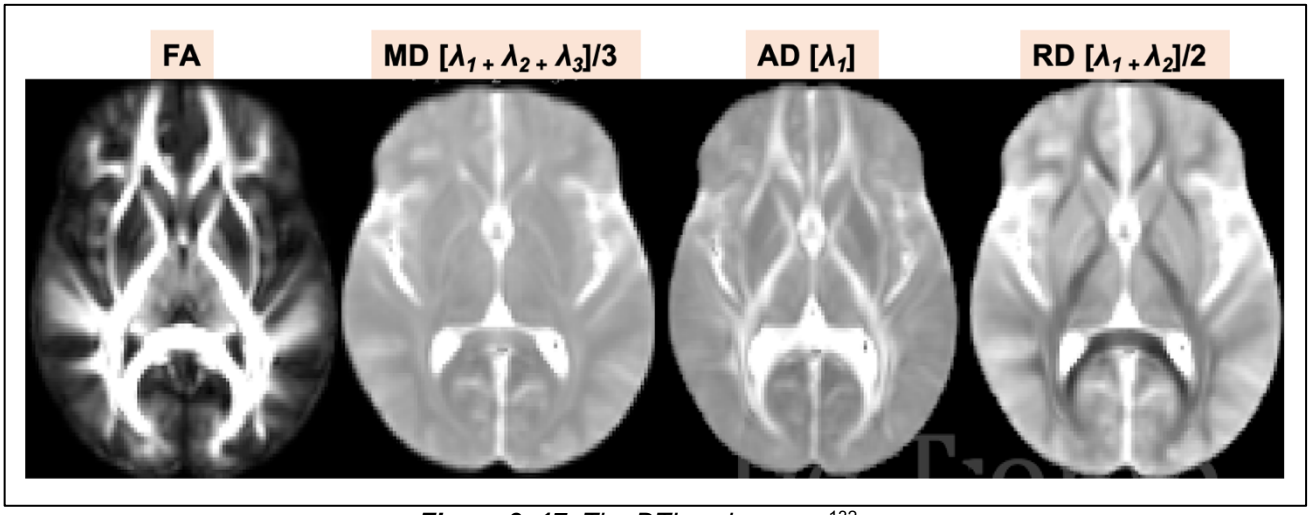


Figure 3. 17*. The DTI scalar maps*[132]*.*

3.4.1.4. Beyond The Diffusion Tensor

Although the DTI is a useful clinical model, it is restricted in its capacity to represent certain features of the brain anatomy, including heterogeneous fibre populations and complicated fibre architecture. Each voxel in DTI is represented by a single tensor of a single Gaussian profile. Because neurons and axons are so small (micrometres) compared to conventional MRI voxel sizes (millimetres), a single diffusion tensor reflects the average of tens to hundreds of thousands of cells and axons. In highly heterogeneous brain regions where large

neuronal bundles of parallel white matter fibres are present, such as the midline of the corpus callosum, the tensor averaging demonstrates a useful, although limited, approximation of diffusion/fibre direction. The contents of a single voxel are complicated: neurons are not precisely packed; thus, "free" space exists; voxels may average across tissue boundaries (e.g., between white matter and CSF); and various fibre populations may exist, resulting in crossing, merging, fanning, and kissing fibres. These issues are depicted graphically in Fig.3.18.

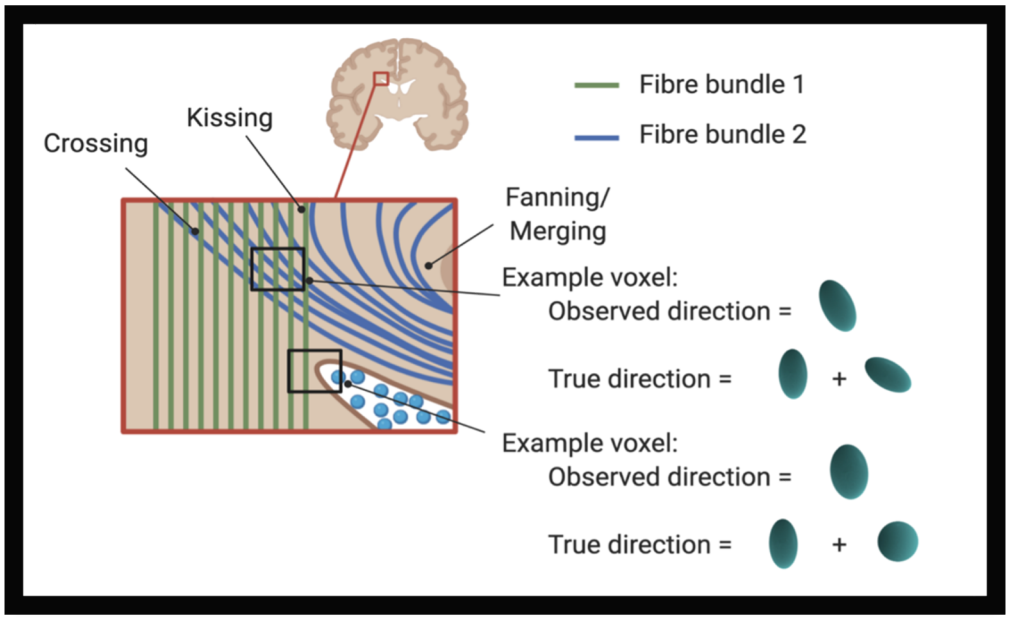


Figure 3. 18. *Fanning fibres are observed in a small brain area. There are examples of how the observed diffusion direction may consist of several compartments*[133]*.*

These limitations encouraged the development of more advanced diffusion modelling systems that attempt to describe different types of tissue compartments inside a voxel, relating different diffusion profiles (e.g., isotropic and anisotropic) and multiple fibre bundles[133]. NODDI is one of these models, and several other diffusion models are beyond the scope of this thesis[92].

3.4.2. Neurite Orientation Dispersion and Density Imaging (NODDI)

3.4.2.1. Introduction to NODDI

The unique ability of diffusion MRI to characterise microstructural environments has been demonstrated in numerous clinical investigations and research fields. In clinical research, diffusion tensor imaging[108] has been useful in many aspects, including neurology and psychology[134–136]. However, advanced diffusion methods beyond the DTI have been achievable clinically, with modern MRI units allowing more diffusion directions and stronger weightings. These methods with higher b-values up to 2500-3000 s/mm^2 may further assist with explaining and understanding the disorders of the CNS. In diffusion MRI, clinical information is extracted by two fundamental approaches: representation of the signal and modelling tissues biophysically[137,138]. The signal representation models summarise the detected signal only. On the contrary, the biophysical diffusion models rely on specifying and converting the diffusion signal biophysically to parameters[18].

NODDI has been proposed as a new biophysical model to probe tissue microstructures[17]. Introducing new diffusion imaging models is essential for two reasons: First, studying the microstructural impact of disease requires an improved sensitivity to detect pathologies. Second, advanced diffusion models may better explain the detected abnormalities. The first reason aligns with the signal representation, which requires an improved sensitivity to target diseases. The second reason aligns with NODDI, which requires increased specificity to better explain the detected tissue abnormalities. These biophysical diffusion models are based on assumptions, and an extreme degree of care is needed to interpret the results[18,137,138].

3.4.2.2. NODDI Mathematical Description

NODDI is a member of the family of models based on Gaussian distribution assumptions (i.e., diffusion tensor). The NODDI models the signal in the three compartments for a particular matrix as follows:

$$S(\mathbf{B}) = S_0((1 - f_{\mathrm{fw}})(f_{\mathrm{i}}A_{\mathrm{i}} + (1 - f_{\mathrm{i}})A_{\mathrm{e}}) + f_{\mathrm{fw}}A_{\mathrm{fw}}) \quad (10)$$

S refers to no diffusion signal. The signal of the free water and intra-neurite compartments are denoted as f_{i} and f_{fw}. The compartmental fractions of NODDI are adopted and described uniquely. A_{i}, A_{e} and A_{fw} are signals derived from neurite, extra neurite and free water compartments and are described as follows:

$$\begin{aligned} A_{\mathrm{i}} &= \int_{\mathbb{S}^2} \exp(-bd_{\mathrm{i},\|}(\mathbf{g}\bullet\mathbf{n})^2)P(\mathbf{n})d\mathbf{n} \\ A_{\mathrm{e}} &= \exp\left(-b\mathbf{g}^t\left(\int_{\mathbb{S}^2} \mathbf{D}_{\mathrm{e}}(\mathbf{n})P(\mathbf{n})d\mathbf{n}\right)\mathbf{g}\right) \\ A_{\mathrm{fw}} &= \exp(-bd_{\mathrm{fw}}) \end{aligned} \quad (11)$$

$d_{\mathrm{i},||}$ refers to the diffusivity parallel to the intra-neurite compartment, $d_{\mathrm{e},||}$ refers to the parallel diffusivity and *D*e(n) to the extra-neurite tensor with the principal direction n. $d_{\mathrm{e},\perp}$ refers to the perpendicular diffusivity. *P*(n) is the orientation distribution (Fig.3.19). The intra-neurite compartment is represented as a number of small "sticks" (the signal attenuation due to perpendicular diffusion is minimal, $d_{\mathrm{e},\perp} \approx 0$ m^2/ms)[139]. Isotropic diffusion with the diffusivity = d_{fw} 3 m^2/ms represents the free water compartment. Except for neurites and free water, the extra-neurite compartment contains astrocytes, microglia, cell bodies (somas), oligodendrocytes, ependymal cells, extracellular matrices, and vascular structures[18].

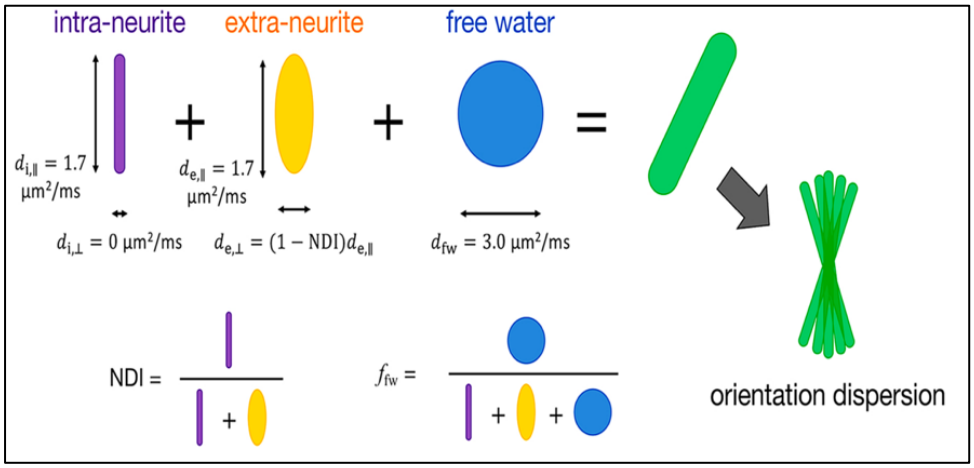


Figure 3. 19. *An illustration of the NODDI model and parameters*[18].

3.4.2.3. NODDI Model and Compartments

The NODDI model assesses three types of tissue compartments: An intracellular compartment reflected by neurite density index (NDI) or intracellular volume fraction (ICVF), an extracellular compartment reflected by the orientation dispersion index (ODI), a free water fraction or CSF compartments are reflected by isotropic volume fraction (IsoVF). These whole-brain maps are always shown alongside the FA map derived from fitting the diffusion tensor model (Fig.3.20)[17].

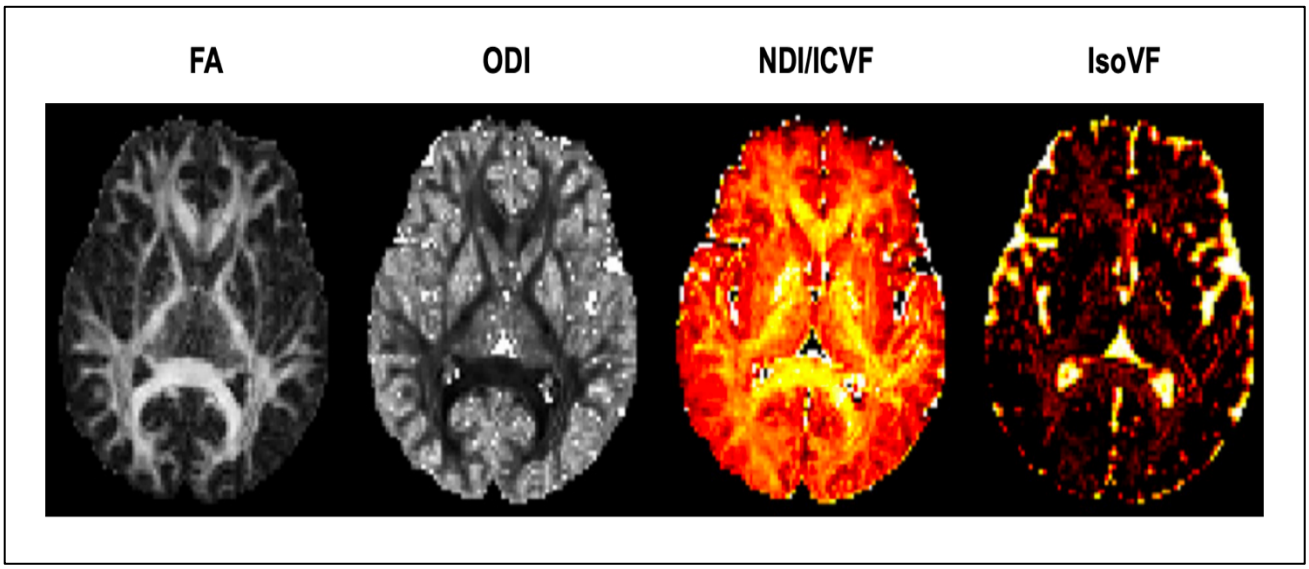


Figure 3. 20*. NODDI microstructural maps*[17].

NODDI represents each voxel as one of three compartments: Intra neurite (restricted diffusion), extra neurite (hindered diffusion), and CSF (isotropic diffusion) (Fig.3.21)[140,141].

The space within the membrane of neurites (the intracellular compartment) is modelled as sticks or a zero-radius cylinder to assess the highly restricted diffusion vertical to neurites[95,142]. The intracellular compartment includes white matter structures with a high orientation, such as corpus callosum, white matter structures formed of fanning and bending axons such as the centrum semiovale, subcortical grey matter and cerebral cortex. The space is situated around the extracellular compartment of neurites and is occupied by different cell bodies (somas) and glial cells. The water diffusion in this space is hindered because of neurites; however, it is unrestricted. Unlike DTI, this model can directly estimate CSF volume fraction, which minimizes the effects of CSF contamination from brain regions such as corpus callosum[18] (Fig.3.22).

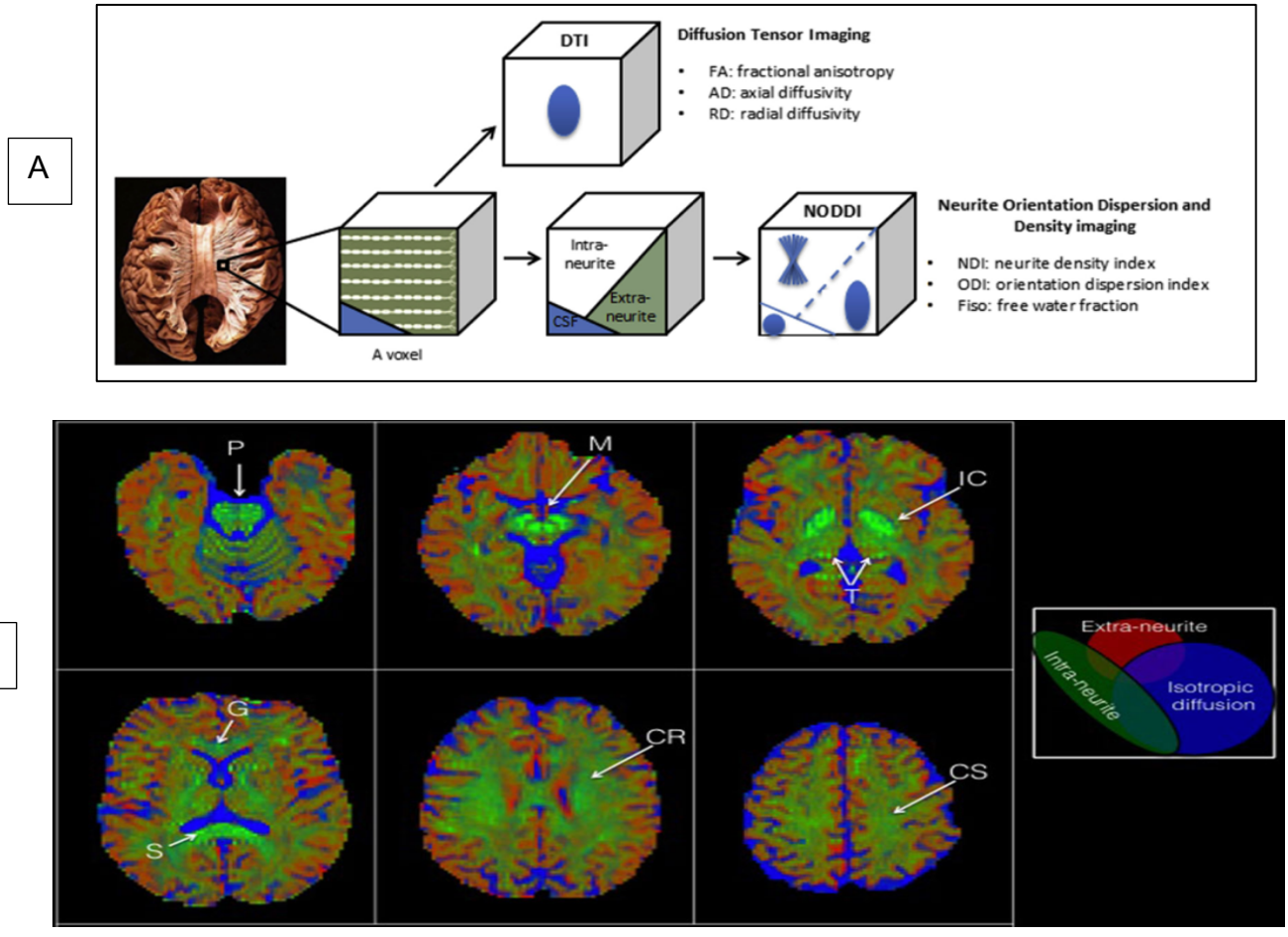


Figure 3. 21. *(A) DTI and NODDI compartments in a voxel; (B) NODDI colored maps of a healthy subjects at pons (P), midbrain (M), internal capsule (IC), corona radiata (CR), genu (G) and splenium (S) of corpus callosum and centrum semiovale (CS)*[140]*.*

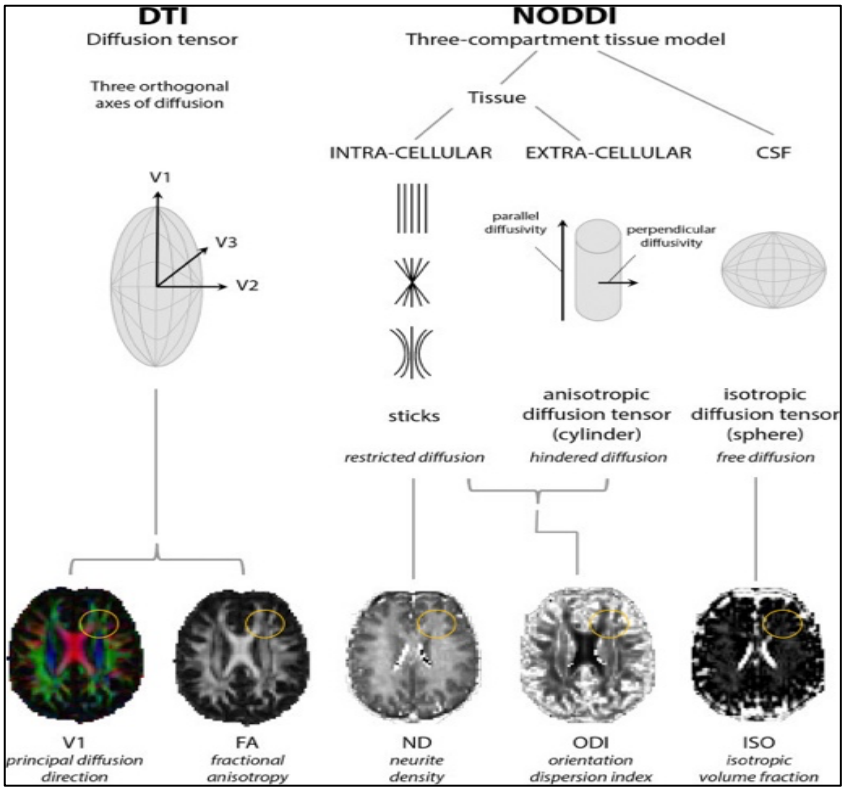


Figure 3. 22. *DTI represents three orthogonal diffusion axes in DTI, from which FA and MD may be determined. NODDI divides diffusion into three compartments: limited diffusion within the cell, impeded diffusion outside the cell and free diffusion in CSF. This model may be used to estimate parameter maps for NDI/ICVF and ODI. Changes in FA can be followed by changes in both ND/ICVFI and ODI, as indicated by the yellow circles*[18]*.*

3.4.2.4. NODDI Specificity and Validity

Although the NODDI model primarily aims at specificity, this cannot be accomplished unless the model describes the biophysical effects and its parameters are estimated. NODDI can describe the multi-shell data compared to other models, making it suitable for this acquisition. At present, NODDI extended scan time impedes the clinical application of this technique[138,143–145]. The NODDI model constraints often show promising results[146–148], but an agreement is not always assured and does not prove the NODDI validity.

It has been recently suggested that optimising the diffusivity in NODDI but not the model is the leading cause for NODDI to be incompatible with b-tensor encoding[18,149]. Depending on the clinical condition and anatomical regions of interest (grey matter or white matter[150], spinal cord or brain[151], and cerebrum/cerebellum[152]), the correct selection of the

NODDI model may vary. The debates on how specific and valid the NODDI model has confused researchers and clinicians who are not experts in diffusion modelling. Nevertheless, there is no direct answer to clear the confusion[153]. However, the specificity and validity depend on the purpose of the study. As reported in the original NODDI paper[17], NODDI is found to be more specific than FA in DTI.

3.4.2.5. NODDI Reliability

Although NODDI specificity is not without limitations, researchers are primarily interested in quantitative metrics that can predict the neurological impact by elucidating the effects of the disease or treatment. For clinical applications, the short scanning time and precision are more crucial than accuracy. Using the in vivo data, the original NODDI paper[17] reported robustness and reliability of NODDI against the variation of acquisitions within the same scanner if we use more than 30 directions and more than two b-values for each shell. When comparing data from different scanners, extreme caution should be taken. Field strength has been reported to significantly impact the NODDI metrics[154,155]. It has also been demonstrated that inter-scanner reproducibility is lower than intra-scanner reproducibility, even at similar magnetic field strength[18,156].

3.4.2.6. NODDI and Translation to Clinical Practice

Translating a new technique to clinical practice is an issue for all imaging biomarkers. NODDI requires passing two translational gaps and three validating phases each: NODDI must pass the technical validation phase in which the model's accuracy and precision are tested and validated. The performance of the NODDI must be tested in measuring biological and clinical outcomes. In addition, the cost-effectiveness of including study design and scan cost must be tested. For NODDI to pass the second translational gap, it must be widely accessible to populations, and multicentre testing studies must be conducted to enhance the statistical power and inter-scan reproducibility[157].

According to the MRI biomarker road maps, NODDI is nearly passing the first translational gap and has become a valuable diagnostic research tool[157]. Recently, researchers have put efforts towards multi-centre data sharing and harmonisation[152,158,159], which are anticipated to contribute to rapid clinical validation. There is no perfect validation in clinical practice; however, it is essential to identify and reduce uncertainties about making a final clinical decision, considering the balance between theory and usability. At the current stage, ongoing technical and clinical studies advancing the application, hardware and acquisition are very important to increase the robustness of NODDI[18].

3.5. Diffusion Image Artefacts

Artefacts are signals in MRI images that do not represent the tissue signal in the corresponding voxel but occur due to MRI scanning. Some artefacts are inevitable, while others can be prevented or reduced by choosing the correct acquisition parameters and providing clear instructions to participants. Some of the most common artefacts seen in diffusion images are the following:

3.5.1. Eddy Current Artefact

Eddy current or distortion artefact occurs when the strong gradient pulses are turned on and off rapidly. Due to the time-varying gradients, current induction occurs during the application of the diffusion-gradient pulses. This artefact can start in conductive parts of the MRI unit (RF coils, cryostat, etc.) and grow as the gradient pulses get stronger. The gradients experienced by spins in the imaged subjects differ from all those programmed to reconstruct the final image. As a result, geometric distortion in the final images is caused by this inaccuracy in the local gradients (not considered by the reconstruction software). Three patterns of artefacts can be seen in diffusion images: image dilation or contraction, general shift, and shear (Fig.3.23). When the gradient pulse is stronger, the easily identified distortions worsen[92,160].

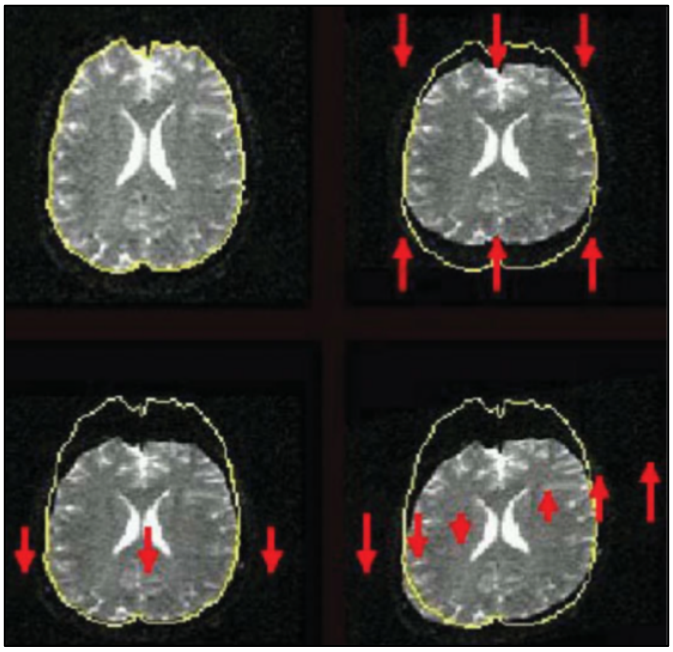


Figure 3. 23. *Types of distortion: contraction (top right), shift (bottom left), and shear (bottom right)*[160].

3.5.2. Motion Artefact

Patients' motion is the second significant source of artefacts that are still linked to strong gradient pulses. While all MRI sequences are susceptible to motion artefacts, diffusion imaging is sensitive to object motion. Diffusion of molecular water displacements generates phase changes when long and intense gradient pulses are present. Due to the random nature of the motion and the direction changes of the molecules, the phase shift distribution causes a reduction in signal amplitude. When tissue macroscopic movement is present (due to motion of the head, pulsing flow, etc.), spins undergo enormous displacements, resulting in large phase shifts. This phase shift increases when the strength of the gradient pulses increases. The problem occurs when the pulse sequence is repeated with various patterns of motion.

On the other hand, the macroscopic motion has no reason to repeat itself in the same way every time. Depending on the direction and magnitude of the motion, each echo will exhibit a different phase shift. Due to the distribution of phase shifts over time and k-space,

the image will exhibit "ghost-shaped artefacts" along the direction of the phase-encoding gradient (Fig.3.24)[92,160].

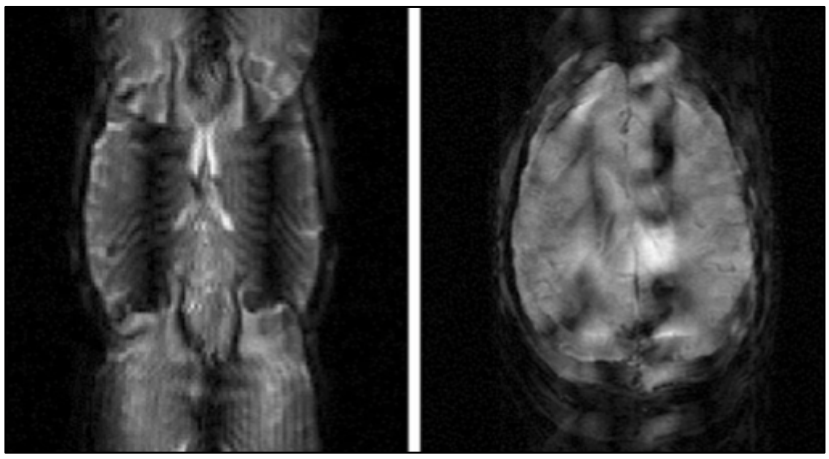


Figure 3. 24*. Motion artefact in diffusion MRI image*[160]*.*

3.7. Diffusion Image Processing and Analysis

Diffusion MRI artefacts need to be corrected before proceeding with image analysis to avoid misinterpretation and improve image analysis accuracy. This step is known as image processing which can be performed using a few software libraries such as FMRIB Software Library (FSL). Diffusion images can be processed via FMRIB's Diffusion Toolbox (FDT)[161], and the processing pipeline includes the following:

1. Converting raw data (MRI images) from DICOM to NIFTI and removing images affected by major artefacts.
2. Checking diffusion data (b-values and b-vectors).
3. Correcting for susceptibility-induced distortion artefacts using the top-up tool within FSL[162].
4. Extracting brain tissue only using non-sensitized diffusion images (b0 images) using Brain Extraction Tool (BET) within FSL[163].
5. Correcting both eddy currents and subject motion artefacts simultaneously using the eddy tool within FSL[164].

All the diffusion-weighted images should be aligned and undistorted after running eddy. The diffusion models can now be fitted (in the NODDI optimisation chapter, I fitted DTI and NODDI) using the following tools:

- DtiFit - Diffusion tensor fitting on eddy-corrected images[165].
- AMICO (Accelerated Microstructure Imaging via Convex Optimization)[166]-NODDI fitting on eddy-corrected images.

After calculating and fitting the diffusion indices, the next step is image analysis (Fig.3.25). Popular quantitative analysis methodologies in diffusion MRI of human brain white matter include regions of interest (ROI) analysis (this method is used in this PhD project), voxel-based analysis (VBA)[167] and tract-based spatial statistics (TBSS)[168].

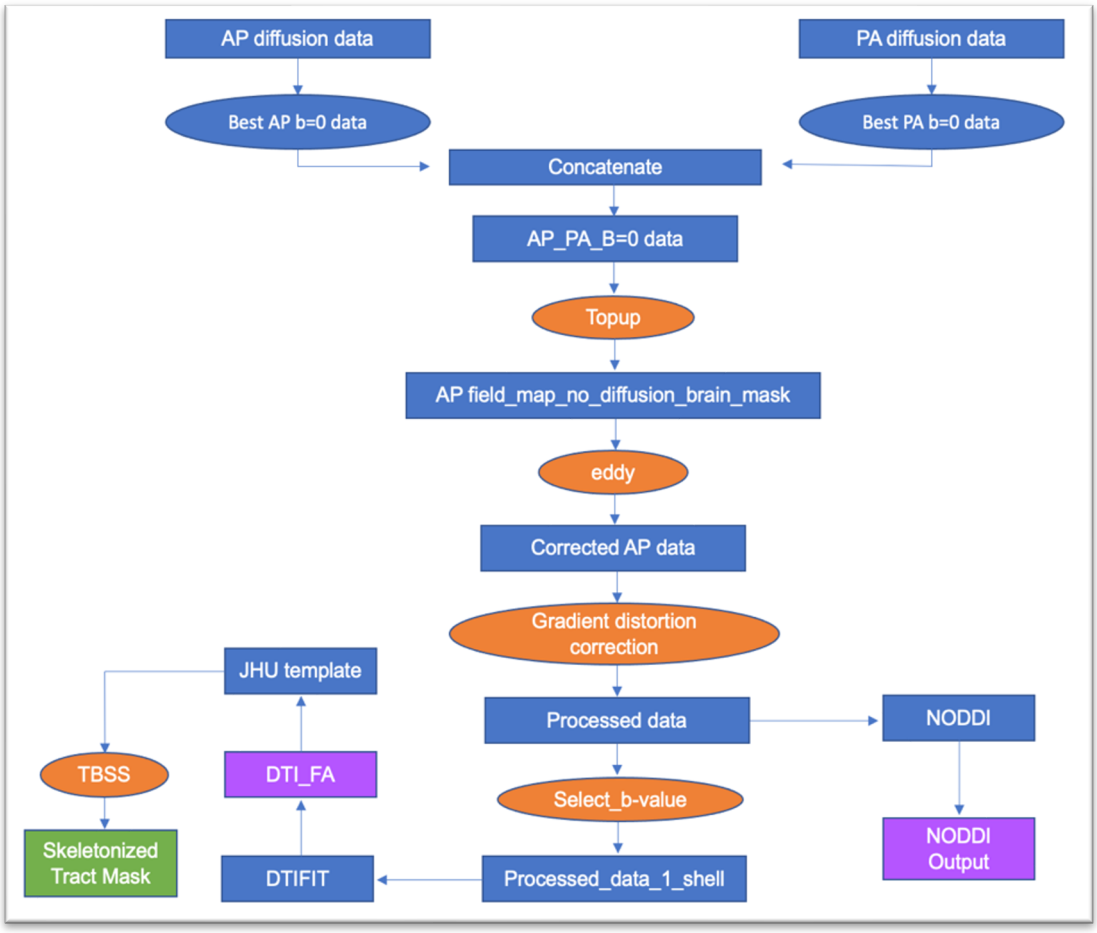


Figure 3. 25. *Diffusion image processing and analysis steps*[169].

3.7.1. Region of Interest (ROI) Analysis

ROI analysis combines voxels within the same anatomical area, systematically minimizing location information from many voxels to a small number of ROIs (Fig.3.26A). Inaccuracy issues can also be solved by manually defining the ROIs. However, manual ROI-based analyses have reproducibility concerns and therefore are not appropriate for whole-brain studies (time-consuming to draw many 3D ROIs). To overcome the limitations of manual ROI-based analysis, a voxel-based and an atlas-based ROI analysis was introduced to segment the whole brain automatically to anatomical regions, including white matter. Experts design those atlases with a comprehensive understanding of neuroanatomy, which helped increase the analysis validity and reproducibility. In ROI analysis of diffusion imaging metrics, the values are computed over all voxels for each ROI, such as mean/median or histogram. These generated values in the selected ROIs can be statistically analysed[170].

3.7.2. Voxel-Based Analysis (VBA)

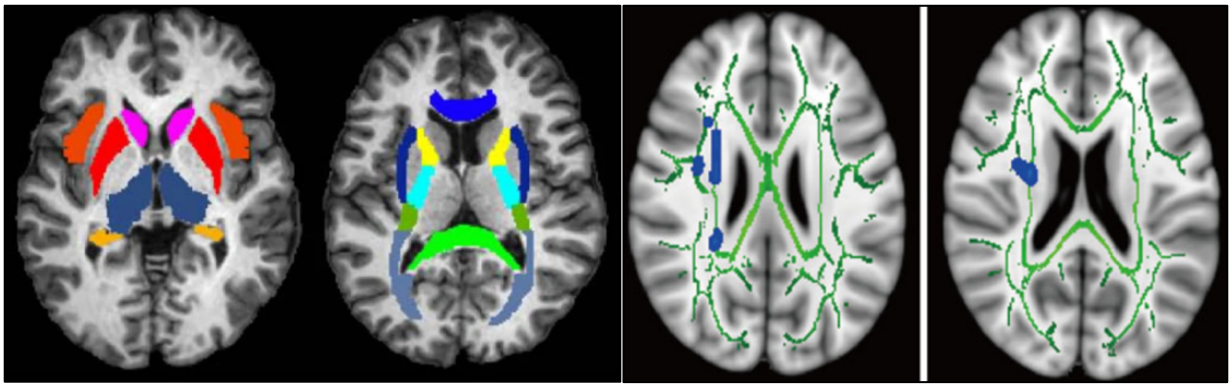
VBA is an automatic method of analysis used in diagnostic-imaging research that involves voxel-by-voxel group comparisons[167], and it is also an excellent choice for exploratory experiments. Many studies have used VBA, which was first created to detect local changes in the density of grey matter in T1-weighted brain imaging[167,171]. Then, medical imaging researchers started using VBA to analyse diffusion MRI images. VBA is used to analyse FA images registered into a standard space. Then voxel-wise methods are used for identifying regions related to their covariate of interest (e.g., patients vs controls, disability score, and age). However, the benefits and drawbacks of VBA are still debatiable[172–174]. Scientific researchers continue to question the interpretation of the results of this approach as it is unclear whether the changes are caused by alterations in grey matter density or local misalignment. Using VBA, structural neuroimaging studies can provide valid conclusions through careful application and validation[175]. However, the potential issues with VBA

techniques for neuroimaging data, such as multi-subject FA images, have yet to be well addressed. This application presents an important question that has yet to be answered: how can I be certain that the registration of each subject to a common space was highly accurate, both in resolving topological variabilities and the precise alignment of small structures? Another issue is the spatial smoothing before computing voxel-wise analysis, as the smoothing degree can influence the findings. Still, there is no way of knowing how much the correct degree of smoothing is[176]. Smoothing also increases partial volume effectiveness, a concern with VBA techniques, especially when applied to images like FA. In diffusion MRI, VBA is generally quite effective but is also limited. For this reason, additional analysis methods, such as TBSS, were introduced to overcome VBA limitations.

3.7.3. Tract-Based Spatial Statistics (TBSS)

TBSS is another method that combines the strengths of VBA and tractography (Fig.3.26B). TBSS focuses on overcoming the smoothing and alignment concerns while being entirely automated, examining the brain without needing pre-specified tracts of interest. TBSS is accomplished by estimating the mean FA skeleton of a group, representing the centre of all fibre bundles commonly shared by the subjects in a study. Afterwards, the FA data from each participant is projected onto the mean FA skeleton. From the central area of the nearest-related tract, a voxel of each skeleton takes its FA value to resolve any alignment and smoothing issues[168].

A



B

Figure 3. 26. *Commonly used diffusion image analysis methods*[177,178].

3.8. Summary of Aims and Hypothesis

T2DM and MS have both been linked to white matter microstructural alterations. These disease-related alterations may result in brain atrophy and neurocognitive deficits, which may result in a lower quality of life. It has been observed clinically that T2DM coexisting with MS causes a greater degree of microstructural alterations, more atrophy, and a worsening of the MS course. These microstructural alterations in the white matter of the brain appear to be an early indicator of neurodegeneration, preceding volumetric losses, and functional abnormalities. Researchers have encountered challenges in characterizing microstructural white matter alterations in brain voxels with crossing or bending and fanning filaments using traditional DTI. As a result, I'm curious about investigating the white matter changes in T2DM and MS using NODDI, and what advantage it has over conventional DTI.

Because NODDI has discovered white matter alterations in a few neurodegenerative diseases[18], using NODDI to explore microstructural changes in white matter in T2DM and MS may help better understand white matter neurodegeneration. Since MS and T2DM diseases may have similar effects on white matter connectivity, it would be interesting to see if there are any changes in the level of white matter damage, distribution, and diffusion parameters.

In this thesis, I hypothesize that NODDI may contribute to DTI by providing quantitative biophysical information to understand the impact of T2DM and MS on brain white matter microstructure. Also, diffusion measures in white matter may correlate with patients' clinical and metabolic profiles.

Chapter 4

4. Optimising the NODDI Scanning Protocol (Word count: 1050)

This chapter discusses a newly optimised NODDI protocol and compares it with other NODDI protocols from the original NODDI paper[17].

4.1. Introduction

NODDI optimisation procedure specifies the optimal protocol based on parameter settings and hardware specifications under a reasonable acquisition time. As there is no standard protocol for NODDI, the optimisation procedure divided the measurements of the protocol into at least two HARDI (High Angular Resolution Diffusion Imaging) shells with a minimum of 711 and a maximum of 2855 s/mm^2 as b-values. The higher b-value is at twice the resolution of the lower b-value to overcome the high variations of signal intensity caused by the sensitivity to complicated brain microstructures. Reducing the protocol resolution and shells reduces the scan time and the accuracy of the fibre orientation. Also, it may cause a minimal effect on the accuracy of the neurite morphology estimation[17]. Researchers compared optimised protocols with various HARDI shells and b-values (Table 4.1). They found that the two HARDI shell protocols have the best acquisition time and optimal signal intensity (highlighted in Table 4.1).

In this experiment, my research group and I aimed to optimise the NODDI scanning protocol for the first time at the University of Nottingham imaging centre (Sir Peter Mansfield Imaging Centre or SPMIC) and test several scanning protocols on the Philips MRI scanner (Ingenia 3T).

NODDI Protocols	Settings
Protocol # 1	b=711 (30)
Protocol # 2	b=1000 (30)
Protocol # 3	b=2000 (60)
Protocol # 4	b=2855 (60)
Protocol # 5	b=711 (30) and b=2000 (60)
Protocol # 6	**b=711 (30) and b=2855 (60)**
Protocol # 7	**b=1000 (30) and b=2000 (60)**
Protocol # 8	**b=1000 (30) and b=2855 (60)**

Table 4. 1. *The practical shells and b-values compared in the original NODDI paper*[17]*.*

4.2. Methods and Materials

4.2.1. Subjects and Scanning Site

A middle-aged healthy subject volunteered to be scanned four times to test different NODDI scanning protocols. The research team and I tested this newly optimised NODDI protocol, including an experienced neuroradiologist (Rob Dineen), neurologist (Cris Constantinescu), medical physicist (Paul Morgan), and imaging scientist (Stam Sotiropoulos) from the University of Nottingham Hospital (Queens Medical Centre). The research team contributed equally to the optimisation process, from manipulating the technical parameters to the image quality check.

4.2.2. NODDI Protocols and Technical Characteristics

Two tested protocols were derived from a previously published study known as the original NODDI paper[17]. The other two protocols were modified based on updated technical recommendations from the UK Biobank and the developer of the NODDI model (Hui Zhang) from University College London (UCL)[179] (See Table 4.2 for the details of the scanning protocol).

Protocol	Gradient direction	b-value	Voxel size	Slice thickness	Multi-band factor	Head coil	Matrix
#1	50-50	711-2800	2.0	2	3	32	112
#2	50-50	711-2800	2.2	2	3	32	112
#3	50-50	1000-2000	2	2	3	32	112
#4	50-50	1000-2000-300	2	2	3	32	112

Table 4. 2. *The technical information of the four tested NODDI protocols at SPMIC.*

4.2.3. Data Processing and NODDI Fitting

All acquired datasets were converted to NIFTI format. Eddy tool with the FMRIB Software Library (FSL)[180] was utilised for diffusion-weighted MRI images to enable simultaneous correction for eddy-current distortions and rigid-body head motion. The brain was then extracted using the brain extraction tool (BET) within FSL[181]. For DTI fitting, only diffusion-weighted images with b= 0 and 711 and 1000 s/mm^2 were employed. DTIFIT tool[161] within FSL was used to generate FA, MD, AD, and RD maps by fitting the diffusion MRI signal values to the DTI signal model voxel by voxel. The NODDI-related indices ICVF, ODI, and IsoVF, were computed using the NODDI toolbox based on MATLAB[182]. Lastly, a region of interest (ROI) analysis was run on the posterior limb of internal capsules (PLIC), posterior cingulate cortex (PCC) and basal ganglia (BG) to assess the NODDI metrics across the four tested protocols (Fig. 4.1).

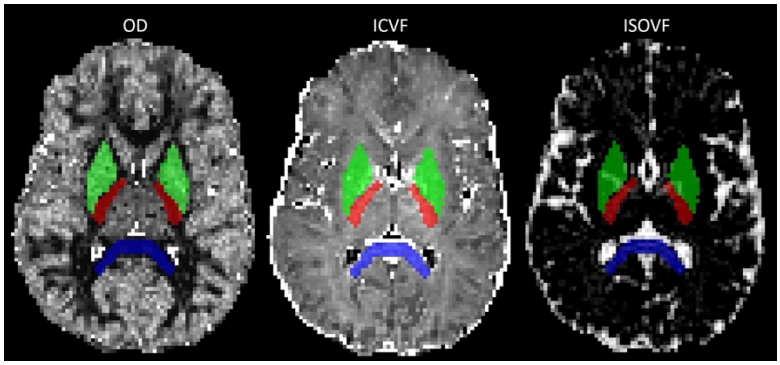


Figure 4. 1*. Selected ROIs to assess NODDI values in the tested protocols.*

4.3. Result and Discussion

After six months of discussion, scanning and image processing, the four protocols were optimal and yielded a good resolution (Fig.4.2-4.5). The values of the NODDI in PLIC, PCC and BG for all three metrics (ICVF, ODI and ISOVF) seem to be consistent with the range of NODDI values in healthy subjects from the UK Biobank (Table 4.3). However, protocol #4 showed lower values, possibly due to the one additional low b-value or partial volume effects. As the first three protocols are reasonable for clinical scanners and provide consistent results, the research team agreed and recommended using the third optimised protocol (#3 in Table 4.2 and Fig.4.4) as it has been applied in the UK Biobank project.

Protocol	**OD**			**ISOVF**			**ICVF**		
	BG	PLIC	PCC	BG	PLIC	PCC	BG	PLIC	PCC
	Mean (S.D)	Mean (S.D)	Mean (S.D)	Mean (S.D)	Mean (S.D)	Mean (S.D)	Mean (S.D)	Mean (S.D)	Mean (S.D)
#1	0.522 (0.131)	0.173 (0.057	0.099 (0.057)	0.089 (0.131)	0.092 (0.088	0.246 (0.264)	0.619 (0.137)	0.755 (0.093)	0.801 (0.135)
#2	0.531) (0.124)	0.181 (0.086)	0.099 (0.073)	0.081 (0.123)	0.082 (0.079)	0.171 (0.185)	0.574 (0.117)	0.692 (0.100)	0.752 (0.142)
#3	0.502 (0.119)	0.158 (0.062)	0.108 (0.086)	0.060 (0.112)	0.092 (0.083)	0.206 (0.243)	0.576 (0.128)	0.703 (0.110)	0.721 (0.141)
#4	0.506 (0.133)	0.095 (0.060)	0.055 (0.033)	0.052 (0.117)	0.070 (0.091)	0.127 (0.128)	0.575 (0.133)	0.702 (0.114)	0.777 (0.119)

Table 4. 3. *NODDI values extracted from PLIC, PCC and BG using ROI of analysis.*

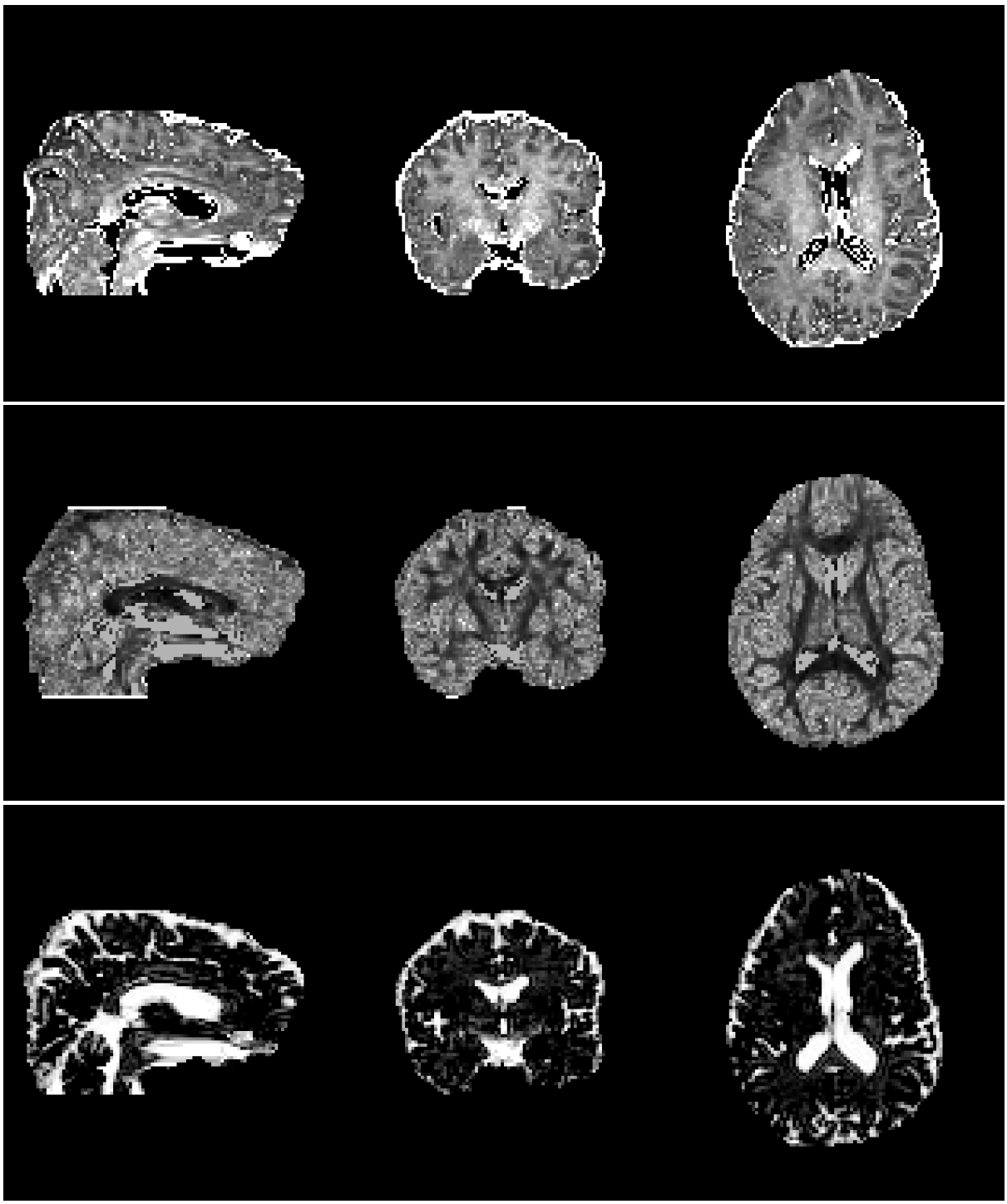


Figure 4. 2. *The resultant NODDI maps are acquired by scanning protocol #1 in Table 5.2. Top images: ICVF, middle images: ODI, bottom images: IsoVF.*

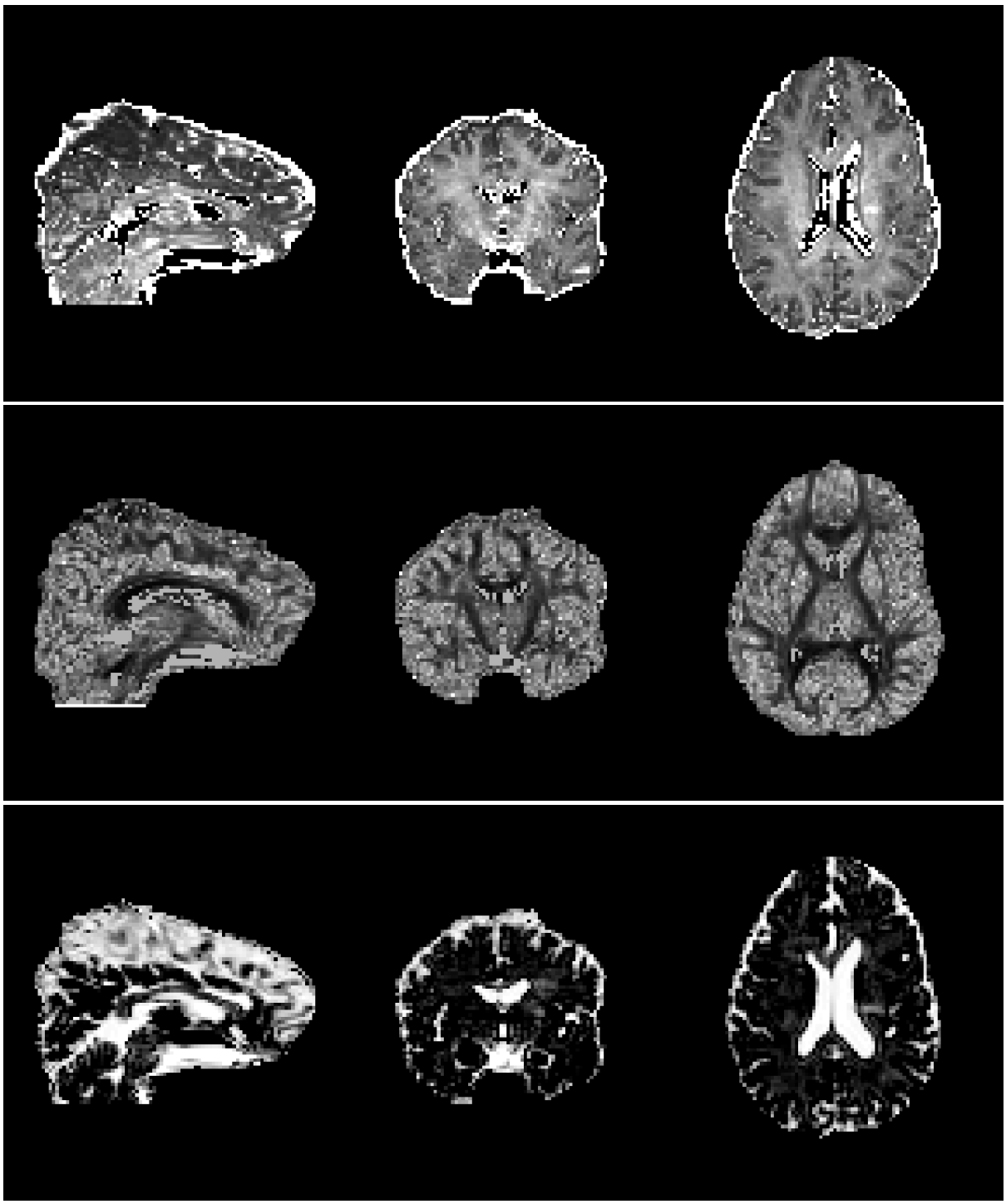


Figure 4. 3. *The resultant NODDI maps are acquired by scanning protocol #2 in Table 5.2. Top images: ICVF, middle images: ODI, bottom images: IsoVF.*

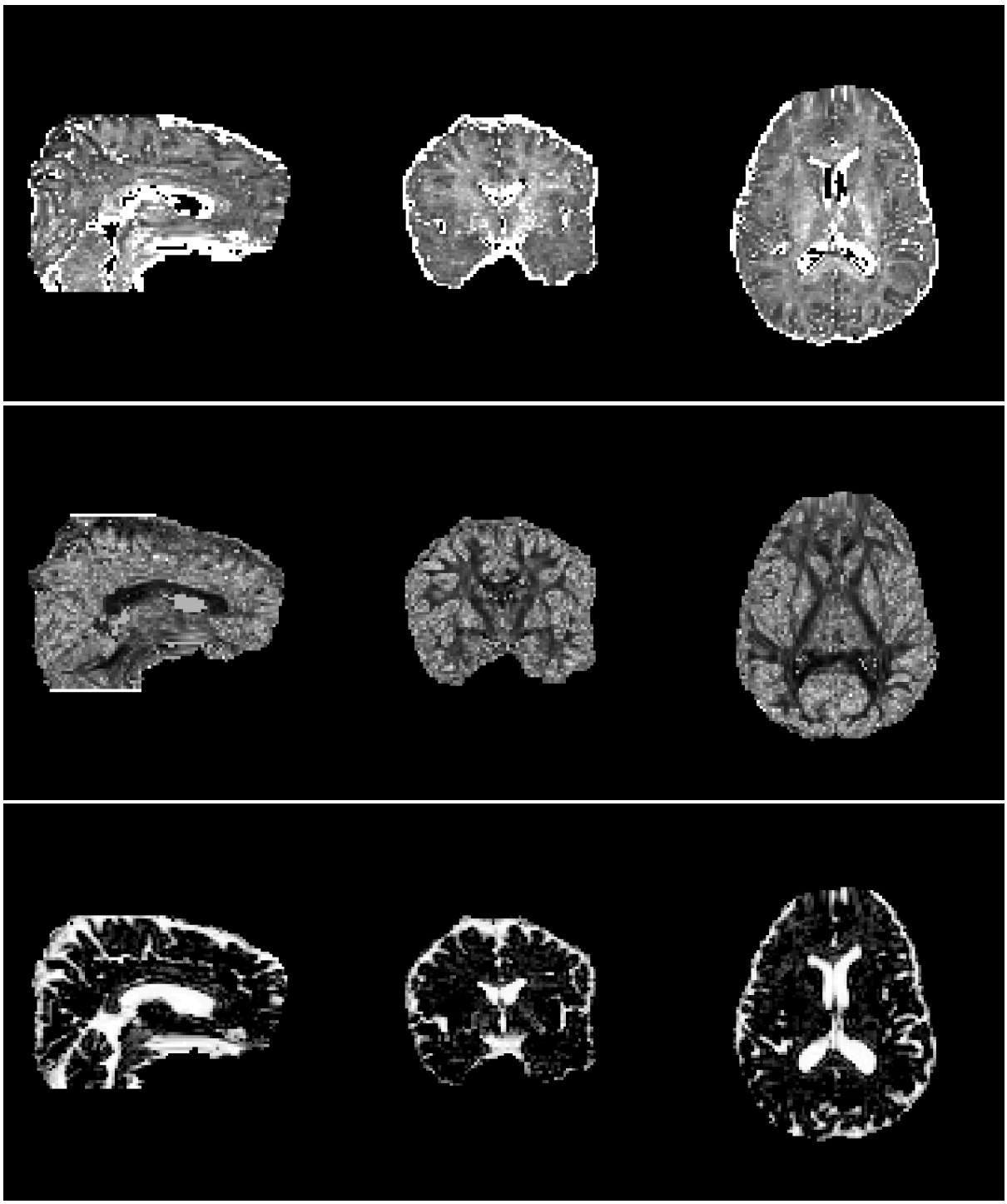


Figure 4. 4. *The resultant NODDI maps are acquired by scanning protocol #3 in Table 5.2. Top images: ICVF, middle images: ODI, bottom images: IsoVF.*

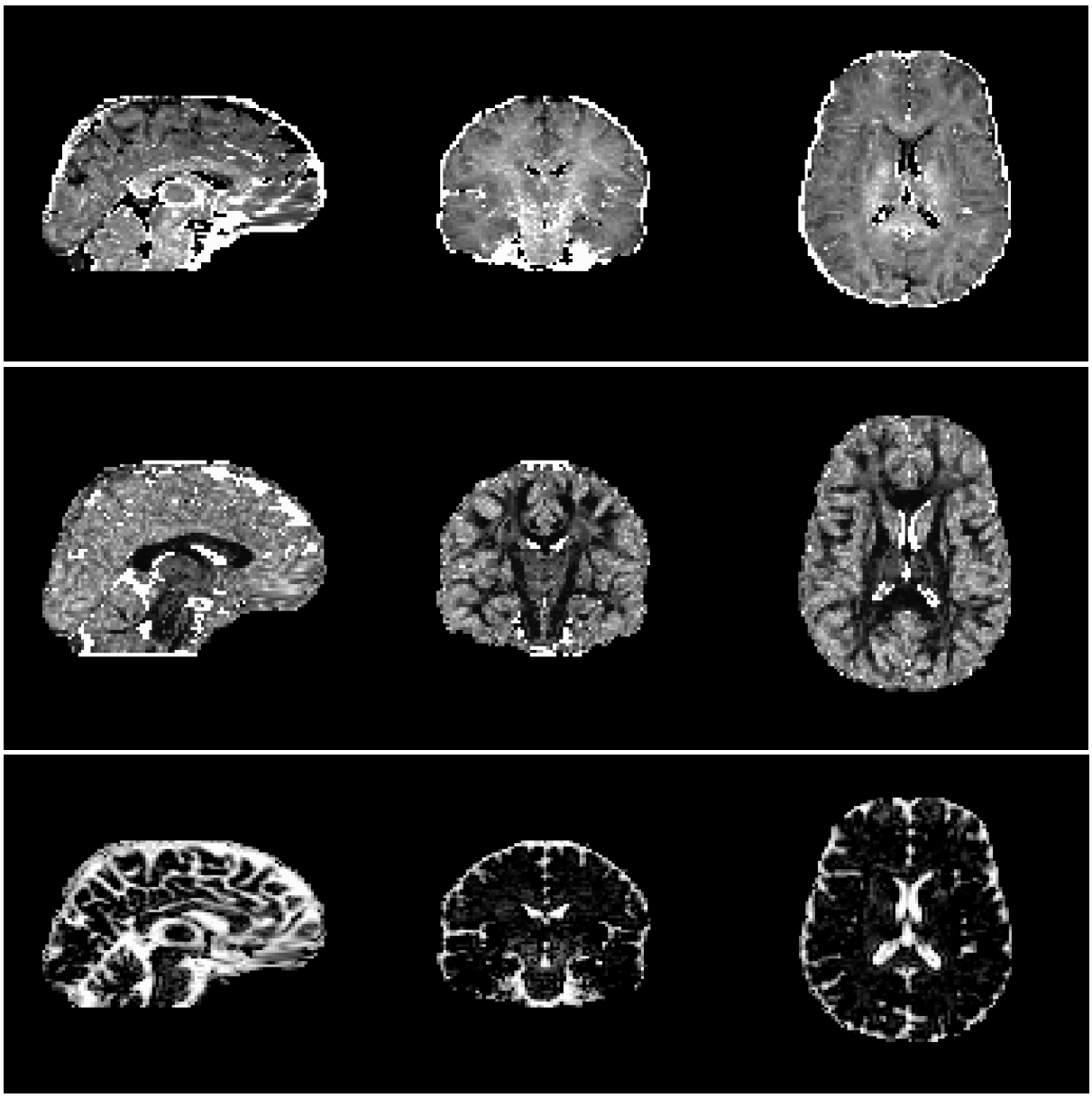


Figure 4. 5. *The resultant NODDI maps are acquired by scanning protocol #4 in Table 5.2. Top images: ICVF, middle images: ODI, bottom images: IsoVF.*

4.4. Conclusion

The evaluated NODDI scanning protocols showed consistent brain microstructure characterisation and were successfully optimised at SPMIC. Research team members, including an experienced neuroradiologist, neurologist, medical physicist and imaging scientist, agreed and recommended the third optimised NODDI protocol (#3 in Table 4.2 and Fig.4.4), which was developed based on recommendations from the UK Biobank team and our colleagues from UCL.

Chapter 5

5. Investigating Brain Microstructural Alterations in Type 1 and Type 2 Diabetes Using Diffusion Tensor Imaging: A Systematic Review **(Word count: 6142)**

This chapter is published (as a review article[8]) in a peer-reviewed journal, and permission from the journal has been obtained to re-use the same work in my thesis. As a first author, I primarily conducted the literature search, inclusion/exclusion criteria, study identification and screening. Also, I extracted the data and wrote the entire content of this published paper. Prof. Dineen and Prof. Constantinescu helped with reviewing the inclusion/exclusion criteria and the article content. Other co-authors assisted with specifying the keywords, identifying the best databases for literature searching, and re-conducting the literature search and study screening.

5.1. Introduction

Diabetes Mellitus (DM) is a metabolic disorder characterised by persistent high blood glucose levels (hyperglycaemia) and inadequate insulin production or dysfunctionality. This disorder is classified into two types with different mechanisms known as type 1 diabetes mellitus (T1DM) and type 2 diabetes mellitus (T2DM)[41]. Both types of DM impact brain functions and microstructure, and this has become a topic of interest for many researchers in the neuroimaging field[8].

T1DM is associated with a modest decline in cognitive ability and brain volume reductions in several regions, most noticeable in T1DM patients with early childhood onset of diabetes[183,184]. However, reductions in volume and microstructural abnormalities in adults may occur after prolonged exposure to diabetes[185]. A previous meta-analysis has shown worse performance in multiple cognitive domains in T1DM due to abnormal brain changes, including intelligence, information processing speed,

psychomotor efficiency, visual and sustained attention, visual perception, cognitive flexibility, and executive functions[183–186]. On the other hand, T2DM is associated with general brain atrophy and microstructural changes that microvascular complications and ageing may cause[187]. The microstructural abnormalities are seen in the WM; when occurring in the temporal lobe, these were associated with poor memory performance[187,188], whereas abnormalities in frontal and temporal lobes were associated with a reduced speed of information processing[187]. T2DM is additionally associated with a modest decline in executive functioning[189].

DTI is a quantitative method that can reveal microstructural alterations in cerebral structures, mainly in the tracts of the WM. DTI detects these changes before anatomical abnormalities become obvious on conventional structural MRI scans[109,190,191]. DTI quantitively measures the motion of water molecules within the brain tissues and can be sensitive to axonal and water orientations in intracellular and extracellular compartments[192]. The water molecules in free spaces diffuse uniformly in many different orientations, known as isotropic water motion. In contrast, the movement of water molecules becomes oriented in a specific direction when cellular barriers are present, such as cellular membranes and myelin sheaths, known as anisotropic diffusion[193,194]. DTI has primary and supplementary metrics for evaluating the diffusivity of water molecules in the white matter microstructure. FA is a primary parameter which increases with the coherence of fibre tracts/myelination and decreases with extracellular water diffusion[195,196]. FA is sensitive to axonal integrity, but changes in extracellular or intracellular liquid content, inflammation, cell death, gliosis, axonal loss, and demyelination can all cause FA alterations[197–199].

AD and RD are additional metrics that quantify the water diffusion of molecules perpendicular and parallel to the dominant nerve fibre orientation, respectively[190]. AD and RD measurements are also affected by axonal loss, demyelination, gliosis, or

inflammation[198]. MD is also a primary metric that calculates the overall diffusivity of water molecules within a voxel and reports the average effects of diffusivity changes in the WM. Increased MD suggests freedom of diffusion as a result of expanded extracellular spaces brought on by tissue demyelination or axonal degeneration[195,196,198].

These DTI metrics have different indications; lower FA and higher MD values indicate a reduction of microstructural tissue integrity. In contrast, altered AD values reflect axonal damage, and altered RD primarily indicates the integrity of the myelin sheath[117]. However, in some cases, the DTI metrics may reflect inaccurate levels of water molecules diffusivity, which can be due to neuronal inflammation or crossing fibres[117,196,200].

A previous systematic review only focused on investigating the impact of T2DM on brain tissues using DTI[193]. However, the T1DM impact was not systematically reviewed. In a recent T2DM systematic review, the author showed that included studies used different methods of image analysis. Since T1DM and T2DM have different mechanisms, they both have been observed to have similar effects on brain microstructure. Conducting a large systematic review on T1DM and T2DM using DTI to investigate the impact on brain microstructure would be interesting and help researchers understand the difference between the impact of T1DM and T2DM on brain microstructure. Therefore, I systematically reviewed the DTI studies that investigated the impact of T1DM and T2DM on brain microstructure and its correlation with cognitive functions and metabolic profile.

5.2. Materials and Methods

This review was registered in the International Prospective Register of Systematic Reviews (PROSPERO) database (CRD42020177420) and conducted according to

the Preferred Reporting Items for Systematic Reviews and Meta-Analysis (PRISMA) guidelines.

5.2.1. Data Sources and Search Strategy

Three electronic databases (Medline (Northfield, IL, USA), Embase (Amsterdam, Netherlands), and PubMed (Bethesda, Maryland, USA)) were searched to identify relevant studies from April 2020 to October 2020. As a first author, A.A. (Abdulmajeed Alotaibi) conducted all systematic review stages from search to writing up the manuscript. An experienced librarian R.S. (Rebecca Stevenson) helped to develop the search terms, and strategies ("Diabetes Mellitus;" "Type 1 Diabetes"; "Type 2 Diabetes"; "Diffusion Imaging"; "Diffusion Tensor Imaging"; "DTI"; "Microstructural Abnormalities"; "Cognitive Dysfunction"). The database identification and screening stages were performed by A.A. (Abdulmajeed Alotaibi). Additional screening (titles, abstracts, and full texts) was conducted independently and blindly by four reviewers with a medical imaging background and have conducted many systematic reviews (A.A (Amjad Altokhis), G.F (Ghadah Felmban), C.T (Chris Tench) and A.A. (Ali Aldhebaib)). All references listed in the included studies were reviewed carefully by an experienced MRI scientist A.A. (Abdulmajeed Alotaibi) and an experienced neuroradiologist R.A.D (Rob Dineen) for eligible study inclusion. An experienced neurologist C.S.C (Cris Constantinescu) and an experienced neuroradiologist R.A.D reviewed the entire content. Finally, disagreements between all reviewers were solved by a mutual discussion.

5.2.2. Study Selection and Inclusion Criteria

Studies in this review were selected and included based on an agreed list of inclusion and exclusion criteria (Table 5.1). All articles written in a language other than English or involving animals were excluded from this review. The age range of participants in all included studies had to be between 5 and 75 years. Studies which recruited patients

with T1DM and T2DM were included only. However, studies that recruited patients with neurological/metabolic disorders other than diabetes, cancer, brain implants, and surgeries were excluded.

Study Selection and Inclusion Criteria (a)	
Inclusion	**Exclusion**
• Cross-sectional design • Cohort: Prospective/retrospective	• Reviews or systematic literature reviews • Qualitative studies • Editorials, comments, news, and letters
• Studies published in peer-review journals or the grey literature are considered for inclusion.	
• Written in English	
Participants' Selection and Inclusion Criteria (b)	
Inclusion	**Exclusion**
Age: 5–75 years old (flexible)	• Neurological disorders and other diseases not due to diabetes • Animal or in-vitro
Healthy controls: • No neurological disorders • No history of diabetes	
Patients: • People with T1DM • People with T2DM	

Table 5. 1. *Study and participant selection criteria: (a) represents the list of study selection and inclusion criteria, and (b) represents the list of participant selection criteria.*

5.2.3. Data Extraction and Management

In July 2020, A.A. (Abdulmajeed Alotaibi) extracted and organised all data from included studies using Microsoft Excel. Three tables of each diabetes group were designed to extract the data ideally. The first table had patients' and healthy individuals' demographic and clinical characteristics. The second table extracted the DTI analysis and between-group diffusion findings, specifically, the microstructural changes and DTI metrics. Lastly, the associations of diffusion metrics with cognitive dysfunctions and metabolic profiles were extracted in the third table. Meta-analysis was not feasible due to the variation in image analysis methods.

5.3. Results

The electronic search of the three databases retrieved 649 studies, and after removing the duplicated studies, 519 studies remained. The title and abstract screening excluded 394 studies that did not meet the eligibility criteria. After the title and abstract

review, 125 studies remained for full-text assessment. Following the full-text evaluation, 87 studies were excluded based on the reasons shown in the PRISMA diagram. A total of 38 studies that explored the brain microstructure in T1DM and T2DM patients using DTI were included as they met the inclusion criteria of this review. The detailed process of article searching, identification, and screening is in Fig.5.1.

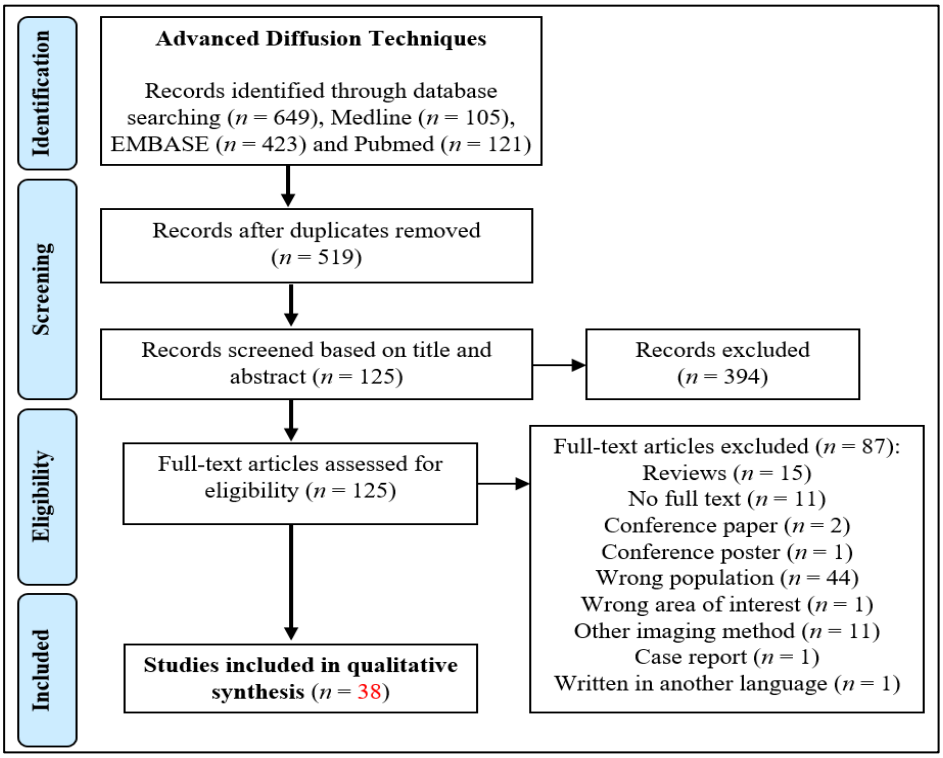


Figure 5. 1. *Systematic search strategies include study identifications, screening, eligibility, and inclusion.*

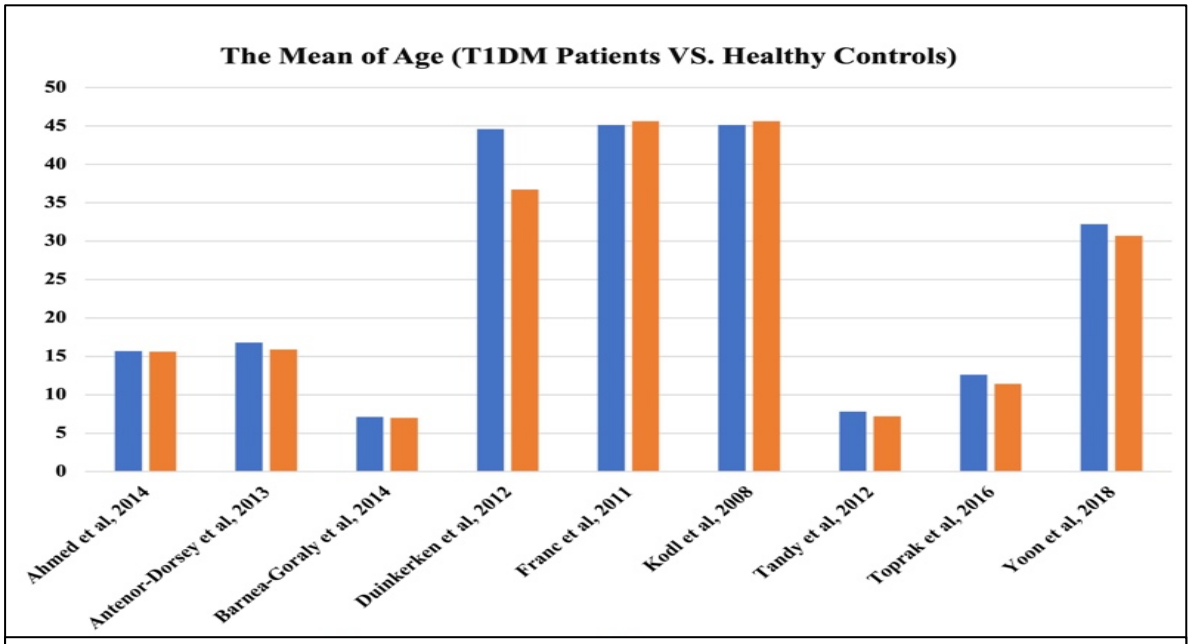
5.3.1. Overview of Reviewed DTI-T1DM Studies

A total of 9 DTI-T1DM studies investigating the brain microstructural changes and their relationships with cognitive functions and metabolic profiles in T1DM were included in this comprehensive review. The studies were designed cross-sectionally, most of which were performed in the United States between 2008 and 2018. The participants were young adults and individuals in their teens, except for two studies[201,202], conducted on children under 10 years of age (Fig.5.2A). Regarding the clinical characteristics, the mean disease duration, the mean of haemoglobin A1c (Hb1Ac),

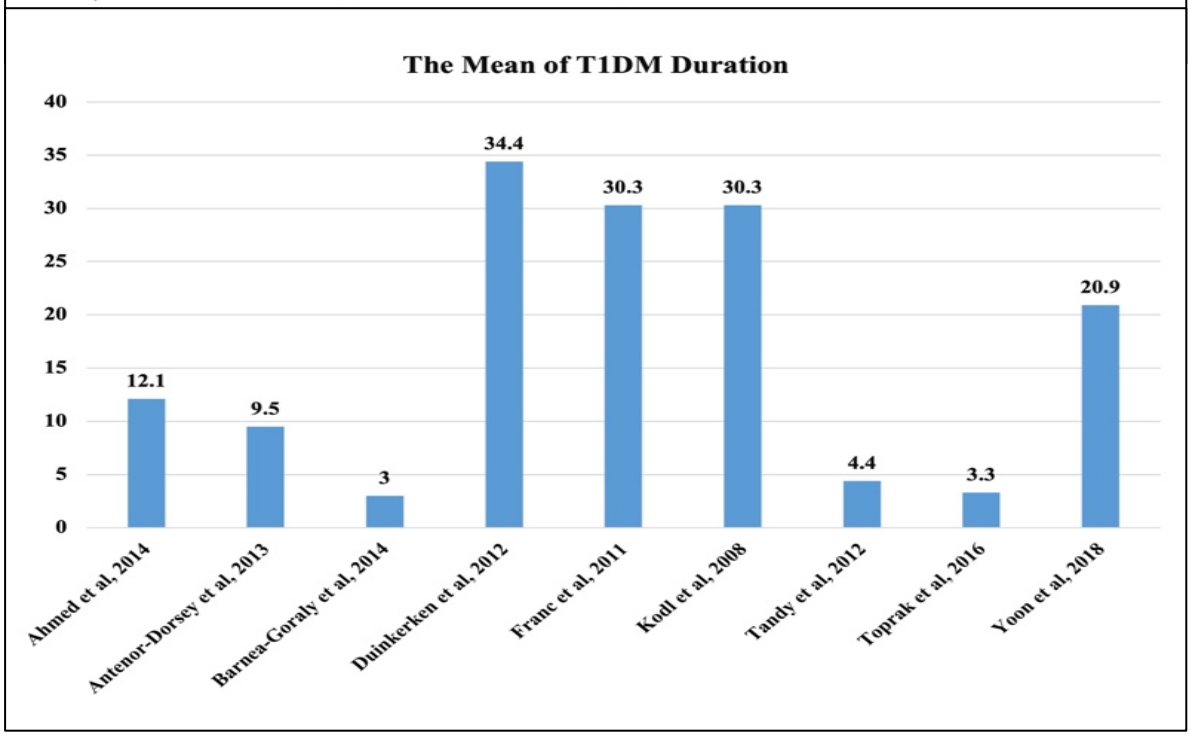
and the mean of fasting blood sugar (FBS) in the included studies are summarised in Fig.5.2B–D. Also, the technical characteristics are summarised in Table 5.2.

A total of 5 studies examined the DTI diffusion parameters such as MD, FA, AD or RD, while the other 4 articles only investigated the white matter using FA[183,203–205]. Three different analysis methods were used; tract-based spatial statistics (TBSS) analysis was used frequently for the whole brain (Fig.5.3). A total of 6 studies acquired the data on 1.5T MRI scanners, and 3 studies obtained the images on 3T MRI units[183,202,205].

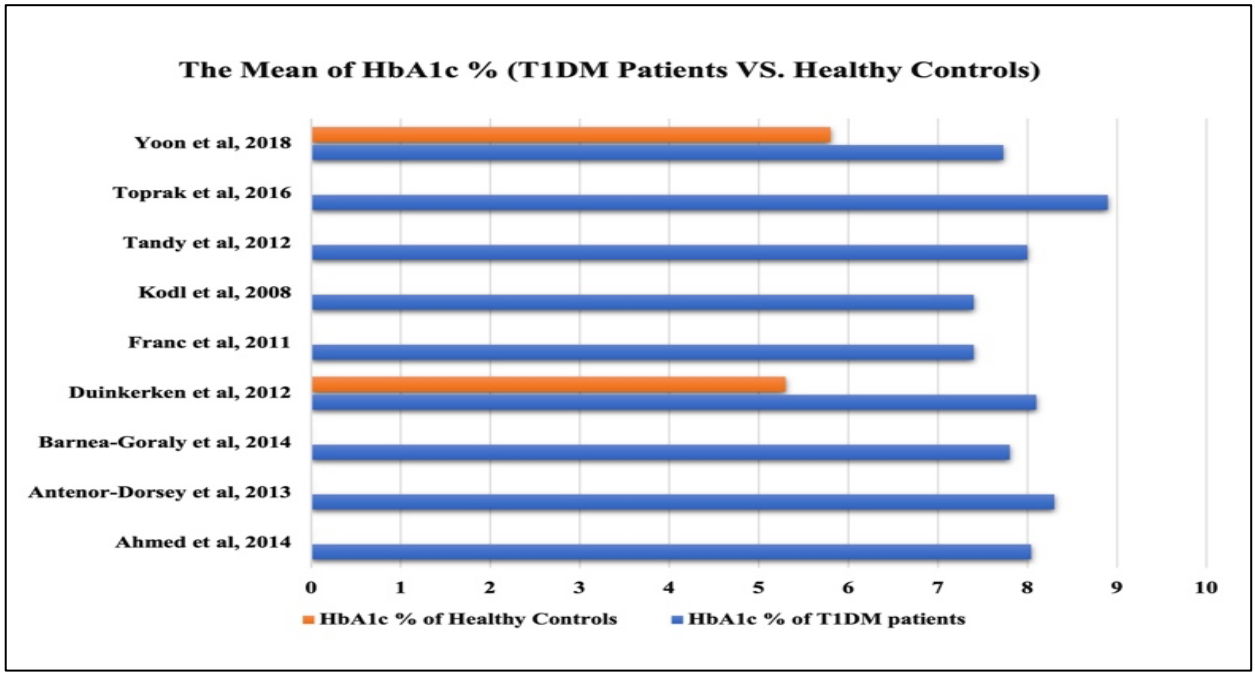
A



B



C



D

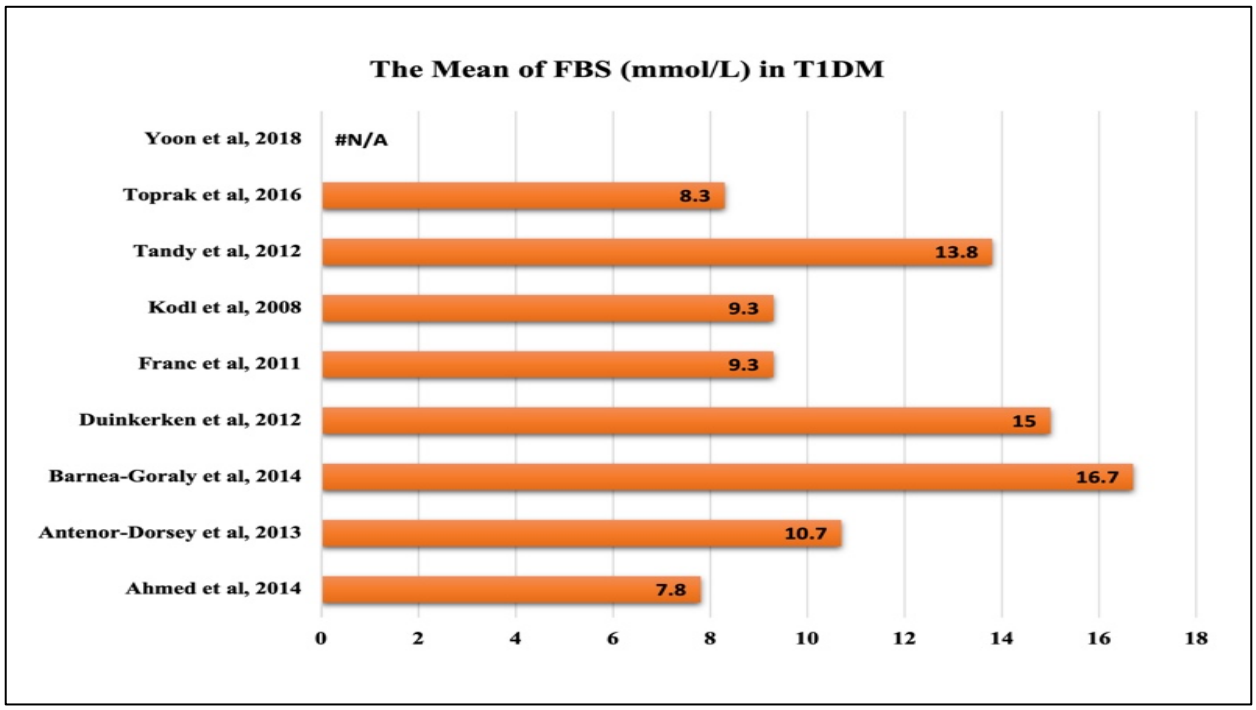


Figure 5. 2. *Mean values of clinical characteristics. (A) represents the mean age of T1DM and healthy controls; (B) represents the mean duration of T1DM; (C) represents the mean HbA1C of T1DM and healthy controls; (D) represents the mean FBS of T1DM.*

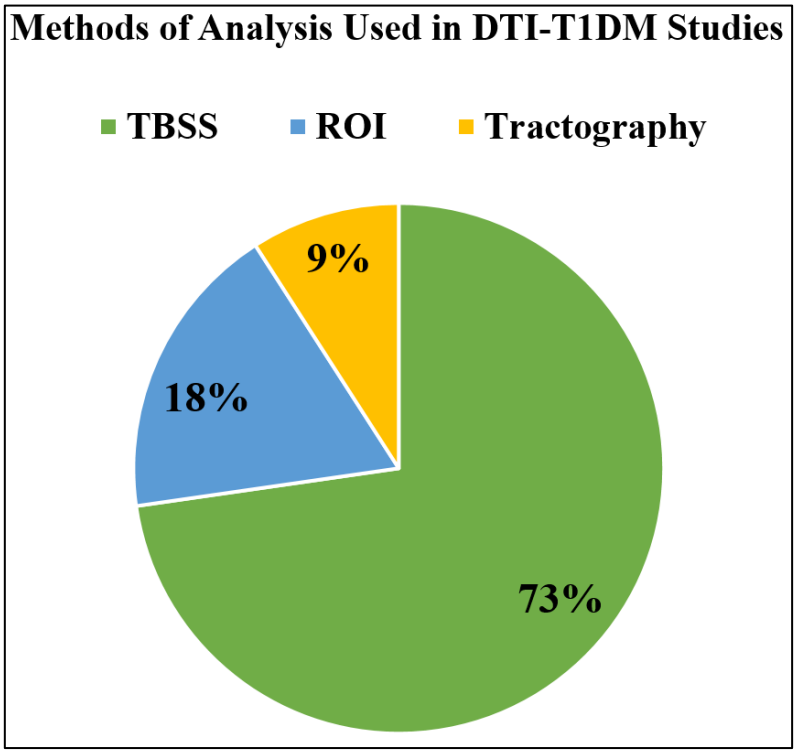


Figure 5. 3. *Methods used to analyse brain microstructural changes in T1DM patients.*

Technical Characteristics of the Included Studies					
T1DM Studies					
Study	**Author**	**Field Strength**	**RF Coil/ Fitting Toolbox**	**b-values (s/mm^2)**	**Method of Analysis/Regions**
1	Naama Barnea-Goraly, 2014	3.0 T	12 DTI studio FSL	1000	TBSS
2	Sujung Yoon, 2018	1.5 T	-- FSL	1000	TBSS/ROI analysis
3	Daniel T. Franc, 2011	3.0 T	-- FSL FreeSurfer	1000	TBSS/Fibre tract projection
4	Christopher T. Kodl, 2008	1.5 T	-- FSL	1000	TBSS
5	Tandy Aye, 2012	1.5 T	-- DTI studio FSL	850	TBSS
6	E. Van Duinkerken, 2012	1.5 T	-- FSL	700	TBSS/VBA
7	Hanan H. Ahmed, 2014	1.5 T	-- FSL	700	TBSS
8	Jo Ann V. Antenor-Dorsey, 2013	1.5 T	-- FSL	800-1000-1200	TBSS/ROI analysis
9	Huseyin Toprak, 2016	1.5 T	-- FSL	1000	ROI analysis

Table 5.2. Technical characteristics of included T1DM studies. Abbreviations: -- = not available; T = tesla; ROI = region of interest.

5.3.2. Between-Group Differences: Microstructural Alterations in T1DM

A total of 8 of the included studies consistently revealed the reduction of FA in T1DM[183,185,202–207], lower MD, AD, and higher RD in the white matter of T1DM patients compared to healthy controls (Table 5.3) (Fig.5.4)[185,201–207]. Most of the studies analysed DTI images using only voxel-wise brain analysis, while other studies used both region of interest (ROI) and voxel-wise analysis[203–207], except for one study, which used DTI tractography[205].

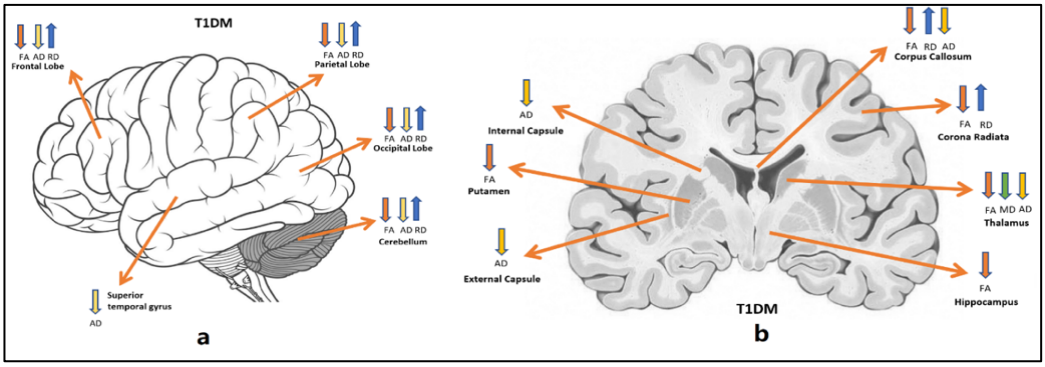


Figure 5. 4. Altered diffusion measures in T1DM brain structures. (A) shows the affected brain lobes and cerebellum, and (B) a cross-sectional view of deep brain tissues. Orange: FA; green: MD; yellow: AD; blue: RD. Directions: down: decrease; up: increase.

In all the included studies, FA values in individuals with T1DM were measured; in general, most studies reported consistent results of reduced FA values in a wide range of cortical brain regions, including frontal, temporal, and parietal white matter, as well as subcortical white matter, in individuals with T1DM compared to healthy controls. One study reported a widespread reduction of FA in T1DM patients with and without microangiopathy compared to controls[185]. In T1DM patients with microangiopathy, reduced FA was observed bilaterally in the thalamic radiation, corpus callosum, superior longitudinal fasciculus and forceps minor, while reduced FA in patients without microangiopathy was limited to the corpus callosum and right corona radiata[185]. Another study reported a reduction of FA in the white matter tracts of adolescents with T1DM; this decreased FA was mainly observed in optic radiation and superior longitudinal fasciculus[204]. Kodl et al. reported reduced FA in the optic

radiation, posterior corona radiata, splenium and the posterior body of the corpus callosum, which partially overlaps with the study by van Duinkerken et al., who reported lower FA in the corpus callosum and right corona radiata of T1DM patients without microangiopathy[183,185]. However, two studies reported no significant difference in FA values between T1DM and controls in adolescents[201] and adults[210]. A widespread reduction in FA was observed in T1DM patients with younger age onset[202] and middle-aged patients[205]. One more study reported an extended observation of FA reduction in the white matter of young adult patients, where reduced FA was found bilaterally in the superior longitudinal fasciculi, corpus callosum, and right inferior frontal-occipital fasciculus[206].

Antenor-Dorsey et al. found variations in MD and RD values in adolescents with T1DM. However, lower AD was significantly reported in the superior parietal lobule, corpus callosum, external capsule, posterior limb of the internal capsule and cerebral peduncle compared with healthy volunteers[207]. Individuals with T1DM and more than three episodes of severe hyperglycaemia had lower FA and higher RD in the superior parietal lobule than HC. More frequent episodes of hypoglycaemia are also associated with lower FA of the superior parietal lobule in T1DM[207]. Barnea-Goraly et al. examined the effects of disease onset and duration in children with T1DM. The results showed no significant differences in MD but a widespread reduction in AD in the white matter throughout patients' brains, significantly in patients with longer disease duration. Contrarily, the study reported a general increase in RD in the white matter of patients of younger age at disease onset[202]. In middle-aged adults with T1DM, there were no significant MD differences reported. However, a substantial increase in RD was in the posterior portion of the corpus callosum, bilateral corticospinal and inferior frontal occipital tracts, forceps minor and corona radiata in T1DM patients with and without microangiopathy. The authors also observed significantly lower AD in the corpus

callosum, forceps minor and major, superior longitudinal fasciculus and thalamic radiation in patients with and without microangiopathy[185]. Aye et al. observed no significant RD differences in children with T1DM, which may be due to the short disease duration; however, a considerable decrease in AD was found in the internal capsule, the body of the corpus callosum, right cingulate gyrus, right thalamus, right superior temporal gyrus, and posterior parietal lobe[201].

Using the DTI tractography method, one study investigated the grey matter in middle-aged adults with T1DM, reporting a significant reduction of cortical thickness for cortical regions with high connectivity to the optic radiations and posterior corona radiata tracts[205]. Using the ROI-analysis method, two studies reported a pronounced FA reduction in the white matter and grey matter of adolescents with T1DM compared to controls. Antenor-Dorsey et al. noticed lower FA in the superior parietal lobule[207]. Likewise, Toprak et al. observed FA reduction in various regions of the T1DM brain, such as in the putamen, inferior longitudinal fasciculus, thalamus, corticospinal tracts at the pons, frontal white matter, hippocampus, and corona radiata[203]. In adolescents with T1DM, only one study investigated the between-group changes of the additional diffusion indices such as MD, AD and RD using the ROI analysis method. The study significantly reported a reduction of MD in the thalamus and an increase in RD in the cerebellum; however, lower AD was observed in the cerebellum, and no FA, MD, RD, and AD differences were seen between groups in the hippocampus[207].

Microstructural Alterations in T1DM Patients

Region	↓ **FA** (Fractional anisotropy)	↓ **MD** (Mean diffusivity)	↑ **RD** (Radial diffusivity)	↓ **AD** (Axial diffusivity)
Corpus callosum	van Duinkerken et al. 2012 (with/without microangiopathy), Kodl et al. 2008, Yoon et al. 2018.	--	Van Duinkerken et al. 2012 (with/without microangiopathy).	Antenor-Dorsey et al. 2013, van Duinkerken et al. 2012 (with/without microangiopathy), Tandy et al. 2012.
Corona radiata	van Duinkerken et al. 2012 (without microangiopathy), Kodl et al. 2008, Franc et al. 2011, Toprak et al. 2016.	--	Van Duinkerken et al. 2012 (with/without microangiopathy).	--
Thalamic radiation	van Duinkerken et al. 2012 (with microangiopathy).	--	--	Van Duinkerken et al. 2012 (with/without microangiopathy).

Forceps minor and major	van Duinkerken et al. 2012 (with microangiopathy).	--	Van Duinkerken et al. 2012 (with/without microangiopathy).	Van Duinkerken et al. 2012 (with/without microangiopathy).
Superior longitudinal fasciculi (SLF)	Van Duinkerken et al. 2012 (with microangiopathy), Ahmed et al. 2014, Yoon et al. 2018.	--	--	Van Duinkerken et al. 2012 (with/without microangiopathy).
Optic radiation	Ahmed et al. 2014, Kodl et al. 2008, Franc et al. 2011.	--	--	--
Putamen	Toprak et al., 2016	--	--	--
Inferior longitudinal fasciculus (ILF)	Toprak et al. 2016	--	--	--
Thalamus	Toprak et al. 2016	Antenor-Dorsey et al. 2013	--	Antenor-Dorsey et al. 2013, Tandy et al. 2012
Hippocampus	Toprak et al., 2016	--	--	--
Inferior frontal-occipital fasciculus	Yoon et al., 2018	--	van Duinkerken et al. 2012 (with/without microangiopathy)	--
Superior parietal lobule	Antenor-Dorsey et al., 2013	--	Antenor-Dorsey et al., 2013	Antenor-Dorsey et al., 2013
Cerebellum	--	--	Antenor-Dorsey et al., 2013	Antenor-Dorsey et al., 2013
Internal capsules	--	--	--	Antenor-Dorsey et al., 2013; Tandy et al., 2012
External capsules	--	--	--	Antenor-Dorsey et al., 2013
Cerebral peduncle	--	--	--	Antenor-Dorsey et al., 2013
Cingulate gyrus	--	--	--	Tandy et al., 2012
Superior temporal gyrus	--	--	--	Tandy et al., 2012
White matter (Widespread changes)	Barnea-Goraly et al., 2014	--	Barnea-Goraly et al. 2014 (reduced RD with longer disease duration and increased RD with younger age at disease onset).	Barnea-Goraly et al., 2014

Table 5. 3. *Illustrates the diffusion findings between the groups of T1DM. (↓) increased values, and (↑) decreased values.*

5.3.3. Microstructural and Cognitive Abnormalities in T1DM

The findings of the reviewed studies suggest that brain changes caused by T1DM are associated with attention deficits, information processing, psychomotor speed, and executive functions. In adolescents with T1DM, Ahmed et al. reported that the Wisconsin Card Sorting Test (WCST) score was positively correlated with FA at the midbrain region. This correlation showed worse performances on tests for attention, speed of information processing, and executive functions. The Benton Visual Retention Test (BVRT) was used to test visual perception, visual memory, and constructive visual abilities, which showed a positive relationship between impairment and changes in corona radiata, cingulum, splenium and optic radiation[204]. In contrast, a negative correlation between the intelligence quotient (IQ) level and FA of the midbrain, thalamus, and the posterior portion of the internal capsule with verbal points[203].

In children with T1DM, a correlation between lower FA and Full-Scale Intelligence Quotient (FSIQ) approached significance in the bilateral parietal lobes and the right superior temporal gyrus, which caused modest alterations in cognitive abilities such as visuospatial abilities, attention, general intellectual ability, memory, processing speed, and executive functions[202]. Another study reported a positive correlation between the Wechsler Intelligence Scale for Children (WISC) and FSIQ with FA values and information processing speed[201].

In young adults with T1DM, Franc et al. found a significant relationship between the performance and cortical thickness in posterior grey matter regions, which suggested the involvement of these regions in executive functions and psychomotor speed[205]. Recruiting the same subjects, Kodl et al. confirmed that reduced FA values in the white matter correlated with poor cognitive performance[183]. Lastly, Yoon et al. noted that lower working memory performance was associated with low FA values in the bilateral superior longitudinal fasciculi in young adults with T1DM (Fig.5.5)[206].

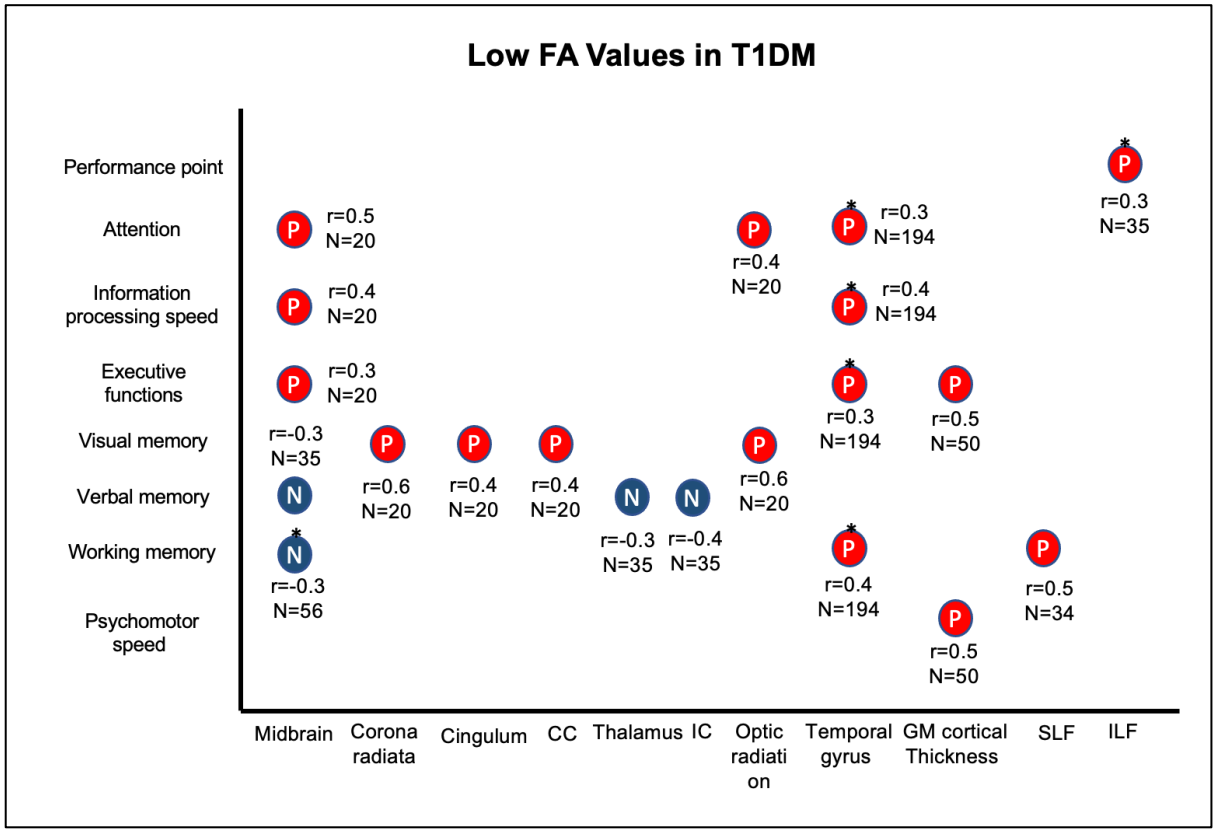


Figure 5. 5. *The association of FA diffusion metrics with cognitive functions in T1DM. (CC: corpus callosum, IC: internal capsule, GM: grey matter, SLF: superior longitudinal fasciculus; ILF: inferior longitudinal fasciculus). P-value =0.05; N=sample size; *=Children; P=positive correlation; N=negative correlation; r=correlation coefficient.*

5.3.4. Microstructural Alterations and Metabolic Profile in T1DM

The findings of included studies suggest that longer disease duration and increased HbA1c values correlated with the severity of microstructural abnormalities in optic radiation[183,204], posterior corona radiata, right internal capsule, anterior forceps, inferior frontal occipital fasciculi, splenium of the corpus callosum[183], uncinate fasciculi, subgenual white matter, superior, middle, inferior temporal gyri, superior longitudinal fasciculi, and occipital white matter[201,202,206].

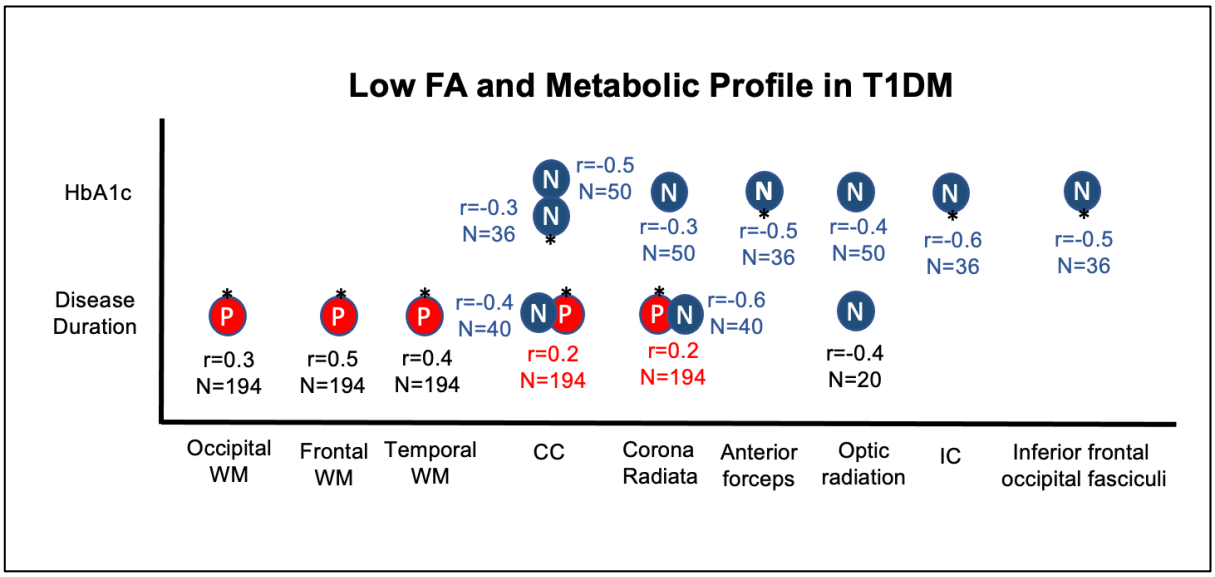
In adolescents, Ahmed et al. reported an inverse relationship between the duration of diseases and lower FA in optic radiation only[204]. However, Barnea-Goraly et al. found that the increased duration of T1DM was positively associated with FA in the occipital, frontal, temporal, parietal lobes, and multiple white matter tracts. This correlation is likely because of the younger age and the effect of age in this study. Additionally, the increased duration of T1DM was associated with AD and RD at the younger age of T1DM onset. HbA1c values at baseline were negatively associated with FA values and positively associated with RD values[202].

In middle-aged adults, reduced FA values in the posterior corona radiata, the optic radiation, splenium, and the posterior body of the corpus callosum were correlated with the duration of diabetes and the increased values of HbA1c[183]. In young adults, there was a negative relationship between FA values and current HbA1c. However, long-lasting glycaemic control levels, severe hypoglycaemia, and disease duration were not correlated with FA in the T1DM group[206].

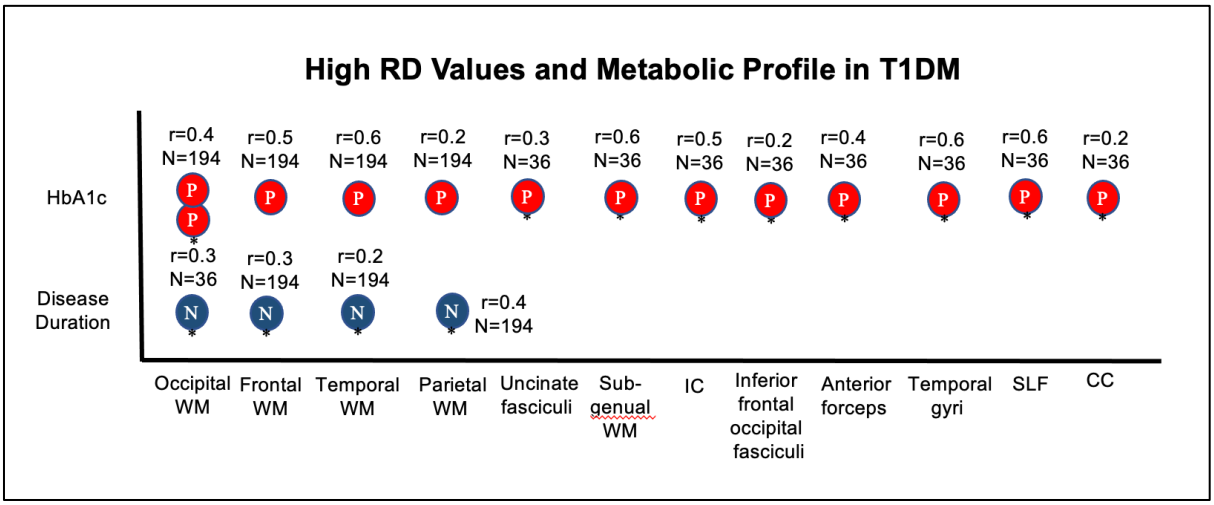
In children, Aye et al. described a negative correlation between HbA1c values and FA in the anterior forceps, right internal capsule, inferior frontal occipital fasciculi, and splenium of the corpus callosum. Conversely, a positive correlation was reported

between HbA1c and RD in inferior frontal occipital fasciculi, uncinate fasciculi, subgenual white matter, anterior forceps, the right internal capsule, superior middle and inferior temporal gyri, the splenium of the corpus callosum, superior longitudinal fasciculi, and occipital white matter[201] (Fig.5.6A–C).

A



B



C

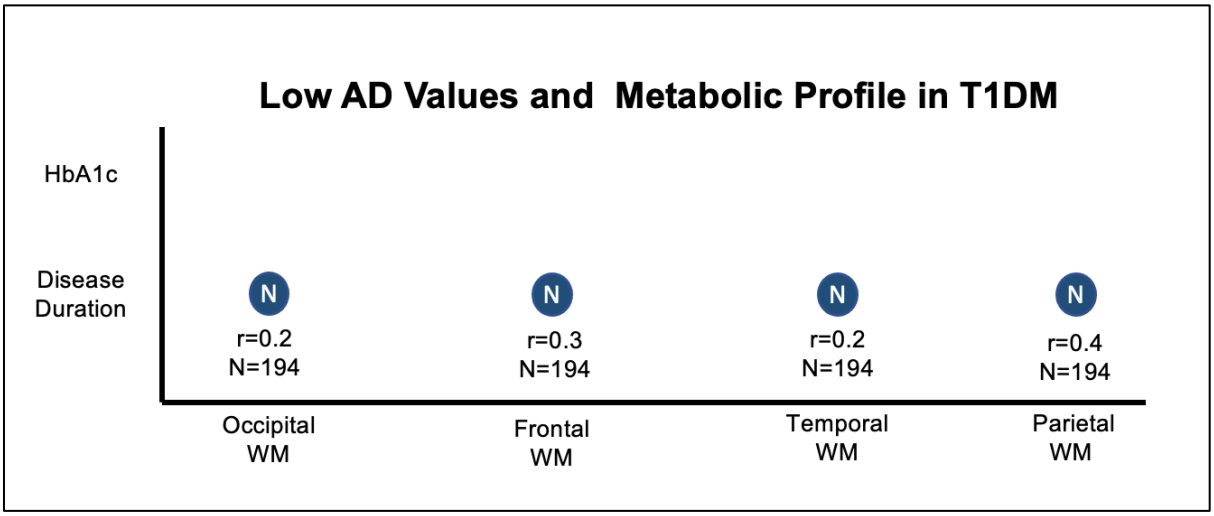


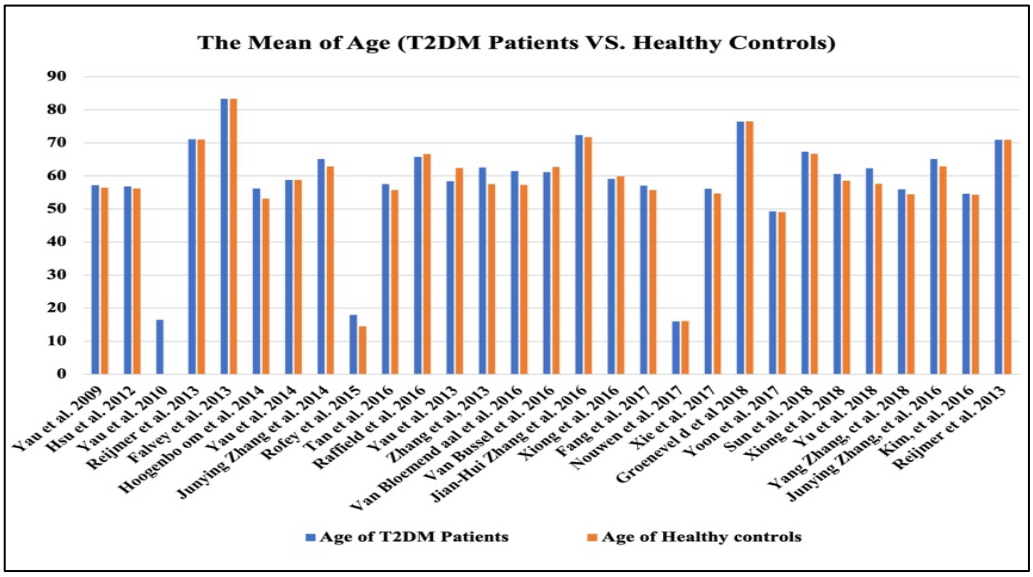
Figure 5. 6. *The association of diffusion metrics and metabolic profile in T1DM. (A) illustrates the correlation between FA and metabolic profile; (B) illustrates the correlation between RD and metabolic profile; (C) illustrates the correlation between AD and metabolic profile. (CC: corpus callosum, IC: internal capsule, WM: white matter, SLF: superior longitudinal fasciculus). P-value =0.05; N=sample size; *=Children; P=positive correlation; N=negative correlation; r=correlation coefficient.*

5.3.5. Overview of Reviewed DTI-T2DM Studies

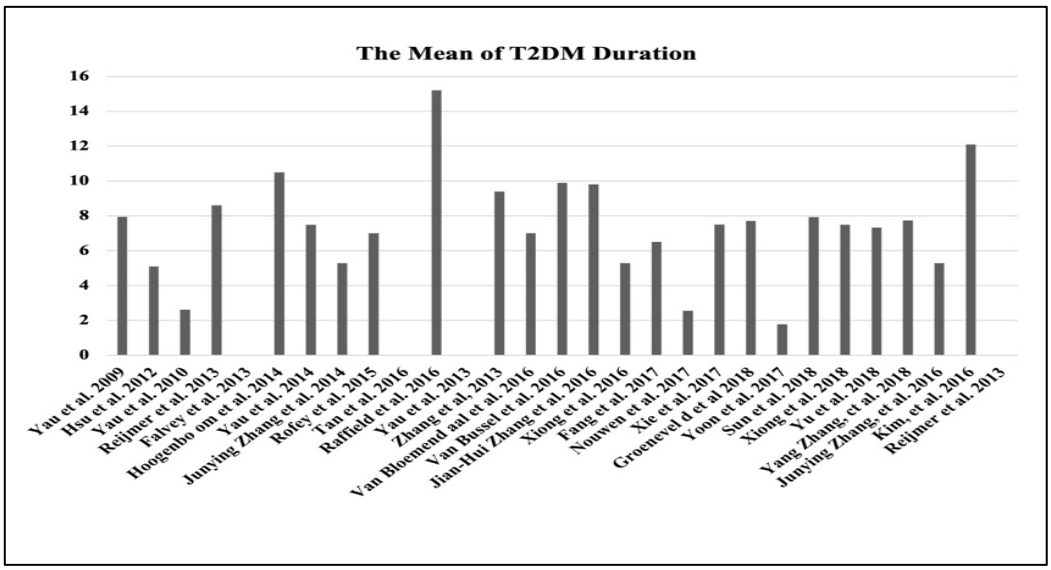
A total of 29 DTI-T2DM studies investigating the brain microstructural changes and their relationships with cognitive functions and metabolic profiles in T2DM patients were included in this review. These studies were designed cross-sectionally, and most of the included studies were performed in China and the United States since 2016. The participants were mostly adults in their middle age or older, except for three DTI-T2DM studies conducted on young adult patients[188,208,209](Fig.5.7A). Regarding the clinical characteristics, the mean disease duration, the mean of haemoglobin A1c (Hb1Ac), and the mean of fasting blood sugar (FBS) in the included studies are summarised in Fig.5.7B–D. Also, the technical characteristics are summarised in Table 5.4.

A total of 25 reviewed articles examined DTI diffusion indices such as FA, AD, RD, or MD, while four other studies utilised graphical theory to analyse the network of white matter using the DTI technique. The TBSS technique of the whole brain was used more frequently in the reviewed studies, and FA maps were often investigated (Fig.5.8). Most of the data were acquired on 3T MRI scanners in the included studies, while a few other datasets were obtained on 1.5T MRI units.

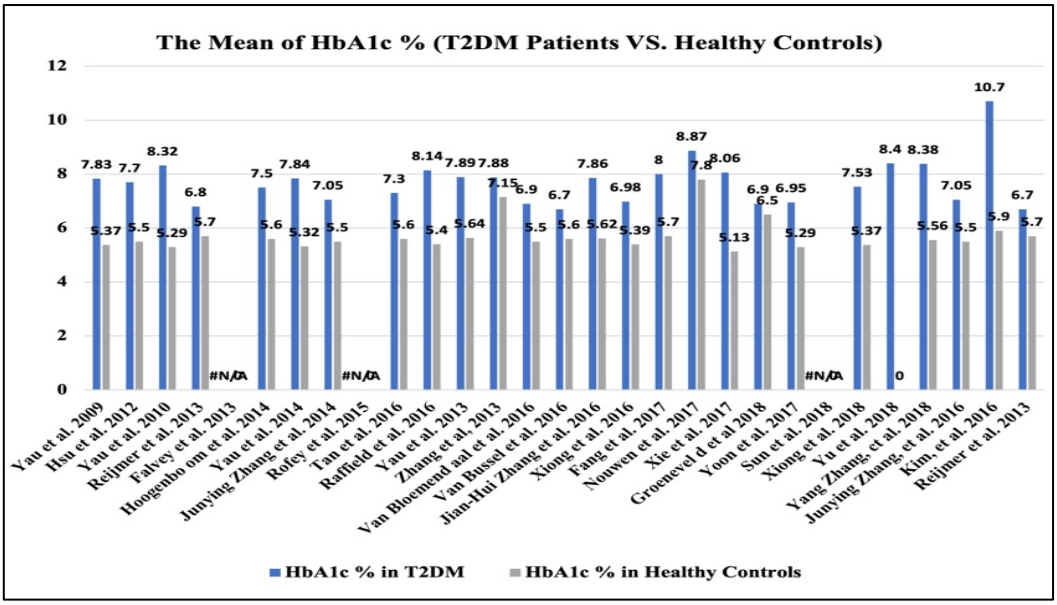
A


The Mean of Age (T2DM Patients VS. Healthy Controls)
90
80
70
60
50
40
30
20
10
0
Yau et al. 2009
Hsu et al. 2012
Yau et al. 2010
Reijmer et al. 2013
Falvey et al. 2013
Hoogenbo om et al. 2014
Junying Zhang et al. 2014
Yau et al. 2014
Rofey et al. 2015
Tan et al. 2016
Raffield et al. 2016
Yau et al. 2013
Zhang et al. 2013
Van Bloemend aal et al. 2016
Van Bussel et al. 2016
Jian-Hui Zhang et al. 2016
Xiong et al. 2016
Fang et al. 2017
Nouwen et al. 2017
Xie et al. 2017
Groenevel d et al 2018
Yoon et al. 2017
Sun et al. 2018
Xiong et al. 2018
Yu et al. 2018
Yang Zhang, et al. 2018
Junying Zhang, et al. 2016
Kim, et al. 2016
Reijmer et al. 2013
Age of T2DM Patients
Age of Healthy controls

B


The Mean of T2DM Duration
16
14
12
10
8
6
4
2
0
Yau et al. 2009
Hsu et al. 2012
Yau et al. 2010
Reijmer et al. 2013
Falvey et al. 2013
Hoogenbo om et al. 2014
Junying Zhang et al. 2014
Yau et al. 2014
Rofey et al. 2015
Tan et al. 2016
Raffield et al. 2016
Yau et al. 2013
Zhang et al. 2013
Van Bloemend aal et al. 2016
Van Bussel et al. 2016
Jian-Hui Zhang et al. 2016
Xiong et al. 2016
Fang et al. 2017
Nouwen et al. 2017
Xie et al. 2017
Groenevel d et al 2018
Yoon et al. 2017
Sun et al. 2018
Xiong et al. 2018
Yu et al. 2018
Yang Zhang, et al. 2018
Junying Zhang, et al. 2016
Kim, et al. 2016
Reijmer et al. 2013

C


The Mean of HbA1c % (T2DM Patients VS. Healthy Controls)
12
10
8
6
4
2
0
7.83 7.7 8.32 6.8 #N/A 7.5 7.84 7.05 #N/A 7.3 8.14 7.89 7.88 6.9 6.7 7.86 6.98 8 8.87 8.06 6.9 6.95 #N/A 7.53 8.4 8.38 7.05 10.7 6.7
5.37 5.5 5.29 5.7 5.6 5.32 5.5 5.6 5.4 5.64 7.15 5.5 5.6 5.62 5.39 5.7 7.8 5.13 6.5 5.29 5.37 0 5.56 5.5 5.9 5.7
Yau et al. 2009
Hsu et al. 2012
Yau et al. 2010
Reijmer et al. 2013
Falvey et al. 2013
Hoogenbo om et al. 2014
Junying Zhang et al. 2014
Yau et al. 2014
Rofey et al. 2015
Tan et al. 2016
Raffield et al. 2016
Yau et al. 2013
Zhang et al. 2013
Van Bloemend aal et al. 2016
Van Bussel et al. 2016
Jian-Hui Zhang et al. 2016
Xiong et al. 2016
Fang et al. 2017
Nouwen et al. 2017
Xie et al. 2017
Groenevel d et al 2018
Yoon et al. 2017
Sun et al. 2018
Xiong et al. 2018
Yu et al. 2018
Yang Zhang, et al. 2018
Junying Zhang, et al. 2016
Kim, et al. 2016
Reijmer et al. 2013
HbA1c % in T2DM
HbA1c % in Healthy Controls

D

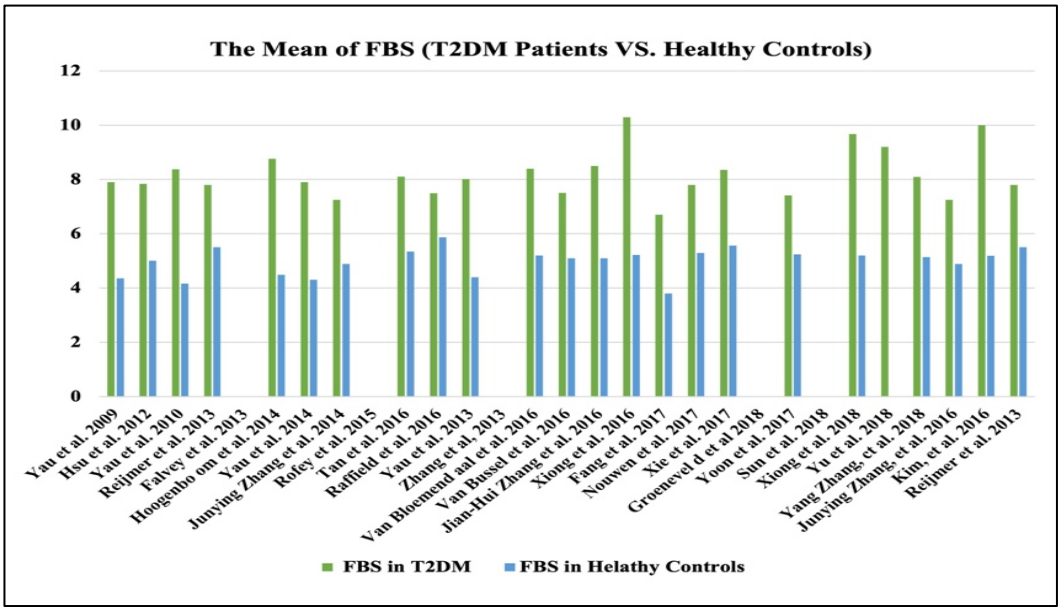


Figure 5. 7. *Mean values of clinical characteristics. (A) illustrates the mean age of type 2 diabetes mellitus (T2DM) and healthy controls; (B) illustrates the mean duration of T2DM; (C) illustrates the mean HbA1C of T2DM and healthy controls; (D) illustrates the mean fasting blood sugar (FBS) of T2DM.*

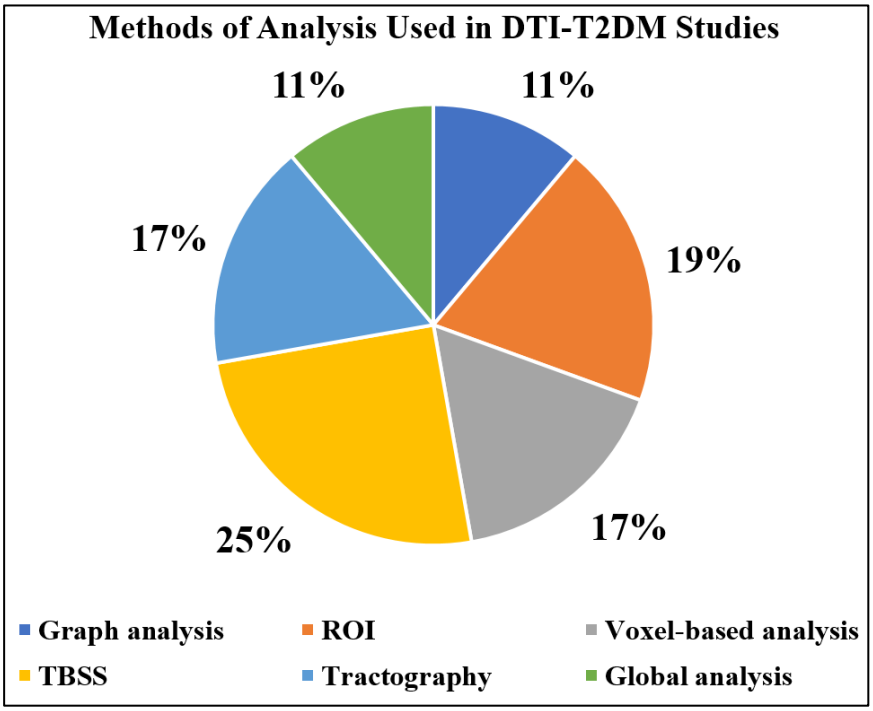


Figure 5. 8. *Methods used to analyse brain microstructural changes in T2DM patients. (ROI: region of interest, TBSS: tract-based spatial statistics, T2DM: type 2 diabetes mellitus).*

Technical Characteristics of the Included Studies					
T2DM Studies					
1	Yael Reijmer, 2013 (a)	3.0 T	-- ExploreDTI	1200	ROI-based tractography
2	Y. Xiong, X, 2016	3.0 T	32 FSL	1000	TBSS
3	Ying Cui, 2020	3.0 T	32 DSI Studio	1000	VBA/ROI-based tractography
4	Qian Sun, 2018	3.0 T	8 FSL	1000	TBSS/VBA
5	P. L. Yau, 2013	3.0 T	16 ART2	1000	ROI analysis
6	Aifeng Zhang, 2013	3.0 T	8 DSI Studio	700	ROI analysis
7	Xin Tan, 2016	3.0 T	8 FSL	1000	TBSS
8	Arie Nouwen, 2017	3.0 T	8 SPM	1500	TBSS/VBA
9	Sujung Yoon, 2017	1.5 T	-- FSL	1000	ROI analysis
10	Xie, Y, 2017	3.0 T	-- SPM	1000-2000	ROI analysis
11	Xinfeng Yu, 2019	3.0 T	8 FSL	1000	ROI analysis
12	Dae-Jin Kim, 2016	3.0 T	-- FSL FreeSurfer	1000	TBSS
13	Xiong, Y, 2018	3.0 T	32 FSL	1000	ROI analysis
14	Tan, X, 2016	3.0 T	8 FSL	1000	TBSS
15	Hoogenboom, 2014	3.0 T	8 3DSlicer FSL	1000	ROI analysis
16	Bloemendaal, 2016	3.0 T	8 FSL SPM	1000	TBSS/VBA
17	Zhang, 2016	3.0 T	8 FSL	1000	TBSS
18	Fang, 2017	3.0 T	8 FSL	1000	ROI analysis
19	Hsu, 2012	1.5 T	-- FSL	1000	Global analysis/VBA
20	Van Bussel, 2016	3.0 T	32 FreeSurfer	1500	ROI analysis
21	Falvey, 2013	3.0 T	12 FSL	1000	TBSS
22	Rofey, 2015	3.0 T	32 FSL	1000	TBSS
23	Raffield, 2017	1.5 T	16 DTI-TK SPM	1000	--
24	Yang Zhang, 2018	3.0 T	-- FSL PANDA	1000	ROI analysis
25	Groeneveld, 2018	3.0 T	32 FSL	1000	ROI-based tractography
26	P. L. Yau, 2010	1.5 T	-- SPM	1000	ROI analysis
27	Po Lai Yau, 2009	1.5 T	-- MIDAS ART2	1000	ROI analysis
28	Y Reijmer, 2013 (b)	3.0 T	-- ExploreDTI	1200	ROI-based tractography
29	Junying Zhang,2014	3.0 T	-- FSL PANDA	1000	TBSS/ ROI analysis

Table 5.4. Technical characteristics of included T2DM studies. Abbreviations: -- = not available; T = tesla; ROI = region of interest.

5.3.6. Between-Group Differences: Microstructural Alterations in T2DM

Most of the reviewed studies consistently revealed lower FA and higher AD, MD and RD in the white matter and grey matter using voxel-wise whole-brain or global brain analyses (Table 5.5) (Fig.5.9). Methods of analysis used in these studies included TBSS, tractography, and voxel-based analysis methods.

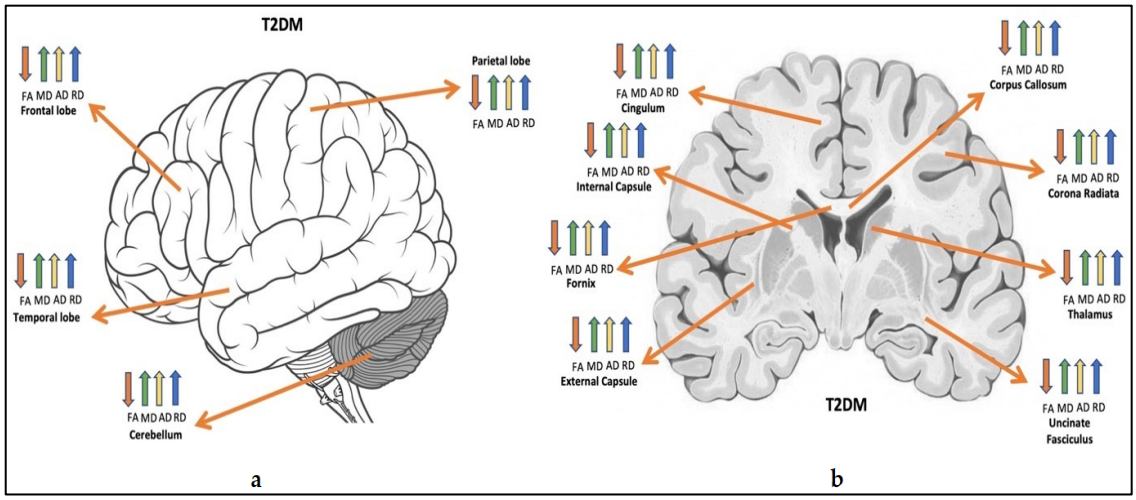


Figure 5. 9*. Altered diffusion measures in T2DM brain structures. (A) shows the affected brain lobes and cerebellum, and (B) a cross-sectional view of deep brain tissues. Orange: FA; green: MD; yellow: AD; blue: RD. Directions: down: decrease; up: increase.*

Most of the findings were reported in the frontal and temporal lobes in T2DM patients[188,209,210] and reported the differences between groups of additional diffusion parameters such as RD and AD. Some other studies reported increased diffusion of additional parameters, such as AD and RD, in the regions with low FA values or high MD values. However, different analysis methods showed changes in RD values[209,211–213] or AD only[214,215]. Disruption in the brain network using graph theoretical network analysis was described by network integrity parameters, characterised by the lower overall efficiency and the path length in all four studies[211,216–218]. The parameters of network integrity in these studies provided a clear representation of the speed and volume of a cerebral network in the recruited subjects. Notably, they proved that some brain regions lost the ability to interact due to the effects of T2DM. Reijmer et al. investigated the network characteristics in T2DM and reported a lower diffusion

coefficient in patients[190,201]. However, Y. Zhang et al. observed a higher coefficient in T2DM patients without vascular complications[219]. The other two studies detected no differences in local parameters in T2DM patients compared to healthy controls[216,218].

Major voxels with reduced microstructural integrity were observed mainly in the temporal lobe, frontal lobe, and parietal regions of the cortex and subcortex in individuals with T2DM. Some studies conducted a whole-brain comparison of DTI metrics by voxel-based analysis and confirmed significant interruption in the integrity of tissue microstructure of the temporal and frontal lobes. Specifically, T2DM patients showed reduced FA in the left, right or bilateral white matter of the frontal lobe[208,210,214,220–222]. Additionally, the decreased nodal efficiency of temporal, frontal and parietal lobes in the topological network analysis was reported by two authors[218,219]. Various analysis methods showed microstructural disruption of the prefrontal subcortical and cortical regions in T2DM patients[188,223,224]. Rofey et al. revealed a reduction of FA and the microstructural disruptions in prefrontal white matter and striatum using tractography[208]. Likewise, Fang et al. reported the disruption in frontal-cerebellar pathways and a few abnormal microstructural clusters were identified within the parietal lobe[225]. Correspondingly, several studies detected decreased FA in parietal white matter in T2DM patients[188,218,226].

Additionally, higher MD values were observed in the parietal cortex in T2DM patients[188,224]. In the temporal lobe, microstructural changes were detected, including some structures with lower DTI parameters in T2DM patients[210,218,220,222,226]. These structures include the hippocampus, the temporal stem and the fusiform gyrus[210,224,227]. Moreover, lower hippocampal white matter connections with the regions of frontotemporal lobes were found in T2DM patients compared to healthy participants[228].

In T2DM patients, the studies showed abnormalities in specified subregions of the corpus callosum, including genu, body and splenium[187,209,212,216,218,229]. Impaired white matter integrity in T2DM patients was found in corona radiata, corticospinal tracts, internal capsules, and cingulum, which showed the effects of diabetes [209,211,212,216,218,221,230]. Additionally, diabetes was associated with changes in the internal capsule, including the anterior, posterior, and retro lenticular parts[209,212,218,221]. Reduced FA, increased AD, RD or MD in the forceps major, minor, and arcuate fasciculus, superior frontal occipital fasciculus and optic radiation were reported in T2DM patients compared to non-diabetic controls[212,215,216,220,224,226].

In the subcortical regions, few studies reported thalamus, fornix, and thalamic radiations to have lower integrity. One of these studies showed lower significant FA values in the tracts between the dorsal lateral side of the prefrontal cortex in diabetic and obese participants. The results suggest an association between T2DM and the changes in hippocampus structure and related limbic structures[208]. Other results showed decreased FA in the hippocampus[218,228], and the corona radiata and cingulum[230]. In the same regions, higher MD in patients with T2DM was observed[227,228,230]. Additionally, increased MD in T2DM patients was observed in the cingulate and parahippocampal gyrus[222,227]. Network analysis also showed a decrease in nodal efficiency for the hippocampus, amygdala[219] and cingulate gyrus[218], suggesting brain network abnormalities in T2DM patients.

In the cerebellum, T2DM patients were found to have decreased white matter FA values, specifically, the peduncles and vermis[214,220,226,229]. Likewise, the cerebellar grey matter was also found to have differences in microstructural integrity[222,224]. Moreover, Fang et al. examined fibre connectivity and found lower connectivity in T2DM patients, and this reduced connectivity affected the cerebellar circuits[225].

Microstructural Alterations in T2DM Patients				
Region	**↓ FA**	**↑ MD**	**↑ RD**	**↑ AD**
Corpus callosum	Yau et al. 2013; Zhang et al. 2014; Tan et al. 2016; Zhang et al. 2016; Nouwen et al. 2017; Yoon et al. 2017; Xie et al. 2017; Sun et al. 2018; Yu et al. 2018, Kim et al. 2016.	Reijmer et al. 2013; Zhang et al. 2014; Xie et al. 2017; Sun et al. 2018; Xiong et al. 2018	Zhang et al. 2014; Nouwen et al. 2017; Xie et al. 2017; Sun et al. 2018; Yu et al. 2018	Reijmer et al. 2013; Xie et al. 2017; Sun et al. 2018
Corona radiata	Zhang et al. 2014; Yoon et al. 2017; Xiong et al. 2018; Sun et al. 2018.	Zhang et al. 2014; Xiong et al. 2016; Sun et al. 2018; Xiong et al. 2018.	Zhang et al. 2014; Xiong et al. 2016; Sun et al. 2018; Nouwen et al. 2017.	Xiong et al. 2016; Sun et al. 2018.
Cingulum	Yau et al. 2010; Hoogenboom et al. 2014; Zhang et al. 2014; Tan et al. 2016; Nouwen et al. 2017; Yoon et al. 2017; Sun et al. 2018; Xion et al. 2018; Zhang et al. 2016; Xiong et al. 2016.	Falvey et al. 2012; Zhang et al. 2014; Sun et al. 2018; Xiong et al. 2018.	Zhang et al. 2014; Xiong et al. 2016; Nouwen et al. 2017; Sun et al. 2018.	Tan et al. 2016; Xiong et al. 2016; Sun et al. 2018.
Uncinate Fasciculus	Reijmer et al. 2013; Hoogenboom et al. 2014; Zhang et al. 2014; Tan et al. 2016; Nouwen et al. 2017; Yoon et al. 2017; Xiong et al. 2018.	Reijmer et al. 2013; Tan et al. 2016; Xiong et al. 2018.	Reijmer et al. 2013; Zhang et al. 2014; Nouwen et al. 2017.	Reijmer et al. 2013.
Superior longitudinal fasciculi (SLF)	Yau et al. 2014; Zhang et al. 2014; Tan et al. 2016; Zhang et al. 2016.	Reijmer et al. 2013; Zhang et al. 2014.	Reijmer et al. 2013; Zhang et al. 2014.	Reijmer et al. 2013; Bloemendaal et al.
Inferior longitudinal fasciculus (ILF)	Zhang et al. 2014; Kim et al. 2016; Tan et al. 2016; Yoon et al. 2017.	Reijmer et al. 2013; Tan et al. 2016.	Reijmer et al., 2013	Reijmer et al., 2013
Thalamus	Zhang et al. 2014; Zhang et al. 2016; Tan et al. 2016; Xiong et al. 2016; Fang et al. 2017; Nouwen et al. 2017; Yoon et al. 2017; Sun et al. 2018.	Zhang et al. 2014; Tan et al. 2016	Zhang et al. 2014; Xiong et al. 2016; Nouwen et al. 2017.	Tan et al. 2016; Xiong et al. 2016; Sun et al. 2018.
Corticospinal tract	Xiong et al. 2016; Sun et al. 2018; Nouwen et al. 2017; Yoon et al. 2017.	--	Nouwen et al., 2017	Bloemendaal et al., 2016
Inferior frontal-occipital fasciculus	Zhang et al. 2014; Zhang et al. 2016; Kim et al. 2016; Nouwen et al. 2017; Yoon et al. 2017.	--	Nouwen et al., 2017	Bloemendaal et al., 2016
Cerebellum	Yau et al. 2013; Yoon et al. 2017; Tan et al. 2017; Fang et al. 2017; Xiong et al. 2016.	Yau et al. 2014; Hsu et al. 2012.	Xiong et al. 2016; Hsu et al. 2012.	Xiong et al. 2016; Hsu et al. 2012.
Internal capsules	Yau et al. 2013; Zhang et al. 2013; Zhang et al. 2014; Kim et al. 2016; Xiong et al. 2016; Nouwen et al. 2017; Sun et al. 2018.	Zhang et al. 2014; Xiong et al. 2016; Xiong et al. 2018.	Zhang et al. 2013; Zhang et al. 2014; Xiong et al. 2016; Nouwen et al. 2017.	Xiong et al. 2016; Sun et al. 2018.
External capsules	Yau et al. 2013; Zhang et al. 2014; Kim et al. 2016; Xiong et al. 2016; Nouwen et al. 2017; Yoon et al. 2017; Sun et al. 2018; Xion et al. 2018.	Zhang et al. 2014; Xiong et al. 2016; Xie et al. 2017; Xiong et al.	Xie et al. 2017; Xiong et al. 2016; Nouwen et al. 2017.	Xiong et al. 2016; Xie et al. 2017; Sun et al. 2018.
Fornix	Zhang et al. 2014; Zhang et al. 2016; Tan et al. 2016; Xiong et al. 2016; Fang et al. 2017; Nouwen et al. 2017; Yoon et al. 2017; Sun et al. 2018.	Zhang et al. 2014; Tan et al. 2016.	Zhang et al. 2014; Xiong et al. 2016; Nouwen et al. 2017.	Tan et al. 2016; Xiong et al. 2016; Sun et al. 2018.
Hippocampus	Van Bussel et al. 2016, Jian-Hui Zhang et al. 2016, Xiong et al. 2016, Xiong et al. 2018, Falvey et al. 2013.	Van Bussel et al. 2016, Xiong et al. 2018, Falvey et al. 2013.	--	--

Table 5. 5. *Illustrates the diffusion findings between groups in T2DM.*

5.3.7. Microstructural and Cognitive Abnormalities in T2DM

The findings of several included studies suggest an association between T2DM and general cognitive deficits[188,218,228,231]. Reduced cognitive performance was noticed in different cognitive domains, including working memory[188,210,212,215,218,224,226,230,231], attention[188,212,226,231], the speed of information processing[218,232], and executive function

[188,212,231]. Surprisingly, some studies demonstrated that cognitive abnormalities may occur at early diabetic stages or may not be noticed even in old patients and after a long duration of illness[218,233,234]. Xiong et al. demonstrated that T2DM patients with cognitive impairments had more microstructural changes noticed in the cingulum, corona radiata, the frontotemporal region, external and internal capsules, corticospinal tract, and thalamic radiation[221].

Other studies concluded that low FA values in the cingulum were negatively associated with verbal memory deficits[231]. Additionally, increased MD values in the inferior longitudinal fasciculus and parahippocampal gyrus were positively related to verbal memory deficits[187,224,228]. In addition, one study reported fewer white matter connections in the area between the hippocampus and temporal lobe in patients with memory deficits[228]. J. Zhang et al. found that the lower performance of working memory in T2DM patients had a positive correlation with the network of the hippocampus and superior temporal lobe[212].

The executive dysfunction in T2DM patients was related to network disorganization and reduced external capsule integrity compared to healthy controls [212,218]. Zhang et al. demonstrated a significant correlation between the increased MD and the reduced FA of the prefrontal white matter with the attention network test. Additionally, the same study found significant associations between attention and local nodal efficiency of the temporal lobe[218].

The association between MD and FA values of inferior longitudinal fascicules and corpus callosum and the scores of the substitution test suggested an impaired information-processing speed in patients[189]. Moreover, the FA values in grey matter volume and the speed of information processing were negatively correlated in

patients[189]. Lastly, Yoon et al. found a relationship between the disorganised network and slower information processing speed (Fig.5.10A–C).

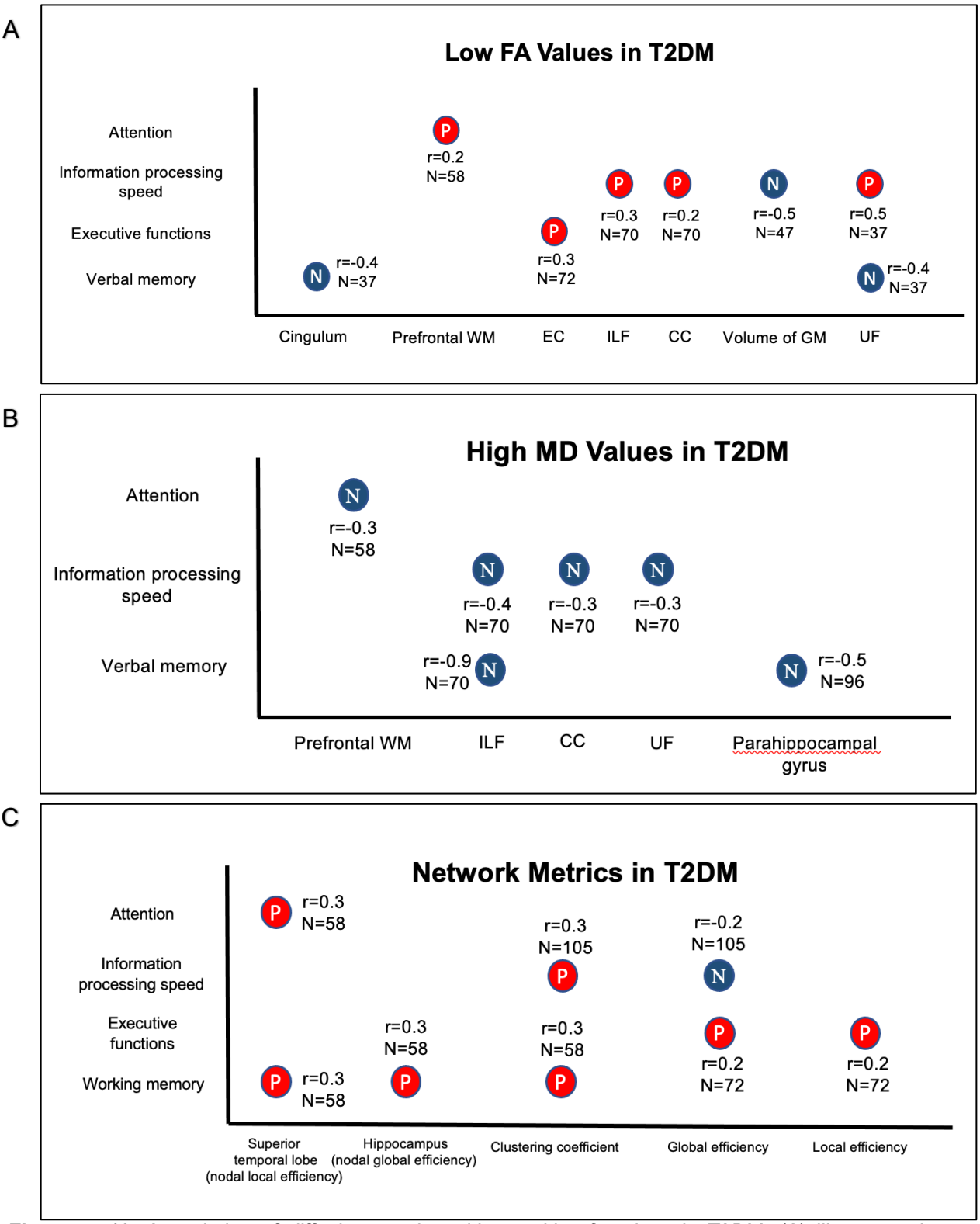


Figure 5. 10*. Association of diffusion metrics with cognitive functions in T2DM. (A) illustrates the association between FA and cognitive functions; (B) illustrates the association between MD and cognitive functions; (C) illustrates the association between network parameters and cognitive functions. (CC: corpus callosum, EC: external capsule, WM: white matter, ILF: inferior longitudinal fasciculus).* P-value =0.05; N=sample size; *=Children; P=positive correlation; N=negative correlation; r=correlation coefficient.

5.3.8. Microstructural Alterations and Metabolic Profile in T2DM

The findings suggested that the severity of microstructural alterations in brain regions and structures, including the frontal lobe, temporal lobe, prefrontal region, praecuneus, cerebral crus, cerebral lobule, and superior frontal gyrus, were associated with a longer duration of diabetes[222,234]. However, a negative correlation between the duration of illness and FA values in white matter was reported[209,232]. Some microstructural changes in specific white matter structures, such as longitudinal fasciculi, cingulum, corpus callosum and uncinate fasciculus, did not have any association with the illness duration[187,213,231]. Moreover, network studies confirmed no relationships between the parameters of the brain network and the duration of illness[216–219].

Some studies reported that HbA1c has a negative relationship with the reduction of global microstructural tissue integrity[209], specifically in inferior longitudinal fasciculus, thalamic radiation, external capsule, internal capsule, fornix, and corpus callosum[216]. In the network organization of T2DM patients, HbA1c was positively correlated with the shortest path length and negatively correlated with global efficiency[216]. However, other articles reported no associations between the microstructural integrity/network organization and HbA1c[213,215,216,218,219,225,232]. In terms of FBS, few included studies reported an association between the brain tissue changes and FBS in the internal and external capsules, cingulum, inferior lobule, splenium, fornix, and tracts of the frontal lobe[215,216,228,231] (Fig.5.11A and B).

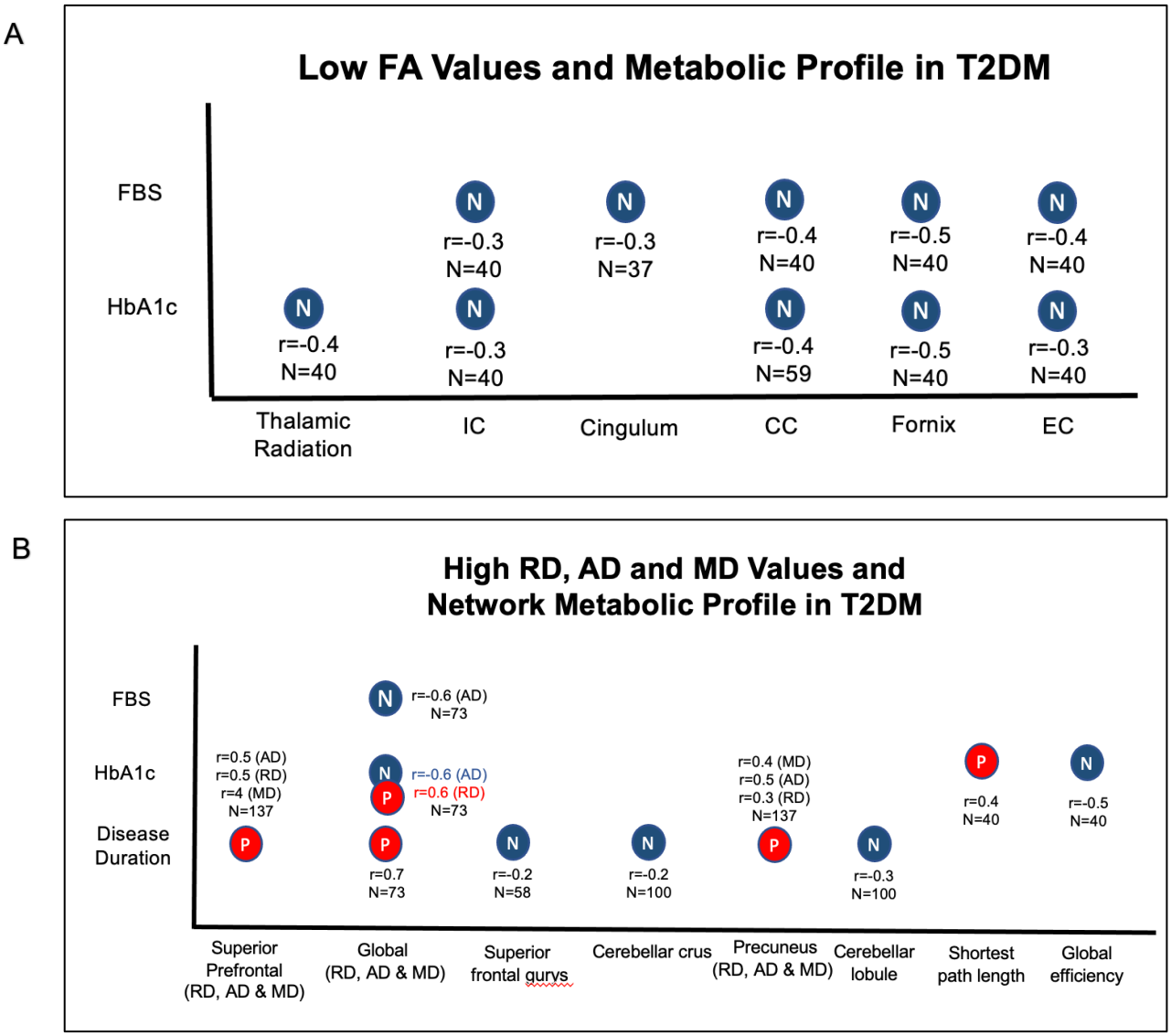


***Figure 5. 11**. Association of diffusion metrics with the metabolic profile. (A) represents the association between FA and metabolic profile; (B) represents the association between MD, RD, AD and network parameters and the metabolic profile. (CC: corpus callosum, EC: external capsule, and IC: internal capsule). P-value =0.05; N=sample size; *=Children; P=positive correlation; N=negative correlation; r=correlation coefficient.*

5.4. Discussion

5.4.1. T1DM Patients versus Healthy Controls

The reviewed studies reveal a relationship between the brain tissue changes and cognitive disability in T1DM, and the widespread FA reduction observed in DTI-T1DM studies is in line with another study[235]. The reduced diffusivity in the thalamus in adolescent patients is associated with T1DM and glycaemic exposure; also, this observation agrees with other studies of adults[236] and youth[237]. The lower scores on

the digit span test in adolescent patients are associated with lower FA at the midbrain and optic radiation, which indicate more impaired memory and attention performance. In addition, the visual memory impairment in adolescent patients with T1DM agrees with another study and meta-analyses[183,185,238].

Studies conducted on adults with T1DM confirmed that reduced FA values in posterior corona radiata and optic radiation are correlated with hyperglycemic exposure[207]. In contrast, the same result is not confirmed in adolescents with T1DM due to shorter disease duration or lesser exposure to hyperglycemia[203]. Hyperglycemia could increase the risk of brain tissue damage or dysfunction by a metabolism-dependent cascade, such as hyperglycemia-induced oxidative stress. For this reason, the DTI alterations presented in this review could be due to other glycolysis-independent biological factors that are changed simultaneously with severe hyperglycemic episodes[207].

The decreased FA values in various brain structures may reflect a complex involvement of tissue properties, suggesting white matter disruption, axonal damage, degeneration, or irregularity of axonal structure. These low DTI measurements are correlated with reduced neurocognitive performance indicating for the first time that brain microstructural abnormalities may underlie cognitive dysfunction[183]. Kodl et al. confirmed a link between reduced FA in the white matter and a few regions with reduced cortical thickness in middle-aged adults[187,205]. These findings suggest that long-standing T1DM may cause microstructural changes in the posterior cerebrum. In addition, the reduced FA values in the splenium of the corpus callosum, optic radiations, and the posterior corona radiata with posterior cortical atrophy are found to be correlated with volume loss in the occipital cortex in T1DM patients, which may suggest the effects of T1DM on executive functions and psychomotor speed[206].

In children with T1DM, the microstructural differences in white matter are more apparent among those with higher HbA1c. Additionally, the lack of significant differences in FA between diabetics and controls may be due to young age and shorter disease duration of children[201]. However, children with T1DM who have lower AD values have axonal damage and less axonal coherence, which agrees with another study[202]. Within the same group, the significant positive correlation between HbA1c and RD indicates that higher blood glucose may affect fibre myelination[233]. The reduced AD and increased RD values in patients are likely due to the domination of the age effect, which significantly correlates with white matter structures and disease duration. There is a notable difference between this study and another study of DTI in children with T1DM[201]. The latter found a significant relationship between lifetime HbA1c values and white matter changes, whereas Barnea-Goraly et al. found only significant associations with HbA1c values at the study baseline[202]. These findings in a large-size study may suggest that HbA1c values at baseline represent diabetic complications in the brain more than lifetime HbA1c values.

5.4.2. T2DM Patients versus Healthy Controls

The reviewed studies demonstrate a significant association between T2DM and low global integrity and network organisation of brain microstructures. Additionally, they showed that T2DM micro-vascular changes in the brain had been linked to cognitive deficits, supporting the hypothesis that neuroinflammation and microvascular pathology are involved in the cerebral complications/changes of diabetes, which DTI is sensitive to compared with other MRI conventional techniques[239,240]. The findings agree with a previous study that shows the relationship between T2DM and abnormalities in the temporal lobe, particularly in the hippocampus[241]. Similarly, included DTI studies revealed the relationship between microstructural changes and network impairment in the temporal lobe and hippocampus, responsible for grasping

new information and the learning process[242]. The results from the reviewed studies demonstrated that abnormalities in the microstructure of the hippocampus and the temporal white matter and grey matter are linked to dysfunctionalities in memory.

Another agreement is seen with a previous study in which decreased volume of the prefrontal area is confirmed in patients with T2DM and correlates with higher values of HbA1c[243]. Moreover, the prefrontal white matter and cortex abnormalities have a significant relationship with diabetes duration. They may underlie attention, memory deficits, and executive dysfunction in patients with T2DM. This association signifies that the diabetic impact on the prefrontal white matter may cause these defects.

Due to the complicated environment of brain networks and white matter tracts, it is difficult to determine the association between white matter disruptions and cognitive functions. However, preliminary results of DTI tractography and network studies suggest that diabetes may affect white matter major tracts. In the investigated studies, the brain network, nodal efficiency, and diffusivity are correlated with various cognitive domains in the temporal and prefrontal lobes. Some of the included findings display the association between the impaired microstructure of the thalamus and the disorganised brain network in the frontal cortex. Additionally, changes in the frontal-striatum thalamic region in patients are correlated with cognitive deficits (executive function, memory, attention, and information processing speed) and higher levels of HbA1c[244]. Lastly, DTI-T2DM studies show that the white matter and grey matter of the cerebellum are disrupted in patients, and all patients with a longer duration of illness are observed to have more abnormalities in cerebellar connections, which may significantly affect cognitive performance and executive functions.

5.4.3. Common Microstructural Alterations, Cognitive Deficits and Comorbidities

The DTI studies reviewed here demonstrate that T1DM and T2DM patients have brain microstructural changes compared to healthy volunteers. According to the reported findings, there are common regions of microstructural changes in diabetic brains, including internal and external capsules, corona radiata, hippocampus, thalamus, inferior and superior longitudinal fasciculi, cerebellum, and corpus callosum (Fig.6.12) and in Table 5.6. Microstructural changes in diabetic brains are linked with observed cognitive dysfunction, including the speed of information processing, memory, executive functions, and attention in individuals with T1DM and T2DM. These reported microstructural and cognitive deficits are correlated with uncontrolled glycaemia in both types of diabetes. Regarding the comorbidities, the presence of microangiopathy in T1DM patients significantly increases the severity of microstructural abnormalities in the brain compared to other T1DM patients. Similarly, T2DM patients with other comorbidities such as obesity, stroke and hypertension increase the seriousness of microstructural changes in the brain.

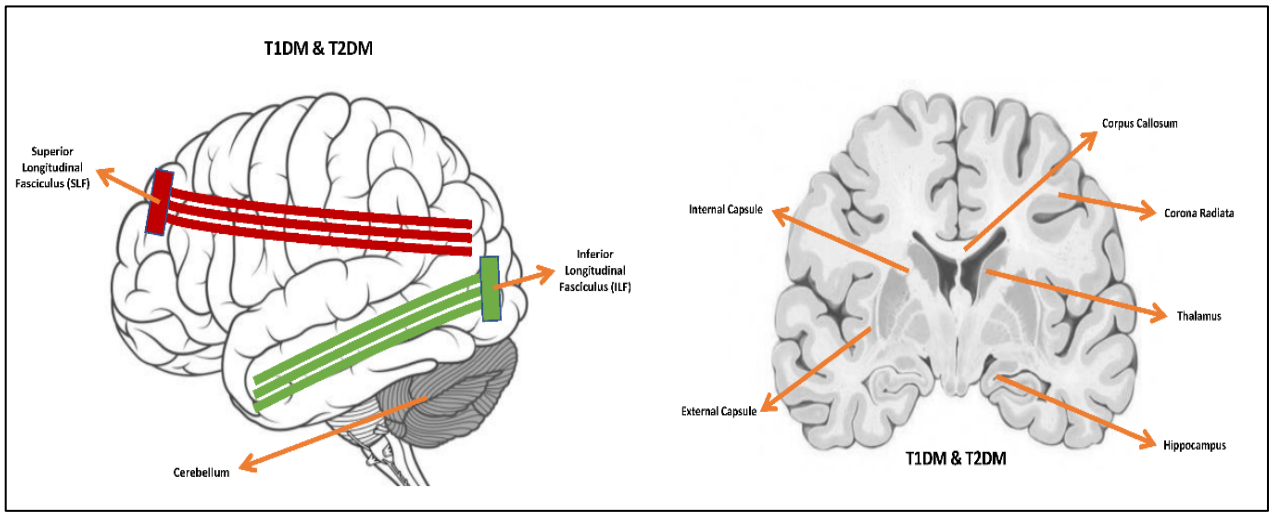


Figure 5. 12. *Common microstructural tissue alterations in the brain of patients with T1DM and T2DM.*

Microstructural Alterations in T1DM/T2DM Patients

Region	↓ FA (T2DM)	↓ FA (T1DM)	↑ MD (T2DM)	↓ MD (T1DM)	↑ RD (T2DM)	↑ RD (T1DM)	↑ AD (T2DM)	↓ AD (T1DM)
Corpus callosum	Yau et al. 2013; Zhang et al. 2014; Tan et al. 2016; Zhang et al. 2016; Nouwen et al. 2017; Yoon et al. 2017; Xie et al. 2017; Sun et al. 2018; Yu et al. 2018, Kim et al. 2016.	van Duinkerken et al. 2012 (with/without microangiopathy), Kodl et al. 2008, Yoon et al. 2018.	Reijmer et al. 2013; Zhang et al. 2014; Xie et al. 2017; Sun et al. 2018; Xiong et al. 2018.	--	Zhang et al. 2014; Nouwen et al. 2017; Xie et al. 2017; Sun et al. 2018; Yu et al. 2018.	Van Duinkerken et al. 2012 (with/without microangiopathy).	Reijmer et al. 2013; Xie et al. 2017; Sun et al. 2018.	Antenor-Dorsey et al. 2013, van Duinkerken et al. 2012 (with/without microangiopathy), Tandy et al. 2012.
Corona radiata	Zhang et al. 2014; Yoon et al. 2017; Xiong et al. 2018; Sun et al. 2018.	van Duinkerken et al. 2012 (without microangiopathy), Kodl et al. 2008, Franc et al. 2011, Toprak et al. 2016.	Zhang et al. 2014; Xiong et al. 2016; Sun et al. 2018; Xiong et al. 2018.	--	Zhang et al. 2014; Xiong et al. 2016; Sun et al. 2018; Nouwen et al. 2017.	Van Duinkerken et al. 2012 (with/without microangiopathy).	Xiong et al. 2016; Sun et al. 2018.	--
Thalamic radiation		van Duinkerken et al. 2012 (with microangiopathy).		--		--		Van Duinkerken et al. 2012 (with/without microangiopathy).
Cingulum	Yau et al. 2010; Hoogenboom et al. 2014; Zhang et al. 2014; Tan et al. 2016; Nouwen et al. 2017; Yoon et al. 2017; Sun et al. 2018; Xion et al. 2018; Zhang et al. 2016; Xiong et al. 2016.		Falvey et al. 2012; Zhang et al. 2014; Sun et al. 2018; Xiong et al. 2018.		Zhang et al. 2014; Xiong et al. 2016; Nouwen et al. 2017; Sun et al. 2018.		Tan et al. 2016; Xiong et al. 2016; Sun et al. 2018.	
Uncinate Fasciculus	Reijmer et al. 2013;Hoogenboom et al. 2014; Zhang et al. 2014; Tan et al. 2016; Nouwen et al. 2017; Yoon et al. 2017; Xiong et al. 2018.		Reijmer et al. 2013; Tan et al. 2016; Xiong et al. 2018.		Reijmer et al. 2013; Zhang et al. 2014; Nouwen et al. 2017.		Reijmer et al. 2013.	
Superior longitudinal fasciculi (SLF)	Yau et al. 2014; Zhang et al. 2014; Tan et al. 2016; Zhang et al. 2016.	Van Duinkerken et al. 2012 (with microangiopathy), Ahmed et al. 2014, Yoon et al. 2018.	Reijmer et al. 2013; Zhang et al. 2014.	--	Reijmer et al. 2013; Zhang et al. 2014.	--	Reijmer et al. 2013; Bloemendaal et al.	Van Duinkerken et al. 2012 (with/without microangiopathy).
Inferior longitudinal fasciculus (ILF)	Zhang et al. 2014; Kim et al. 2016; Tan et al. 2016; Yoon et al. 2017.	Toprak et al. 2016.	Reijmer et al. 2013; Tan et al. 2016.	--	Reijmer et al., 2013.	--	Reijmer et al., 2013.	--
Thalamus	Zhang et al. 2014; Zhang et al. 2016; Tan et al. 2016; Xiong et al. 2016; Fang et al. 2017; Nouwen et al. 2017; Yoon et al. 2017; Sun et al. 2018.	Toprak et al. 2016.	Zhang et al. 2014; Tan et al. 2016	Antenor-Dorsey et al. 2013.	Zhang et al. 2014; Xiong et al. 2016; Nouwen et al. 2017.	--	Tan et al. 2016; Xiong et al. 2016; Sun et al. 2018.	Antenor-Dorsey et al. 2013, Tandy et al. 2012.
Corticospinal tract	Xiong et al. 2016; Sun et al. 2018; Nouwen et al. 2017; Yoon et al. 2017.				Nouwen et al., 2017.		Bloemendaal et al., 2016.	
Inferior frontal-occipital fasciculus	Zhang et al. 2014; Zhang et al. 2016; Kim et al. 2016; Nouwen et al. 2017; Yoon et al. 2017.	Yoon et al., 2018	--	van Duinkerken et al. 2012 (with/without microangiopathy).	Nouwen et al., 2017	--	Bloemendaal et al., 2016	--
Cerebellum	Yau et al. 2013; Yoon et al. 2017; Tan et al. 2017; Fang et al. 2017; Xiong et al. 2016.	--	Yau et al. 2014; Hsu et al. 2012.	--	Xiong et al. 2016; Hsu et al. 2012.	Antenor-Dorsey et al., 2013.	Xiong et al. 2016; Hsu et al. 2012.	Antenor-Dorsey et al., 2013.
Internal capsules	Yau et al. 2013; Zhang et al. 2013; Zhang et al. 2014; Kim et al. 2016; Xiong et al. 2016; Nouwen et al. 2017; Sun et al. 2018.	--	Zhang et al. 2014; Xiong et al. 2016; Xiong et al. 2018.	--	Zhang et al. 2013; Zhang et al. 2014; Xiong et al. 2016; Nouwen et al. 2017	--	Xiong et al. 2016; Sun et al. 2018.	Antenor-Dorsey et al., 2013; Tandy et al., 2012.
External capsules	Yau et al. 2013; Zhang et al. 2014; Kim et al. 2016; Xiong et al. 2016; Nouwen et al. 2017; Yoon et al. 2017; Sun et al. 2018; Xion et al. 2018.	--	Zhang et al. 2014; Xiong et al. 2016; Xie et al. 2017; Xiong et al.	--	Xie et al. 2017; Xiong et al. 2016; Nouwen et al. 2017.	--	Xiong et al. 2016; Xie et al. 2017; Sun et al. 2018.	Antenor-Dorsey et al., 2013; Tandy et al., 2012.
Fornix	Zhang et al. 2014; Zhang et al. 2016; Tan et al. 2016; Xiong et al. 2016; Fang et al. 2017; Nouwen et al. 2017; Yoon et al. 2017; Sun et al. 2018.		Zhang et al. 2014; Tan et al. 2016.		Zhang et al. 2014; Xiong et al. 2016; Nouwen et al. 2017.		Tan et al. 2016; Xiong et al. 2016; Sun et al. 2018.	
Hippocampus	Van Bussel et al. 2016, Jian-Hui Zhang et al. 2016, Xiong et al. 2016, Xiong et al. 2018, Falvey et al. 2013.	Toprak et al. 2016.	Van Bussel et al. 2016, Xiong et al. 2018, Falvey et al. 2013.	--	--	--	--	--

Forceps minor and major		van Duinkerken et al. 2012 (with microangiopathy).		--		Van Duinkerken et al. 2012 (with/without microangiopathy).		Van Duinkerken et al. 2012 (with/without microangiopathy).
Optic radiation		Ahmed et al. 2014, Kodl et al. 2008, Franc et al. 2011.		--		--		--
Putamen		Toprak et al., 2016.		--		--		--
Superior parietal lobule		Antenor-Dorsey et al., 2013.		--		Antenor-Dorsey et al., 2013.		Antenor-Dorsey et al., 2013.
Cingulate gyrus		--		--		--		Tandy et al., 2012.
Superior temporal gyrus		--		--		--		Tandy et al., 2012.
White matter (Widespread changes)		Barnea-Goraly et al., 2014		--		Barnea-Goraly et al. 2014 (reduced RD with longer disease duration and increased RD with younger age at disease onset).		Barnea-Goraly et al., 2014.

***Table 5.6**. Common microstructural tissue alterations in the brain of patients with T1DM and T2DM (combined results to understand common themes for differences). Red highlights = not reported.*

5.4.4. Multi-Shell Diffusion Imaging Models

Enough studies suggest that DTI is sensitive in detecting microstructural changes in T1DM and T2DM patients and is more sensitive to white matter disruptions than grey matter abnormalities. Nonetheless, DTI metrics could be misleading when imaging complex crossing fibres[109,131,245]. The lack of specificity in DTI metrics has encouraged the development of advanced diffusion methods, and these methods yield higher sensitivity and specificity to subtle brain changes. Diffusion Kurtosis Imaging (DKI) and NODDI have been recently used to investigate microstructural changes in T2DM, but not T1DM[229,230].

Unlike DTI, DKI can estimate the Gaussian distribution of water molecules. This technique calculates kurtosis parameters, including mean kurtosis, radial kurtosis, and axial kurtosis, which reflect more structural complexity[246]. In T2DM only, two studies have assessed brain microstructural integrity using DKI and have confirmed that DKI

has more sensitivity to brain microstructural changes than DTI, predominantly in the temporal WM. DKI superiority over DTI may be due to its ability to assume the non-gaussian water diffusion, which is more robust[247]. In addition to the non-gaussian assumption, DKI metrics are not affected by the restricted crossing fibres in white matter and can accurately detect the grey matter microstructural alterations.

NODDI is used to adopt a diffusion tissue model that can distinguish three types of microstructural environment: CSF, extracellular and intracellular compartments[17]. Unlike DTI and other diffusion models, NODDI has two broad applications, including white matter and grey matter evaluation. In WM, the orientation dispersion index quantifies complex structures, such as the bending and fanning of axons which helps map brain connectivity. In GM, the neurite index quantifies sprawling dendrites in the brain, which quantifies grey matter complexity compared to other diffusion models[17]. A recent study showed significant differences in NODDI parameters between T2DM patients and healthy participants, suggesting that NODDI is a specific imaging biomarker for early detection and monitoring of microstructural alterations in the white matter of T2DM patients compared to DTI[229].

5.4.5. Limitations

The reviewed DTI studies for both types of diabetes have some limitations. First, the majority of the studies recruited fewer than 80 diabetic patients with different clinical characteristics. Second, the clinical information, such as the age of disease onset, cardiovascular disorders, history of metabolic treatment, and blood pressure, were not well described in all studies. Third, the small sample size and the differences in patients' clinical features may affect the result consistency, leading to an unsatisfactory conclusion. Fourth, some of the reviewed studies evaluated FA only, but they did not take into account other DTI parameters, including RD, MD and AD. Fifth, several DTI studies of T1DM reported only once timed HbA1c, unlike other

studies, which reported a lifetime HbA1c of patients. Lastly, this review lacks quantitative synthesis, which is vital to draw a reliable conclusion about the microstructural alterations in T1DM and T2DM. However, several differences in the methods of analysing DTI images made the implementation of meta-analysis unfeasible. As shown in the review results, there was heterogeneity in T1DM groups indicated by variations in age, disease duration and fasting glucose which may also influence the findings and limit the review conclusion.

5.4.6. Future Directions

Simultaneous assessments of white matter and grey matter alterations would be interesting, and well-designed longitudinal studies are needed to recognise the mechanism of the diffusion changes as the disease progresses. Additional cross-sectional studies will help confirm whether FA reduction correlates with the duration of diabetes independent of patients' ages. Furthermore, functional MRI (fMRI) and DTI observational studies are essential to explore the brain structural and functional connectivity in T1DM and to confirm the previous observations in T2DM studies. Finally, additional observational studies are needed to examine and confirm the applicability of NODDI and DKI in quantifying the microstructural abnormalities in T1DM and T2DM.

5.5. Conclusion

DTI provides imaging biomarkers for microstructural alterations in both types of DM. Moreover, the different analysing methods of DTI parameters have assisted researchers in reporting disrupted integrity in the white matter and grey matter and network disorganization of cortical and subcortical areas in both types of diabetes. DM microstructurally affects the four major lobes of the brain and major structures, such as the corpus callosum, thalamus, corona radiata, hippocampus, and external and internal capsules. These detected microstructural changes in diabetic brains are

associated with cognitive impairments, including attention, executive functions, memory, and information-processing speed. There is an association between the clinical profiles of patients with T1DM and T2DM (i.e., disease duration and HbA1c) and altered DTI metrics in various brain regions. However, longitudinal DTI studies from early to advanced stages of T1DM and T2DM should be considered to provide a robust conclusion and better understand the neural damage in diabetes.

Chapter 6

6. Investigating Microstructural Changes in White Matter in Multiple Sclerosis: A Systematic Review and Meta-Analysis of Neurite Orientation Dispersion and Density Imaging **(Word count: 3706)**

This chapter is also published (as a review article[12]) in a peer-reviewed journal, and permission from the journal has been obtained to re-use the same work in my thesis. As a first author, I primarily conducted the literature search, inclusion/exclusion criteria, study identification and screening. Also, I obtained the data from the authors of the included studies and wrote the entire content of this published paper. Prof. Dineen and Prof. Constantinescu again helped with reviewing the inclusion/exclusion criteria and the article content. Anna Podlasek advised on how to improve the statistical analysis. Other co-authors assisted with specifying the keywords, identifying the best databases for literature searching, and re-conducting the literature search and study screening.

6.1. Introduction

MS is an autoimmune disease that affects almost 2.5 million individuals worldwide, often in young adulthood[248]. MS is characterised by widespread damage to the central nervous system that includes alterations in normal-appearing white matter (NAWM) and demyelinating white matter lesions[249]. MRI plays an essential role in diagnosing and monitoring the disease course and the treatment effectiveness in MS. However; conventional MRI techniques have limited sensitivity to quantify microstructural alterations accompanying neuroaxonal degeneration in brain white matter and MS lesions[250–252]. Quantitative MRI biomarkers of the brain provide more sensitive detection of axonal degeneration and may become a more reliable outcome measure[253,254]. DTI is a quantitative technique widely used to characterise the microstructural abnormalities within both NAWM and white matter lesions in MS[255].

Many studies have reported reduced FA and increased MD in NAWM in MS patients compared with healthy participants[256–259]. One meta-analysis confirmed a significant FA reduction that suggested widespread white matter damage in MS[260]. Although these abnormalities may occur early in MS[261], DTI changes in the NAWM in patients with MS are linked with significant disability[262]. MRI-histopathological studies have confirmed a high correlation between the DTI changes and axonal count in white matter lesions and NAWM, indicating that these abnormalities may reflect pathological alterations related to disability[263–265]. Despite the DTI sensitivity in detecting microstructural changes in WM, the lack of tissue specificity is one of the caveats of DTI. DTI indices are affected by the orientation dispersion of fibres[15], which may lead to misinterpretation. Furthermore, the interpretation of DTI parameters becomes more complex when two or more different tissues with diffusion properties are present in a single voxel[266].

A biophysical diffusion model known as NODD has been proposed to overcome some DTI limitations, providing a more precise characterization of white matter microstructures[17]. NODDI describes brain tissue as a simplified combination of three compartments. A Watson distribution assumption of sticks models the first compartment, known as the intracellular compartment (axons and dendrites), and the signal of each stick is assumed to be a degenerated diffusion tensor with a perpendicular diffusivity equal to zero. The extracellular compartment is a Gaussian anisotropic diffusion, as seen in DTI, and the free water compartment is an isotropic Gaussian diffusion, such as CSF. After fitting the NODDI model, maps can be calculated for the neurite density index (NDI) or intracellular volume fraction (ICVF), the orientation dispersion index (ODI), and an isotropic signal fraction (isoVF). These maps explicitly estimate the orientation dispersion and neurite density, contributing to conventional DTI parameters such as FA[266]. Although NODDI has not been widely applied in MS, this technique is promising in investigating the complexity of MS

pathology, as it is more specific than DTI in detecting microstructural alterations[155,266–269]. Recent studies found that DTI and myelin-sensitive imaging are less sensitive than NODDI to neurite density and changes in NAWM and white matter lesions in patients with MS[10,268,270,271]. In addition, changes in NODDI parameters in specific brain WM[267,268], such as the internal capsule and corpus callosum in which long-tract axons are found[11], are associated with disability[267,268]. However, some other studies have unexpectedly reported increased fibre coherence (as shown by the low ODI) in white matter lesions and NAWM compared to healthy WM, which suggests careful interpretation in the presence of severe axonal loss (as indicated by low NDI)[10,155,266,270]. Unfortunately, longitudinal studies, which may help clarify the relationship between disease activity/progression and NODDI-detected white matter changes, are absent in the literature.

To summarise the current literature in this area, I conducted a systematic review and meta-analysis of studies using NODDI metrics to assess brain microstructural changes and neuroaxonal pathology in white lesions and NAWM in patients with MS.

6.2. Materials and Methods

6.2.1. Study Registration

This systematic review and meta-analysis were conducted according to the Preferred Reporting Items for Systematic Reviews and Meta-Analysis (PRISMA) guidelines[272] and registered in the International Prospective Register of Systematic Reviews (PROSPERO) database (CRD42021239169) in February 2021.

6.2.2. Study Selection (Inclusion and Exclusion Criteria)

Studies were considered for inclusion if they: (i) used a cross-sectional and cohort design; (ii) were published in peer-review journals; (iii) were written in English; (iv) reported NODDI coordinates (NDI and ODI) of NAWM and white matter lesions in

people with MS compared to the healthy white matter at 3.0T MRI only (participants scanned at 7T MRI were excluded); (v) included participants aged 18–75 years old; (vi) included healthy controls with no neurological disorders; (vii) included MS participants who could have any MS sub-types; or (viii) investigated the brain microstructural alterations in white matter MS lesions and NAWM. Studies were considered for exclusion if they: (i) were published as reviews or systematic reviews, qualitative studies, opinion pieces, editorials, comments, technical or validation/reproducibility studies, or were published as not full-text articles; (ii) reported subjects with neurological disorders and other diseases not due to MS; or (iii) reported results on animals, in-vitro, or MS patients only. Before the review registration, all inclusion/exclusion criteria were reviewed carefully by an experienced neurologist (C.S.C) and neuroradiologist (R.A.D).

6.2.3. Sources, Search Strategy and Screening

Four electronic databases were searched (Medline (Northfield, IL, USA), Embase (Amsterdam, Netherlands), Scopus (Amsterdam, Netherlands), and PubMed (Bethesda, Maryland, USA)) with the keywords ("Neurite Orientation Dispersion and Density Imaging" or "NODDI," "Multi-shell Diffusion," "Multi-compartment Diffusion" and "Multiple Sclerosis" or "MS"). Three subspecialised reviewers, namely A.A (Abdulmajeed Alotaibi), A.D (Ali Aldhebaib), and A.T (Amjad Altokhis), conducted the search strategy, database selections, study screening/identification, and study eligibility/inclusion independently and blindly. Citation chaining from reviews and other papers discovered by reviewers was carried out, and the searches were re-run before the final analysis in April 2021. Mutual discussions solved disagreements between reviewers.

6.2.4. Data Extraction and Collection

In March 2021, the first author, A.A., extracted and organised the desired data from all included studies using Microsoft Excel. The demographics of the MS, control

groups and clinical features of MS patients were extracted (age, gender, disease duration, Expanded Disability Status Scale (EDSS) score, population groups, and sample size). The between-group findings based on the region of interest analysis (ROI) were extracted and organised for analysis (mean/standard deviation (SD) of the NDI/ICVF and ODI values in white matter lesions, NAWM, and healthy WM). For the data synthesis, corresponding authors from the identified studies were emailed for a maximum of three times, separated by one week, to determine their willingness to contribute the raw data. The requested data included the SD and mean of the NDI/ICVF and ODI values for MS lesions and NAWM per subject, corresponding EDSS and MS duration.

6.2.5. Outcome Measures

The primary outcome measure was assessing the NDI/ICVF used to quantify microstructural abnormalities in neuroaxonal pathology (loss of axonal density or integrity) in white matter MS lesions and NAWM compared with the white matter in healthy controls. The secondary outcome measure assessed the ODI, which was used to quantify the loss of fibre coherence (an increase in fibre dispersion) in NAWM and white matter MS lesions compared with the white matter in healthy controls.

6.2.6. Statistical Analysis

Study characteristics and extracted variables were summarized using standard descriptive statistics. Continuous variables were expressed as means and SD, and categorical variables were expressed as frequencies or percentages. The continuous variables in this meta-analysis are presented as standardised mean differences (MD) with a 95% CI. A random-effects model and the Mantel–Haenszel method were used. Heterogeneity tests were conducted with the Q statistic distributed as a chi-square variate (assumption of homogeneity of effect sizes). The I^2 statistic was used to assess the extent of between-study heterogeneity. Study heterogeneity I^2 values > 50% were considered substantial, and > 75% were deemed considerable heterogeneity. Funnel

plots and Egger's tests were used to assess publication bias for the primary outcome. P-values were two-tailed, with values < 0.05 considered statistically significant. JASP 0.14.1.0 (University of Amsterdam, Amsterdam, Netherlands) and Review Manager 5.4.1 software (Cochrane organisation, London, UK) were used to implement all analyses.

6.3. Results

6.3.1. Included Studies and Sample Characteristics

The electronic search of the four databases retrieved 142 studies. A total of 76 studies remained after removing the duplicate studies and screening the title and abstract excluded 51 studies that did not meet the eligibility criteria. A total of 25 studies remained for retrieval; 13 studies were excluded. 12 studies remained for the eligibility assessment; 5 studies were excluded based on the reasons shown on the PRISMA diagram (Fig.6.1). A total of 7 studies investigating the brain microstructure in patients with MS using NODDI were included and met the inclusion/exclusion criteria for this meta-analysis[10,11,160, 274,276,278,281].

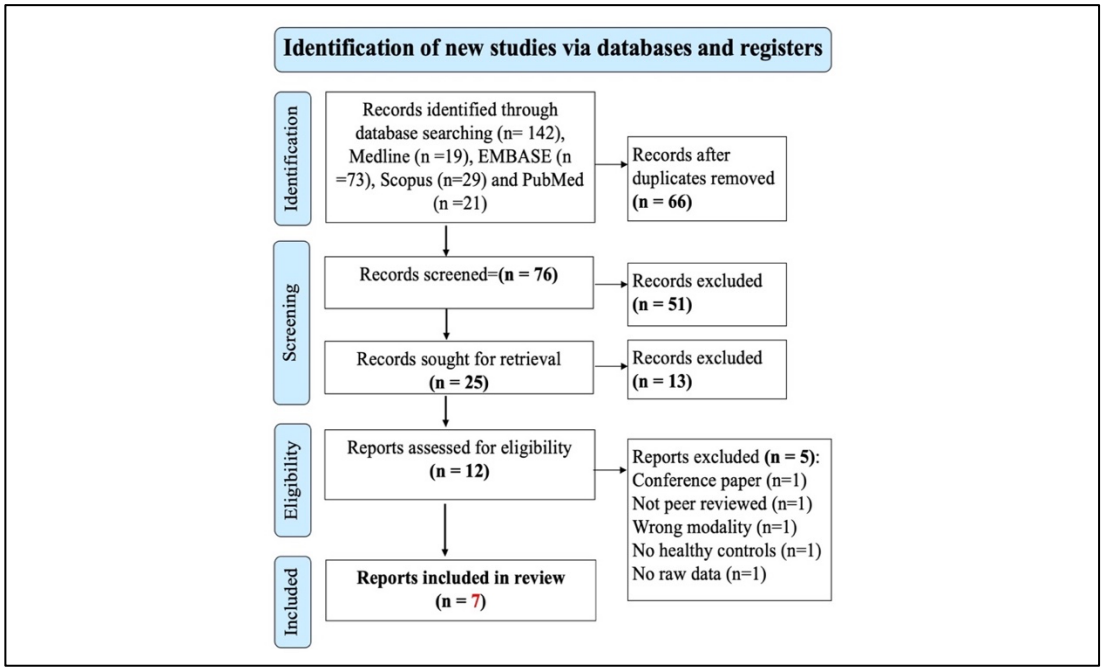


***Figure 6. 1**. Prisma flow diagram showing the systematic search strategy, study identification, screening, and eligibility and inclusion criteria.*

A total of 202 patients with MS (mean age of 40.1 years) and 172 healthy controls (mean age of 35.1 years) were included. The mean MS duration of all the studies was 8.3 years; however, two studies did not report disease duration[270,273]. There was no significant difference in the age and sex distribution between MS patients and healthy controls, with the caveat that one study did not provide information relating to the sex of participants[155]. In total, 125 of the included participants with MS were on treatment (diemtyhyl fumarate = 24, glatiramer acetate = 11, interferon-beta 1a = 10, natalizumab = 5, glucocorticoids = 6, glucocorticoids and on unspecified disease-modifying treatment = 1, unspecified disease-modifying therapy and no glucocorticoids, mitoxantrone = 1, fingolimod = 5, rituximab = 10, and ocrelizumab = 49). Additional clinical and technical characteristics are summarised in Tables 6.1 and 6.2.

Demographic and Clinical Characteristics of MS Patients and Healthy Individuals							
Study	**Author**	**Population Group**	**Sample Size**	**Gender (Number of Females)**	**Age (Mean ± SD)**	**Disease Duration Year (Mean ± SD)**	**EDSS (Median (Range))**
1	Collorone, 2019	RRMS	28	23	39.4 ± 6.6	8 ± 5.6	2.5 (1–6.5)
		HC	20	13	36.6 ± 12.5	--	--
2	De Santis, 2019	RRMS	7	7/NA	42 ± 15	21 ± 11	1 (0–3)
		HC	6	6/NA	42 ± 15	--	--
3	Granberg, 2017	RRMS	26	21	39.0 ± 8.2	2.5 ± 1.4	1.5 (0–4)
		HC	24	17	37.7 ± 10.6	--	--
4	Hagiwara, 2019	RRMS	24	19	39.83 ± 8.25	11.82 ± 5.99	1 (0–7)
		HC	24	19	39.50 ± 11.13	--	--
5	Rahmanzadeh, 2021	RRMS & PPMS	91	56	46 ± 14	NA	2.5 (0–8)
		HC	72	43	36 ± 12		--
6	Sacco, 2020	RRMS, CIS, PPMS	21	17	36.4 ± 8.7	NA	* 2.6 ± 1.6
		HC	21	17	36.4 ± 8.7		
7	Schneider, 2017	RRMS	5	3	39.2 ± 8.6	11 ± 3.4	4 (3–6)
		HC	5	3	37.6 ± 12.3	--	--

Table 6. 1. *Demographics and clinical characteristics of the included NODDI studies on MS. Abbreviations: NA = not available; HC = healthy controls; * = mean and standard deviation; -- = not applicable; SD = standard deviation; RRMS = relapsing-remitting multiple sclerosis; PPMS = primary progressive multiple sclerosis; and CIS = clinically isolated syndromes.*

Technical Characteristics of the Included Studies					
Study	**Author**	**Field Strength**	**RF Coil/ Fitting Toolbox**	**b-values (s/mm^2)**	**Method of Analysis/Regions**
1	Collorone, 2020	3.0 T	32 NODDI MATLAB	300–1000–2855	ROI: NAWM
2	De Santis, 2019	3.0 T	NA MDT	700–2000	ROI: WM lesions, NAWM, and NAGM
3	Granberg, 2017	3.0 T	64 NODDI MATLAB	1000–5000	ROI: cortical lesions, WM lesions, and NAWM
4	Hagiwara, 2019	3.0 T	19 (AMICO)	1000–2000	Voxel wise whole brain: WM ROI: NAWM and WM lesions
5	Rahmanzadeh, 2021	3.0 T	64 (AMICO)	700–1000–2000–3000	ROI: WM lesions, NAWM, and NAGM
6	Sacco, 2020	3.0 T	NA NODDI MATLAB	700–2000	ROI: WM lesions, NAWM, and DAWM
7	Schneider, 2017	3.0 T	32 NODDI MATLAB	300–711–2000	ROI: WM, NAWM, and WM lesions

Table 6. 2. *Technical characteristics of included studies. Abbreviations: NA = not available; T = tesla; ROI = region of interest; NAWM = normal-appearing white matter; DAWM = dirty-appearing white matter; NAGM = normal-appearing grey matter; WM = white matter; RF = radiofrequency; and s/mm^2 = second per millimetre.*

6.3.2. NDI in White Matter Lesions (MS Subjects) vs Controls

Six studies reported the NDI/ICVF and white matter lesions among 174 MS patients and 152 healthy controls[10,155,266,268,270,273]. The standardised mean difference was –3.08 (95% CI −4.22 to (−1.95)), $p \leq 0.00001$ (Fig.6.2). There is considerable heterogeneity between studies $I^2 = 88\%$. The Egger's test was z = 2.135, $p = 0.033$, which suggests potential publication bias (Fig.6.3).

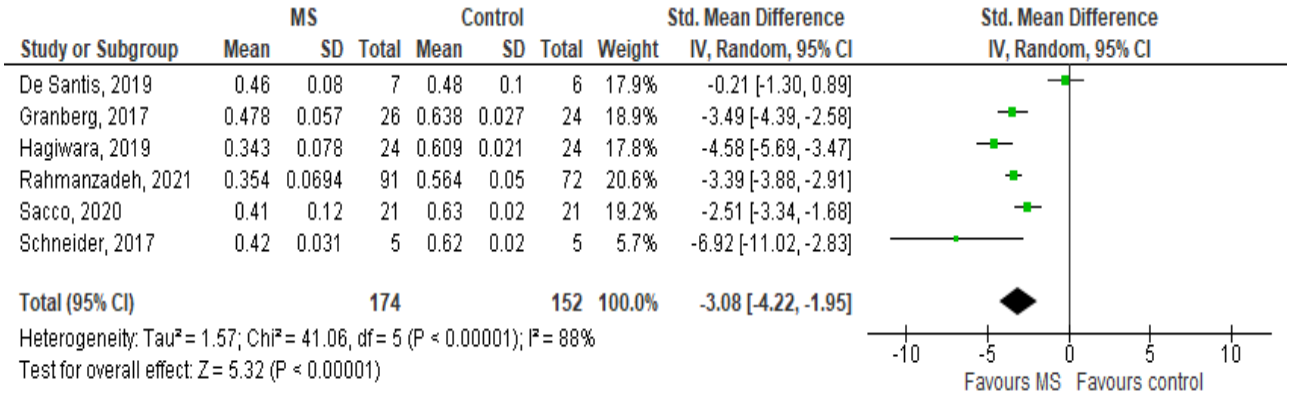


Figure 6. 2. *Forest plot for the standardised mean difference of the NDI/ICVF in MS white matter lesions (MS vs control). Abbreviations: SD = standard deviation; CI = confidence interval; NDI = Neurite Density Index; MS = multiple sclerosis; WM = white matter; vs = versus; and I2 = Heterogeneity Index.*

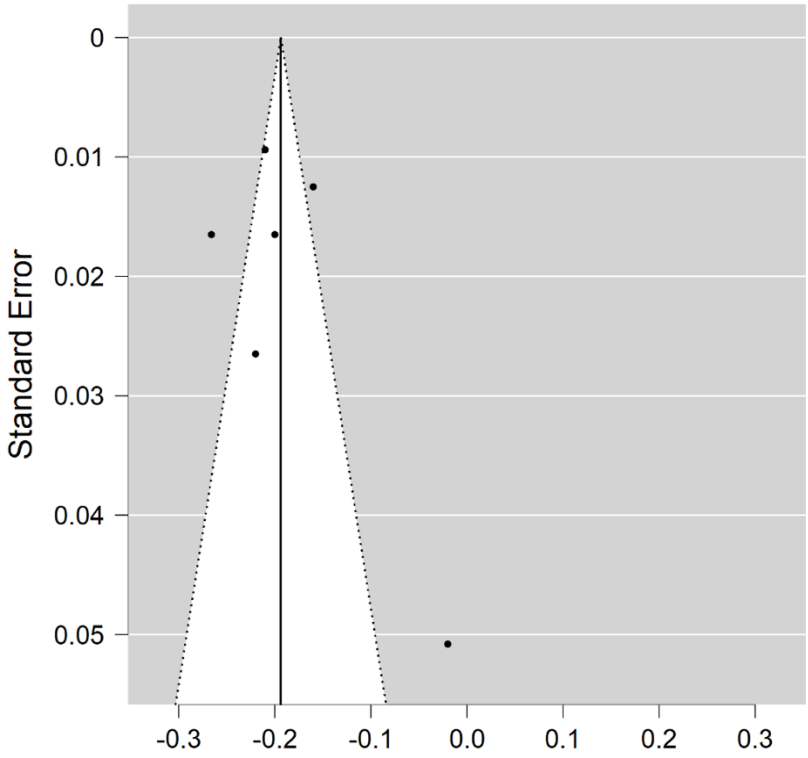


Figure 6. 3. *Funnel plot for the NDI in MS White matter lesions (MS vs control).*

6.3.3. NDI in NAWM (MS Subjects) vs Controls

Seven studies reported the NDI/ICVF and NAWM among 202 MS patients and 172 healthy controls[10,155,266,268,270,271,273]. The standardised mean difference was –0.70 (95% CI −0.99 to (−0.40)), *p* = <0.00001 (Fig.6.4). Thus, there is moderate heterogeneity between studies I^2 = 35%. Egger's test was z = −0.377, *p* = 0.706, suggesting no publication bias (Fig.6.5).

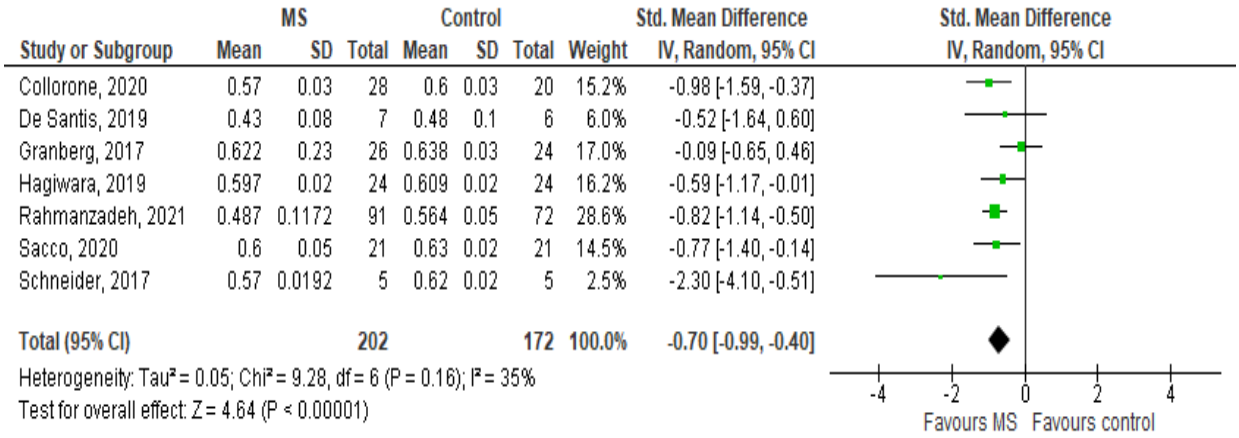


Figure 6. 4*. Forest plot for the standardized mean difference of the NDI/ICVF in NAWM (MS vs control). Abbreviations: SD = standard deviation; CI = confidence interval; NDI = Neurite Density Index; MS = multiple sclerosis; NAWM = normal-appearing white matter; vs = versus; and I2 = Heterogeneity Index.*

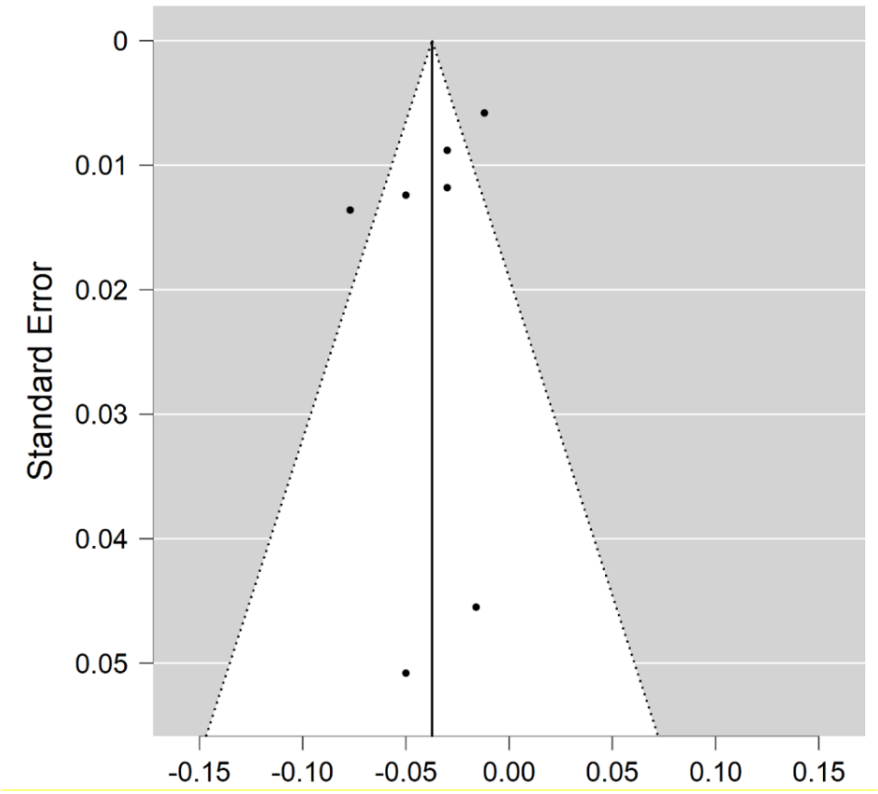


Figure 6. 5. *Funnel plot for the NDI in NAWM (MS vs control).*

6.3.4. ODI in MS White Matter Lesions (MS Subjects) vs Controls

Five studies reported the ODI and MS white matter lesions among 83 MS patients and 80 healthy controls[10,155,266,268,270]. The standardised mean difference was –0.44 (95% CI −1.60 to (−0.71)), p = 0.45. There is considerable heterogeneity between studies as I^2 = 89% (Fig.6.6).

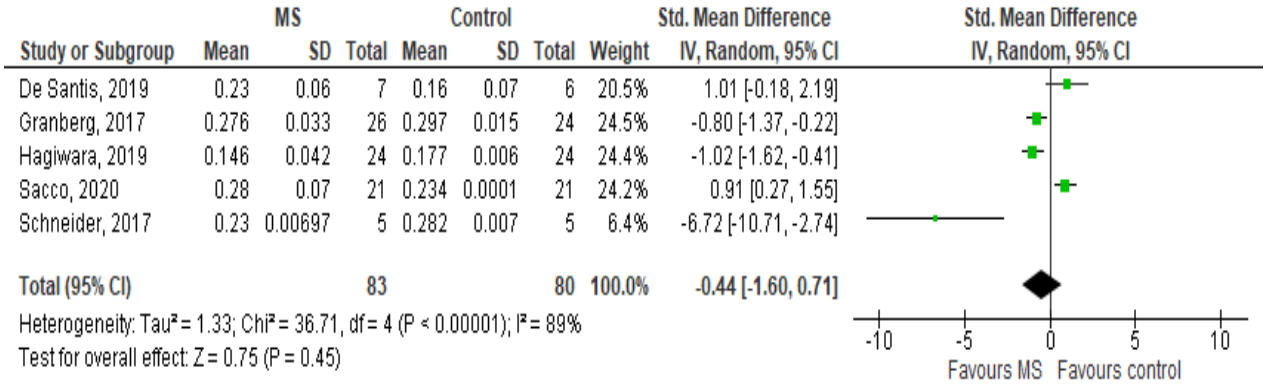


Figure 6. 6*. Forest plot for the standardised mean difference of the ODI in MS white matter lesions (MS vs control). Abbreviations: SD = standard deviation; CI = confidence interval; ODI = Orientation Dispersion Index; MS = multiple sclerosis; WM = white matter; vs = versus; and I2 = Heterogeneity Index.*

6.3.5. ODI in NAWM (MS Subjects) vs Controls

Six studies reported the ODI and NAWM among 111 MS patients and 100 healthy controls[10,155,266,268,270,271,273]. The standardised mean difference was –0.46 (95% CI −2.07 to (−1.15)), $p = 0.58$. Thus, there is considerable heterogeneity between studies as $I^2 = 95\%$ (Fig.6.7).

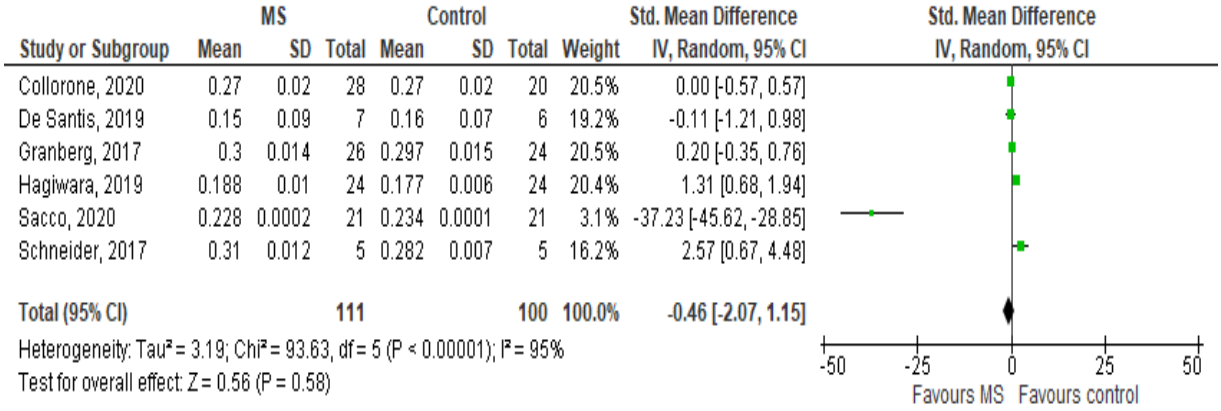


Figure 6. 7. *Forest plot for the standard mean difference of the ODI in NAWM (MS vs control). Abbreviations: SD = standard deviation; CI = confidence interval; ODI = Orientation Dispersion Index; MS = multiple sclerosis; NAWM = normal-appearing white matter; vs = versus; and I2 = Heterogeneity Index.*

6.4. Discussion

This systematic review of published NODDI studies comparing NODDI metrics from lesions and NAWM in MS with the white matter in healthy controls identified sufficient studies to allow for meta-analysis.

The key finding of this meta-analysis of ROI data concerned that the NDI/ICVF was reduced in MS lesions and NAWM compared to healthy controls (Fig.6.8)[12]. This significant reduction of the NDI/ICVF corresponds to reduced intracellular signal fraction or neurite density and may reflect underlying damage or loss of neurites. Previous work has shown that this reduction is accompanied by higher MD and lower FA[10]. The higher ODI suggests demyelination, axonal loss, and less coherence in the fibre orientation (bending or fanning axons)[268]. This meta-analysis demonstrates a significant reduction of intracellular signal fraction or neurite density in the NAWM of MS subjects compared with the white matter of controls, suggesting early axonal

pathology outside demyelination in white matter lesions[274–277]. This consistent reduction among all studies proves that the NDI/ICVF (through its sensitivity to the intra-axonal compartment) may quantify and differentiate microstructural changes in MS white matter lesions, the NAWM of MS, and healthy WM. This suggests a loss of axonal density in white matter lesions and NAWM in MS compared with healthy controls, consistent with previous DTI studies[257,278], reporting altered water diffusion in NAWM and white matter MS lesions compared with controlled subjects. Interestingly, the reduction of the NDI/ICVF in white matter lesions and NAWM is in line with previous pathological studies showing axonal loss within white matter lesions and a lesser degree in NAWM[264,277,279]. This consistent reduction of the NDI/ICVF reported in this meta-analysis may further assist researchers in relying on NODDI metrics in biophysically understanding the axonal loss/damage in white matter lesions and NAWM. Without publication bias, the funnel plot would show a symmetric distribution of study estimates, with smaller studies spread widely at the bottom and larger studies concentrated more closely around the real effect size at the top. In white matter MS lesions and NDI results, a potential publication bias has been indicated. Asymmetry in the funnel plot may suggest the presence of publication bias, which is the tendency for studies with statistically significant or positive results to be published more frequently than those with non-significant or negative results. Smaller studies with non-significant results may be absent from the plot due to publication bias, resulting in an uneven shape. This could indicate that the effect size was overestimated. Regarding the outliers, they can also be indicative of publishing bias. As previously stated, publication bias arises when research with statistically significant or positive findings is more likely to be published, causing the effect size to be overestimated. Therefore, outliers with a systematic bias toward one side of the funnel plot (e.g., an excess of studies with positive outcomes) may indicate the influence of publication bias.

Few studies reported a reduced ODI within the white matter lesions than in healthy WM, suggesting that neurites have less orientation variability or loss of neuronal fibres, which can be more severe in lesions[10,155,266]. In contrast, the higher ODI within the white matter lesions and NAWM, more than in healthy WM, might suggest a loss of fibre coherence and relatively maintained neuronal fibre density[10,155,266,270]. However, the meta-analysed results contradict these reported results, showing no differences in the orientation dispersion of neurites in patients with MS. In addition, the ODI may vary across regions of the brain and can be diverse across MS subjects, depending on the stage of MS. Therefore, the ODI may be extracted from heterogeneous areas of interest. Most importantly, the variability of b-values/scanning protocols may lead to heterogeneity and influence the ODI findings of this meta-analysis. For this reason, prospective researchers in the field may consider that NODDI metrics require careful interpretation and a harmonised study design/scanning protocol. There are some limitations to this systematic review. First, the NDI/ICVF and ODI from the ultra-high-field MRI have not been pooled due to a limited number of studies. Second, the isoVF was not included and pooled because it has only been investigated in two studies [10,266]. Third, the few studies included in this review may lead to insufficient conflicting ODI results, suggesting that the ODI is a less robust biomarker of MS microstructural damage and requires more studies and careful assessment. Fourth, this review lacks the evaluation of neurite density and orientation in grey matter and cortical lesions or between white matter lesions and NAWM. Fifth, the NODDI model is based on several assumptions that may be violated in abnormal tissue structures, leading to a few limitations in interpreting results. The T2 relaxation effect modulates the diffusion MRI signal is not modelled in NODDI. Therefore, any alteration in the T2 relaxation times of the tissue compartments may affect the NODDI parameters. In addition, NODDI assumes a fixed parallel diffusivity for intra-axonal and extra-axonal compartments. If this parameter increases within a white matter lesion,

the estimated NODDI parameters will be biased. Sixth, interpreting ODI alterations is challenging and dependent on the examined ROI. For instance, axonal loss in single or multiple fibre white matter regions may increase or decrease ODI values. Therefore, knowing the local fibre structure is important to interpret the ODI correctly. Seventh, there is moderate to considerable heterogeneity between studies, suggesting publication bias between studies that reported the NDI/ICVF in white matter lesions; however, no publication bias was found among studies that reported the NDI/ICVF in NAWM. In addition, data for white matter lesions and NAWM are derived largely from the same publications, thus making publication bias an unlikely explanation for the heterogeneity. This heterogeneity between the included studies possibly arises from the methodology, scanning protocol, data acquisition, and hardware variations. Importantly, the heterogeneity may be explained by the known lack of pathological specificity of the white matter lesions. Finally, data on the effect of the disease-modifying treatment on NODDI measures are lacking.

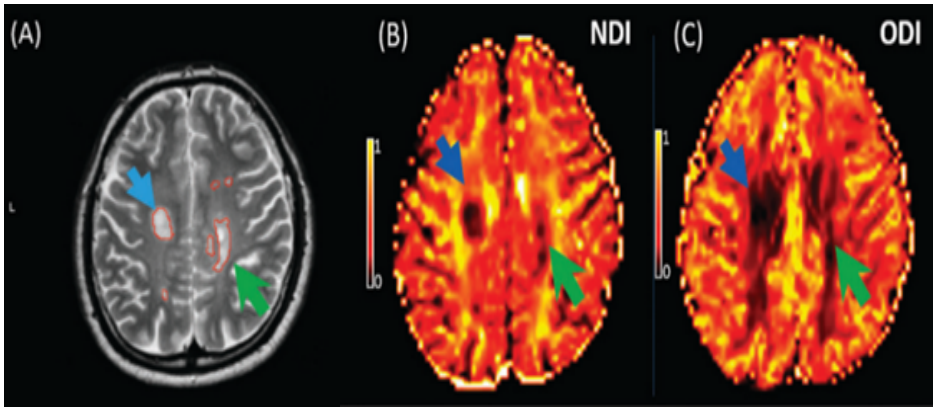


Figure 6. 8. *Illustrates NODDI metrics in a single slice of one MS subject. The MS lesion in the major WM tracts (blue arrow) and periventricular lesion (green arrow) are marked in a structural MRI image (A), NDI/ICVF map (B), and ODI map (C). Both the NDI/ICVF and ODI are decreased in the MS lesion*[266]*.*

6.5. Conclusions

This systematic review and meta-analysis confirmed that the NDI/ICVF is significantly reduced in MS lesions and NAWM than white matter in healthy participants, which corresponds to the reduced intracellular signal fraction and may reflect underlying

damage or loss of neurites. I was unable to demonstrate differences in the ODI in MS lesions and NAWM compared to white matter from healthy participants, but I have identified that heterogeneity in studies may limit the meta-analysis. Further analysis of the NODDI approach in MS for characterising disease-related ultrastructural changes is justified.

7. White Matter Microstructural Alteration in Type 2 Diabetes: A Combined UK Biobank Study of Diffusion Tensor Imaging and Neurite Orientation Dispersion and Density Imaging (Word count: 5421)

This chapter is published as a preprint[280] on medRixv. As a first author, I conducted the entire research project, from formulating the research questions to writing the content. The research questions were developed in consultation with Prof. Dineen, Prof. Constantinescu, and Dr Lee. Also, the entire work was supervised by them. Dr Ali-Reza Mohammadi-Nejad, Dr Stamatios N. Sotiropoulos and Dr Sieun Lee assisted with accessing the UK Biobank database and acquiring all datasets. Also, Ali, Stamatios, and Sieun helped improve the methods section (advised to use the de-confounded data and updated inclusion criteria for better results). Dr Chris Tench, Dr Anna Podlasek, and Amjad Altokhis advised on the statistical analysis steps.

7.1. Introduction

T2DM is a common metabolic disorder[281] that impacted approximately 462 million people in 2017, accounting for 6.28% of the worldwide population (4.4% of those aged 15-49 years, 15% of those aged 50-69 years, and 22% of those aged 70+), or prevalence rate of 6059 cases per 100,000[44]. T2DM results in microvascular and macrovascular complications[46], leading to microvascular abnormalities, generally recognised as risk factors for brain atrophy, microstructural alterations, and cognitive impairment[8,188,282]. Using advanced neuroimaging techniques, researchers have recently focused on understanding the link between T2DM and microstructural abnormalities in the brain. Advanced MRI techniques such as DTI have been widely used to explore microstructural changes in the brain. It has been adopted in several

studies to identify global/local network abnormalities and microstructural changes in white matter[216–218]. White matter tracts microstructurally affected by T2DM as detected by DTI include the corpus callosum, corona radiata, cingulum, internal/external capsules, fornix, uncinate fasciculus, and corticospinal tracts[8,193,283]. DTI is based on a single-compartment Gaussian diffusion model of brain microstructure with anisotropic water diffusion[16]. Although DTI is sensitive to white matter microstructural changes, it lacks specificity for the tissue microstructure [15,223,230]. When two or more distinct tissues with heterogeneous diffusion properties are present in a single voxel, the interpretation of DTI measures becomes more complicated[15]. Furthermore, DTI may not be an appropriate diffusion model to describe the non-Gaussian diffusion in biological tissues[284].

An alternative biophysical diffusion model, known as NODDI, has been proposed to theoretically provide more specific characterisations of white matter microstructure[17]. NODDI uses a multi-shell diffusion model with a high angular resolution that describes brain tissue as a simplified combination of three compartments and separates the signals from each compartment[17]. A Watson distribution assumption of sticks models the first compartment, known as the intracellular or intra-neurite compartment (axons and dendrites), and the signal of each stick is assumed to be a perfectly anisotropic diffusion tensor with a perpendicular diffusivity equal to zero. Also, it represents extracellular space with a Gaussian anisotropic diffusion and a free water compartment that represents an isotropic Gaussian diffusion, such as CSF[17]. NODDI uses three scalar parameters: neurite density index (NDI), also known as intra-cellular volume fraction (ICVF), orientation dispersion index (ODI) (0 for perfectly aligned straight fibres and 1 for entirely isotropic), and free water fraction or isotropic volume fraction (IsoVF)[18]. These parameters estimate the orientation dispersion and neurite density, contributing to conventional DTI parameters such as FA[17].

Although NODDI has not been widely applied in diabetes, it is promising in evaluating the complexity of white matter neuroaxonal pathology. A previous study has demonstrated that NODDI parameters can detect differences between T2DM and non-T2DM participants, suggesting their promising role as a biomarker for assessing white matter microstructural deficits in T2DM patients[229]. However, this study was performed on 18 patients with T2DM only, the slice thickness was large, and the diffusion encoding direction of 25 was relatively small to estimate the fibre orientation. These technical and sample size limitations may have limited the quantification of NODDI-derived parameters in T2DM patients.

Herein, the brain white matter microstructural changes in a large cohort of participants with T2DM from a population-level study (the UK Biobank[285,286]) using measures derived from DTI and NODDI were explored. The UK Biobank is a large-scale epidemiological project with a large cohort. The data available through the UK Biobank is rich, with roughly 500,000 participants in the cohort. A large cohort was produced by inviting approximately 9.2 million people to participate. Data is gathered utilising a variety of diagnostic methods, including MRI. One of the UK Biobank imaging study goals is to collect brain MRI data from 100,000 healthy people and track their health over several decades[287]. The UK Biobank has enrolled 503,317 individuals, with participants between the ages of 40 and 69 and living within 25 miles of one of 22 UK Biobank centres spread across England, Wales, and Scotland. The cohort is healthy at the time of recruitment. Still, one of the project's main goals is to track the subjects' health over time, allowing researchers to identify early signs of diseases[287].

The aims of this large-scale study are 1) to investigate brain white matter microstructural alterations of T2DM participants using NODDI and determine its use in detecting global and regional white matter differences; 2) to assess ODI and isoVF in detecting white matter as it has not been investigated in a previous study due to

limitations in the scanning protocol; and 3) to examine the association between the altered NODDI metrics, the duration of diabetes, and the glycated haemoglobin (HbA1c) levels.

7.2. Materials and Methods

7.2.1. UK Biobank Data

Non-imaging dataset comprises questionnaires on lifestyle, family, and medical history, physical and cognitive tests, blood, urine, and saliva samples, and genetic information. A subset of these measures is used in the current PhD project. Self-report questionnaires on diet, lifestyle, family, and medical history; summary assessments of physical and heart health derived from other modalities (e.g., ultrasonography and electrocardiograms); body impedance analysis; and scores from a variety of cognitive tests[287]. Imaging datasets in the UK Biobank are collected utilising various techniques and modalities[169,285].

All participants provided informed consent forms. Ethical approval was obtained from the Northwest Multi-centre Research Ethics Committee. The current study was approved under the UK Biobank application ID 43822. Details of the UK Biobank cohort and consent are available on the UK Biobank website[288].

7.2.2. Clinical Characteristics and Sample Selection

A total of 31,767 participants were included in this study (1023 participants with T2DM and 30744 non-T2DM participants). Touch-screen questionnaires, health exams, brief computer-assisted interviews, biological samples, and imaging data were among the baseline assessments[286]. At the time of the imaging visit, data on age, sex, qualification, diabetes history, body mass index (BMI), blood pressure (BP), glycated haemoglobin (HbA1c), cardiovascular disease history, and neurological disorders were collected and reported. Socioeconomic status, family history, lifestyle, and health status were among the datasets acquired through questionnaires and interviews.

Based on self-reports and the hospital inpatient ICD10 record (International Classification of Diseases) across all UK hospitals, participants with T2DM who did not have neurological diseases such as stroke, haemorrhage, cerebral infarction, Parkinson's disease, Alzheimer's disease, epilepsy, head injuries, or tumours were included. Subjects with other neurological disorders were excluded according to their self-reports through touchscreens and verbal interviews. Participants in the UK Biobank with no history of diabetes or neurological disorders were used as a control group.

7.2.3. Brain MRI Acquisition

Participants in UK Biobank were invited to attend MRI scans at one of three dedicated imaging centres equipped with identical scanners (3T Siemens Skyra, software VD13A via Siemens Healthcare) and using a Siemens 32-channel receive head coil. Diffusion images were acquired using echo-planar with a single-shot Stejskal-Tanner pulse sequence in 100 diffusion-weighted directions (b-values=0, 1000, and 2000 s/mm^2). T1-weighted structural brain images were acquired using a three-dimensional MPRAGE sequence. The brain imaging protocol details are available online and in the UK Biobank imaging report[169,288].

7.2.4. Diffusion Image Processing

In the diffusion data, the anterior-posterior (AP) encoding direction was corrected for eddy currents, head motion, and outlier slices (individual slices in the 4D data). The diffusion images were corrected using the eddy tool in the first step of this pipeline[169,289,290]. This step required knowledge of the "best" b = 0 images in the AP direction. The gradient distortion correction was applied after eddy to produce a more precise correction[291]. The diffusion images were analysed based on tract-skeleton (TBSS) processing. Then, the output was a wide range of diffusion MRI-derived measures within different tract areas: 1) measurements derived from diffusion-tensor

modelling and 2) measurements derived from microstructural model fitting. More details on image processing are available in previous UK Biobank reports[169,179,285].

7.2.4.1. *DTI and NODDI fitting*

The DTI fitting was applied to the b=1000 shell (50 directions) using DTIFIT tool[161]. In addition to DTI fitting, the entire two-shell diffusion data set was fed into NODDI modelling, performed with the AMICO (Accelerated Microstructure Imaging via Convex Optimization) tool[166]. This aimed to generate voxel-wise microstructural parameters such as ICVF, ODI and IsoVF.

7.2.4.2. *White matter tract skeleton analysis*

The DTI FA image was fed into TBSS[168], which aligned the FA image onto a standard-space-white-matter skeleton, with additional alignment that improved the original TBSS skeleton projection by employing a high-dimensional FNIRT-based warping technique[292]. The resulting standard-space warp was applied to DTI/NODDI output maps. For each DTI/NODDI map, the skeletonized images were averaged within a set of 48 standard-space tract masks defined by the Johns Hopkins University group (JHU-ICBM atlas)[293] to generate a set of diffusion imaging-derived phenotypes (IDPs).

7.2.5. Confound Modelling in UK Biobank Brain Imaging

A huge imaging dataset, such as the UK Biobank data, may contain confounds that must be corrected before running the final statistical analysis. In this study, the following imaging and demographic features were de-confounded from the brain IDPs: age, sex, head motion, head size scaling, and confounds related to bed/table position in the scanner (for the three axes X, Y, Z), confounds of acquisition date/time, and imaging sites[285,294]. The UK Biobank dataset was de-confounded with a linear model concurrently (i.e., in a single regression-based de-confounding employing all confound variables combined). For instance, Y is the N-vector of interest, and X is the N-by-P matrix of all confounds. In that case, the confound-adjusted variables are the residuals from the linear model fit Y to X[294].

7.2.6. Statistical Analysis

Statistical analysis was performed using SPSS 27.0 (IBM, NY, USA). Continuous data were presented as mean ± standard deviation, and categorical data were presented as percentages. Intergroup differences, including clinical characteristics and brain white matter differences, were compared by student's t-test and Pearson's chi-square test. The Intergroup analysis was performed on the already generated IDPs and was not performed on images obtained from the UK Biobank. Pearson correlation analyses were conducted to explore the association between HbA1c, disease duration and diffusion measures. Pearson's correlation coefficient was considered weak (0< r ≤0.4). The defined *P-value* threshold was set to a *P*-value of 0.05 (false discovery rate).

7.3. Result

7.3.1. Clinical Characteristics

In this UK Biobank study, 1023 participants with T2DM and 30,744 non-T2DM participants had undergone diffusion MRI. They were retained in this analysis after applying the inclusion/exclusion criteria. The clinical characteristics of both groups are presented in Table 7.1.

Cohort Characteristics

	(*N* = 1023) T2DM (mean ± SD) %	(*N* = 30744) Non-T2DM (mean ± SD) %	χ2/T	Mean difference	95% CI Lower	95% CI Upper
Gender F (%)	339/39%	16588/53%	172.4	--	--	--
Age (years)	66 ± 7.04	64 ± 7.5	11.2	2.5	2.09	2.9
Systolic blood pressure (mmHg)	142.6 ± 18.05	136.03 ± 18.6	11.3	6.7	5.6	7.9
Diastolic blood pressure (mmHg)	83.7 ± 10.4	81.2 ± 10.4	7.6	2.6	1.9	3.4
Hb1AC (mmol/mol)	47.08 ± 12.06	34.3 ± 3.5	32.6	12.9	12.1	13.6
BMI (kg/m^2)	29.8 ± 5.1	26.3 ± 4.3	21.3	3.5	3.2	3.8
Disease duration (years)	12.3 ± 9.3	--	--	--	--	--
Education level	Missing 128	Missing 2062				
(A)	183 (17.8%)	4429 (14.4%)	82.03	--	--	--
(B)	200 (19.5%)	5394 (17.5%)				
(C)	117 (11.4%)	3735 (12.1%)				

(D)	395 (38.6%)	15124 (49.1%)

Table 7. 1. *The clinical characteristics of the included participants from the UK Biobank database. ± = mean and standard deviation; A = College or University degree; B = A levels/AS levels or equivalent; C = O levels/GCSEs or equivalent; D = CSEs or equivalent, -- = not applicable.*

7.3.2. White Matter Intergroup Differences and Association with Metabolic Profile: Overview

Parametric maps of DTI and NODDI were generated from each subject. This large sample study revealed subtle but global white matter microstructural changes in the participants with T2DM compared to non-T2DM individuals, which were reflected by reduced FA and ICVF, increased MD, AD, RD, ODI, and IsoVF. These subtle alterations had weak correlations with disease duration and HbA1c.

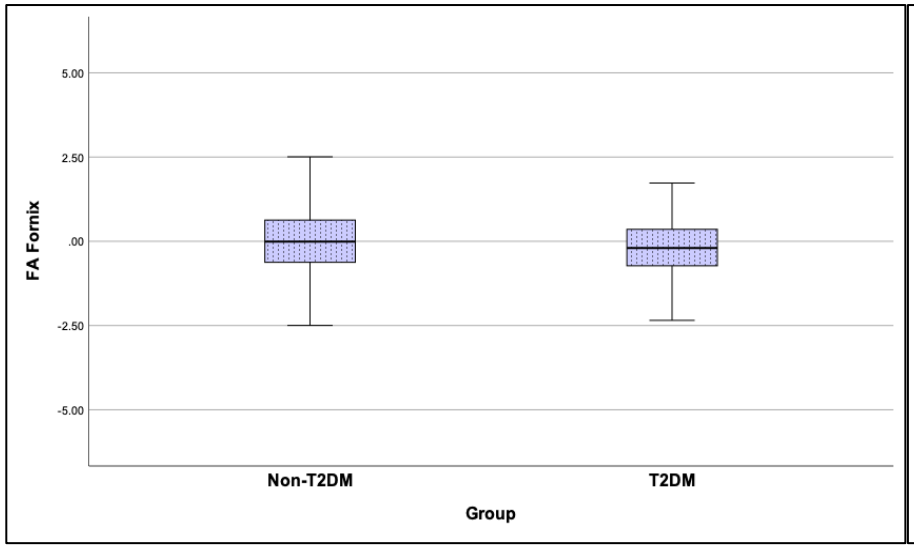
7.3.2.1. DTI Intergroup White Matter Differences

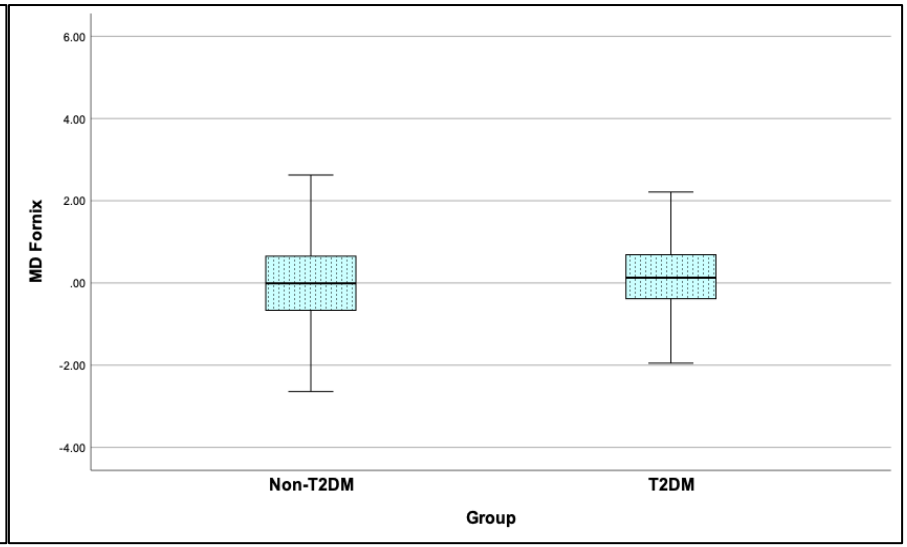
FA showed a significant reduction in most of the examined white matter tracts of participants with T2DM compared to non-T2DM individuals (All $p<0.05$, $d \leq 0.3$). Also, MD, AD and RD showed a significant increase in the majority of investigated white matter tracts of participants with T2DM (All $p<0.05$, $d \leq 0.3$) (See Appendix Table 4 and Fig.7.1). Details on statistics of DTI differences are shown in Appendix Tables 1A-D.

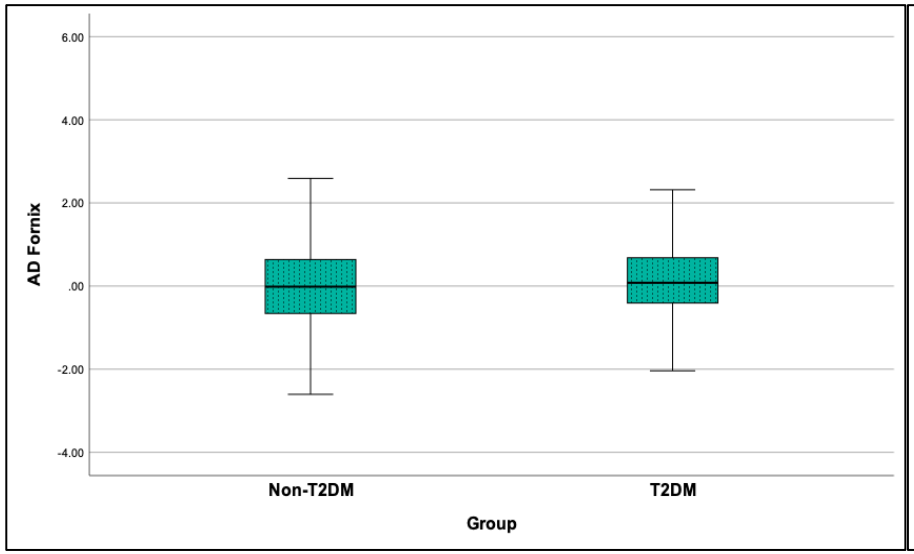
7.3.2.2. NODDI Intergroup White Matter Differences

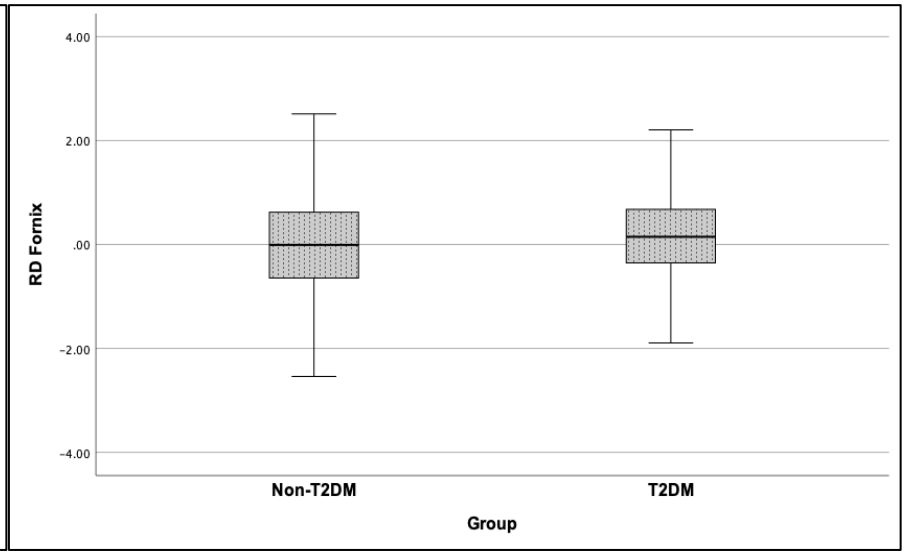
ICVF was significantly reduced in the majority of the investigated white matter tracts of participants with T2DM compared to non-T2DM individuals (All $p<0.05$, $d < 0.3$). ODI and IsoVF were significantly increased in the majority of investigated white matter tracts of participants with T2DM compared to non-T2DM individuals (All $p<0.05$, $d < 0.3$). In contrast, there was a decrease in ODI in the bilateral posterior limbs of the internal capsules, bilateral superior corona radiata and right posterior corona radiata ($p<0.05$, $d < 0.3$) (See Appendix Table 4 and Fig.7.1). Details on statistics of NODDI differences are shown in Appendix Tables 2A-D.

White Matter Alterations in the Fornix in T2DM Participants









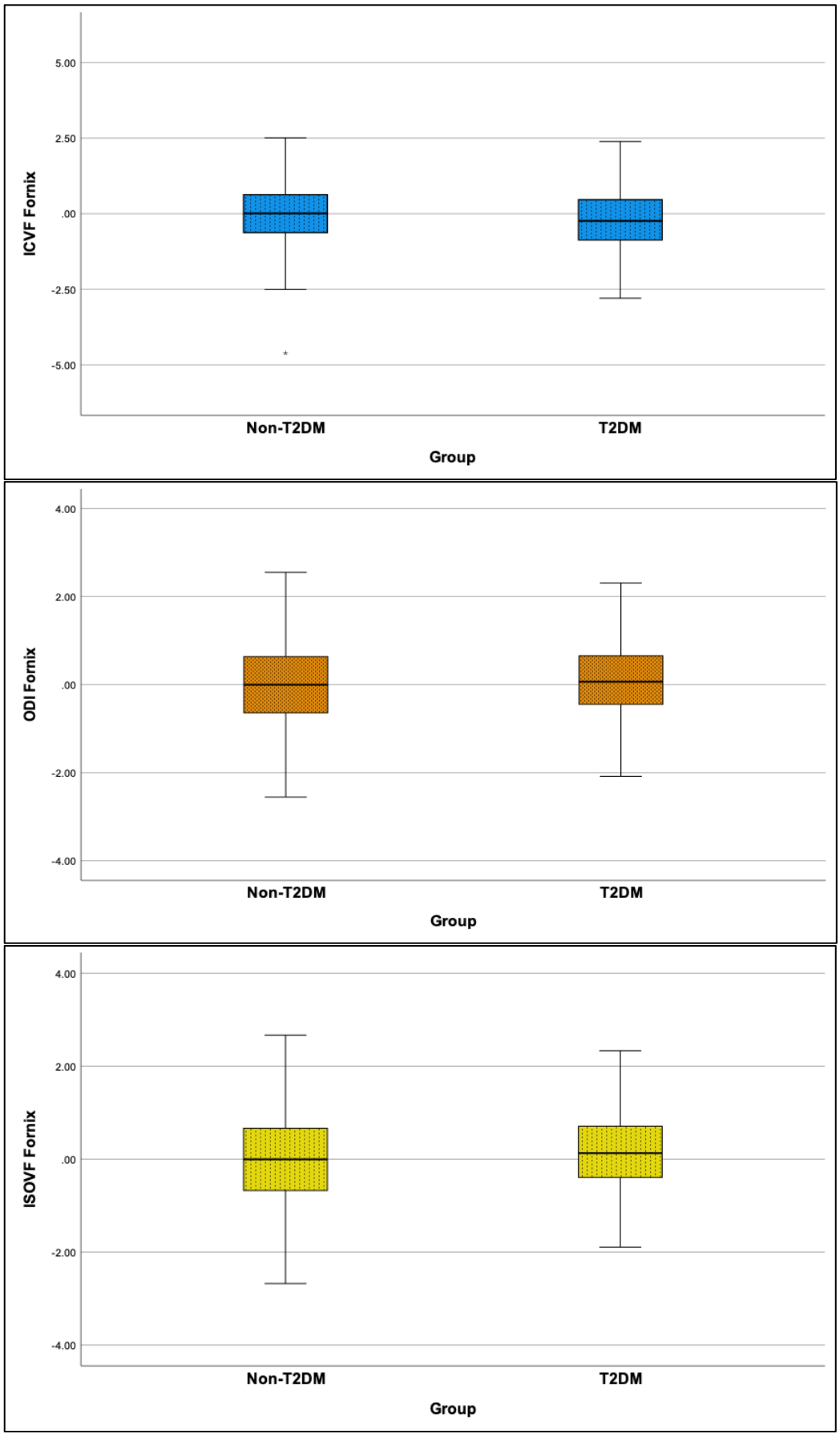


Figure 7. 1. *The boxplots for the fornix as a selected white matter tract (from the de-confounded dataset) with a larger effect size to visualise the intergroup DTI and NODDI-white matter alteration in patients with T2DM (P <0.05, false discovery rate adjustment).*

7.3.3. Diffusion Measures and Correlation with Metabolic Profile

7.3.3.1. Disease duration, HbA1c and DTI

Correlation analysis showed a weak association between disease duration, HbA1c, and DTI changes in white matter tracts of participants with T2DM. Reduced FA and increased MD, AD and RD correlated with longer disease duration in most examined white matter tracts (all $p<.05$) ($0< r <0.2$). Also, reduced FA and increased MD, AD and RD weakly correlated with higher levels of HbA1c (all $p<.05$) ($0< r <0.2$) (See Fig.7.2, Table 7.2, and Appendix Table 3).

7.3.3.2. Disease duration, HbA1c and NODDI

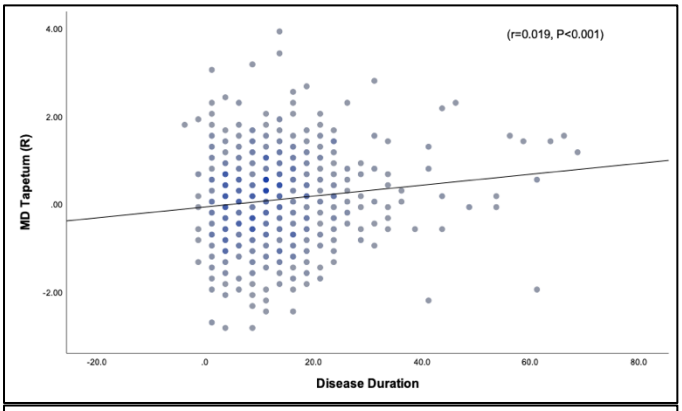
Reduced ICVF and increased ODI and IsoVF had weak correlations with longer disease duration and HbA1c in most examined white matter tracts (all $p<.05$) ($0< r <0.2$). Also, reduced ICVF and increased ODI and IsoVF had a weak but significant correlation with higher levels of HbA1c (All $p<.05$) ($0< r <0.2$) (See Fig.7.2, Fig. 7.3, Table 7.2, and Appendix Table 3).

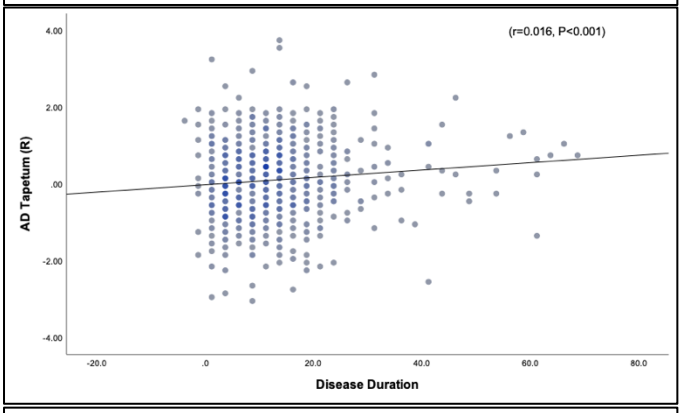
Diffusion Indices	Disease Duration	HbA1c
Reduced FA	Number of tracts: 31/48 WM tracts	35/48 WM tracts
	Direction: Negative correlation	Negative correlation
	Strength: weak ($0< r \leq 0.2$)	Weak ($0< r \leq 0.2$)
Increased MD	Number of tracts: 30/48 WM tracts	35/48 WM tracts
	Direction: positive correlation	Positive correlation
	Strength: weak ($0< r \leq 0.2$)	Weak ($0< r \leq 0.2$)
Increased AD	Number of tracts: 13/48 WM tracts	18/48 WM tracts
	Direction: positive correlation	Positive correlation
	Strength: weak ($0< r \leq 0.2$)	Weak ($0< r \leq 0.2$)
Increased RD	Number of tracts: 39/48 WM tracts	40/48 WM tracts
	Direction: positive correlation	Positive correlation
	Strength: weak ($0< r \leq 0.2$)	Weak ($0< r \leq 0.2$)
Reduced ICVF	Number of tracts: 43/48 WM tracts	40/48 WM tracts
	Direction: negative correlation	Negative correlation
	Strength: weak ($0< r \leq 0.2$)	Weak ($0< r \leq 0.2$)
Increased ODI	Number of tracts: 3/48 WM tracts	23/48 WM tracts
	Direction: positive correlation	Positive correlation
	Strength: weak ($0< r \leq 0.2$)	Weak ($0< r \leq 0.2$)
Increased IsoVF	Number of tracts: 8/48 WM tracts	13/48 WM tracts
	Direction: positive correlation	Positive correlation
	Strength: weak ($0< r \leq 0.2$)	Weak ($0< r \leq 0.2$)

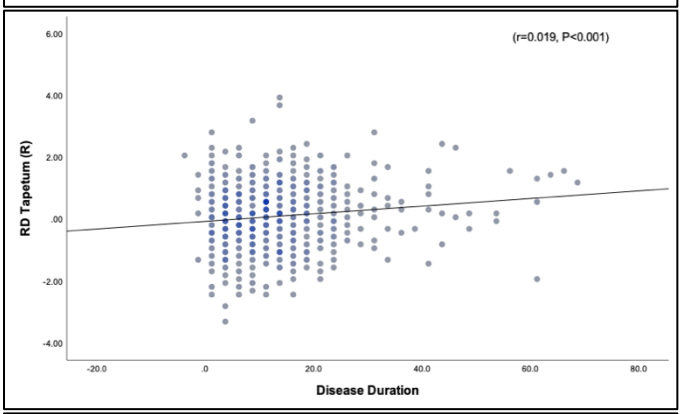
Table 7. 2. *The number of white matter tracts correlated with disease duration and HbA1c levels, direction, and strength of the correlations (P <0.05 after false discovery rate adjustment). WM= white matter.*

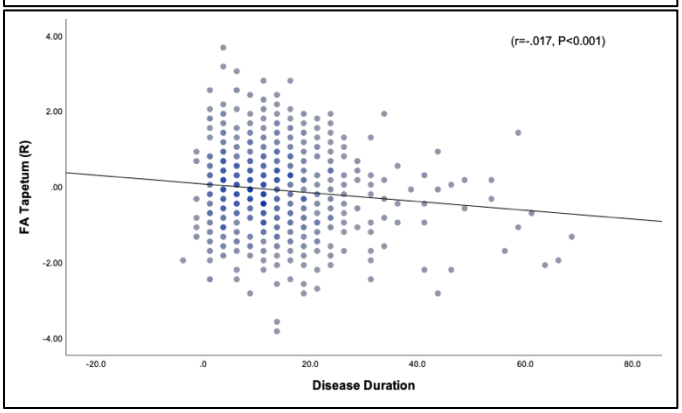
Association Between White Matter Alterations in the Right Tapetum and Disease Duration/HbA1c

A

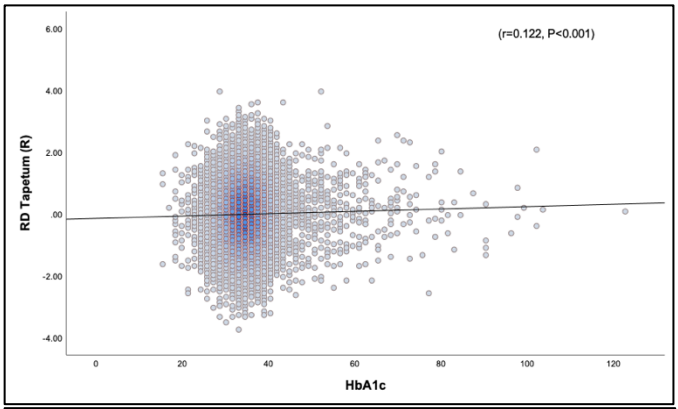


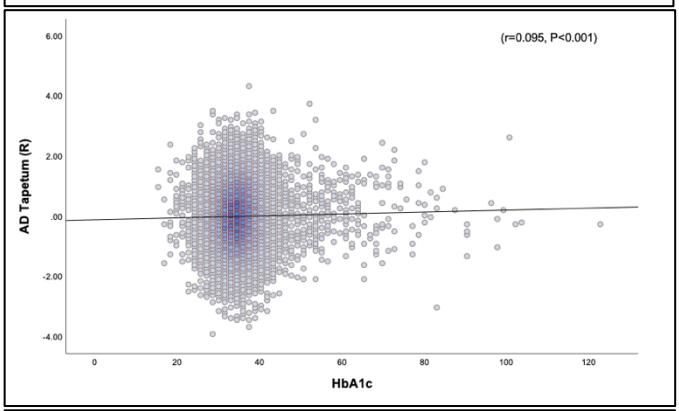


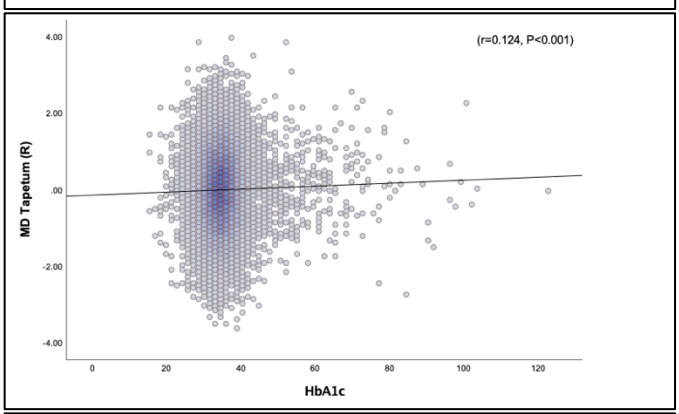


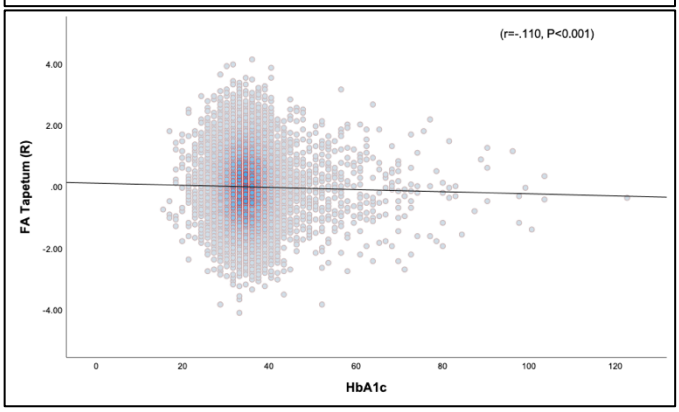


B









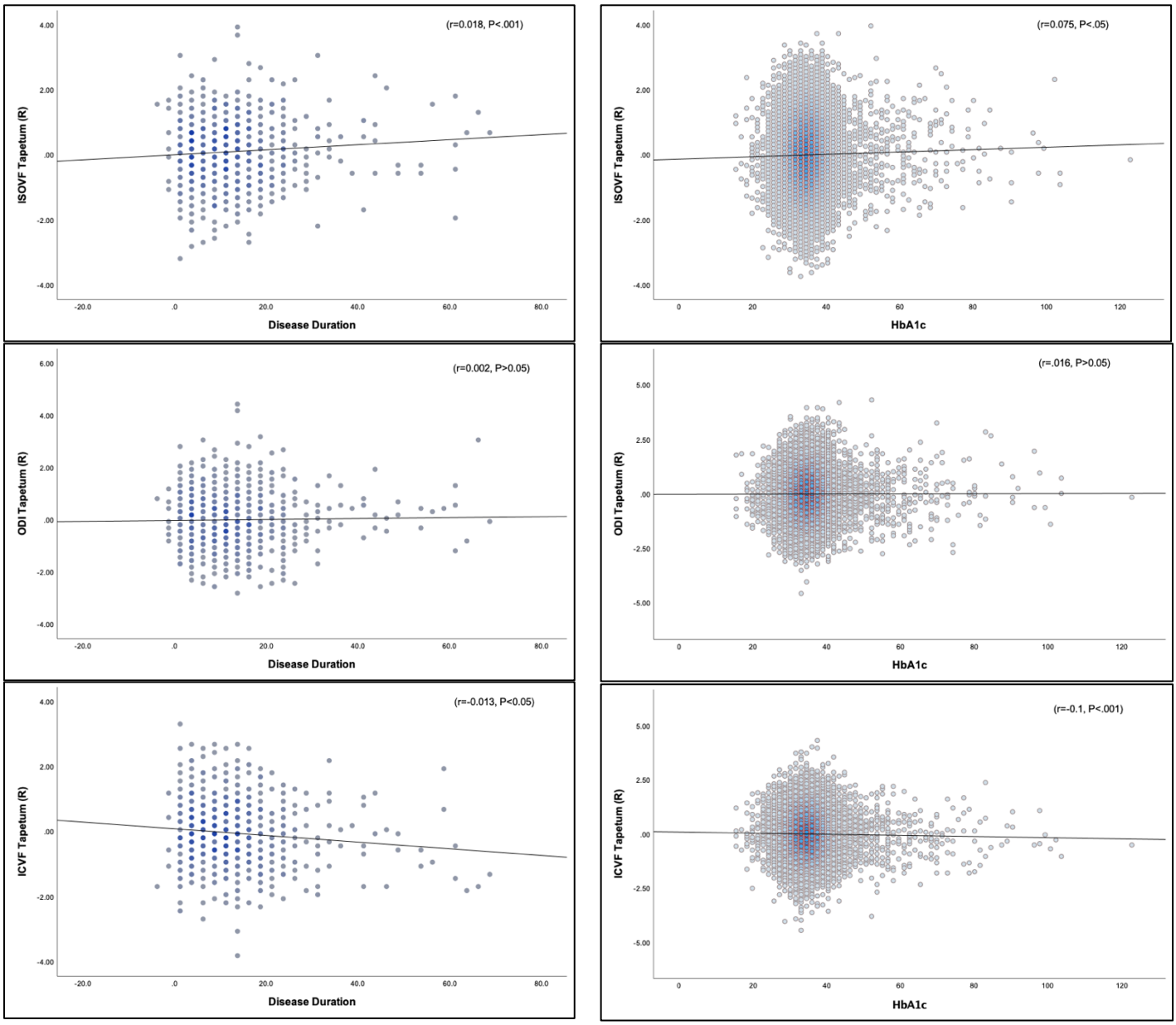
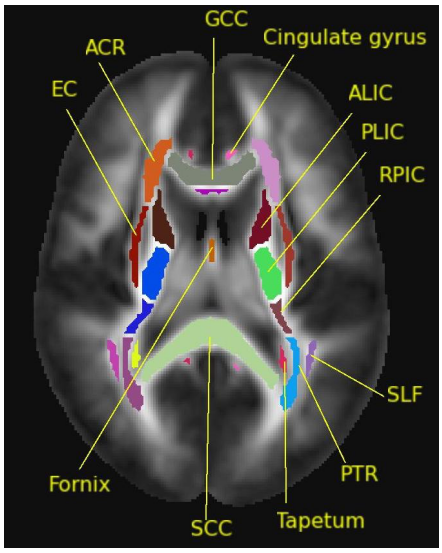


Figure 7. 2. *The right tapetum as a selected white matter tract from the de-confounded dataset to visualise the association between the white matter change detected by DTI/NODDI and metabolic profile. (A) illustrates the association between white matter alterations in the right tapetum and disease duration; (B) shows the association between white matter alterations in the right tapetum and HbA1c.*

A



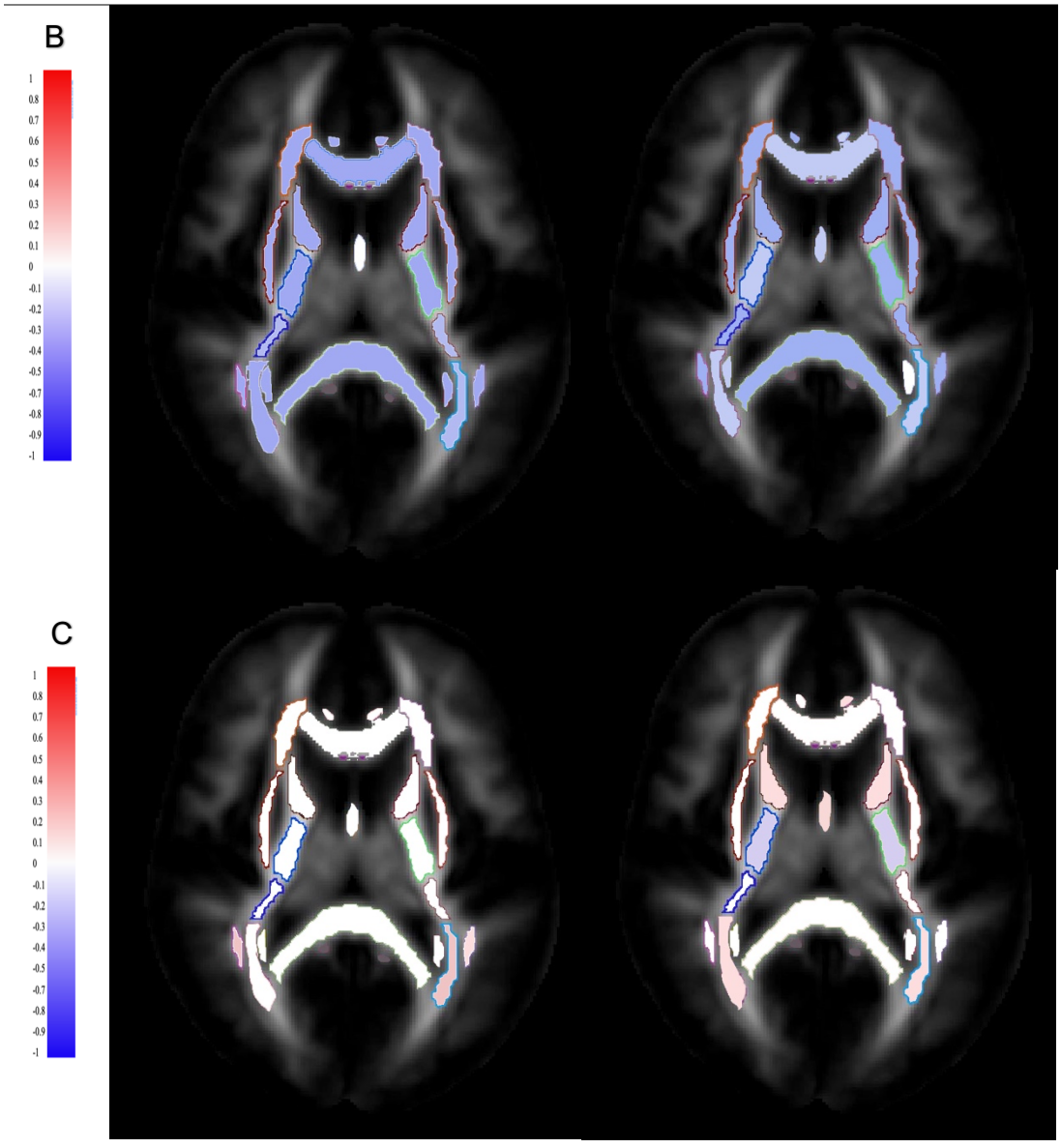
Disease Duration HbA1c

B

C

ICVF

ODI



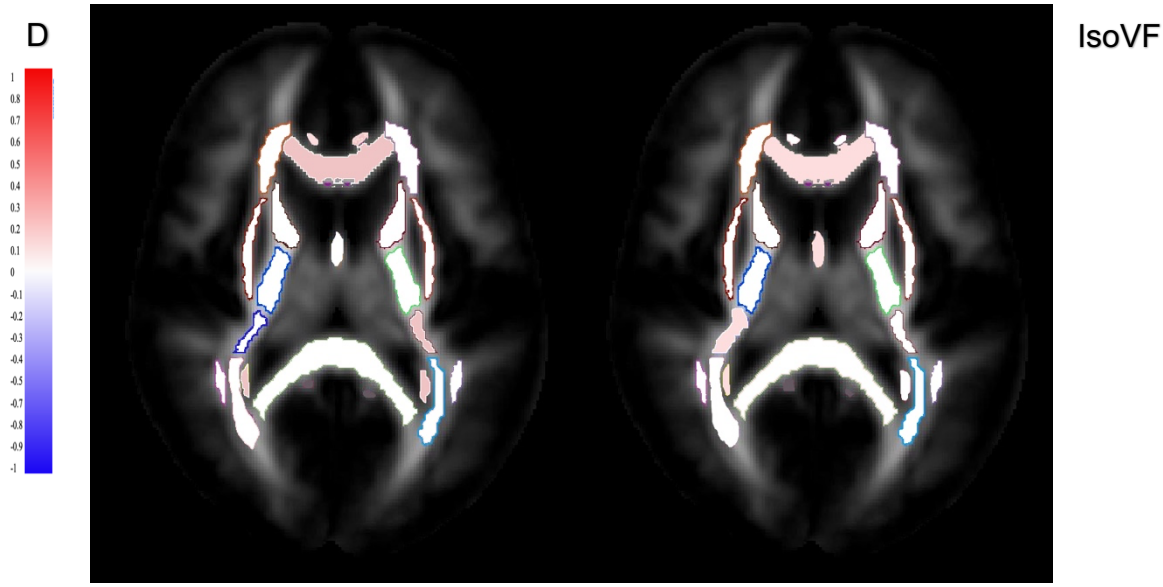


Figure 7. 3. *The correlations between disease duration and HbA1c with major white matter tracts in participants with T2DM, and these white matter structures are only selected for visualising purposes. (A) White matter tracts included: Genu of corpus callosum (GCC), fornix, cingulate of gyrus, superior longitudinal fasciculus (SLF), anterior corona radiata (ACR), anterior limb of the internal capsule (ALIC), posterior limb of the internal capsule (PLIC), posterior thalamic radiation (PTR), tapetum, splenium of corpus callosum (SCC), external capsule (EC), and retrolenticular part of the internal capsule (RPIC). (B)Altered ICVF and disease duration/HbA1c. (C)Altered ODI and disease duration/HbA1c. (D)Altered IsoVF and disease duration/HbA1c. Red = positive correlation; blue = negative correlation.*

7.4. Discussion

Using this large-scale diffusion imaging data from 31,767 participants from the UK Biobank, the ability of DTI and NODDI-derived metrics to capture microstructural changes in the white matter in participants with T2DM were evaluated. Moreover, we examined whether disease duration and HbA1c were associated with altered DTI/NODDI parameters.

In T2DM participants, white matter tracts and fibres mostly show reduced FA, ICVF, and increased MD, AD, RD, ODI, and IsoVF, as presented in Appendix Table 4. Reduced anisotropy and increased diffusivity reflected by reduced FA and higher MD confirm widespread microstructural alterations and broadly agree with previous DTI studies (see the previous reviews[8,193,283]). The elevation of AD and RD in participants with T2DM might lead to changes in FA and MD, as AD is linked to axonal

integrity and RD is linked to myelin abnormalities. Therefore, the findings of the UK Biobank study suggest that increased interstitial space between the myelin-covered axons (expansion of extracellular space due to the degeneration of fibres/axonal injury) and reduced myelin integrity play a role in white matter deficits in T2DM participents[221,223,295,296].

The reduction of ICVF in the white matter of T2DM in this study was consistent with a previous study[229], which indicates reduced neurite density. The reduced ICVF or neurite density in T2DM is likely relevant to structural changes such as axonal loss, axonal damage, or axonal demyelination/degeneration[140,268]. Furthermore, the decreased neurite density in the participants with T2DM may be accompanied by axonal disorganization, myelin loss, or loss of fibre orientation coherence that may lead to increased ODI in response to the alterations in white matter[13,193,297,298]. Interestingly, decreased ODI is observed in bilateral posterior limbs of internal capsules, bilateral superior corona radiata and right posterior corona radiata, which may reflect the loss of neuronal/crossing fibres, reorganisation of fibres, or reduced axonal dispersion in T2DM[140,299,300]. In addition, higher coherence of axonal packing in the white matter of T2DM patients reflected by the decrease of ODI may suggest either a reduced collateral branching driven by the pathology or alterations in the morphology of an individual axon. Lastly, the elevated IsoVF may indicate vasogenic oedema or increased extracellular free water, which may be caused by the disruption of BBB due to T2DM[141], or may indicate a degree of atrophy by reflecting cell shrinkage and decreased tissue volume fraction[301].

By examining the relationship between the metabolic profile and white matter intergroup differences, statistically significant associations were identified between altered DTI and NODDI parameters in T2DM participants and glycaemic control/disease duration. The neurite density in the white matter of T2DM participants reflected by a reduced ICVF has a consistent association with disease duration and

poorly-controlled blood glucose, suggesting that T2DM participants with longer disease duration and higher plasma glucose tend to have reduced neurite density. Poorly-controlled blood glucose and disease duration correlate with loss of coherence of white matter fibres or axonal disorganisation reflected by higher ODI. However, the ODI association with the metabolic profile was not as consistent as the ICVF correlation, particularly with disease duration. Also, reduced ODI in the posterior limbs of the internal capsule, right posterior corona radiata and bilateral superior corona radiata shows an association with disease duration, indicating the loss of neuronal fibres or neurodegeneration may occur with longer disease duration. Finally, the increased interstitial fluids reflected by increased IsoVF in T2DM participants were associated with longer disease duration and higher HbA1c levels. However, this correlation has less consistency compared to ICVF. The correlation coefficient is weak, but there is still a statistical relationship, suggesting that the effect of glycaemic control on brain white matter is not major but does have an effect. For this reason, T2DM patients must aim for good glycaemic control to minimize the microstructural impact of T2DM on brain white matter. It is also worth noting that two models with and without age adjustment were tested. The results suggest that age may not affect the association between white matter alterations in T2DM participants and disease duration. In a previous study, the majority of T2DM patients over the age of fifty, indicating a correlation between cellular age and diabetes. T2DM was associated with an increase in biological age (a reflection of aging at the cellular level) compared to chronological age (defined by time since birth)[302], which may agree with our NODDI changes in T2DM white matter.

The findings of this study demonstrate that DTI still has a potential value as a clinical biomarker in T2DM. Also, it shows that the changes captured by NODDI parameters may contribute to FA alterations (especially in areas with complex mircostrcutre[303]) in the brain white matter of T2DM participants. However, NODDI may

suffer the constant diffusivity assumption when pathology changes diffusivity. The NODDI model relies on assumptions to speculate the microstructural alterations; nevertheless, the NODDI parameters with different neurological disorders must be interpreted carefully[149,304,305].

The results show that NODDI parameters could detect white matter neuropathological changes in white matter microstructure, suggesting its potential role for monitoring microstructural alterations in T2DM. This study has limitations. First, it is retrospective and based on a biobank rather than a prospective case-control study. Second, there could have been other non-excluded systemic conditions that could impact the DTI and NODDI metrics, such as previous chemotherapy, cardiac surgery, chronic diseases, and psychiatric disorders. Third, further work to improve this novel study is suggested as follows: the impact of T2DM on brain functions and neurocognition and their association with the altered NODDI parameters was not explored. Also, the study did not include a follow-up assessment to monitor the white matter changes longitudinally in T2DM participants. Fourth, T2DM duration was calculated by subtracting the earliest-diagnosis age from the assessment-centre-visit age. Furthermore, the diabetes duration in the UK Biobank datasets may not have been accurately completed, and T2DM may have existed before patients were formally diagnosed. Lastly, the microstructural impact of T2DM on the grey matter is not evaluated in this study.

7.5. Conclusion

White matter microstructural abnormalities occur in T2DM participants and are weakly associated with longer disease duration and higher glycated haemoglobin, reflecting poorer glycaemic control. As an advanced diffusion model, NODDI can characterise white matter neuroaxonal pathology in T2DM, giving quantitative-biophysical information for understanding the impact of T2DM on white matter microstructure.

Chapter 8

8. Discussion, Conclusion and Future Directions (Word count: 2485)

8.1. Summary of Major Findings

This PhD thesis aims to assess the use of DTI and NODDI in characterising in vivo white matter microstructural changes in T2DM using the UK Biobank datasets. Also, it aims to meta-analyse the ability of NODDI to characterise white matter microstructural changes in MS. The findings of this thesis demonstrate that DTI still has a potential value as a clinical biomarker and suggest that the tissue-specificity of NODDI provides an explanation of white matter microstructural damage in T2DM and MS. The white matter microstructural changes captured by NODDI parameters can contribute to DTI and statistically correlate with clinical and metabolic profiles.

Chapter 4 discussed my experiment to optimise the NODDI scanning protocol on the 3T MRI system at SPMIC-University of Nottingham. Also, it described the resultant diffusion values and their differences among four scanning protocols based on visual rating, ROI analysis, and an experienced neuroradiologist's decision.

Chapter 5 systematically reviewed previous DTI studies which investigated microstructural changes in the brain, demonstrating the ability of DTI in detecting microstructural changes and cognitive deficits in both types of diabetes. Moreover, it showed the relationship between the clinical profiles of patients (i.e., disease duration and HbA1c) and altered DTI metrics in various brain regions.

Chapter 6 summarised the current literature in this area and meta-analysed studies using NODDI metrics to assess brain microstructural changes and neuroaxonal pathology in white matter lesions and NAWM in patients with MS. The key finding of this meta-analysis of ROI data concerned that the NDI/ICVF was reduced in MS lesions and NAWM compared to healthy controls. This significant

reduction of the ICVF corresponds to a reduced intracellular signal fraction. It may reflect underlying damage or loss of neurites in white matter lesions and NAWM in patients with MS.

Chapter 7 discussed a large cohort study from the UK Biobank that characterised white matter microstructural pathology in T2DM using DTI and NODDI. In this study, the previous sample size and technical limitations indicated in my published systematic review were overcome (chapter 5). A large cohort of participants with and without T2DM was investigated, demonstrating that DTI was sensitive to white matter microstructural changes in T2DM participants. This study also demonstrated the feasibility of NODDI in detecting white matter microstructural changes in T2DM using the same large dataset from the UK Biobank. The DTI findings confirmed widespread microstructural alterations in the same cohort and broadly agreed with previous DTI studies. Also, NODDI parameters were able to detect white matter neuropathological changes, suggesting its potential role for monitoring microstructural alterations in T2DM.

8.2. Characterising microstructural changes in DM using DTI

In chapter 5, my systematic review demonstrates a correlation between DTI changes in brain tissue, metabolic profile, and cognitive impairment in T1DM patients. The observed decreased FA values in various brain structures may reflect a complex involvement of tissue properties, and may suggest white matter disruption, axonal damage, degeneration, or irregularity of axonal structure in patients with T1DM. These altered DTI measurements are correlated with reduced neurocognitive performance, indicating that brain microstructural abnormalities may underlie cognitive dysfunction[183]. Neurocognitive test scores in adolescent patients with T1DM are associated with lower FA at the midbrain and optic radiation, indicating worse memory and attention performance. Also, the reported visual memory impairment in adolescent

T1DM patients is consistent with other studies and meta-analyses[183,185,238]. In addition to cognition disability, the reduced diffusivity in the thalamus in adolescents with T1DM is associated with glycaemic exposure; this observation is consistent with other adults[236] and youth[237] studies. However, the lack of significant differences in FA between children with T1DM and controls may be attributable to children's young age and shorter disease duration. Also, children with T1DM who have lower AD values have axonal damage and decreased axonal coherence, which is consistent with the findings of another study[202]. The significant positive correlation between HbA1c and RD within the same group suggests that higher blood glucose levels may affect fibre myelination[233]. Lastly, the decreased AD and RD values in patients are likely attributable to the dominance of the age effect, which correlates significantly with white matter structures and disease duration.

The systematic review also reveals lower FA and higher AD, MD, and RD in the brain white matter of patients with T2DM, which reflect the underlying impact of T2DM on white matter integrity and agrees with my UK Biobank study in chapter 8. In addition, this systematic review demonstrates a link between T2DM brain microvascular changes and cognitive deficits (executive function, memory, attention, and information processing speed), supporting the hypothesis that neuroinflammation and microvascular pathology are involved in the cerebral complications/changes of diabetes, which DTI is more sensitive to than other conventional MRI techniques[239,240]. The systematic review results are consistent with a previous study that demonstrated a link between T2DM and abnormalities in the temporal lobe, specifically the hippocampus[241]. Changes in the prefrontal region/cortex are confirmed in T2DM patients and correlate with higher HbA1c levels[243]. These changes in the prefrontal white matter and cortex have a significant relationship with longer diabetes duration, which may underlie deficits in attention, memory, and executive function in T2DM patients.

In summary, microstructural alterations in T1DM and T2DM patients detected by DTI are associated with observed cognitive dysfunction, including impairments in information processing speed, memory, executive functions, and attention. These microstructural and cognitive deficits are primarily associated with uncontrolled glycemia in both types of diabetes. In terms of comorbidities, the presence of microangiopathy in T1DM patients significantly exacerbates microstructural abnormalities in the brain compared to other T1DM patients. Similarly, T2DM patients with additional comorbidities such as obesity, stroke, and hypertension exacerbate the severity of microstructural brain changes.

Based on the systematic review of previous DTI studies on T2DM patients in chapter 5, I have observed that a few studies yielded contradictory results; one study reported that T2DM patients had decreased FA only in the right uncinate fasciculus but increased MD in superior longitudinal fasciculi and uncinate fasciculi bilaterally[187]. On the other hand, a different study reported a decline in FA in the cingulum bundle and uncinate fasciculi but no change in MD, AD, or RD[231]. A further study showed that T2DM participants had significantly lower FA, increased MD, and RD in extensive white matter regions but no significant differences in AD between the two groups[212]. Using UK Biobank datasets in chapter 8, the result showed that DTI metrics, including FA, MD, AD, and RD, were significantly altered between the T2DM and non-T2DM groups. Reduced FA and increased MD in T2DM patients are consistent with the previous findings[8,193,283,306], reflecting the underlying impact of T2DM on white matter integrity. Also, the results revealed that the increase of AD and RD in participants with T2DM might result in changes in FA and MD, suggesting that both increased interstitial space between the myelin-covered axons and decreased myelin integrity[221,223,295,296].

Interestingly, this study showed that T2DM and Alzheimer's disease might share similar pathogeneses, including insulin deficiency, glucose-mediated toxicity, and amyloid peptide accumulation, based on the discovery of similar white matter

changes in Alzheimer's disease patients[307,308]. Consistent with the previous findings[222,223], the white matter changes indicated by MD, AD, and RD alterations in participants with T2DM were correlated with longer disease duration. In addition, some previous studies failed to find an association between the duration of the disease and FA[193]. However, in my UK Biobank study, decreased FA was associated with longer disease duration, which is consistent with a previous study[226].

8.3. Characterising microstructural changes in T2DM and MS using NODDI

The UK Biobank study in chapter 7 showed a reduction of ICVF in T2DM white matter consistent with a previous study[229], indicating reduced neurite density. This reduction of neurite density is most likely related to structural changes like axonal loss, axonal damage, or axonal demyelination/degeneration[140,268]. In addition, decreased neurite density in T2DM participants may be accompanied by axonal disorganisation, myelin loss, and loss of fibre orientation coherence (or an increase in fibre dispersion), which may lead to increased ODI in response to white matter changes[13,193,297,298]. An increase of IsoVF may indicate vasogenic oedema or increased extracellular free water, which may be caused by the breakdown of BBB due to T2DM as indicated in a previous study[141], or it may indicate a degree of atrophy by reflecting cell shrinkage and decreased tissue volume fraction[301]. I identified that reduced ICVF, increased ODI and IsoVF in the white matter of T2DM participants has a consistent association with disease duration and poorly-controlled blood glucose, suggesting that T2DM participants with longer disease duration and higher plasma glucose tend to have reduced neurite density, loss of fibre orientation in white matter, and increased interstitial fluids. The weak correlation between disease duration/HbA1c and reduced ICVF agrees with a previous study[229].

As I was unable to obtain NODDI data from the UK Biobank to investigate its use on MS patients, I was able to meta-analyse previous NODDI studies on MS (chapter 6). The most important findings of this meta-analysis are that the ICVF was lower in MS lesions and NAWM than in healthy controls. This significant decrease in ICVF corresponds to a decrease in intracellular signal fraction or neurite density, which may indicate underlying damage or neurite loss. Previous research has shown that this decrease is accompanied by an increase in MD and a decrease in FA[10]. Also, this meta-analysis demonstrates a significant decrease in ICVF in the NAWM of MS patients compared to the white matter of controls, indicating early axonal pathology outside demyelination in white matter lesions[274–277]. This consistent decrease across studies demonstrates that the ICVF (due to its sensitivity to the intra-axonal compartment) can quantify and differentiate microstructural changes in white matter lesions, NAWM of MS, and healthy white matter. This suggests a decrease in axonal density in white matter lesions and NAWM lesions in MS compared to healthy controls, which is consistent with previous DTI studies[257,278], reporting altered water diffusion in NAWM and white matter MS lesions compared to healthy controls. Interestingly, the decrease in ICVF in white matter lesions and NAWM is consistent with previous pathological studies demonstrating axonal loss in white matter lesions and, to a lesser extent in NAWM[264,277,279]. Few studies found that ODI was lower in white matter lesions than in healthy white matter, indicating that neurites have less orientation variability or that neuronal fibre loss is more severe in lesions[10,155,266]. In contrast, other studies found higher ODI within white matter lesions and NAWM than healthy white matter, which may indicate a loss of fibre coherence and relatively preserved neuronal fibre density[10,155,266,270]. The meta-analysis results contradict these reported findings, revealing no differences in neurite orientation dispersion in MS patients.

It is worth comparing the NODDI metrics changes in T2DM and MS. Based on the results of this thesis; they were affected in both diseases. ICVF was reduced in

both T2DM and MS patients, but a greater degree of reduction was seen in MS focal lesions compared to NAWM in MS and T2DM patients. ODI showed no difference in the meta-analysis; however, previous studies yielded different results. A few studies reported higher ODI in both MS lesions and NAWM, while other studies reported reduced ODI. However, ODI was consistently higher in the white matter of T2DM patients compared to healthy white matter. Although T2DM and MS are two different neurological disorders, changes in NODDI metrics have shown how they may have similar effects on brain white matter.

8.4. Thesis Limitations

8.4.1. Experimental Design

The research studies included in this thesis are retrospective and based on a biobank rather than a prospective case-control design. Also, there could have been other non-excluded systemic conditions that could impact the NODDI metrics, such as previous chemotherapy, cardiac surgery, chronic diseases, and psychiatric disorders. Due to the lack of access to the MS cohort, I evaluated the use of NODDI in detecting white matter microstructural changes in MS through my meta-analysis of previous studies. Also, I had no time to extract neurocognitive data available in the UK Biobank database; therefore, I was unable to include the association between diffusion-altered metrics in white matter tracts and multiple cognitive domains (including attention, concentration, executive functions, memory, language, visuospatial skills, abstraction, calculation, and orientation) in the experimental research design. However, I am going to add a neurocognitive analysis to the UK Biobank study before sending it for publication. Lastly, research studies in this thesis did not include a follow-up assessment to monitor white matter changes in T2DM and MS participants longitudinally.

8.4.2. NODDI Model Assumption

The NODDI model is based on several assumptions to simplify the model and make it clinically viable. However, this may result in some limitations. First, NODDI may suffer the constant diffusivity assumption. When pathology changes diffusivity, this may speculate the microstructural alterations. For this reason, the NODDI parameters with different neurological disorders must be interpreted carefully. Second, the T2 relaxation effect modulates the diffusion MRI signal is not modelled in NODDI. Therefore, any alteration in the T2 relaxation times of the tissue compartments may affect the NODDI parameters[309]. Third, NODDI assumes a fixed parallel diffusivity for intra-axonal and extra-axonal compartments. If this parameter increases within a white matter lesion, the estimated NODDI parameters will be biased. Fourth, the NODDI model assumption of quick exchange in the extracellular compartment across all orientations is debatable. Finally, NODDI utilises a single Watson distribution, which may fail in regions where fibres cross. Despite this, it has been demonstrated that the ODI decreases in white matter areas with crossing fibres when one of the crossing fibres degenerates[126].

8.5. Future Directions

This thesis highlights interesting new opportunities and research challenges that may further improve this work. First, the impact of T2DM and MS on brain functions and their association with the altered NODDI parameters was not explored. Assessing neurocognitive functions (either using fMRI or neurocognitive testes) and their relationship with altered NODDI parameters in white matter microstructure may allow a better understanding the impact of both diseases on neurocognition. Second, future longitudinal investigations are important to consider and could provide a deep understanding of white matter neuropathologic progression and treatments. Lastly,

investigating the NODDI feasibility in MS using the UK Biobank cohort is essential as it may reveal more interesting findings that lower-powered studies could have missed.

8.6. Conclusion

- The findings of this thesis showed that DM and MS are associated with white matter microstructural alterations that can be detected by advanced diffusion imaging techniques such as DTI and NODDI. T2DM generally affects NAWM, while MS affects NAWM and shows a higher degree of neuroaxonal damage in white matter focal lesions.
- There was a weak but statistically significant correlation between altered diffusion measures in white matter in T2DM participants and disease duration/HbA1c.
- The results indicated the potential role of using NODDI in characterising white matter neuroaxonal pathology in T2DM and MS, providing quantitative biophysical information (contributing to conventional DTI) for understanding the impact of T2DM and MS on brain white matter microstructure, which may lead to better monitoring of disease progression.

Bibliography

1 Lassmann H. Multiple Sclerosis Pathology. *Cold Spring Harb Perspect Med* 2018; **8**. DOI:10.1101/CSHPERSPECT.A028936.

2 Verdile G, Fuller SJ, Martins RN. The role of type 2 diabetes in neurodegeneration. *Neurobiol Dis* 2015; **84**: 22–38.

3 Lassmann H. Multiple sclerosis pathology. Cold Spring Harb. Perspect. Med. 2018. DOI:10.1101/cshperspect.a028936.

4 Andravizou A, Dardiotis E, Artemiadis A, *et al.* Brain atrophy in multiple sclerosis: mechanisms, clinical relevance and treatment options. *Autoimmun Highlights 2019 101* 2019; **10**: 1–25.

5 Moran C, Phan TG, Chen J, *et al.* Brain atrophy in type 2 diabetes: Regional distribution and influence on cognition. *Diabetes Care* 2013; **36**: 4036–42.

6 Anderson VM, Fox NC, Miller DH. Magnetic resonance imaging measures of brain atrophy in multiple sclerosis. *J Magn Reson Imaging* 2006; **23**: 605–18.

7 Bao J, Tu H, Li Y, *et al.* Diffusion Tensor Imaging Revealed Microstructural Changes in Normal-Appearing White Matter Regions in Relapsing-Remitting Multiple Sclerosis. *Front Neurosci* 2022; **16**. DOI:10.3389/FNINS.2022.837452.

8 Alotaibi A, Tench C, Stevenson R, *et al.* brain sciences Review Investigating Brain Microstructural Alterations in Type 1 and Type 2 Diabetes Using Diffusion Tensor Imaging: A Systematic Review. 2021. DOI:10.3390/brainsci11020140.

9 Brownlee W, Alves Da Mota P, Prados F, *et al.* Neurite Orientation Dispersion and Density Imaging (NODDI) Is Sensitive to Microstructural Damage Related to Disability in Relapse-Onset MS (S41.003). *Neurology* 2016.

10 Hagiwara A, Kamagata K, Shimoji K, *et al.* White matter abnormalities in multiple sclerosis evaluated by quantitative synthetic MRI, diffusion tensor imaging, and neurite orientation dispersion and density imaging. *Am J Neuroradiol* 2019; **40**: 1642–8.

11 Collorone S, Cawley N, Grussu F, *et al.* Reduced neurite density in the brain and cervical spinal cord in relapsing–remitting multiple sclerosis: A NODDI study. *Mult Scler J* 2020. DOI:10.1177/1352458519885107.

12 Alotaibi A, Podlasek A, Altokhis A, Aldhebaib A, Dineen RA, Constantinescu CS. Investigating Microstructural Changes in White Matter in Multiple Sclerosis: A Systematic Review and Meta-Analysis of Neurite Orientation Dispersion and Density Imaging. *Brain Sci* 2021; **11**. DOI:10.3390/BRAINSCI11091151.

13 Grussu F, Schneider T, Tur C, *et al.* Neurite dispersion: a new marker of multiple sclerosis spinal cord pathology? 2017; **4**: 663–79.

14 Enzinger C, Barkhof F, Ciccarelli O, *et al.* Nonconventional MRI and microstructural cerebral changes in multiple sclerosis. *Nat Rev Neurol 2015 1112* 2015; **11**: 676–86.

15 Alexander AL, Hasan KM, Lazar M, Tsuruda JS, Parker DL. Analysis of partial volume effects in diffusion-tensor MRI. *Magn Reson Med* 2001; **45**: 770–80.

16 ALEXANDER DC. Multiple-Fiber Reconstruction Algorithms for Diffusion MRI. *Ann N Y Acad Sci* 2005; **1064**: 113–33.

17 Zhang H, Schneider T, Wheeler-Kingshott CA, Alexander DC. NODDI: Practical in vivo neurite orientation dispersion and density imaging of the human brain. *Neuroimage* 2012; **61**: 1000–16.

18 Kamiya K, Hori M, Aoki S. NODDI in clinical research. J. Neurosci. Methods. 2020. DOI:10.1016/j.jneumeth.2020.108908.

19 Schmahmann JD, Caplan D. Cognition, emotion and the cerebellum. *Brain* 2006; **129**: 290–2.

20 Brain anatomy, Anatomy of the human brain | Mayfield Brain & Spine Cincinnati, Ohio. https://mayfieldclinic.com/pe-anatbrain.htm (accessed Aug 11, 2022).

21 Wang SSH, Shultz JR, Burish MJ, *et al.* Functional Trade-Offs in White Matter Axonal Scaling. *J Neurosci* 2008; **28**: 4047–56.

22 Fields RD. Change in the Brain's White Matter: The role of the brain's white matter in active learning and memory may be underestimated. *Science* 2010; **330**: 768.

23 The Human Cortical White Matter: Quantitative Aspects of Cortico-Cortical Long-Range Connectivity. 2002; : 389–98.

24 Perge JA, Niven JE, Mugnaini E, Balasubramanian V, Sterling P. Why do axons differ in caliber? *J Neurosci* 2012; **32**: 626–38.

25 Axons: the cable transmission of neurons - Queensland Brain Institute - University of Queensland. https://qbi.uq.edu.au/brain/brain-anatomy/axons-cable-transmission-neurons (accessed April 16, 2022).

26 Araque A, Navarrete M. Glial cells in neuronal network function. *Philos Trans R Soc B Biol Sci*

2010; **365**: 2375.
27 Types of glia - Queensland Brain Institute - University of Queensland. https://qbi.uq.edu.au/brain-basics/brain/brain-physiology/types-glia (accessed April 16, 2022).
28 Waxman SG, Bennett MVI. Relative conduction velocities of small myelinated and non-myelinated fibres in the central nervous system. *Nat New Biol* 1972; **238**: 217–9.
29 Smith RS, Koles ZJ. Myelinated nerve fibers: computed effect of myelin thickness on conduction velocity. *Am J Physiol* 1970; **219**: 1256–8.
30 Breij ECW, Brink BP, Veerhuis R, *et al.* Homogeneity of active demyelinating lesions in established multiple sclerosis. *Ann Neurol* 2008; **63**: 16–25.
31 Nicholson C, Hrabětová S. Brain Extracellular Space: The Final Frontier of Neuroscience. *Biophys J* 2017; **113**: 2133–42.
32 Shepherd VA. The cytomatrix as a cooperative system of macromolecular and water networks. *Curr Top Dev Biol* 2006; **75**: 171–223.
33 Barbara B. Aquaporin Biology and Nervous System. *Curr Neuropharmacol* 2010; **8**: 97.
34 Chandra A, Li WA, Stone CR, Geng X, Ding Y. The cerebral circulation and cerebrovascular disease I: Anatomy. *Brain Circ* 2017; **3**: 45.
35 Weber B, Keller AL, Reichold J, Logothetis NK. The microvascular system of the striate and extrastriate visual cortex of the macaque. *Cereb Cortex* 2008; **18**: 2318–30.
36 Le Bihan D, Breton E, Lallemand D, Aubin ML, Vignaud J, Laval-Jeantet M. Separation of diffusion and perfusion in intravoxel incoherent motion MR imaging. *Radiology* 1988; **168**: 497–505.
37 White Matter Anatomy | Radiology Key. https://radiologykey.com/white-matter-anatomy-2/ (accessed Aug 2, 2022).
38 Wycoco V, Shroff M, Sudhakar S, Lee W. White matter anatomy: what the radiologist needs to know. *Neuroimaging Clin N Am* 2013; **23**: 197–216.
39 Zaccardi F, Webb DR, Yates T, Davies MJ. Pathophysiology of type 1 and type 2 diabetes mellitus: a 90-year perspective. *Postgrad Med J* 2016; **92**: 63–9.
40 Goldman M. Formal Theory of Spin–Lattice Relaxation. *J Magn Reson* 2001; **149**: 160–87.
41 Ozougwu O. The pathogenesis and pathophysiology of type 1 and type 2 diabetes mellitus. *J Physiol Pathophysiol* 2013. DOI:10.5897/jpap2013.0001.
42 Ferri FF. Ferri's Clinical Advisor 2015 E-Book: 5 Books in 1. 2014.
43 Classification and diagnosis of diabetes. *Diabetes Care* 2017; **40**: S11–24.
44 Khan MAB, Hashim MJ, King JK, Govender RD, Mustafa H, Kaabi J Al. Epidemiology of Type 2 diabetes - Global burden of disease and forecasted trends. *J Epidemiol Glob Health* 2020; **10**: 107–11.
45 Zhou B, Lu Y, Hajifathalian K, *et al.* Worldwide trends in diabetes since 1980: A pooled analysis of 751 population-based studies with 4.4 million participants. *Lancet* 2016. DOI:10.1016/S0140-6736(16)00618-8.
46 Chatterjee S, Khunti K, Davies MJ. Type 2 diabetes. Lancet. 2017. DOI:10.1016/S0140-6736(17)30058-2.
47 Li W, Abdul Y, Ward R, Ergul A. Endothelin and diabetic complications: A brain-centric view. Physiol. Res. 2018. DOI:10.33549/physiolres.933833.
48 Goldenberg MM. Multiple sclerosis review. *P T* 2012; **37**: 175–84.
49 Howard J, Trevick S, Younger DS. Epidemiology of Multiple Sclerosis. Neurol. Clin. 2016. DOI:10.1016/j.ncl.2016.06.016.
50 Lublin FD, Reingold SC. Defining the clinical course of multiple sclerosis: results of an international survey. National Multiple Sclerosis Society (USA) Advisory Committee on Clinical Trials of New Agents in Multiple Sclerosis. *Neurology* 1996; **46**: 907–11.
51 Lublin FD, Reingold SC, Cohen JA, *et al.* Defining the clinical course of multiple sclerosis: The 2013 revisions. Neurology. 2014. DOI:10.1212/WNL.0000000000000560.
52 Viglietta V, Baecher-Allan C, Weiner HL, Hafler DA. Loss of functional suppression by CD4+CD25+ regulatory T cells in patients with multiple sclerosis. *J Exp Med* 2004; **199**: 971–9.
53 Shi Y, Feng Y, Kang J, *et al.* Critical regulation of CD4+ T cell survival and autoimmunity by beta-arrestin 1. *Nat Immunol* 2007; **8**: 817–24.
54 Kutzelnigg A, Lucchinetti CF, Stadelmann C, *et al.* Cortical demyelination and diffuse white matter injury in multiple sclerosis. *Brain* 2005; **128**: 2705–12.
55 Lassmann H, Van Horssen J, Mahad D. Progressive multiple sclerosis: pathology and pathogenesis. *Nat Rev Neurol* 2012; **8**: 647–56.
56 Cannistraro RJ, Badi M, Eidelman BH, Dickson DW, Middlebrooks EH, Meschia JF. CNS small vessel disease. *Neurology* 2019; **92**: 1146–56.
57 Umemura T, Kawamura T, Hotta N. Pathogenesis and neuroimaging of cerebral large and small vessel disease in type 2 diabetes: A possible link between cerebral and retinal

microvascular abnormalities. *J Diabetes Investig* 2017; **8**: 134–48.
58 Domingueti CP, Dusse LMSA, Carvalho MDG, De Sousa LP, Gomes KB, Fernandes AP. Diabetes mellitus: The linkage between oxidative stress, inflammation, hypercoagulability and vascular complications. *J Diabetes Complications* 2016; **30**: 738–45.
59 Sun J, Xu B, Zhang X, *et al.* The Mechanisms of Type 2 Diabetes-Related White Matter Intensities: A Review. *Front Public Heal* 2020; **8**: 498056.
60 Lassmann H, Brück W, Lucchinetti CF. The immunopathology of multiple sclerosis: an overview. *Brain Pathol* 2007; **17**: 210–8.
61 Pérez-Cerdá F, Sánchez-Gómez MV, Matute C. The link of inflammation and neurodegeneration in progressive multiple sclerosis. *Mult Scler Demyelinating Disord 2016 11* 2016; **1**: 1–8.
62 Brück W. Inflammatory demyelination is not central to the pathogenesis of multiple sclerosis. *J Neurol* 2005; **252 Suppl 5**. DOI:10.1007/S00415-005-5003-6.
63 Bö L, Mörk S, Kong PA, Nyland H, Pardo CA, Trapp BD. Detection of MHC class II-antigens on macrophages and microglia, but not on astrocytes and endothelia in active multiple sclerosis lesions. *J Neuroimmunol* 1994; **51**: 135–46.
64 Ruce B, Rapp DT, Ohn J, *et al.* Axonal transection in the lesions of multiple sclerosis. *N Engl J Med* 1998; **338**: 278–85.
65 Prins M, Schul E, Geurts J, van der Valk P, Drukarch B, van Dam AM. Pathological differences between white and grey matter multiple sclerosis lesions. *Ann N Y Acad Sci* 2015; **1351**: 99–113.
66 Le Bihan D, Johansen-Berg H. Diffusion MRI at 25: exploring brain tissue structure and function. *Neuroimage* 2012; **61**: 324–41.
67 Van Geuns RJM, Wielopolski PA, De Bruin HG, *et al.* Basic principles of magnetic resonance imaging. *Prog Cardiovasc Dis* 1999; **42**: 149–56.
68 Zhang J. Applications of NODDI for imaging in vivo white matter pathology in neurodegenerative diseases. *Dr thesis, UCL (University Coll London)* 2019.
69 Le Bihan D. Diffusion MRI: what water tells us about the brain. *EMBO Mol Med* 2014; **6**: 569.
70 Rabi II, Zacharias JR, Millman S, Kusch P. A New Method of Measuring Nuclear Magnetic Moment. *Phys Rev* 1938; **53**: 318.
71 Purcell EM, Torrey HC, Pound R V. Resonance absorption by nuclear magnetic moments in a solid [7]. *Phys Rev* 1946; **69**: 37–8.
72 Image formation by induced local interactions. Examples employing nuclear magnetic resonance. 1973 - PubMed. https://pubmed.ncbi.nlm.nih.gov/2663289/ (accessed Jan 24, 2022).
73 Advanced perfusion quantification methods for dynamic PET and MRI data modelling. https://iris.uniroma1.it/handle/11573/1241979 (accessed Aug 3, 2022).
74 Wang J, Mao W, Qiu M, Smith MB, Constable RT. Factors influencing flip angle mapping in MRI: RF pulse shape, slice-select gradients, off-resonance excitation, and B0 inhomogeneities. *Magn Reson Med* 2006; **56**: 463–8.
75 Mlynárik V. Introduction to nuclear magnetic resonance. *Anal Biochem* 2017; **529**: 4–9.
76 MRI in Practice - Catherine Westbrook, John Talbot - Google Books. https://books.google.co.uk/books?hl=en&lr=&id=HrBlDwAAQBAJ&oi=fnd&pg=PA89&dq=+MRI+in+Practice&ots=-SQJxGArDS&sig=M2OoAti-BULHc13t1vWaGgKLVxw&redir_esc=y#v=onepage&q=MRI in Practice&f=false (accessed Jan 26, 2022).
77 BERNSTEIN MA, KING KF, ZHOU XJ. INTRODUCTION TO PULSE SEQUENCES. *Handb MRI Pulse Seq* 2004; : 573–7.
78 Hahn EL. Spin Echoes. *Phys Rev* 1950; **80**: 580.
79 Carr HY, Purcell EM. Effects of Diffusion on Free Precession in Nuclear Magnetic Resonance Experiments. *Phys Rev* 1954; **94**: 630.
80 Stejskal EO, Tanner JE. Spin Diffusion Measurements: Spin Echoes in the Presence of a Time Dependent Field Gradient. *Cit J Chem Phys* 1965; **42**: 288.
81 Sinnaeve D. The Stejskal-Tanner equation generalized for any gradient shape-An overview of most pulse sequences measuring free diffusion. *Concepts Magn Reson Part A Bridg Educ Res* 2012; **40 A**: 39–65.
82 Moratal D, Vallés-Luch A, Martí-Bonmati L, Brummers ME. k-Space tutorial: an MRI educational tool for a better understanding of k-space. *Biomed Imaging Interv J* 2008; **4**. DOI:10.2349/BIIJ.4.1.E15.
83 Bracewell RN. The Fourier transform. *Sci Am* 1989; **260**. DOI:10.1038/SCIENTIFICAMERICAN0689-86.
84 Mezrich R. A perspective on K-space. *Radiology* 1995; **195**: 297–315.
85 k-space: data - Questions and Answers in MRI. https://mriquestions.com/data-for-k-space.html

(accessed Aug 3, 2022).
86 Loecher M, Wieben O. k-Space. *Basic Princ Cardiovasc MRI Phys Imaging Tech* 2015; : 13–23.
87 Stehling MK, Turner R, Mansfield P. Echo-planar imaging: magnetic resonance imaging in a fraction of a second. *Science* 1991; **254**: 43–50.
88 Mansfield P, Pykett IL. Biological and medical imaging by NMR. 1978. *J Magn Reson* 2011; **213**: 513–31.
89 Poustchi-Amin M, Mirowitz SA, Brown JJ, McKinstry RC, Li T. Principles and applications of echo-planar imaging: a review for the general radiologist. *Radiographics* 2001; **21**: 767–79.
90 Hahn EL. Spin Echoes. *Phys Today* 2009; **3**: 21.
91 Chabert S, Scifo P. Diffusion signal in magnetic resonance imaging: Origin and interpretation in neurosciences. *Biol Res* 2007; **40**: 385–400.
92 Alexander DC, Dyrby TB, Nilsson M, Zhang H, Daniel Alexander CC. Imaging brain microstructure with diffusion MRI: practicality and applications. John Wiley & Sons Inc., 2019.
93 Nilsson M, Van Westen D, Ståhlberg F, Sundgren PC, Lätt J. The role of tissue microstructure and water exchange in biophysical modelling of diffusion in white matter. *MAGMA* 2013; **26**: 345–70.
94 Stanisz GJ, Szafer A, Wright GA, Henkelman RM. An analytical model of restricted diffusion in bovine optic nerve. *Magn Reson Med* 1997; **37**: 103–11.
95 Panagiotaki E, Schneider T, Siow B, Hall MG, Lythgoe MF, Alexander DC. Compartment models of the diffusion MR signal in brain white matter: a taxonomy and comparison. *Neuroimage* 2012; **59**: 2241–54.
96 Özarslan E, Koay CG, Shepherd TM, *et al.* Mean apparent propagator (MAP) MRI: a novel diffusion imaging method for mapping tissue microstructure. *Neuroimage* 2013; **78**: 16–32.
97 Ozarslan E, Koay C, Basser P. Simple harmonic oscillator based estimation and reconstruction for one-dimensional q-space MR. 2007.
98 Kiselev VG. The Cumulant Expansion: An Overarching Mathematical Framework For Understanding Diffusion NMR. *Diffus MRI* 2013; : 152–68.
99 Yablonskiy DA, Sukstanskii AL. Theoretical models of the diffusion weighted MR signal. *NMR Biomed* 2010; **23**: 661–81.
100 Assemlal HE, Tschumperlé D, Brun L. Efficient and robust computation of PDF features from diffusion MR signal. *Med Image Anal* 2009; **13**: 715–29.
101 Descoteaux M, Angelino E, Fitzgibbons S, Deriche R. Regularized, fast, and robust analytical Q-ball imaging. *Magn Reson Med* 2007; **58**: 497–510.
102 Jensen JH, Helpern JA, Ramani A, Lu H, Kaczynski K. Diffusional kurtosis imaging: the quantification of non-gaussian water diffusion by means of magnetic resonance imaging. *Magn Reson Med* 2005; **53**: 1432–40.
103 Tuch DS. Q-ball imaging. *Magn Reson Med* 2004; **52**: 1358–72.
104 Liu C, Bammer R, Acar B, Moseley ME. Characterizing non-Gaussian diffusion by using generalized diffusion tensors. *Magn Reson Med* 2004; **51**: 924–37.
105 Ferizi U, Scherrer B, Schneider T, *et al.* Diffusion MRI microstructure models with in vivo human brain Connectome data: results from a multi-group comparison Christian Pötter 12 Robert F. Dougherty 12 Ken Sakaie 13. 2017. DOI:10.1002/nbm.3734.
106 Le Bihan D, Breton E, Lallemand D, Grenier P, Cabanis E, Laval-Jeantet M. MR imaging of intravoxel incoherent motions: application to diffusion and perfusion in neurologic disorders. *Radiology* 1986; **161**: 401–7.
107 Bihan D Le. Apparent diffusion coefficient and beyond: what diffusion MR imaging can tell us about tissue structure. *Radiology* 2013; **268**: 318–22.
108 Basser PJ, Mattiello J, Lebihan D. Estimation of the Effective Self-Diffusion Tensor from the NMR Spin Echo. *J Magn Reson Ser B* 1994. DOI:10.1006/jmrb.1994.1037.
109 Basser PJ, Mattiello J, LeBihan D. MR diffusion tensor spectroscopy and imaging. *Biophys J* 1994; **66**: 259–67.
110 Le Bihan D, Mangin JF, Poupon C, *et al.* Diffusion tensor imaging: Concepts and applications. *J Magn Reson Imaging* 2001; **13**: 534–46.
111 Chua TC, Wen W, Slavin MJ, Sachdev PS. Diffusion tensor imaging in mild cognitive impairment and Alzheimer's disease: a review. *Curr Opin Neurol* 2008; **21**: 83–92.
112 Atkinson-Clement C, Pinto S, Eusebio A, Coulon O. Diffusion tensor imaging in Parkinson's disease: Review and meta-analysis. *NeuroImage Clin* 2017; **16**: 98–110.
113 Potgieser ARE, Wagemakers M, Van Hulzen ALJ, De Jong BM, Hoving EW, Groen RJM. The role of diffusion tensor imaging in brain tumor surgery: a review of the literature. *Clin Neurol Neurosurg* 2014; **124**: 51–8.
114 Asken BM, DeKosky ST, Clugston JR, Jaffee MS, Bauer RM. Diffusion tensor imaging (DTI) findings in adult civilian, military, and sport-related mild traumatic brain injury (mTBI): a

systematic critical review. *Brain Imaging Behav* 2018; **12**: 585–612.
115 Jones DK, Knösche TR, Turner R. White matter integrity, fiber count, and other fallacies: the do's and don'ts of diffusion MRI. *Neuroimage* 2013; **73**: 239–54.
116 Winklewski PJ, Sabisz A, Naumczyk P, Jodzio K, Szurowska E, Szarmach A. Understanding the Physiopathology Behind Axial and Radial Diffusivity Changes-What Do We Know? *Front Neurol* 2018; **9**. DOI:10.3389/FNEUR.2018.00092.
117 Wheeler-Kingshott CAM, Cercignani M. About 'axial' and 'radial' diffusivities. *Magn Reson Med* 2009; **61**: 1255–60.
118 Berlot R, Metzler-Baddeley C, Jones DK, O'Sullivan MJ. CSF contamination contributes to apparent microstructural alterations in mild cognitive impairment. 2014; **92**. DOI:10.1016/J.NEUROIMAGE.2014.01.031.
119 Jensen JH, Helpern JA. MRI quantification of non-Gaussian water diffusion by kurtosis analysis. *NMR Biomed* 2010; **23**: 698–710.
120 Gong NJ, Wong CS, Chan CC, Leung LM, Chu YC. Aging in deep gray matter and white matter revealed by diffusional kurtosis imaging. *Neurobiol Aging* 2014; **35**: 2203–16.
121 Lee CY, Tabesh A, Spampinato M V., Helpern JA, Jensen JH, Bonilha L. Diffusional kurtosis imaging reveals a distinctive pattern of microstructural alternations in idiopathic generalized epilepsy. *Acta Neurol Scand* 2014; **130**: 148–55.
122 Raab P, Hattingen E, Franz K, Zanella FE, Lanfermann H. Cerebral gliomas: diffusional kurtosis imaging analysis of microstructural differences. *Radiology* 2010; **254**: 876–81.
123 Assaf Y, Basser PJ. Composite hindered and restricted model of diffusion (CHARMED) MR imaging of the human brain. *Neuroimage* 2005; **27**: 48–58.
124 Barazany D, Basser PJ, Assaf Y. In vivo measurement of axon diameter distribution in the corpus callosum of rat brain. *Brain* 2009; **132**: 1210–20.
125 Alexander DC, Hubbard PL, Hall MG, *et al.* Orientationally invariant indices of axon diameter and density from diffusion MRI. *Neuroimage* 2010; **52**: 1374–89.
126 Tariq M, Schneider T, Alexander DC, Gandini Wheeler-Kingshott CA, Zhang H. Bingham-NODDI: Mapping anisotropic orientation dispersion of neurites using diffusion MRI. *Neuroimage* 2016; **133**: 207–23.
127 Kaden E, Kelm ND, Carson RP, Does MD, Alexander DC. Multi-compartment microscopic diffusion imaging. *Neuroimage* 2016; **139**: 346–59.
128 KÄRGER J, Pfeifer H, Heink W. Principles and Application of Self-Diffusion Measurements by Nuclear Magnetic Resonance. *Adv Magn Opt Reson* 1988; **12**: 1–89.
129 Lasič S, Nilsson M, Lätt J, Ståhlberg F, Topgaard D. Apparent exchange rate mapping with diffusion MRI. *Magn Reson Med* 2011; **66**: 356–65.
130 Nedjati-Gilani GL, Schneider T, Hall MG, *et al.* Machine learning based compartment models with permeability for white matter microstructure imaging. *Neuroimage* 2017; **150**: 119–35.
131 Tournier JD, Mori S, Leemans A. Diffusion tensor imaging and beyond. Magn. Reson. Med. 2011; **65**: 1532–56.
132 Tromp D. The diffusion tensor, and its relation to FA, MD, AD and RD. *The Winnower* 2016; published online Feb 29. DOI:10.15200/WINN.146119.94804.
133 Brain connectivity mapping with diffusion MRI across individuals and species - Nottingham ePrints. http://eprints.nottingham.ac.uk/65487/ (accessed March 15, 2022).
134 Goveas J, O'Dwyer L, Mascalchi M, *et al.* Diffusion-MRI in neurodegenerative disorders. Magn. Reson. Imaging. 2015. DOI:10.1016/j.mri.2015.04.006.
135 Andica C, Kamagata K, Hatano T, *et al.* Neurite orientation dispersion and density imaging of the nigrostriatal pathway in Parkinson's disease: Retrograde degeneration observed by tract-profile analysis. *Park Relat Disord* 2018. DOI:10.1016/j.parkreldis.2018.02.046.
136 Pasternak O, Kelly S, Sydnor VJ, Shenton ME. Advances in microstructural diffusion neuroimaging for psychiatric disorders. Neuroimage. 2018. DOI:10.1016/j.neuroimage.2018.04.051.
137 Jelescu IO, Budde MD. Design and validation of diffusion MRI models of white matter. Front. Phys. 2017; **5**: 61.
138 Novikov DS, Veraart J, Jelescu IO, Fieremans E. Rotationally-invariant mapping of scalar and orientational metrics of neuronal microstructure with diffusion MRI. *Neuroimage* 2018; **174**: 518–38.
139 Kroenke CD, Ackerman JJH, Yablonskiy DA. On the nature of the NAA diffusion attenuated MR signal in the central nervous system. *Magn Reson Med* 2004; **52**: 1052–9.
140 Slattery CF, Zhang J, Paterson RW, *et al.* ApoE influences regional white-matter axonal density loss in Alzheimer's disease. *Neurobiol Aging* 2017; **57**: 8–17.
141 Caverzasi E, Papinutto N, Castellano A, *et al.* Neurite Orientation Dispersion and Density Imaging Color Maps to Characterize Brain Diffusion in Neurologic Disorders. *J Neuroimaging* 2016. DOI:10.1111/jon.12359.

142 Behrens TEJ, Woolrich MW, Jenkinson M, *et al.* Characterization and propagation of uncertainty in diffusion-weighted MR imaging. *Magn Reson Med* 2003; **50**: 1077–88.
143 Lampinen B, Szczepankiewicz F, Mårtensson J, *et al.* Towards unconstrained compartment modeling in white matter using diffusion-relaxation MRI with tensor-valued diffusion encoding. *Magn Reson Med* 2020. DOI:10.1002/mrm.28216.
144 Veraart J, Novikov DS, Fieremans E. TE dependent Diffusion Imaging (TEdDI) distinguishes between compartmental T2 relaxation times. *Neuroimage* 2018. DOI:10.1016/j.neuroimage.2017.09.030.
145 McKinnon ET, Helpern JA, Jensen JH. Modeling white matter microstructure with fiber ball imaging. *Neuroimage* 2018. DOI:10.1016/j.neuroimage.2018.04.025.
146 Huber E, Henriques RN, Owen JP, Rokem A, Yeatman JD. Applying microstructural models to understand the role of white matter in cognitive development. *Dev Cogn Neurosci* 2019. DOI:10.1016/j.dcn.2019.100624.
147 Jelescu IO, Veraart J, Adisetiyo V, Milla SS, Novikov DS, Fieremans E. One diffusion acquisition and different white matter models: How does microstructure change in human early development based on WMTI and NODDI? *Neuroimage* 2015. DOI:10.1016/j.neuroimage.2014.12.009.
148 Kamiya K, Hori M, Irie R, *et al.* Diffusion imaging of reversible and irreversible microstructural changes within the corticospinal tract in idiopathic normal pressure hydrocephalus. *NeuroImage Clin* 2017. DOI:10.1016/j.nicl.2017.03.003.
149 Lampinen B, Szczepankiewicz F, Mårtensson J, van Westen D, Sundgren PC, Nilsson M. Neurite density imaging versus imaging of microscopic anisotropy in diffusion MRI: A model comparison using spherical tensor encoding. *Neuroimage* 2017; **147**: 517–31.
150 Veraart J, Nunes D, Rudrapatna U, *et al.* Noninvasive quantification of axon radii using diffusion MRI. *Elife* 2020. DOI:10.7554/eLife.49855.
151 Schilling KG, By S, Feiler HR, *et al.* Diffusion MRI microstructural models in the cervical spinal cord – Application, normative values, and correlations with histological analysis. *Neuroimage* 2019. DOI:10.1016/j.neuroimage.2019.116026.
152 Tax CMW, Szczepankiewicz F, Nilsson M, Jones DK. The dot-compartment revealed? Diffusion MRI with ultra-strong gradients and spherical tensor encoding in the living human brain. *Neuroimage* 2020. DOI:10.1016/j.neuroimage.2020.116534.
153 Novikov DS, Kiselev VG, Jespersen SN. On modeling. *Magn Reson Med* 2018; **79**: 3172–93.
154 Chung AW, Seunarine KK, Clark CA. NODDI reproducibility and variability with magnetic field strength: A comparison between 1.5 T and 3 T. *Hum Brain Mapp* 2016; **37**: 4550–65.
155 De Santis S, Bastiani M, Droby A, *et al.* Characterizing Microstructural Tissue Properties in Multiple Sclerosis with Diffusion MRI at 7T and 3T: The Impact of the Experimental Design. *Neuroscience* 2019; **403**: 17–26.
156 Andica C, Kamagata K, Hayashi T, *et al.* Scan–rescan and inter-vendor reproducibility of neurite orientation dispersion and density imaging metrics. *Neuroradiology* 2020; **62**: 483–94.
157 O'Connor JPB, Aboagye EO, Adams JE, *et al.* Imaging biomarker roadmap for cancer studies. *Nat Rev Clin Oncol* 2017. DOI:10.1038/nrclinonc.2016.162.
158 Poldrack RA, Gorgolewski KJ. Making big data open: Data sharing in neuroimaging. Nat. Neurosci. 2014. DOI:10.1038/nn.3818.
159 Mirzaalian H, Ning L, Savadjiev P, *et al.* Multi-site harmonization of diffusion MRI data in a registration framework. *Brain Imaging Behav* 2018. DOI:10.1007/s11682-016-9670-y.
160 Le Bihan D, Poupon C, Amadon A, Lethimonnier F. Artifacts and pitfalls in diffusion MRI. *J Magn Reson Imaging* 2006; **24**: 478–88.
161 FDT/UserGuide - FslWiki. https://fsl.fmrib.ox.ac.uk/fsl/fslwiki/FDT/UserGuide#DTIFIT (accessed Jan 20, 2022).
162 topup - FslWiki. https://fsl.fmrib.ox.ac.uk/fsl/fslwiki/topup (accessed April 11, 2022).
163 BET/UserGuide - FslWiki. https://fsl.fmrib.ox.ac.uk/fsl/fslwiki/BET/UserGuide (accessed April 11, 2022).
164 eddy/UsersGuide - FslWiki. https://fsl.fmrib.ox.ac.uk/fsl/fslwiki/eddy/UsersGuide (accessed April 11, 2022).
165 FDT - FMRIB's Diffusion Toolbox - User Guide. https://users.fmrib.ox.ac.uk/~behrens/fdt_docs/fdt_dtifit.html (accessed April 11, 2022).
166 Daducci A, Canales-Rodríguez EJ, Zhang H, Dyrby TB, Alexander DC, Thiran JP. Accelerated Microstructure Imaging via Convex Optimization (AMICO) from diffusion MRI data. *Neuroimage* 2015; **105**: 32–44.
167 Ashburner J, Friston KJ. Voxel-Based Morphometry—The Methods. *Neuroimage* 2000; **11**: 805–21.
168 Smith SM, Jenkinson M, Johansen-Berg H, *et al.* Tract-based spatial statistics: Voxelwise analysis of multi-subject diffusion data. *Neuroimage* 2006; **31**: 1487–505.

169 Alfaro-Almagro F, Jenkinson M, Bangerter NK, *et al.* Image processing and Quality Control for the first 10,000 brain imaging datasets from UK Biobank. *Neuroimage* 2018. DOI:10.1016/j.neuroimage.2017.10.034.
170 Faria A V., Zhang J, Oishi K, *et al.* Atlas-Based Analysis of Neurodevelopment from Infancy to Adulthood Using Diffusion Tensor Imaging and Applications for Automated Abnormality Detection. *Neuroimage* 2010; **52**: 415.
171 Good CD, Johnsrude IS, Ashburner J, Henson RNA, Friston KJ, Frackowiak RSJ. A voxel-based morphometric study of ageing in 465 normal adult human brains. *Neuroimage* 2001; **14**: 21–36.
172 Bookstein FL. 'Voxel-based morphometry' should not be used with imperfectly registered images. *Neuroimage* 2001; **14**: 1454–62.
173 Ashburner J, Friston KJ. Why voxel-based morphometry should be used. *Neuroimage* 2001; **14**: 1238–43.
174 Davatzikos C. Why voxel-based morphometric analysis should be used with great caution when characterizing group differences. *Neuroimage* 2004; **23**: 17–20.
175 Watkins KE, Dronkers NF, Vargha-Khadem F. Behavioural analysis of an inherited speech and language disorder: comparison with acquired aphasia. *Brain* 2002; **125**: 452–64.
176 The effectof filter size on VBM analyses of DT-MRI data. - Google Search. https://www.google.com/search?q=The+effectof+filter+size+on+VBM+analyses+of+DT-MRI+data.+&rlz=1C5CHFA_enGB971GB971&ei=HpU4YqOrAvCA9u8P_IOj4AQ&ved=0ahUKEwijsuaKvtf2AhVwgP0HHfzBCEwQ4dUDCA8&uact=5&oq=The+effectof+filter+size+on+VBM+analyses+of+DT-MRI+data.+&gs_lcp=Cgdnd3Mtd2I6EANKBAhBGABKBAhGGABQAFgAYPAGaABwAXgAgAGtAogBrQKSAQMzLTGYAQCgAQKgAQHAAQE&sclient=gws-wiz (accessed March 21, 2022).
177 Oh SW, Shin NY, Choi JY, Lee SK, Bang MR. Altered white matter integrity in human immunodeficiency virus-associated neurocognitive disorder: A tract-based spatial statistics study. *Korean J Radiol* 2018; **19**: 431–42.
178 Uddin MN, Figley TD, Solar KG, Shatil AS, Figley CR. Comparisons between multi-component myelin water fraction, T1w/T2w ratio, and diffusion tensor imaging measures in healthy human brain structures. *Sci Rep* 2019; **9**. DOI:10.1038/S41598-019-39199-X.
179 Smith SM, Alfaro-Almagro F, Miller KL. UK Biobank Brain Imaging Documentation UK Biobank Brain Imaging Documentation Contributors to UK Biobank Brain Imaging. 2020. http://www.ukbiobank.ac.uk (accessed Oct 22, 2021).
180 eddy - FslWiki. https://fsl.fmrib.ox.ac.uk/fsl/fslwiki/eddy (accessed March 15, 2022).
181 BET - FslWiki. https://fsl.fmrib.ox.ac.uk/fsl/fslwiki/BET (accessed March 15, 2022).
182 Microstructure Imaging Group | NODDI Matlab toolbox. http://mig.cs.ucl.ac.uk/index.php?n=Tutorial.NODDImatlab (accessed March 15, 2022).
183 Kodl CT, Franc DT, Rao JP, *et al.* Diffusion tensor imaging identifies deficits in white matter microstructure in subjects with type 1 diabetes that correlate with reduced neurocognitive function. *Diabetes* 2008; **57**: 3083–9.
184 Biessels GJ, Deary IJ, Ryan CM. Cognition and diabetes: a lifespan perspective. Lancet Neurol. 2008. DOI:10.1016/S1474-4422(08)70021-8.
185 van Duinkerken E, Schoonheim MM, Ijzerman RG, *et al.* Diffusion tensor imaging in type 1 diabetes: decreased white matter integrity relates to cognitive functions. *Diabetologia* 2012; **55**: 1218–20.
186 Brands AMA, Biessels GJ, De Haan EHF, Kappelle LJ, Kessels RPC. The effects of type 1 diabetes on cognitive performance: A meta-analysis. Diabetes Care. 2005. DOI:10.2337/diacare.28.3.726.
187 Reijmer YD, Brundel M, de Bresser J, *et al.* Microstructural white matter abnormalities and cognitive functioning in type 2 diabetes: a diffusion tensor imaging study. *Diabetes Care* 2013; **36**: 137–44.
188 Yau PL, Javier DC, Ryan CM, *et al.* Preliminary evidence for brain complications in obese adolescents with type 2 diabetes mellitus. *Diabetologia* 2010; **53**: 2298–306.
189 Groeneveld O, Reijmer Y, Heinen R, *et al.* Brain imaging correlates of mild cognitive impairment and early dementia in patients with type 2 diabetes mellitus. *Nutr Metab Cardiovasc Dis* 2018; **28**: 1253–60.
190 Pierpaoli C, Jezzard P, Basser PJ, Barnett A, Di Chiro G. Diffusion tensor MR imaging of the human brain. *Radiology* 1996. DOI:10.1148/radiology.201.3.8939209.
191 Fox LA, Hershey T, Mauras N, *et al.* Persistence of abnormalities in white matter in children with type 1 diabetes. *Diabetologia* 2018. DOI:10.1007/s00125-018-4610-6.
192 Walhovd KB, Johansen-Berg H, Káradóttir RT. Unraveling the secrets of white matter - Bridging the gap between cellular, animal and human imaging studies. Neuroscience. 2014.

DOI:10.1016/j.neuroscience.2014.06.058.
193 Sanjari Moghaddam H, Ghazi Sherbaf F, Aarabi MH. Brain microstructural abnormalities in type 2 diabetes mellitus: A systematic review of diffusion tensor imaging studies. Front. Neuroendocrinol. 2019. DOI:10.1016/j.yfrne.2019.100782.
194 Beaulieu C. The basis of anisotropic water diffusion in the nervous system - A technical review. NMR Biomed. 2002. DOI:10.1002/nbm.782.
195 Jelescu IO, Zurek M, Winters K V., *et al.* In vivo quantification of demyelination and recovery using compartment-specific diffusion MRI metrics validated by electron microscopy. *Neuroimage* 2016. DOI:10.1016/j.neuroimage.2016.02.004.
196 Song SK, Sun SW, Ramsbottom MJ, Chang C, Russell J, Cross AH. Dysmyelination revealed through MRI as increased radial (but unchanged axial) diffusion of water. *Neuroimage* 2002; **17**: 1429–36.
197 Madden DJ, Bennett IJ, Burzynska A, Potter GG, Chen N kuei, Song AW. Diffusion tensor imaging of cerebral white matter integrity in cognitive aging. *Biochim Biophys Acta* 2012; **1822**: 386–400.
198 Tromp D. DTI Scalars (FA, MD, AD, RD) - How do they relate to brain structure? *The Winnower* 2016; published online Feb 29. DOI:10.15200/WINN.146119.94778.
199 O'Donnell LJ, Westin CF. An introduction to diffusion tensor image analysis. *Neurosurg Clin N Am* 2011; **22**: 185–96.
200 Jeurissen B, Leemans A, Tournier JD, Jones DK, Sijbers J. Investigating the prevalence of complex fiber configurations in white matter tissue with diffusion magnetic resonance imaging. *Hum Brain Mapp* 2013; **34**: 2747–66.
201 Aye T, Barnea-Goraly N, Ambler C, *et al.* White matter structural differences in young children with type 1 diabetes: A diffusion tensor imaging study. *Diabetes Care* 2012. DOI:10.2337/dc12-0017.
202 Barnea-Goraly N, Raman M, Mazaika P, *et al.* Alterations in white matter structure in young children with type 1 diabetes. *Diabetes Care* 2014; **37**: 332–40.
203 Toprak H, Yetis H, Alkan A, *et al.* Relationships of DTI findings with neurocognitive dysfunction in children with Type 1 diabetes mellitus. *Br J Radiol* 2016; **89**: 20150680.
204 Ahmed HH, Azzam HME, Farid SM, Abdelmaksoud AA, Rassem IMM. Neurocognitive profile and diffusion tensor imaging in pediatric patients with type 1 diabetes mellitus. *Middle East Curr Psychiatry* 2014; **21**: 205–11.
205 Franc DT, Kod CT, Mueller BA, Muetze RL, Lim KO, Seaquist ER. High connectivity between reduced cortical thickness and disrupted white matter tracts in long-standing type 1 diabetes. *Diabetes* 2011; **60**: 315–9.
206 Yoon S, Kim J, Musen G, *et al.* Prefronto-Temporal White Matter Microstructural Alterations 20 years after the Diagnosis of Type 1 Diabetes Mellitus HHS Public Access. *Pediatr Diabetes* 2018; **19**: 478–85.
207 Antenor-Dorsey JA V, Meyer E, Rutlin J, *et al.* White matter microstructural integrity in youth with type 1 diabetes. *Diabetes* 2013; **62**: 581–9.
208 Rofey DL, Arslanian SA, El Nokali NE, *et al.* Brain volume and white matter in youth with type 2 diabetes compared to obese and normal weight, non-diabetic peers: A pilot study. *Int J Dev Neurosci* 2015. DOI:10.1016/j.ijdevneu.2015.07.003.
209 Nouwen A, Chambers A, Chechlacz M, *et al.* Microstructural abnormalities in white and gray matter in obese adolescents with and without type 2 diabetes. *NeuroImage Clin* 2017; **16**: 43–51.
210 Yau PL, Javier D, Tsui W, *et al.* Emotional and neutral declarative memory impairments and associated white matter microstructural abnormalities in adults with type 2 diabetes. *Psychiatry Res* 2009; **174**: 223–30.
211 Zhang A, Ajilore O, Zhan L, *et al.* White matter tract integrity of anterior limb of internal capsule in major depression and type 2 diabetes. *Neuropsychopharmacology* 2013; **38**: 1451–9.
212 Zhang J, Wang Y, Wang J, *et al.* White matter integrity disruptions associated with cognitive impairments in type 2 diabetic patients. *Diabetes* 2014; **63**: 3596–605.
213 Yu X, Jiaerken Y, Xu X, *et al.* Abnormal corpus callosum induced by diabetes impairs sensorimotor connectivity in patients after acute stroke. *Eur Radiol* 2019. DOI:10.1007/s00330-018-5576-y.
214 Tan X, Fang P, An J, *et al.* Micro-structural white matter abnormalities in type 2 diabetic patients: a DTI study using TBSS analysis. *Neuroradiology* 2016; **58**: 1209–16.
215 van Bloemendaal L, Ijzerman RG, Ten Kulve JS, *et al.* Alterations in white matter volume and integrity in obesity and type 2 diabetes. *Metab Brain Dis* 2016; **31**: 621–9.
216 Kim DJ, Yu JH, Shin MS, Shin YW, Kim MS. Hyperglycemia Reduces Efficiency of Brain Networks in Subjects with Type 2 Diabetes. *PLoS ONE [Electronic Resour* 2016; **11**: e0157268.

217 Reijmer YD, Leemans A, Brundel M, Kappelle LJ, Biessels GJ, Utrecht Vascular Cognitive Impairment Study G. Disruption of the cerebral white matter network is related to slowing of information processing speed in patients with type 2 diabetes. *Diabetes* 2013; **62**: 2112–5.
218 Zhang J, Liu Z, Li Z, *et al.* Disrupted White Matter Network and Cognitive Decline in Type 2 Diabetes Patients. *J Alzheimer's Dis* 2016; **53**: 185–95.
219 Zhang Y, Cao Y, Xie Y, *et al.* Altered brain structural topological properties in type 2 diabetes mellitus patients without complications. *J Diabetes* 2019; **11**: 129–38.
220 Yau PL, Hempel R, Tirsi A, Convit A. Cerebral white matter and retinal arterial health in hypertension and type 2 diabetes mellitus. *Int J Hypertens* 2013; **2013 (no p**. DOI:http://dx.doi.org/10.1155/2013/329602.
221 Xiong Y, Sui Y, Xu Z, *et al.* A Diffusion Tensor Imaging Study on White Matter Abnormalities in Patients with Type 2 Diabetes Using Tract-Based Spatial Statistics. *Ajnr Am J Neuroradiol* 2016; **37**: 1462–9.
222 Hsu JL, Chen YL, Leu JG, *et al.* Microstructural white matter abnormalities in type 2 diabetes mellitus: a diffusion tensor imaging study. *Neuroimage* 2012; **59**: 1098–105.
223 Xie XY, Zhang XYQ, Qin XW, Lu XS, Ni XC, Zhang XYQ. White Matter Microstructural Abnormalities in Type 2 Diabetes Mellitus: A Diffusional Kurtosis Imaging Analysis. DOI:10.3174/ajnr.A5042.
224 Yau PL, Kluger A, Borod JC, Convit A. Neural substrates of verbal memory impairments in adults with type 2 diabetes mellitus. *J Clin Exp Neuropsychol Off J Int Neuropsychol Soc* 2014; **36**: 74–87.
225 Fang P, An J, Tan X, *et al.* Changes in the cerebellar and cerebro-cerebellar circuit in type 2 diabetes. *Brain Res Bull* 2017; **130**: 95–100.
226 Yoon S, Cho H, Kim J, *et al.* Brain changes in overweight/obese and normal-weight adults with type 2 diabetes mellitus. *Diabetologia* 2017; **60**: 1207–17.
227 Falvey CM, Rosano C, Simonsick EM, *et al.* Macro-andmicrostructural magnetic resonance imaging indices associated with diabetes among community-dwelling older adults. *Diabetes Care* 2013. DOI:10.2337/dc12-0814.
228 van Bussel FC, Backes WH, Hofman PA, *et al.* Altered Hippocampal White Matter Connectivity in Type 2 Diabetes Mellitus and Memory Decrements. *J Neuroendocrinol* 2016; **28**: 12366.
229 Xiong Y, Zhang S, Shi J, Fan Y, Zhang Q, Zhu W. Application of neurite orientation dispersion and density imaging to characterize brain microstructural abnormalities in type-2 diabetics with mild cognitive impairment. *J Magn Reson Imaging* 2019; **50**: 889–98.
230 Xiong Y, Sui Y, Zhang S, *et al.* Brain microstructural alterations in type 2 diabetes: diffusion kurtosis imaging provides added value to diffusion tensor imaging. *Eur Radiol* 2019; **29**: 1997–2008.
231 Hoogenboom WS, Marder TJ, Flores VL, *et al.* Cerebral white matter integrity and resting-state functional connectivity in middle-aged patients with type 2 diabetes. *Diabetes* 2014; **63**: 728–38.
232 Raffield LM, Brenes GA, Cox AJ, *et al.* Associations between anxiety and depression symptoms and cognitive testing and neuroimaging in type 2 diabetes. *J Diabetes Complications* 2016; **30**: 143–9.
233 Biessels GJ, Reijmer YD. Brain changes underlying cognitive dysfunction in diabetes: What can we learn from MRI? In: Diabetes. American Diabetes Association, 2014: 2244–52.
234 Xie Y, Zhang Y, Qin W, Lu S, Ni C, Zhang Q. White Matter Microstructural Abnormalities in Type 2 Diabetes Mellitus: A Diffusional Kurtosis Imaging Analysis. *Ajnr Am J Neuroradiol* 2017; **38**: 617–25.
235 López Fernández ML, Barrio Castellanos R, Portellano Pérez JA, Martínez Arias R. Executive functions in children with type 1 diabetes using the neuropsychology test. *An Pediatr* 2013. DOI:10.1016/j.anpedi.2012.05.005.
236 Northam EA, Rankins D, Lin A, *et al.* Central nervous system function in youth with type 1 diabetes 12 years after disease onset. *Diabetes Care* 2009. DOI:10.2337/dc08-1657.
237 Northam EA, Anderson PJ, Jacobs R, Hughes M, Warne GL, Werther GA. Neuropsychological profiles of children with type 1 diabetes 6 years after disease onset. *Diabetes Care* 2001. DOI:10.2337/diacare.24.9.1541.
238 Naguib JM, Kulinskaya E, Lomax CL, Garralda ME. Neuro-cognitive performance in children with type 1 diabetesa meta-analysis. *J Pediatr Psychol* 2009. DOI:10.1093/jpepsy/jsn074.
239 Geijselaers SLC, Sep SJS, Stehouwer CDA, Biessels GJ. Glucose regulation, cognition, and brain MRI in type 2 diabetes: A systematic review. Lancet Diabetes Endocrinol. 2015. DOI:10.1016/S2213-8587(14)70148-2.
240 Feinkohl I, Price JF, Strachan MWJ, Frier BM. The impact of diabetes on cognitive decline: Potential vascular, metabolic, and psychosocial risk factors. Alzheimer's Res. Ther. 2015. DOI:10.1186/s13195-015-0130-5.

241 Xia W, Chen YC, Ma J. Resting-state brain anomalies in type 2 diabetes: A meta-analysis. Front. Aging Neurosci. 2017. DOI:10.3389/fnagi.2017.00014.
242 McCrimmon RJ, Ryan CM, Frier BM. Diabetes and cognitive dysfunction. Lancet. 2012. DOI:10.1016/S0140-6736(12)60360-2.
243 Bruehl H, Sweat V, Tirsi A, Shah B, Convit A. Obese Adolescents with Type 2 Diabetes Mellitus Have Hippocampal and Frontal Lobe Volume Reductions. *Neurosci Med* 2011. DOI:10.4236/nm.2011.21005.
244 Yang S, Ajilore O, Wu M, Lamar M, Kumar A. Impaired macromolecular protein pools in fronto-striato-thalamic circuits in type 2 diabetes revealed by magnetization transfer imaging. *Diabetes* 2015. DOI:10.2337/db14-0316.
245 Basser PJ, Jones DK. Diffusion-tensor MRI: Theory, experimental design and data analysis - A technical review. NMR Biomed. 2002. DOI:10.1002/nbm.783.
246 Steven AJ, Zhuo J, Melhem ER. Diffusion kurtosis imaging: An emerging technique for evaluating the microstructural environment of the brain. *Am J Roentgenol* 2014. DOI:10.2214/AJR.13.11365.
247 Bihan D Le. Molecular diffusion, tissue microdynamics and microstructure. *NMR Biomed* 1995. DOI:10.1002/nbm.1940080711.
248 Ellwardt E, Zipp F. Molecular mechanisms linking neuroinflammation and neurodegeneration in MS. Exp. Neurol. 2014; **262**: 8–17.
249 Mustafi SM, Harezlak J, Kodiweera C, *et al.* Detecting white matter alterations in multiple sclerosis using advanced diffusion magnetic resonance imaging. *Neural Regen Res* 2019; **14**: 114–23.
250 Filippi M, Rocca MA, Ciccarelli O, *et al.* MRI criteria for the diagnosis of multiple sclerosis: MAGNIMS consensus guidelines. Lancet Neurol. 2016; **15**: 292–303.
251 Wattjes MP, Rovira À, Miller D, *et al.* Evidence-based guidelines: MAGNIMS consensus guidelines on the use of MRI in multiple sclerosis - Establishing disease prognosis and monitoring patients. *Nat Rev Neurol* 2015; **11**: 597–606.
252 De Groot CJA, Bergers E, Kamphorst W, *et al.* Post-mortem MRI-guided sampling of multiple sclerosis brain lesions: Increased yield of active demyelinating and (p)reactive lesions. *Brain* 2001; **124**: 1635–45.
253 Cortese R, Collorone S, Ciccarelli O, Toosy AT. Advances in brain imaging in multiple sclerosis. Ther. Adv. Neurol. Disord. 2019. DOI:10.1177/1756286419859722.
254 Tur C, Moccia M, Barkhof F, *et al.* Assessing treatment outcomes in multiple sclerosis trials and in the clinical setting. Nat. Rev. Neurol. 2018; **14**: 75–93.
255 Sbardella E, Tona F, Petsas N, Pantano P. DTI Measurements in Multiple Sclerosis: Evaluation of Brain Damage and Clinical Implications. *Mult Scler Int* 2013; **2013**: 1–11.
256 Rovaris M, Iannucci G, Falautano M, *et al.* Cognitive dysfunction in patients with mildly disabling relapsing-remitting multiple sclerosis: An exploratory study with diffusion tensor MR imaging. *J Neurol Sci* 2002; **195**: 103–9.
257 Werring DJ, Clark CA, Barker GJ, Thompson AJ, Miller DH. Diffusion tensor imaging of lesions and normal-appearing white matter in multiple sclerosis. *Neurology* 1999; **52**: 1626–32.
258 Filippi M, Agosta F. Diffusion tensor imaging and functional MRI. In: Handbook of Clinical Neurology. Elsevier B.V., 2016: 1065–87.
259 Ciccarelli O, Werring DJ, Barker GJ, *et al.* A study of the mechanisms of normal-appearing white matter damage in multiple sclerosis using diffusion tensor imaging: Evidence of Wallerian degeneration. *J Neurol* 2003; **250**: 287–92.
260 Welton T, Kent D, Constantinescu CS, Auer DP, Dineen RA. Functionally Relevant White Matter Degradation in Multiple Sclerosis: A Tract-based Spatial Meta-Analysis. *Radiology* 2015; **275**: 89–96.
261 Gallo A, Rovaris M, Riva R, *et al.* Diffusion-tensor magnetic resonance imaging detects normal-appearing white matter damage unrelated to short-term disease activity in patients at the earliest clinical stage of multiple sclerosis. *Arch Neurol* 2005; **62**: 803–8.
262 Preziosa P, Rocca MA, Mesaros S, *et al.* Intrinsic damage to the major white matter tracts in patients with different clinical phenotypes of multiple sclerosis: A voxelwise diffusion-tensor MR study. *Radiology* 2011; **260**: 541–50.
263 Budde MD, Xie M, Cross AH, *et al.* Axial diffusivity is the primary correlate of axonal injury in the experimental autoimmune encephalomyelitis spinal cord: A quantitative pixelwise analysis. *J Neurosci* 2009; **29**: 2805–13.
264 Schmierer K, Wheeler-Kingshott CAM, Boulby PA, *et al.* Diffusion tensor imaging of post mortem multiple sclerosis brain. *Neuroimage* 2007; **35**: 467–77.
265 Kim JH, Budde MD, Liang HF, *et al.* Detecting axon damage in spinal cord from a mouse model of multiple sclerosis. *Neurobiol Dis* 2006; **21**: 626–32.
266 Schneider T, Brownlee W, Zhang H, Ciccarelli O, Miller DH, Wheeler-Kingshott CG. Sensitivity

of multi-shell NODDI to multiple sclerosis white matter changes: A pilot study. *Funct Neurol* 2017. DOI:10.11138/FNeur/2017.32.2.097.
267 B. S, G. G, V. P, *et al.* Disruption of neurite morphology parallels MS progression. *Neurol Neuroimmunol NeuroInflammation* 2018; **5**: e502–e502.
268 Granberg T, Fan Q, Treaba CACA, *et al.* In vivo characterization of cortical and white matter neuroaxonal pathology in early multiple sclerosis. *Brain* 2017; **140**: 2912–26.
269 Hagiwara A, Kamagata K, Shimoji K, *et al.* White Matter Abnormalities in Multiple Sclerosis Evaluated by Quantitative Synthetic MRI, Diffusion Tensor Imaging, and Neurite Orientation Dispersion and Density Imaging. DOI:10.3174/ajnr.A6209.
270 Sacco S, Caverzasi E, Papinutto N, *et al.* Neurite orientation dispersion and density imaging for assessing acute inflammation and lesion evolution in MS. *Am J Neuroradiol* 2020; **41**: 2219–26.
271 S. C, N. C, F. G, *et al.* Reduced neurite density in the brain and cervical spinal cord in relapsing-remitting multiple sclerosis: A NODDI study. *Mult Scler J* 2020; **26**: 1647–57.
272 Page MJ, McKenzie JE, Bossuyt PM, *et al.* The PRISMA 2020 statement: an updated guideline for reporting systematic reviews. *BMJ* 2021; : n71.
273 Rahmanzadeh R, Lu P-J, Barakovic M, *et al.* Myelin and axon pathology in multiple sclerosis assessed by myelin water and multi-shell diffusion imaging. DOI:10.1093/brain/awab088/6164965.
274 Bonnier G, Roche A, Romascano D, *et al.* Advanced MRI unravels the nature of tissue alterations in early multiple sclerosis. *Ann Clin Transl Neurol* 2014; **1**: 423–32.
275 Filippi M. Mri measures of neurodegeneration in multiple sclerosis: Implications for disability, disease monitoring, and treatment. *J Neurol* 2015; **262**. DOI:10.1007/s00415-014-7340-9.
276 Inglese M, Bester M. Diffusion imaging in multiple sclerosis: Research and clinical implications. NMR Biomed. 2010; **23**: 865–72.
277 Schmierer K, Scaravilli F, Altmann DR, Barker GJ, Miller DH. Magnetization transfer ratio and myelin in postmortem multiple sclerosis brain. *Ann Neurol* 2004; **56**: 407–15.
278 Bammer R, Augustin M, Strasser-Fuchs S, *et al.* Magnetic resonance diffusion tensor imaging for characterizing diffuse and focal white matter abnormalities in multiple sclerosis. *Magn Reson Med* 2000; **44**: 583–91.
279 Klawiter EC, Schmidt RE, Trinkaus K, *et al.* Radial diffusivity predicts demyelination in ex vivo multiple sclerosis spinal cords. *Neuroimage* 2011; **55**: 1454–60.
280 Alotaibi A, Podlasek A, AlTokhis A, *et al.* White Matter Microstructural Alteration in Type 2 Diabetes: A Combined UK Biobank Study of Diffusion Tensor Imaging and Neurite Orientation Dispersion and Density Imaging. *medRxiv* 2022; : 2022.07.09.22277453.
281 Zimmet P, Alberti KGMM, Shaw J. Global and societal implications of the diabetes epidemic. *Nat 2001 4146865* 2001; **414**: 782–7.
282 Bruehl H, Sweat V, Tirsi A, *et al.* Obese Adolescents with Type 2 Diabetes Mellitus Have Hippocampal and Frontal Lobe Volume Reductions. *Neurosci Med* 2011; **2**: 34–42.
283 Huang L, Zhang Q, Tang T, *et al.* Abnormalities of Brain White Matter in Type 2 Diabetes Mellitus: A Meta-Analysis of Diffusion Tensor Imaging. *Front Aging Neurosci* 2021; **0**: 459.
284 De Santis S, Gabrielli A, Palombo M, Maraviglia B, Capuani S. Non-Gaussian diffusion imaging: A brief practical review. *Magn Reson Imaging* 2011; **29**: 1410–6.
285 Miller KL, Alfaro-Almagro F, Bangerter NK, *et al.* Multimodal population brain imaging in the UK Biobank prospective epidemiological study. *Nat Neurosci* 2016. DOI:10.1038/nn.4393.
286 Sudlow C, Gallacher J, Allen N, *et al.* UK Biobank: An Open Access Resource for Identifying the Causes of a Wide Range of Complex Diseases of Middle and Old Age. *PLoS Med* 2015; **12**. DOI:10.1371/journal.pmed.1001779.
287 Fry A, Littlejohns TJ, Sudlow C, *et al.* Comparison of Sociodemographic and Health-Related Characteristics of UK Biobank Participants With Those of the General Population. *Am J Epidemiol* 2017; **186**: 1026–34.
288 UK Biobank. UK Biobank. Available: http://biobank.ctsu.ox.ac.uk/crystal/refer.cgi?id=2367. 2013; **58**: 1–33.
289 Andersson JLR, Sotiropoulos SN. An integrated approach to correction for off-resonance effects and subject movement in diffusion MR imaging. *Neuroimage* 2016; **125**: 1063–78.
290 Andersson JLR, Graham MS, Zsoldos E, Sotiropoulos SN. Incorporating outlier detection and replacement into a non-parametric framework for movement and distortion correction of diffusion MR images. *Neuroimage* 2016; **141**: 556–72.
291 Glasser MF, Sotiropoulos SN, Wilson JA, *et al.* The minimal preprocessing pipelines for the Human Connectome Project. *Neuroimage* 2013; **80**: 105–24.
292 De Groot M, Vernooij MW, Klein S, *et al.* Improving alignment in Tract-based spatial statistics: evaluation and optimization of image registration. *Neuroimage* 2013; **76**: 400–11.
293 MRI Atlas of Human White Matter - Susumu Mori, S. Wakana, Peter C M van Zijl, L.M. Nagae-

Poetscher - Google Books. https://books.google.co.uk/books?hl=en&lr=&id=ltwRYlvFNLIC&oi=fnd&pg=PR5&ots=geIMk92Kgn&sig=SYvCENlh1MXHtwUjO22hXUC-GbU&redir_esc=y#v=onepage&q&f=false (accessed Oct 27, 2021).
294 Alfaro-Almagro F, McCarthy P, Afyouni S, *et al.* Confound modelling in UK Biobank brain imaging. *Neuroimage* 2021; **224**. DOI:10.1016/J.NEUROIMAGE.2020.117002.
295 Song SK, Sun SW, Ju WK, Lin SJ, Cross AH, Neufeld AH. Diffusion tensor imaging detects and differentiates axon and myelin degeneration in mouse optic nerve after retinal ischemia. *Neuroimage* 2003; **20**: 1714–22.
296 Nilsson D, Go C, Rutka JT, *et al.* Bilateral diffusion tensor abnormalities of temporal lobe and cingulate gyrus white matter in children with temporal lobe epilepsy. *Epilepsy Res* 2008; **81**: 128–35.
297 Muriach M, Flores-Bellver M, Romero FJ, Barcia JM. Diabetes and the brain: Oxidative stress, inflammation, and autophagy. *Oxid Med Cell Longev* 2014; **2014**. DOI:10.1155/2014/102158.
298 Mitchell T, Archer DB, Chu WT, *et al.* Neurite orientation dispersion and density imaging (NODDI) and free-water imaging in Parkinsonism. *Hum Brain Mapp* 2019; **40**: 5094–107.
299 Zhang J, Gregory S, Scahill RI, *et al.* In vivo characterization of white matter pathology in premanifest huntington's disease. *Ann Neurol* 2018; **84**: 497–504.
300 Churchill NW, Caverzasi E, Graham SJ, Hutchison MG, Schweizer TA. White matter microstructure in athletes with a history of concussion: Comparing diffusion tensor imaging (DTI) and neurite orientation dispersion and density imaging (NODDI). *Hum Brain Mapp* 2017; **38**: 4201–11.
301 Hara S, Hori M, Ueda R, *et al.* Unraveling Specific Brain Microstructural Damage in Moyamoya Disease Using Diffusion Magnetic Resonance Imaging and Positron Emission Tomography. *J Stroke Cerebrovasc Dis* 2019; **28**: 1113–25.
302 Bahour N, Cortez B, Pan H, Shah H, Doria A, Aguayo-Mazzucato C. Diabetes mellitus correlates with increased biological age as indicated by clinical biomarkers. *GeroScience* 2022; **44**: 415–27.
303 C P, PJ B. Toward a quantitative assessment of diffusion anisotropy. *Magn Reson Med* 1996; **36**: 893–906.
304 Jelescu IO, Veraart J, Fieremans E, Novikov DS. Degeneracy in model parameter estimation for multi-compartmental diffusion in neuronal tissue. *NMR Biomed* 2016; **29**: 33–47.
305 Wen Q, Kelley DAC, Banerjee S, *et al.* Clinically feasible NODDI characterization of glioma using multiband EPI at 7 T. *NeuroImage Clin* 2015; **9**: 291–9.
306 Jing J, Zhou Y, Pan Y, *et al.* Reduced white matter microstructural integrity in prediabetes and diabetes: A population-based study. *eBioMedicine* 2022; **82**: 104144.
307 Jan Biessels G, Deary IJ, Ryan CM. Personal View Cognition and diabetes: a lifespan perspective. 2008; **7**. http://neurology.thelancet.com (accessed Jan 10, 2022).
308 Umegaki H. Type 2 diabetes as a risk factor for cognitive impairment: current insights. *Clin Interv Aging* 2014; **9**: 1011.
309 Mackay A, Whittall K, Adler J, Li D, Paty D, Graeb D. In vivo visualization of myelin water in brain by magnetic resonance. *Magn Reson Med* 1994; **31**: 673–7.
310 Pecheva D, Kelly C, Kimpton J, *et al.* Recent advances in diffusion neuroimaging: Applications in the developing preterm brain [version 1; referees: 2 approved]. *F1000Research* 2018; **7**. DOI:10.12688/F1000RESEARCH.15073.1.
311 (PDF) Advanced dMRI Signal Modeling for Tissue Microstructure Characterization. https://www.researchgate.net/publication/317419497_Advanced_dMRI_Signal_Modeling_for_Tissue_Microstructure_Characterization (accessed Jan 28, 2022).

Appendices

Table 1A. FA and Intergroup Microstructural Differences.

FA WM Tract and Group		N	Mean	Std. Deviation	Mean Difference (95% CI)	P-value	Effect Size
Middle cerebellar peduncle	Non T2DM	30744	0.005450	0.938413	0.01 (-0.04, 0.07)	0.6	.015
	T2DM	1023	-0.008766	0.930215			
Pontine crossing	Non T2DM	30744	0.014516	0.908788	0.03 (-0.01, 0.09)	0.2	.042
	T2DM	1023	-0.023632	0.967857			
Genu of corpus callosum	Non T2DM	30744	0.015710	0.939996	0.17 (0.11, 0.23)	<0.001	.181
	T2DM	1023	-0.154953	0.968473			
Body of corpus callosum	Non T2DM	30744	0.014099	0.975441	0.20 (0.14, 0.26)	<0.001	.208
	T2DM	1023	-0.188581	0.972339			
Splenium of corpus callosum	Non T2DM	30744	0.015518	0.827389	0.07 (0.01, 0.13)	0.01	.092
	T2DM	1023	-0.060867	0.999620			
Fornix	Non T2DM	30744	0.009745	0.933687	0.20 (0.15, 0.25)	<0.001	.219
	T2DM	1023	-0.193458	0.798754			
Corticospinal tract (R)	Non T2DM	30744	0.009919	0.946782	0.03 (-0.02, 0.08)	0.2	.034
	T2DM	1023	-0.022036	0.903851			
Corticospinal tract (L)	Non T2DM	30744	0.011902	0.925655	0.04 (-0.01, 0.10)	0.1	.046
	T2DM	1023	-0.030883	0.960727			
Medial lemniscus (R)	Non T2DM	30744	0.012880	0.929472	0.13 (0.07, 0.19)	<0.001	.142
	T2DM	1023	-0.119164	0.941373			
Medial lemniscus (L)	Non T2DM	30744	0.006319	0.905491	0.14 (0.08, 0.2)	<0.001	.161
	T2DM	1023	-0.139946	0.932239			
Inferior cerebellar peduncle (R)	Non T2DM	30744	0.006266	0.898204	0.08 (0.02, 0.13)	<0.001	.092
	T2DM	1023	-0.076112	0.916704			
Inferior cerebellar peduncle (L)	Non T2DM	30744	0.017283	0.924883	0.11 (0.06, 0.17)	<0.001	.126
	T2DM	1023	-0.099363	0.887749			
Superior cerebellar peduncle (R)	Non T2DM	30744	0.021203	0.928668	0.27 (0.21, 0.33)	<0.001	.296
	T2DM	1023	-0.253829	0.977185			
Superior cerebellar peduncle (L)	Non T2DM	30744	0.015061	0.908900	0.29 (0.23, 0.35)	<0.001	.329
	T2DM	1023	-0.276923	0.957662			
Cerebral peduncle (R)	Non T2DM	30744	0.016233	0.903907	0.13 (0.07, 0.19)	<0.001	.152
	T2DM	1023	-0.121022	0.922485			
Cerebral peduncle (L)	Non T2DM	30744	0.010117	0.946702	0.12 (0.06, 0.18)	<0.001	.130
	T2DM	1023	-0.112698	0.921053			
Anterior limb of internal capsule (R)	Non T2DM	30744	0.011844	0.941595	0.09 (0.03, 0.15)	0.002	.104
	T2DM	1023	-0.086114	0.982984			
Anterior limb of internal capsule (L)	Non T2DM	30744	0.002735	0.952270	0.08 (0.02, 0.14)	0.006	.091
	T2DM	1023	-0.084332	0.992505			
	Non T2DM	30744	-0.000490	0.956689	-0.05 (-0.11, 0.005)	0.7	.059

Posterior limb of internal capsule (R)	T2DM	1023	0.056183	0.997769			
Posterior limb of internal capsule (L)	Non T2DM	30744	0.008421	0.961241	-0.07 (-0.13, -0.013)	0.17	.076
	T2DM	1023	0.081733	0.958225			
Retrolenticular part of internal capsule (R)	Non T2DM	30744	0.008905	0.957573	0.03 (-0.03, 0.09)	0.3	.033
	T2DM	1023	-0.022920	1.017518			
Retrolenticular part of internal capsule (L)	Non T2DM	30744	0.015200	0.907125	0.03 (-0.02, 0.10)	0.2	0.43
	T2DM	1023	-0.024234	1.006436			
Anterior corona radiata (R)	Non T2DM	30744	0.016704	0.883404	0.13 (0.07, 0.19)	<0.001	.148
	T2DM	1023	-0.114314	0.950761			
Anterior corona radiata (L)	Non T2DM	30744	0.009453	0.949038	0.14 (0.08, 0.20)	<0.001	.154
	T2DM	1023	-0.136826	0.925499			
Superior corona radiata (R)	Non T2DM	30744	0.011538	0.947563	0.03 (-0.03, 0.09)	0.3	.034
	T2DM	1023	-0.020285	1.017567			
Superior corona radiata (L)	Non T2DM	30744	0.006058	0.978610	0.03 (-0.03, 0.10)	0.2	.035
	T2DM	1023	-0.028740	1.046162			
Posterior corona radiata (R)	Non T2DM	30744	0.007537	0.966078	0.011 (-0.05, 0.07)	0.7	.012
	T2DM	1023	-0.003977	1.065942			
Posterior corona radiata (L)	Non T2DM	30744	0.015898	0.915362	0.04 (-0.02, 0.10)	0.1	.047
	T2DM	1023	-0.026994	1.030606			
Posterior thalamic radiation (R)	Non T2DM	30744	0.015208	0.920599	0.16 (0.10, 0.22)	<0.001	.183
	T2DM	1023	-0.153359	0.952977			
Posterior thalamic radiata (L)	Non T2DM	30744	0.013604	0.962017	0.17 (0.11, 0.23)	<0.001	.181
	T2DM	1023	-0.160946	0.955437			
Sagittal stratum (R)	Non T2DM	30744	0.015088	0.955336	0.15 (0.09, 0.21)	<0.001	.164
	T2DM	1023	-0.141242	0.960421			
Sagittal stratum (L)	Non T2DM	30744	0.014776	0.906346	0.18 (0.12, 0.24)	<0.001	.204
	T2DM	1023	-0.170771	0.952318			
External capsule (R)	Non T2DM	30744	0.012537	0.902945	0.10 (0.04, 0.16)	<0.001	.120
	T2DM	1023	-0.095713	0.933989			
External capsule (L)	Non T2DM	30744	0.013269	0.948382	0.09 (0.02, 0.15)	<0.001	.095
	T2DM	1023	-0.076815	0.975428			
Cingulum cingulate gyrus (R)	Non T2DM	30744	0.013343	0.937644	0.12 (0.06, 0.18)	<0.001	.133
	T2DM	1023	-0.111779	1.013694			
Cingulum cingulate gyrus (L)	Non T2DM	30744	0.000232	0.949976	0.10 (0.04, 0.17)	0.14	.115
	T2DM	1023	-0.109085	0.981397			
Cingulum hippocampus (R)	Non T2DM	30744	0.000832	0.950110	-0.03 (-0.09, 0.02)	0.2	.041
	T2DM	1023	0.039580	0.956787			
Cingulum hippocampus (L)	Non T2DM	30744	0.013900	0.848218	0.005 (-0.05, 0.06)	0.8	.006
	T2DM	1023	0.008530	0.935880			
Fornix cres+stria terminalis (R)	Non T2DM	30744	0.014593	0.840709	0.16 (0.10, 0.20)	<0.001	.194
	T2DM	1023	-0.148793	0.883083			
Fornix cres+stria terminalis (L)	Non T2DM	30744	0.012292	0.965105	0.14 (0.09, 0.20)	<0.001	.156
	T2DM	1023	-0.137504	0.895269			
Superior longitudinal fasciculus (R)	Non T2DM	30744	0.012050	0.962038	0.07 (0.014, 0.14)	0.01	.083
	T2DM	1023	-0.067619	1.047019			

Superior longitudinal fasciculus (L)	Non T2DM	30744	0.014155	0.930290	0.06 (0.001, 0.12)	0.04	.070
	T2DM	1023	-0.051120	1.017221			
Superior fronto-occipital fasciculus (R)	Non T2DM	30744	0.015462	0.918298	0.19 (0.13, 0.25)	<0.001	.215
	T2DM	1023	-0.182441	0.973257			
Superior fronto-occipital fasciculus (L)	Non T2DM	30744	0.011504	0.973226	0.19 (0.13, 0.25)	<0.001	.200
	T2DM	1023	-0.183004	0.966043			
Uncinate fasciculus (R)	Non T2DM	30744	0.010246	0.976528	0.06 (0.001, 0.12)	0.04	.064
	T2DM	1023	-0.052098	0.974881			
Uncinate fasciculus (L)	Non T2DM	30744	0.008272	0.935015	0.06 (0.005, 0.12)	0.03	.070
	T2DM	1023	-0.057296	0.965086			
Tapetum (R)	Non T2DM	30744	0.006080	0.960705	0.06 (0.001, 0.12)	0.04	.066
	T2DM	1023	-0.056955	0.988803			
Tapetum (L)	Non T2DM	30744	-0.005351	0.878749	0.05 (-0.009, 0.11)	0.5	.061
	T2DM	1023	-0.058803	1.001205			

Table 1B. MD and Intergroup Microstructural Differences.

MD WM Tracts and Group		N	Mean	Std. Deviation	Mean Difference (95% CI)	P-value	Effect Size
Middle cerebellar peduncle	Non T2DM	30744	-0.001583	0.945830	0.05 (0.005, 0.10)	0.07	0.05
	T2DM	1023	0.049991	0.904701			
Pontine crossing tract	Non T2DM	30744	-0.010952	0.852366	0.03 (0.02, 0.08)	0.28	0.03
	T2DM	1023	-0.042247	0.923266			
Genu of corpus callosum	Non T2DM	30744	-0.010638	0.869489	0.14 (0.08, 0.2)	<0.001	0.16
	T2DM	1023	0.132373	0.941657			
Body of corpus callosum	Non T2DM	30744	-0.010577	0.882668	0.15 (0.09, 0.2)	<0.001	0.17
	T2DM	1023	0.141621	0.945618			
Splenium of corpus callosum	Non T2DM	30744	-0.013656	0.814876	0.07 (0.009, 0.12)	0.02	0.08
	T2DM	1023	0.055546	0.952259			
Fornix	Non T2DM	30744	-0.002883	0.972785	0.1 (0.1, 0.2)	<0.001	0.16
	T2DM	1023	0.158132	0.790076			
Corticospinal tract (R)	Non T2DM	30744	-0.003705	0.976772	0.06 (0.001, 0.12)	0.04	0.06
	T2DM	1023	-0.065183	0.956244			
Corticospinal tract (L)	Non T2DM	30744	-0.005291	0.944221	0.03 (0.03, 0.09)	0.3	0.03
	T2DM	1023	-0.035476	0.977784			
Medial lemniscus (R)	Non T2DM	30744	-0.005511	0.943530	0.02 (0.03, 0.09)	0.3	0.03
	T2DM	1023	0.024341	0.964823			
Medial lemniscus (L)	Non T2DM	30744	-0.006934	0.900660	0.04 (0.01, 0.09)	0.18	0.04
	T2DM	1023	0.033513	0.949495			
Inferior cerebellar (R)	Non T2DM	30744	-0.006924	0.934781	0.06 (0.002, 0.12)	0.04	0.06
	T2DM	1023	0.057846	0.994718			
Inferior cerebellar (L)	Non T2DM	30744	-0.012038	0.857666	0.11 (0.05, 0.17)	<0.001	0.13
	T2DM	1023	0.102156	0.979747			
Superior cerebellar peduncle (R)	Non T2DM	30744	-0.013118	0.844110	0.21 (0.15, 0.27)	<0.001	0.25

	T2DM	1023	0.199189	0.966512			
Superior cerebellar peduncle (L)	Non T2DM	30744	-0.004196	0.889285	0.21 (0.15, 0.27)	<0.001	0.23
	T2DM	1023	0.208803	0.951419			
Cerebral peduncle (R)	Non T2DM	30744	-0.008075	0.931104	0.01 (0.04, 0.07)	0.59	0.01
	T2DM	1023	0.008364	0.954517			
Cerebral peduncle (L)	Non T2DM	30744	-0.008396	0.836658	0.03 (0.02, 0.09)	0.31	0.03
	T2DM	1023	0.022206	0.962617			
Anterior limb of internal capsule (R)	Non T2DM	30744	-0.008823	0.866220	0.05 (0.002, 0.11)	0.03	0.06
	T2DM	1023	0.050778	0.903179			
Anterior limb of internal capsule (L)	Non T2DM	30744	-0.008070	0.850539	0.04 (0.01, 0.10)	0.11	0.05
	T2DM	1023	0.039925	0.850539			
Posterior limb of internal capsule (R)	Non T2DM	30744	-0.007736	0.879087	0.07 (0.02, 0.13)	0.01	0.08
	T2DM	1023	0.070374	0.958745			
Posterior limb of internal capsule (L)	Non T2DM	30744	-0.009929	0.896865	0.09 (0.03, 0.15)	0.002	0.10
	T2DM	1023	0.082606	0.956571			
Retrolenticular part of internal capsule (R)	Non T2DM	30744	-0.010464	0.923660	0.05 (0.009, 0.11)	0.09	0.05
	T2DM	1023	0.043860	1.014059			
Retrolenticular part of internal capsule (L)	Non T2DM	30744	-0.013014	0.846507	0.08 (0.01, 0.14)	0.01	0.09
	T2DM	1023	0.067110	1.017404			
Anterior corona radiata (R)	Non T2DM	30744	-0.013743	0.849947	0.11 (0.05, 0.16)	<0.001	0.13
	T2DM	1023	0.098627	0.912647			
Anterior corona radiata (L)	Non T2DM	30744	-0.013365	0.813163	0.11 (0.05, 0.16)	<0.001	0.13
	T2DM	1023	0.097696	0.927430			
Superior corona radiata (R)	Non T2DM	30744	-0.015028	0.828408	0.10 (0.05, 0.16)	<0.001	0.13
	T2DM	1023	0.094478	0.911509			
Superior corona radiata (L)	Non T2DM	30744	-0.011284	0.855678	0.12 (0.07, 0.18)	<0.001	0.14
	T2DM	1023	0.116498	0.903788			
Posterior corona radiata (R)	Non T2DM	30744	-0.012103	0.875230	0.07 (0.016, 0.13)	0.01	0.08
	T2DM	1023	0.063315	0.945364			
Posterior corona radiata (L)	Non T2DM	30744	-0.010690	0.884201	0.09 (0.03, 0.15)	0.001	0.10
	T2DM	1023	0.083618	0.942719			
Posterior thalamic radiation (R)	Non T2DM	30744	-0.008993	0.875661	0.04 (0.01, 0.09)	0.16	0.04
	T2DM	1023	0.031514	0.921754			
Posterior thalamic radiation (L)	Non T2DM	30744	-0.011944	0.878229	0.03 (0.02, 0.08)	0.29	0.03
	T2DM	1023	0.019197	0.924939			
Sagittal stratum (R)	Non T2DM	30744	-0.011511	0.875434	0.07 (0.01, 0.13)	0.01	0.08
	T2DM	1023	0.060282	0.936762			
Sagittal stratum (L)	Non T2DM	30744	-0.014144	0.847473	0.08 (0.02, 0.14)	0.004	0.09
	T2DM	1023	0.069605	0.910546			
External capsule (R)	Non T2DM	30744	-0.013145	0.848591	0.11 (0.05, 0.17)	<0.001	0.13
	T2DM	1023	0.103757	0.919482			
External capsule (L)	Non T2DM	30744	-0.008395	0.853305	0.11 (0.05, 0.16)	<0.001	0.12
	T2DM	1023	0.102117	0.935666			
Cingulum cingulate gyrus (R)	Non T2DM	30744	-0.007566	0.872258	0.05 (0.005, 0.11)	0.07	0.06
	T2DM	1023	0.046486	0.947063			
Cingulum cingulate gyrus (L)	Non T2DM	30744	-0.002794	0.897824	0.04 (0.01, 0.10)	0.13	0.05

	T2DM	1023	0.043909	0.972382			
Cingulum hippocampus (R)	Non T2DM	30744	-0.004606	0.925845	0.06 (0.001, 0.12)	0.04	0.06
	T2DM	1023	-0.067027	0.963989			
Cingulum hippocampus (L)	Non T2DM	30744	-0.013202	0.835398	0.008 (-0.05, 0.06)	0.7	0.009
	T2DM	1023	-0.005012	0.971394			
Fornix cres+stria terminalis (R)	Non T2DM	30744	-0.011869	0.855022	0.15 (0.09, 0.2)	<0.001	0.17
	T2DM	1023	0.140289	0.937627			
Fornix cres+stria terminalis (L)	Non T2DM	30744	-0.011195	0.878797	0.15 (0.09, 0.2)	<0.001	0.17
	T2DM	1023	0.143742	0.931201			
Superior longitudinal fasciculus (R)	Non T2DM	30744	-0.011695	0.903452	0.05 (0.009, 0.11)	0.09	0.05
	T2DM	1023	0.040456	0.980111			
Superior longitudinal fasciculus (L)	Non T2DM	30744	-0.012387	0.809261	0.06 (0.002, 0.12)	0.03	0.07
	T2DM	1023	0.051710	0.978481			
Superior fronto-occipital fasciculus (R)	Non T2DM	30744	-0.015075	0.836346	0.16 (0.10, 0.21)	<0.001	0.19
	T2DM	1023	0.148578	0.888532			
Superior fronto-occipital fasciculus (L)	Non T2DM	30744	-0.012944	0.888199	0.15 (0.10, 0.21)	<0.001	0.17
	T2DM	1023	0.146217	0.913486			
Uncinate fasciculus (R)	Non T2DM	30744	-0.009583	0.858124	0.09 (0.03, 0.14)	0.002	0.10
	T2DM	1023	0.081419	0.930789			
Uncinate fasciculus (L)	Non T2DM	30744	-0.008948	0.912448	0.04 (0.01, 0.09)	0.14	0.04
	T2DM	1023	0.033251	0.910594			
Tapetum (R)	Non T2DM	30744	-0.007780	0.939976	0.09 (0.03, 0.15)	0.001	0.10
	T2DM	1023	0.090924	0.937740			
Tapetum (L)	Non T2DM	30744	-0.003542	0.755926	0.05 (0.008, 0.10)	0.09	0.06
	T2DM	1023	0.047024	0.939205			

Table 1C. AD and Intergroup Microstructural Differences.

AD WM Tracts and Group		N	Mean	Std. Deviation	Mean Difference (95% CI)	P-value	Effect Size
Middle cerebellar peduncle	Non T2DM	30744	-0.000001	0.872135	0.06 (0.012, 0.11)	0.015	0.06
	T2DM	1023	-0.000001	0.933573			
Pontine crossing tract	Non T2DM	30744	-0.003643	0.923278	0.03 (0.09, 0.016)	0.17	0.04
	T2DM	1023	-0.042206	0.961820			
Genu of corpus callosum	Non T2DM	30744	-0.000660	0.923572	0.06 (0.007, 0.12)	0.02	0.07
	T2DM	1023	0.064089	1.022912			
Body of corpus callosum	Non T2DM	30744	-0.003342	0.875846	0.04 (-0.09, 0.016)	0.16	0.04
	T2DM	1023	0.037294	0.970715			
Splenium of corpus callosum	Non T2DM	30744	-0.011976	0.896345	0.04 (0.008, 0.1)	0.09	0.05
	T2DM	1023	0.035632	0.866163			
Fornix	Non T2DM	30744	0.000987	0.868681	0.12 (0.06, 0.17)	<0.001	0.12
	T2DM	1023	0.122381	0.923362			
Corticospinal tract (R)	Non T2DM	30744	0.000177	0.878636	0.08 (0.02, 0.1)	0.007	0.08
	T2DM	1023	-0.080951	0.970260			

Corticospinal tract (L)	Non T2DM	30744	0.001675	0.872132	0.04 (0.01, 0.1)	0.13	0.04
	T2DM	1023	-0.044352	0.957249			
Medial lemniscus (R)	Non T2DM	30744	0.001575	0.912939	0.04 (0.01, 0.10)	0.16	0.04
	T2DM	1023	-0.042412	0.972131			
Medial lemniscus (L)	Non T2DM	30744	-0.001755	0.861372	0.03 (0.02, 0.09)	0.29	0.04
	T2DM	1023	-0.034810	0.982469			
Inferior cerebellar (R)	Non T2DM	30744	-0.001865	0.868967	0.01 (0.03, 0.06)	0.60	0.01
	T2DM	1023	-0.015933	0.927104			
Inferior cerebellar (L)	Non T2DM	30744	-0.000496	0.911460	0.01 (0.03, 0.07)	0.54	0.02
	T2DM	1023	0.017051	0.941059			
Superior cerebellar peduncle (R)	Non T2DM	30744	0.000941	0.760916	0.02 (0.07, 0.02)	0.28	0.03
	T2DM	1023	0.027590	0.774817			
Superior cerebellar peduncle (L)	Non T2DM	30744	0.006260	0.890016	0.01 (0.03, 0.06)	0.55	0.01
	T2DM	1023	0.022111	0.831469			
Cerebral peduncle (R)	Non T2DM	30744	0.003525	0.928097	0.08 (0.03, 0.14)	0.002	0.09
	T2DM	1023	-0.084260	0.917937			
Cerebral peduncle (L)	Non T2DM	30744	-0.004707	0.828934	0.07 (0.01, 0.12)	0.01	0.08
	T2DM	1023	-0.075310	0.915444			
Anterior limb of internal capsule (R)	Non T2DM	30744	0.018812	0.861586	0.02 (0.03, 0.07)	0.42	0.02
	T2DM	1023	-0.006919	0.903230			
Anterior limb of internal capsule (L)	Non T2DM	30744	0.016098	0.905530	0.02 (0.03, 0.08)	0.44	0.02
	T2DM	1023	-0.008404	0.952195			
Posterior limb of internal capsule (R)	Non T2DM	30744	-0.008404	0.923171	0.13 (0.07, 0.1)	<0.001	0.14
	T2DM	1023	0.127141	1.000958			
Posterior limb of internal capsule (L)	Non T2DM	30744	-0.006181	0.872550	0.15 (0.09, 0.2)	<0.001	0.17
	T2DM	1023	0.149775	0.992516			
Retrolenticular part of internal capsule (R)	Non T2DM	30744	-0.005599	0.883038	0.04 (0.01, 0.1)	0.104	0.05
	T2DM	1023	0.043401	0.944375			
Retrolenticular part of internal capsule (L)	Non T2DM	30744	-0.006309	0.892222	0.08 (0.02, 0.1)	0.008	0.08
	T2DM	1023	0.073864	0.958419			
Anterior corona radiata (R)	Non T2DM	30744	-0.006530	0.903225	0.06 (0.004, 0.12)	0.03	0.07
	T2DM	1023	0.057362	0.942926			
Anterior corona radiata (L)	Non T2DM	30744	-0.009355	0.839222	0.05 (0.009, 0.11)	0.09	0.06
	T2DM	1023	0.041539	0.967223			
Superior corona radiata (R)	Non T2DM	30744	-0.010404	0.844803	0.12 (0.06, 0.1)	<0.001	0.14
	T2DM	1023	0.112374	0.934231			
Superior corona radiata (L)	Non T2DM	30744	-0.011164	0.813793	0.14 (0.08, 0.1)	<0.001	0.17
	T2DM	1023	0.130720	0.919593			
Posterior corona radiata (R)	Non T2DM	30744	-0.011291	0.840908	0.09 (0.04, 0.15)	<0.001	0.11
	T2DM	1023	0.087489	0.902386			
Posterior corona radiata (L)	Non T2DM	30744	-0.000015	0.890276	0.09 (0.03, 0.1)	<0.001	0.10
	T2DM	1023	0.096567	0.918733			
Posterior thalamic radiation (R)	Non T2DM	30744	0.001648	0.887365	0.11 (0.05, 0.1)	<0.001	0.12
	T2DM	1023	-0.108784	0.942285			
Posterior thalamic radiation (L)	Non T2DM	30744	-0.004175	0.850097	0.12 (0.06, 0.18)	<0.001	0.14

	T2DM	1023	-0.127565	0.947306			
Sagittal stratum (R)	Non T2DM	30744	-0.002343	0.849107	0.04 (0.09, 0.01)	0.15	0.04
	T2DM	1023	-0.042466	0.872968			
Sagittal stratum (L)	Non T2DM	30744	-0.008432	0.866533	0.05 (0.005, 0.1)	0.03	0.06
	T2DM	1023	-0.066513	0.841665			
External capsule (R)	Non T2DM	30744	-0.008364	0.872135	0.08 (0.02, 0.1)	0.005	0.09
	T2DM	1023	0.073986	0.933573			
External capsule (L)	Non T2DM	30744	0.003084	0.923278	0.08 (0.02, 0.1)	0.008	0.08
	T2DM	1023	0.084580	0.961820			
Cingulum cingulate gyrus (R)	Non T2DM	30744	0.003921	0.923572	0.04 (0.01, 0.1)	0.17	0.04
	T2DM	1023	-0.040130	1.022912			
Cingulum cingulate gyrus (L)	Non T2DM	30744	-0.001900	0.875846	0.04 (0.01, 0.1)	0.18	0.04
	T2DM	1023	-0.043104	0.970715			
Cingulum hippocampus (R)	Non T2DM	30744	-0.002247	0.896345	0.04 (0.006, 0.1)	0.08	0.05
	T2DM	1023	-0.050638	0.866163			
Cingulum hippocampus (L)	Non T2DM	30744	-0.006947	0.868681	0.01 (0.04, 0.07)	0.56	0.01
	T2DM	1023	-0.024074	0.923362			
Fornix cres+stria terminalis (R)	Non T2DM	30744	-0.003274	0.878636	0.07 (0.01, 0.1)	0.01	0.08
	T2DM	1023	0.074426	0.970260			
Fornix cres+stria terminalis (L)	Non T2DM	30744	-0.006183	0.872132	0.06 (0.004, 0.12)	0.03	0.07
	T2DM	1023	0.058095	0.957249			
Superior longitudinal fasciculus (R)	Non T2DM	30744	-0.006986	0.912939	0.02 (-0.08, 0.03)	0.46	0.02
	T2DM	1023	0.015844	0.972131			
Superior longitudinal fasciculus (L)	Non T2DM	30744	-0.005596	0.861372	0.05 (0.008, 0.11)	0.09	0.06
	T2DM	1023	0.046861	0.982469			
Superior fronto-occipital fasciculus (R)	Non T2DM	30744	-0.009234	0.868967	0.06 (0.01, 0.1)	0.01	0.07
	T2DM	1023	0.060081	0.927104			
Superior fronto-occipital fasciculus (L)	Non T2DM	30744	-0.002873	0.911460	0.08 (0.02, 0.1)	0.007	0.08
	T2DM	1023	0.077354	0.941059			
Uncinate fasciculus (R)	Non T2DM	30744	-0.001580	0.889613	0.03 (0.02, 0.09)	0.25	0.03
	T2DM	1023	0.032790	0.948407			
Uncinate fasciculus (L)	Non T2DM	30744	-0.007549	0.914728	0.003 (-0.05, 0.06)	0.9	0.003
	T2DM	1023	-0.010950	0.934566			
Tapetum (R)	Non T2DM	30744	-0.007161	0.930896	0.10 (0.04, 0.1)	<0.001	0.11
	T2DM	1023	0.097121	0.941111			
Tapetum (L)	Non T2DM	30744	-0.004911	0.945215	0.05 (0.003, 0.11)	0.06	0.05
	T2DM	1023	0.049108	0.914327			

Table 1D. RD and Intergroup Microstructural Differences.

RD WM Tracts and Group		N	Mean	Std. Deviation	Mean Difference (95% CI)	P-value	Effect Size
Middle cerebellar peduncle	Non T2DM	30744	-0.002405	0.845976	0.03 (0.02, 0.09)	0.3	0.03
	T2DM	1023	0.028587	0.949222			
Pontine crossing tract	Non T2DM	30744	-0.013399	0.865917	0.4 (0.03, 0.08)	0.4	0.02
	T2DM	1023	-0.037585	0.903659			
Genu of corpus callosum	Non T2DM	30744	-0.013762	0.905275	0.16 (0.10, 0.22)	<0.001	0.18
	T2DM	1023	0.151666	0.943504			
Body of corpus callosum	Non T2DM	30744	-0.013020	0.888151	0.18 (0.12, 0.2)	<0.001	0.2
	T2DM	1023	0.167642	0.966194			
Splenium of corpus callosum	Non T2DM	30744	-0.014229	0.817146	0.06 (0.01, 0.12)	0.02	0.08
	T2DM	1023	0.055221	0.947744			
Fornix	Non T2DM	30744	-0.005132	0.937023	0.17 (0.12, 0.22)	<0.001	0.18
	T2DM	1023	0.170916	0.781074			
Corticospinal tract (R)	Non T2DM	30744	-0.005926	0.941534	0.03 (0.02, 0.08)	0.2	0.03
	T2DM	1023	-0.038568	0.908045			
Corticospinal tract (L)	Non T2DM	30744	-0.009168	0.889440	0.009 (0.06, 0.04)	0.7	0.01
	T2DM	1023	-0.018883	0.935638			
Medial lemniscus (R)	Non T2DM	30744	-0.009746	0.897430	0.08 (0.02, 0.13)	0.005	0.09
	T2DM	1023	0.071706	0.907780			
Medial lemniscus (L)	Non T2DM	30744	-0.007641	0.872308	0.09 (0.03, 0.15)	<0.001	0.10
	T2DM	1023	0.087385	0.889528			
Inferior cerebellar (R)	Non T2DM	30744	-0.007575	0.874592	0.09 (0.03, 0.14)	<0.001	0.10
	T2DM	1023	0.084823	0.916867			
Inferior cerebellar (L)	Non T2DM	30744	-0.017891	0.938018	0.13 (0.07, 0.18)	<0.001	0.14
	T2DM	1023	0.113452	0.890569			
Superior cerebellar peduncle (R)	Non T2DM	30744	-0.020631	0.920749	0.2 (0.2, 0.3)	<0.001	0.3
	T2DM	1023	0.275214	1.023144			
Superior cerebellar peduncle (L)	Non T2DM	30744	-0.011660	0.874132	0.3 (0.2, 0.3)	<0.001	0.3
	T2DM	1023	0.293889	0.982837			
Cerebral peduncle (R)	Non T2DM	30744	-0.012902	0.821892	0.09 (0.04, 0.15)	<0.001	0.11
	T2DM	1023	0.085740	0.935618			
Cerebral peduncle (L)	Non T2DM	30744	-0.013758	0.724479	0.09 (0.04, 0.15)	<0.001	0.13
	T2DM	1023	0.085820	0.863327			
Anterior limb of internal capsule (R)	Non T2DM	30744	-0.008826	0.801761	0.11 (0.06, 0.15)	<0.001	0.13
	T2DM	1023	0.101212	0.775470			
Anterior limb of internal capsule (L)	Non T2DM	30744	-0.004974	0.833259	0.05 (0.001, 0.11)	0.04	0.06
	T2DM	1023	0.051312	0.872308			
Posterior limb of internal capsule (R)	Non T2DM	30744	-0.002669	0.829215	0.003 (-0.05, 0.05)	0.9	0.004
	T2DM	1023	-0.006060	0.900053			
Posterior limb of internal capsule (L)	Non T2DM	30744	-0.009825	0.891815	0.01 (-0.04, 0.06)	0.6	0.01
	T2DM	1023	-0.020992	0.862397			
	Non T2DM	30744	-0.010522	0.906809	0.05 (0.01, 0.11)	0.10	0.05

Retrolenticular part of internal capsule (R)	T2DM	1023	0.040318	0.986493			
Retrolenticular part of internal capsule (L)	Non T2DM	30744	-0.014973	0.838416	0.06 (0.001, 0.12)	0.04	0.07
	T2DM	1023	0.048049	0.980474			
Anterior corona radiata (R)	Non T2DM	30744	-0.015979	0.831029	0.12 (-0.07, 0.18)	<0.001	0.15
	T2DM	1023	0.111630	0.897157			
Anterior corona radiata (L)	Non T2DM	30744	-0.012253	0.793566	0.13 (-0.07, 0.18)	<0.001	0.16
	T2DM	1023	0.119529	0.895658			
Superior corona radiata (R)	Non T2DM	30744	-0.013764	0.803671	0.07 (0.02, 0.13)	0.006	0.09
	T2DM	1023	0.063695	0.887676			
Superior corona radiata (L)	Non T2DM	30744	-0.009088	0.854033	0.08 (0.02, 0.14)	0.003	0.09
	T2DM	1023	0.074668	0.898453			
Posterior corona radiata (R)	Non T2DM	30744	-0.010442	0.865523	0.04 (0.01, 0.10)	0.10	0.05
	T2DM	1023	0.038683	0.953480			
Posterior corona radiata (L)	Non T2DM	30744	-0.014222	0.868883	0.07 (0.01, 0.13)	0.10	0.08
	T2DM	1023	0.063782	0.942532			
Posterior thalamic radiation (R)	Non T2DM	30744	-0.013086	0.870651	0.11 (0.06, 0.17)	<0.001	0.13
	T2DM	1023	0.103241	0.896766			
Posterior thalamic radiation (L)	Non T2DM	30744	-0.013521	0.887723	0.11 (0.05, 0.16)	<0.001	0.12
	T2DM	1023	0.098984	0.909027			
Sagittal stratum (R)	Non T2DM	30744	-0.014187	0.889908	0.12 (0.06, 0.18)	<0.001	0.13
	T2DM	1023	0.109808	0.916825			
Sagittal stratum (L)	Non T2DM	30744	-0.015120	0.841205	0.14 (0.09, 0.2)	<0.001	0.17
	T2DM	1023	0.133580	0.904474			
External capsule (R)	Non T2DM	30744	-0.013700	0.845976	0.1 (0.06, 0.1)	<0.001	0.14
	T2DM	1023	0.108423	0.893220			
External capsule (L)	Non T2DM	30744	-0.012957	0.873688	0.11 (0.05, 0.16)	<0.001	0.12
	T2DM	1023	0.098110	0.919754			
Cingulum cingulate gyrus (R)	Non T2DM	30744	-0.012227	0.884892	0.10 (0.04, 0.16)	<0.001	0.12
	T2DM	1023	0.097294	0.954022			
Cingulum cingulate gyrus (L)	Non T2DM	30744	-0.002255	0.904744	0.09 (0.03, 0.15)	<0.001	0.10
	T2DM	1023	0.092029	0.960273			
Cingulum hippocampus (R)	Non T2DM	30744	-0.004223	0.907273	0.04 (0.01, 0.1)	0.13	0.05
	T2DM	1023	-0.050656	0.960274			
Cingulum hippocampus (L)	Non T2DM	30744	-0.014456	0.805582	0.02 (0.03, 0.07)	0.4	0.02
	T2DM	1023	0.007244	0.931192			
Fornix cres+stria terminalis (R)	Non T2DM	30744	-0.014156	0.810745	0.17 (0.11, 0.22)	<0.001	0.2
	T2DM	1023	0.157755	0.877533			
Fornix cres+stria terminalis (L)	Non T2DM	30744	-0.012158	0.884928	0.17 (0.11, 0.22)	<0.001	0.19
	T2DM	1023	0.158686	0.878216			
Superior longitudinal fasciculus (R)	Non T2DM	30744	-0.011965	0.884860	0.06 (0.002, 0.12)	0.04	0.07
	T2DM	1023	0.052308	0.981165			
Superior longitudinal fasciculus (L)	Non T2DM	30744	-0.014440	0.811348	0.06 (0.006, 0.12)	0.03	0.08
	T2DM	1023	0.051393	0.954990			
Superior fronto-occipital fasciculus (R)	Non T2DM	30744	-0.016098	0.824481	0.1 (-0.1, 0.2)	<0.001	0.2
	T2DM	1023	0.182561	0.864502			

Superior fronto-occipital fasciculus (L)	Non T2DM	30744	-0.013329	0.889710	0.1 (-0.1, 0.2)	<0.001	0.2
	T2DM	1023	0.177257	0.890326			
Uncinate fasciculus (R)	Non T2DM	30744	-0.011117	0.882107	0.08 (0.02, 0.1)	0.003	0.09
	T2DM	1023	0.072304	0.895438			
Uncinate fasciculus (L)	Non T2DM	30744	-0.008503	0.909535	0.05 (0.003, 0.1)	0.03	0.06
	T2DM	1023	0.050920	0.898001			
Tapetum (R)	Non T2DM	30744	-0.007027	0.926095	0.08 (0.02, 0.1)	0.004	0.09
	T2DM	1023	0.078961	0.943502			
Tapetum (L)	Non T2DM	30744	0.008809	0.934078	0.05 (0.003, 0.1)	0.06	0.05
	T2DM	1023	0.064805	0.956323			

Table 2A. ICVF and Intergroup Microstructural Differences.

ICVF WM Tracts and Group		N	Mean	Std. Deviation	Mean Difference (95% CI)	P-value	Effect Size
Middle cerebellar peduncle	Non T2DM	30744	0.007305	0.935464	0.05 (0.0007, 0.11)	0.05	0.06
	T2DM	1023	-0.052008	0.958151			
Pontine crossing tract	Non T2DM	30744	0.013752	0.947362	0.11 (0.05, 0.17)	<0.001	0.12
	T2DM	1023	-0.102644	0.923836			
Genu of corpus callosum	Non T2DM	30744	0.012168	0.982307	0.09 (0.03, 0.15)	0.002	0.09
	T2DM	1023	-0.083856	1.006732			
Body of corpus callosum	Non T2DM	30744	0.013805	0.934921	0.06 (0.0004, 0.12)	0.04	0.06
	T2DM	1023	-0.050644	1.023081			
Splenium of corpus callosum	Non T2DM	30744	0.013228	0.956534	0.12 (0.06, 0.18)	<0.001	0.12
	T2DM	1023	-0.111102	1.008044			
Fornix	Non T2DM	30744	0.006580	0.939642	0.19 (0.13, 0.26)	<0.001	0.21
	T2DM	1023	-0.192190	0.998659			
Corticospinal tract (R)	Non T2DM	30744	0.003378	0.949858	0.02 (-0.03, 0.08)	0.36	0.02
	T2DM	1023	-0.023140	0.910225			
Corticospinal tract (L)	Non T2DM	30744	0.005813	0.830708	0.02 (-0.02, 0.08)	0.32	0.03
	T2DM	1023	-0.022839	0.915464			
Medial lemniscus (R)	Non T2DM	30744	0.005903	0.808081	0.06 (0.01, 0.12)	0.01	0.08
	T2DM	1023	-0.061863	0.861544			
Medial lemniscus (L)	Non T2DM	30744	0.007553	0.907300	0.04 (-0.002, 0.10)	0.05	0.05
	T2DM	1023	-0.042175	0.822183			
Inferior cerebellar (R)	Non T2DM	30744	0.005544	0.900852	0.05 (-0.006, 0.11)	0.07	0.06
	T2DM	1023	-0.049497	0.976566			
Inferior cerebellar (L)	Non T2DM	30744	0.011320	0.928408	0.08 (0.01, 0.1)	0.01	0.08
	T2DM	1023	-0.068900	0.977558			
Superior cerebellar peduncle (R)	Non T2DM	30744	0.013143	0.951835	0.15 (0.09, 0.22)	<0.001	0.16
	T2DM	1023	-0.145144	0.997603			
Superior cerebellar peduncle (L)	Non T2DM	30744	-0.001466	0.949323	0.16 (0.10, 0.23)	<0.001	0.17
	T2DM	1023	-0.169756	1.040100			
Cerebral peduncle (R)	Non T2DM	30744	0.000089	0.960860	0.06 (0.002, 0.12)	0.06	0.06
	T2DM	1023	0.061296	1.023845			

Cerebral peduncle (L)	Non T2DM	30744	0.009419	0.909809	0.03 (0.02, 0.10)	0.2	0.04
	T2DM	1023	0.048258	1.040465			
Anterior limb of internal capsule (R)	Non T2DM	30744	0.008993	0.913770	0.06 (0.001, 0.12)	0.05	0.06
	T2DM	1023	-0.051018	0.986035			
Anterior limb of internal capsule (L)	Non T2DM	30744	0.012157	0.937554	0.05 (0.01, 0.11)	0.10	0.05
	T2DM	1023	-0.039859	0.997528			
Posterior limb of internal capsule (R)	Non T2DM	30744	0.013524	0.946490	0.08 (0.01, 0.14)	0.01	0.08
	T2DM	1023	-0.067725	1.027955			
Posterior limb of internal capsule (L)	Non T2DM	30744	0.014677	0.945950	0.12 (0.18, 0.05)	<0.001	0.12
	T2DM	1023	-0.106113	1.048330			
Retrolenticular part of internal capsule (R)	Non T2DM	30744	0.014723	0.961711	0.12 (0.06, 0.18)	<0.001	0.12
	T2DM	1023	-0.110239	1.013046			
Retrolenticular part of internal capsule (L)	Non T2DM	30744	0.013687	0.898558	0.11 (0.05, 0.18)	<0.001	0.12
	T2DM	1023	-0.103303	1.021569			
Anterior corona radiata (R)	Non T2DM	30744	0.014989	0.901404	0.11 (0.06, 0.17)	<0.001	0.13
	T2DM	1023	-0.104982	0.951211			
Anterior corona radiata (L)	Non T2DM	30744	0.017582	0.915876	0.12 (0.06, 0.18)	<0.001	0.13
	T2DM	1023	-0.109206	0.958018			
Superior corona radiata (R)	Non T2DM	30744	0.018503	0.906818	0.15 (0.09, 0.21)	<0.001	0.17
	T2DM	1023	-0.139659	0.971252			
Superior corona radiata (L)	Non T2DM	30744	0.013050	0.924112	0.15 (0.09, 0.21)	<0.001	0.16
	T2DM	1023	-0.141316	0.958475			
Posterior corona radiata (R)	Non T2DM	30744	0.013777	0.928688	0.09 (0.02, 0.15)	0.003	0.09
	T2DM	1023	-0.077840	0.992335			
Posterior corona radiata (L)	Non T2DM	30744	0.014517	0.929517	0.09 (0.03, 0.16)	0.001	0.10
	T2DM	1023	-0.084202	0.981826			
Posterior thalamic radiation (R)	Non T2DM	30744	0.013779	0.921806	0.09 (0.03, 0.14)	0.002	0.09
	T2DM	1023	-0.076372	0.947578			
Posterior thalamic radiation (L)	Non T2DM	30744	0.014437	0.942606	0.07 (0.01, 0.13)	0.015	0.07
	T2DM	1023	-0.059944	0.956972			
Sagittal stratum (R)	Non T2DM	30744	0.016588	0.934322	0.09 (0.03, 0.15)	0.001	0.10
	T2DM	1023	-0.080705	0.970561			
Sagittal stratum (L)	Non T2DM	30744	0.015540	0.885872	0.11 (0.05, 0.17)	<0.001	0.13
	T2DM	1023	-0.101366	0.966310			
External capsule (R)	Non T2DM	30744	0.015123	0.879652	0.14 (0.08, 0.19)	<0.001	0.15
	T2DM	1023	-0.125699	0.931929			
External capsule (L)	Non T2DM	30744	0.014958	0.923529	0.14 (0.08, 0.20)	<0.001	0.16
	T2DM	1023	-0.133572	0.943206			
Cingulum cingulate gyrus (R)	Non T2DM	30744	0.016090	0.925023	0.11 (0.05, 0.17)	<0.001	0.12
	T2DM	1023	-0.096621	0.986934			
Cingulum cingulate gyrus (L)	Non T2DM	30744	0.006243	0.918606	0.12 (0.06, 0.18)	<0.001	0.13
	T2DM	1023	-0.118774	0.990442			
Cingulum hippocampus (R)	Non T2DM	30744	0.006594	0.934339	0.009 (0.06, 0.04)	0.7	0.009
	T2DM	1023	-0.002724	0.940100			
Cingulum hippocampus (L)	Non T2DM	30744	0.012025	0.951938	0.01 (-0.04, 0.07)	0.6	0.013

	T2DM	1023	-0.001045	0.955866			
Fornix cres+stria terminalis (R)	Non T2DM	30744	0.010863	0.935298	0.05 (0.006, 0.12)	0.07	0.06
	T2DM	1023	-0.046129	1.009935			
Fornix cres+stria terminalis (L)	Non T2DM	30744	0.013831	0.951016	0.05 (0.01, 0.11)	0.10	0.05
	T2DM	1023	-0.039651	1.024503			
Superior longitudinal fasciculus (R)	Non T2DM	30744	0.015077	0.935487	0.08 (0.01, 0.14)	0.01	0.08
	T2DM	1023	-0.066900	1.037746			
Superior longitudinal fasciculus (L)	Non T2DM	30744	0.015536	0.862444	0.09 (0.03, 0.15)	0.002	0.11
	T2DM	1023	-0.080151	1.007992			
Superior fronto-occipital fasciculus (R)	Non T2DM	30744	0.018558	0.853049	0.18 (0.12, 0.24)	<0.001	0.21
	T2DM	1023	-0.164564	0.920750			
Superior fronto-occipital fasciculus (L)	Non T2DM	30744	0.013831	0.914145	0.18 (0.12, 0.24)	<0.001	0.20
	T2DM	1023	-0.171707	0.905407			
Uncinate fasciculus (R)	Non T2DM	30744	0.014541	0.901027	0.08 (0.03, 0.14)	0.003	0.09
	T2DM	1023	-0.074302	0.937474			
Uncinate fasciculus (L)	Non T2DM	30744	0.008865	0.904342	0.08 (0.02, 0.14)	0.003	0.09
	T2DM	1023	-0.078115	0.922350			
Tapetum (R)	Non T2DM	30744	0.009903	0.911257	0.04 (0.10, -0.01)	0.15	0.04
	T2DM	1023	-0.034038	0.962457			
Tapetum (L)	Non T2DM	30744	-0.002873	0.797617	0.05 (0.001, 0.11)	0.04	0.07
	T2DM	1023	-0.062719	0.931776			

Table 2B. ODI and Intergroup Microstructural Differences.

ODI WM Tracts and Group		N	Mean	Std. Deviation	Mean Difference (95% CI)	P-value	Effect Size
Middle cerebellar peduncle	Non T2DM	30744	-0.005190	0.857172	0.02 (-0.02, 0.08)	0.29	0.03
	T2DM	1023	-0.033455	0.839697			
Pontine crossing tract	Non T2DM	30744	-0.007099	0.941694	0.01 (-0.03, 0.07)	0.49	0.02
	T2DM	1023	0.012605	0.904039			
Genu of corpus callosum	Non T2DM	30744	-0.011982	0.952362	0.08 (0.02, 0.14)	0.005	0.09
	T2DM	1023	0.074936	0.968357			
Body of corpus callosum	Non T2DM	30744	-0.001146	0.907609	0.20 (0.14, 0.26)	<0.001	0.2
	T2DM	1023	0.202081	0.974723			
Splenium of corpus callosum	Non T2DM	30744	-0.009731	0.892025	0.02 (-0.02, 0.08)	0.31	0.03
	T2DM	1023	-0.038655	0.904970			
Fornix	Non T2DM	30744	-0.005118	0.958853	0.11 (0.05, 0.17)	<0.001	0.12
	T2DM	1023	0.110051	0.885119			
Corticospinal tract (R)	Non T2DM	30744	-0.003949	0.968740	0.004 (-0.06, 0.05)	0.86	0.005
	T2DM	1023	0.000980	0.911349			
Corticospinal tract (L)	Non T2DM	30744	-0.010414	0.947906	0.0006 (-0.05, 0.05)	0.98	0.0006
	T2DM	1023	-0.011073	0.938046			
Medial lemniscus (R)	Non T2DM	30744	-0.011443	0.959868	0.13 (0.07, 0.19)	<0.001	0.14
	T2DM	1023	0.124786	0.944640			

Medial lemniscus (L)	Non T2DM	30744	-0.004712	0.845930	0.12 (0.06, 0.18)	<0.001	0.15
	T2DM	1023	0.123324	0.940109			
Inferior cerebellar (R)	Non T2DM	30744	-0.004112	0.880042	0.05 (0.0002, 0.10)	0.05	0.05
	T2DM	1023	0.048501	0.840193			
Inferior cerebellar (L)	Non T2DM	30744	-0.010957	0.893798	0.05 (0.006, 0.11)	0.02	0.06
	T2DM	1023	0.048599	0.847591			
Superior cerebellar peduncle (R)	Non T2DM	30744	-0.013024	0.903371	0.17 (0.11, 0.22)	<0.001	0.18
	T2DM	1023	0.158095	0.901599			
Superior cerebellar peduncle (L)	Non T2DM	30744	-0.012037	0.914330	0.16 (0.10, 0.22)	<0.001	0.17
	T2DM	1023	0.150871	0.959364			
Cerebral peduncle (R)	Non T2DM	30744	-0.011015	0.926919	0.14 (0.08, 0.20)	<0.001	0.15
	T2DM	1023	0.135336	0.934380			
Cerebral peduncle (L)	Non T2DM	30744	-0.008090	0.958322	0.12 (0.06, 0.18)	<0.001	0.13
	T2DM	1023	0.118134	0.951124			
Anterior limb of internal capsule (R)	Non T2DM	30744	-0.010268	0.959925	0.13 (0.07, 0.19)	<0.001	0.14
	T2DM	1023	0.126705	1.000312			
Anterior limb of internal capsule (L)	Non T2DM	30744	0.007647	0.955832	0.12 (0.06, 0.18)	<0.001	0.13
	T2DM	1023	0.133409	0.989242			
Posterior limb of internal capsule (R)	Non T2DM	30744	0.007563	0.962214	0.15 (0.08, 0.21)	<0.001	0.15
	T2DM	1023	-0.143466	1.034879			
Posterior limb of internal capsule (L)	Non T2DM	30744	0.000256	0.926209	0.15 (0.08, 0.21)	<0.001	0.16
	T2DM	1023	-0.150181	1.015262			
Retrolenticular part of internal capsule (R)	Non T2DM	30744	-0.000264	0.917092	0.002 (-0.05, 0.05)	0.94	0.002
	T2DM	1023	-0.002305	0.921240			
Retrolenticular part of internal capsule (L)	Non T2DM	30744	-0.006097	0.973955	0.001 (-0.06, 0.05)	0.97	0.001
	T2DM	1023	-0.007204	0.959180			
Anterior corona radiata (R)	Non T2DM	30744	-0.008931	0.969186	0.05 (-0.003, 0.12)	0.06	0.06
	T2DM	1023	0.049916	1.001484			
Anterior corona radiata (L)	Non T2DM	30744	0.005219	0.942173	0.09 (0.03, 0.15)	0.003	0.09
	T2DM	1023	0.097684	0.993173			
Superior corona radiata (R)	Non T2DM	30744	0.004413	0.939878	0.10 (0.03, 0.16)	0.002	0.10
	T2DM	1023	-0.099003	1.028563			
Superior corona radiata (L)	Non T2DM	30744	0.007727	0.897646	0.11 (0.05, 0.18)	<0.001	0.13
	T2DM	1023	-0.109667	1.027891			
Posterior corona radiata (R)	Non T2DM	30744	0.006224	0.915638	0.07 (0.01, 0.13)	0.011	0.08
	T2DM	1023	-0.071236	0.946985			
Posterior corona radiata (L)	Non T2DM	30744	-0.007952	0.935580	0.04 (0.01, 0.11)	0.12	0.05
	T2DM	1023	-0.056359	0.987689			
Posterior thalamic radiation (R)	Non T2DM	30744	-0.010031	0.939926	0.19 (0.13, 0.25)	<0.001	0.20
	T2DM	1023	0.184935	1.007304			
Posterior thalamic radiation (L)	Non T2DM	30744	-0.003149	0.921666	0.23 (0.17, 0.29)	<0.001	0.25
	T2DM	1023	0.235931	0.954791			
Sagittal stratum (R)	Non T2DM	30744	-0.004774	0.918831	0.10 (0.04, 0.16)	<0.001	0.11
	T2DM	1023	0.098195	0.918600			
Sagittal stratum (L)	Non T2DM	30744	-0.002870	0.925468	0.14 (0.08, 0.20)	<0.001	0.15
	T2DM	1023	0.141023	0.922066			

External capsule (R)	Non T2DM	30744	-0.003427	0.934322	0.0005 (-0.05, 0.05)	0.98	0.0006
	T2DM	1023	-0.003990	0.945501			
External capsule (L)	Non T2DM	30744	-0.010075	0.947605	0.003 (-0.05, 0.06)	0.90	0.003
	T2DM	1023	-0.006377	0.977678			
Cingulum cingulate gyrus (R)	Non T2DM	30744	-0.009250	0.942056	0.10 (0.03, 0.16)	0.002	0.10
	T2DM	1023	0.091791	1.009608			
Cingulum cingulate gyrus (L)	Non T2DM	30744	-0.002937	0.894430	0.08 (0.02, 0.14)	0.008	0.09
	T2DM	1023	0.078417	0.964793			
Cingulum hippocampus (R)	Non T2DM	30744	-0.002711	0.885484	0.03 (0.01, 0.09)	0.16	0.04
	T2DM	1023	0.034950	0.845112			
Cingulum hippocampus (L)	Non T2DM	30744	-0.006460	0.879842	0.05 (0.0008, 0.11)	0.04	0.06
	T2DM	1023	0.049238	0.874294			
Fornix cres+stria terminalis (R)	Non T2DM	30744	-0.007578	0.873578	0.11 (0.05, 0.16)	<0.001	0.12
	T2DM	1023	0.104449	0.893969			
Fornix cres+stria terminalis (L)	Non T2DM	30744	-0.002845	0.968626	0.10 (0.04, 0.15)	<0.001	0.10
	T2DM	1023	0.099052	0.864037			
Superior longitudinal fasciculus (R)	Non T2DM	30744	-0.003203	0.978478	0.04 (0.01, 0.11)	0.12	0.05
	T2DM	1023	0.045510	0.994962			
Superior longitudinal fasciculus (L)	Non T2DM	30744	-0.003849	0.975460	0.001 (-0.06, 0.06)	0.97	0.001
	T2DM	1023	-0.002668	0.986645			
Superior fronto-occipital fasciculus (R)	Non T2DM	30744	-0.004571	0.973629	0.07 (0.016, 0.13)	0.013	0.07
	T2DM	1023	0.072452	0.968336			
Superior fronto-occipital fasciculus (L)	Non T2DM	30744	-0.005291	0.962966	0.07 (0.007, 0.13)	0.028	0.07
	T2DM	1023	0.066096	1.016324			
Uncinate fasciculus (R)	Non T2DM	30744	-0.006810	0.952605	0.03 (0.02, 0.09)	0.24	0.03
	T2DM	1023	0.030030	0.984050			
Uncinate fasciculus (L)	Non T2DM	30744	-0.001043	0.971948	0.05 (0.01, 0.11)	0.10	0.05
	T2DM	1023	0.049051	0.970575			
Tapetum (R)	Non T2DM	30744	0.001961	0.953706	0.003 (-0.05, 0.06)	0.90	0.004
	T2DM	1023	-0.001977	1.019943			
Tapetum (L)	Non T2DM	30744	-0.001174	0.920813	0.01 (0.04, 0.07)	0.52	0.02
	T2DM	1023	-0.020590	0.960777			

Table 2C. IsoVF and Intergroup Microstructural Differences.

IsoVF WM Tracts and Group		N	Mean	Std. Deviation	Mean Difference (95% CI)	P-value	Effect Size
Middle cerebellar peduncle	Non T2DM	30744	0.000395	0.962973	0.02 (0.03, 0.07)	0.46	0.02
	T2DM	1023	0.022047	0.925563			
Pontine crossing tract	Non T2DM	30744	-0.005706	0.842666	0.06 (0.01, 0.12)	0.02	0.08
	T2DM	1023	-0.075122	0.936179			
Genu of corpus callosum	Non T2DM	30744	-0.006912	0.820624	0.13 (0.08, 0.19)	<0.001	0.16
	T2DM	1023	0.132276	0.916119			
Body of corpus callosum	Non T2DM	30744	-0.004719	0.893079	0.15 (0.1, 0.2)	<0.001	0.17
	T2DM	1023	0.154832	0.904973			

Splenium of corpus callosum	Non T2DM	30744	-0.012738	0.805552	0.011 (0.04, 0.07)	0.69	0.01
	T2DM	1023	-0.001215	0.946458			
Fornix	Non T2DM	30744	0.153296	0.986212	0.15 (0.10, 0.20)	<0.001	0.15
	T2DM	1023	-0.002194	0.818421			
Corticospinal tract (R)	Non T2DM	30744	-0.071081	0.987462	0.06 (0.008, 0.12)	0.02	0.06
	T2DM	1023	-0.004541	0.967024			
Corticospinal tract (L)	Non T2DM	30744	-0.046536	0.931960	0.04 (0.10, 0.018)	0.17	0.04
	T2DM	1023	-0.004002	0.965029			
Medial lemniscus (R)	Non T2DM	30744	-0.001475	0.909720	0.002 (-0.05, 0.05)	0.93	0.002
	T2DM	1023	-0.002157	0.907755			
Medial lemniscus (L)	Non T2DM	30744	0.023080	0.955348	0.02 (-0.03, 0.08)	0.37	0.02
	T2DM	1023	-0.003175	0.888243			
Inferior cerebellar (R)	Non T2DM	30744	0.024585	0.923092	0.02 (0.03, 0.09)	0.39	0.02
	T2DM	1023	-0.010869	1.029921			
Inferior cerebellar (L)	Non T2DM	30744	0.052014	0.908929	0.06 (0.001, 0.12)	0.04	0.06
	T2DM	1023	-0.011287	0.980363			
Superior cerebellar peduncle (R)	Non T2DM	30744	0.169801	0.885406	0.18 (0.11, 0.24)	<0.001	0.20
	T2DM	1023	-0.007133	0.995268			
Superior cerebellar peduncle (L)	Non T2DM	30744	0.172560	0.898507	0.17 (0.11, 0.24)	<0.001	0.19
	T2DM	1023	-0.011059	0.964452			
Cerebral peduncle (R)	Non T2DM	30744	0.064267	0.933830	0.07 (0.01, 0.13)	0.01	0.08
	T2DM	1023	-0.004303	0.915960			
Cerebral peduncle (L)	Non T2DM	30744	0.066351	0.872339	0.07 (0.01, 0.12)	0.01	0.08
	T2DM	1023	-0.007063	0.939727			
Anterior limb of internal capsule (R)	Non T2DM	30744	-0.007063	0.913543	0.04 (0.01, 0.10)	0.15	0.04
	T2DM	1023	0.036536	0.947847			
Anterior limb of internal capsule (L)	Non T2DM	30744	-0.000411	0.847361	0.04 (0.02, 0.10)	0.19	0.04
	T2DM	1023	0.040179	0.988671			
Posterior limb of internal capsule (R)	Non T2DM	30744	0.001112	0.895080	0.006 (-0.05, 0.06)	0.81	0.007
	T2DM	1023	0.007967	0.941109			
Posterior limb of internal capsule (L)	Non T2DM	30744	0.000211	0.905044	0.008 (-0.04, 0.06)	0.76	0.009
	T2DM	1023	-0.008758	0.936373			
Retrolenticular part of internal capsule (R)	Non T2DM	30744	0.000216	0.948117	0.02 (-0.03, 0.08)	0.38	0.02
	T2DM	1023	-0.026955	0.979318			
Retrolenticular part of internal capsule (L)	Non T2DM	30744	-0.001685	0.864042	0.003 (-0.05, 0.06)	0.90	0.004
	T2DM	1023	0.002206	0.984961			
Anterior corona radiata (R)	Non T2DM	30744	-0.002656	0.867217	0.03 (0.02, 0.09)	0.28	0.03
	T2DM	1023	0.029989	0.962813			
Anterior corona radiata (L)	Non T2DM	30744	0.000485	0.775599	0.03 (0.02, 0.09)	0.21	0.04
	T2DM	1023	0.037163	0.919515			
Superior corona radiata (R)	Non T2DM	30744	0.000005	0.828937	0.01 (-0.03, 0.07)	0.53	0.02
	T2DM	1023	-0.017272	0.878636			
Superior corona radiata (L)	Non T2DM	30744	-0.000889	0.845752	0.007 (-0.04, 0.06)	0.79	0.008
	T2DM	1023	0.006696	0.917607			
Posterior corona radiata (R)	Non T2DM	30744	-0.000258	0.889272	0.01 (-0.03, 0.07)	0.54	0.02

	T2DM	1023	0.017809	0.926113			
Posterior corona radiata (L)	Non T2DM	30744	0.001612	0.878026	0.02 (-0.03, 0.08)	0.35	0.03
	T2DM	1023	0.029965	0.956673			
Posterior thalamic radiation (R)	Non T2DM	30744	0.001934	0.903640	0.03 (-0.02, 0.09)	0.22	0.04
	T2DM	1023	-0.034446	0.933197			
Posterior thalamic radiation (L)	Non T2DM	30744	0.001111	0.868402	0.02 (-0.03, 0.08)	0.40	0.02
	T2DM	1023	-0.024278	0.957416			
Sagittal stratum (R)	Non T2DM	30744	0.003850	0.914507	0.01 (-0.04, 0.06)	0.67	0.01
	T2DM	1023	0.015848	0.898017			
Sagittal stratum (L)	Non T2DM	30744	-0.006177	0.911352	0.03 (-0.02, 0.09)	0.22	0.04
	T2DM	1023	0.030560	0.955080			
External capsule (R)	Non T2DM	30744	-0.006278	0.927114	0.05 (0.01, 0.11)	0.10	0.05
	T2DM	1023	0.045566	0.994139			
External capsule (L)	Non T2DM	30744	0.004396	0.884328	0.05 (0.01, 0.11)	0.10	0.05
	T2DM	1023	0.056082	0.987675			
Cingulum cingulate gyrus (R)	Non T2DM	30744	0.007014	0.897091	0.02 (0.03, 0.08)	0.36	0.03
	T2DM	1023	-0.020400	0.946805			
Cingulum cingulate gyrus (L)	Non T2DM	30744	-0.004294	0.953645	0.04 (0.01, 0.10)	0.14	0.04
	T2DM	1023	-0.049456	0.978928			
Cingulum hippocampus (R)	Non T2DM	30744	-0.008083	0.931541	0.02 (-0.03, 0.08)	0.38	0.02
	T2DM	1023	0.018931	0.967138			
Cingulum hippocampus (L)	Non T2DM	30744	-0.008989	0.862395	0.11 (0.05, 0.16)	<0.001	0.12
	T2DM	1023	0.101430	0.944290			
Fornix cres+stria terminalis (R)	Non T2DM	30744	-0.008366	0.862746	0.13 (0.07, 0.19)	<0.001	0.15
	T2DM	1023	0.126734	0.951706			
Fornix cres+stria terminalis (L)	Non T2DM	30744	-0.001220	0.833280	0.13 (0.07, 0.18)	<0.001	0.15
	T2DM	1023	0.129595	0.933310			
Superior longitudinal fasciculus (R)	Non T2DM	30744	0.000831	0.922646	0.004 (-0.05, 0.06)	0.86	0.005
	T2DM	1023	-0.003976	0.904307			
Superior longitudinal fasciculus (L)	Non T2DM	30744	-0.002597	0.883867	0.01 (-0.04, 0.07)	0.61	0.01
	T2DM	1023	-0.018648	1.003450			
Superior fronto-occipital fasciculus (R)	Non T2DM	30744	-0.004833	0.901788	0.06 (0.006, 0.12)	0.03	0.07
	T2DM	1023	0.061579	0.962467			
Superior fronto-occipital fasciculus (L)	Non T2DM	30744	-0.003185	0.958573	0.06 (0.002, 0.12)	0.04	0.06
	T2DM	1023	0.062018	0.995493			
Uncinate fasciculus (R)	Non T2DM	30744	-0.003881	0.962372	0.05 (0.002, 0.11)	0.06	0.05
	T2DM	1023	0.053758	0.961407			
Uncinate fasciculus (L)	Non T2DM	30744	-0.005729	0.944641	0.01 (-0.04, 0.07)	0.65	0.01
	T2DM	1023	0.008154	0.985841			
Tapetum (R)	Non T2DM	30744	-0.002269	0.955953	0.10 (0.04, 0.16)	<0.001	0.10
	T2DM	1023	0.099335	0.966802			
Tapetum (L)	Non T2DM	30744	-0.002269	0.955953	0.01 (-0.04, 0.07)	0.66	0.01
	T2DM	1023	0.011437	0.989257			

Table 3. Associations between disease duration/HbA1c and White Matter changes in T2DM participants. NS= not significant.

WM Tracts and Fibres		FA		MD		AD		RD		ICVF		ODI		IsoVF	
		Disease duration	Hb1Ac	Disease duration	Hb1Ac	Disease duration	Hb1Ac	Disease duration	Hb1Ac	Disease duration	Hb1Ac	Disease duration	Hb1Ac	Disease duration	Hb1Ac
Middle cerebellar peduncle	Correlation (r)	NS	NS	NS	NS	0.07	0.01	NS	NS	NS	NS	NS	NS	NS	NS
	P-value					0.02	0.001								
Pontine crossing tract	Correlation (r)	NS	NS	NS	NS	NS	NS	NS	NS	-0.06	-0.01	NS	NS	NS	NS
	P-value									0.04	0.001				
Genu of corpus callosum	Correlation (r)	-0.03	-0.02	0.11	0.02	0.01	0.006	0.08	0.02	-0.08	-0.01	-0.01	0.01	0.09	0.01
	P-value	0.22	<0.001	<0.001	<0.001	<0.001	0.2	0.005	<0.001	0.005	0.002	0.59	0.06	0.002	0.002
Body of corpus callosum	Correlation (r)	-0.06	-0.02	0.09	0.01	NS	NS	0.08	0.02	-0.07	-0.01	0.02	0.02	0.05	0.01
	P-value	0.02	<0.001	0.002	0.003			0.005	<0.001	0.01	0.007	0.46	<0.001	0.06	0.05
Splenium of the corpus callosum	Correlation (r)	-0.06	-0.01	0.11	0.019	NS	NS	0.10	0.01	-0.1	-0.02	NS	NS	NS	NS
	P-value	0.03	<0.001	<0.001	<0.001			<0.001	<0.001	<0.001	<0.001				
Fornix	Correlation (r)	-0.08	-0.02	0.04	0.01	0.05	0.007	0.04	0.01	-0.05	-0.02	0.001	0.01	0.05	0.01
	P-value	0.007	<0.001	0.13	0.01	0.07	0.18	0.2	<0.001	0.06	<0.001	0.97	0.003	0.11	0.01
Corticospinal tract (R)	Correlation (r)	NS	NS	NS	NS	0.04	-0.004	NS	NS	NS	NS	NS	NS	0.01	-0.002
	P-value					0.1	0.4							0.6	0.63
Corticospinal tract (L)	Correlation (r)	NS	NS	NS	NS	NS	NS	NS	NS	NS	NS	NS	NS	NS	NS
	P-value														
Medial lemniscus (R)	Correlation (r)	-0.07	-0.02	NS	NS	NS	NS	0.07	0.02	-0.08	-0.02	0.04	0.008	NS	NS
	P-value	0.02	<0.001					0.01	<0.001	0.006	<0.001	0.17	0.16		
Medial lemniscus (L)	Correlation (r)	-0.08	-0.02	NS	NS	NS	NS	0.07	0.02	NS	NS	0.03	0.02	NS	NS
	P-value	0.009	<0.001					0.02	<0.001			0.24	<0.001		
Inferior cerebellar peduncle (R)	Correlation (r)	-0.08	-0.01	0.07	0.01	NS	NS	0.07	0.02	NS	NS	NS	NS	NS	NS
	P-value	0.009	0.003	0.01	0.003			0.01	<0.001						
Inferior cerebellar peduncle (L)	Correlation (r)	-0.05	-0.02	0.07	0.03	NS	NS	0.07	0.03	-0.06	-0.02	0.01	0.01	0.01	0.01
	P-value	0.08	<0.001	0.01	<0.001			0.01	<0.001	0.03	<0.001	0.57	0.07	0.62	0.005
Superior cerebellar peduncle (R)	Correlation (r)	-0.05	-0.04	0.09	0.03	NS	NS	0.09	0.04	-0.02	-0.02	0.03	0.02	0.09	0.03
	P-value	0.09	<0.001	0.002	<0.001			0.002	<0.001	0.46	<0.001	0.21	<0.001	0.003	<0.001
Superior cerebellar peduncle (L)	Correlation (r)	-0.07	-0.03	0.06	0.01	NS	NS	0.07	0.03	-0.03	-0.01	0.03	0.02	0.05	0.01
	P-value	0.02	<0.001	0.05	0.003			0.02	<0.001	0.24	0.02	0.2	<0.001	0.10	0.002
Cerebral peduncle (R)	Correlation (r)	-0.06	-0.01	0.05	-0.003	-0.01	-0.01	0.09	0.01	NS	NS	0.04	0.02	0.02	0.001
	P-value	0.03	0.003	0.08	0.51	0.5	0.001	0.002	0.02			0.16	<0.001	0.42	0.79
Cerebral peduncle (L)	Correlation (r)	-0.09	-0.01	0.02	0.004	-0.02	-0.01	0.09	0.01	NS	NS	0.04	0.01	0.005	0.008
	P-value	<0.001	<0.001	0.36	0.45	0.4	0.06	0.003	0.004			0.12	0.001	0.85	0.12
Anterior limb of internal capsule (R)	Correlation (r)	-0.080	-0.01	0.03	0.007	NS	NS	0.08	0.01	NS	NS	-0.003	0.01	NS	NS
	P-value	0.005	0.01	0.20	0.20			0.009	0.006			0.9	0.02		
Anterior limb of internal capsule (L)	Correlation (r)	-0.03	-0.005	NS	NS	NS	NS	0.04	-0.002	NS	NS	0.02	0.01	NS	NS
	P-value	0.3	0.35					0.19	0.7			0.47	0.01		
Posterior limb of internal capsule (R)	Correlation (r)	NS	NS	0.08	0.006	0.03	0.01	NS	NS	-0.09	-0.01	-0.01	-0.02	NS	NS
	P-value			0.005	0.24	0.2	0.002			0.003	0.01	0.5	<0.001		

	Posterior limb of internal capsule (L)	Correlation (r)	-0.05	0.007	NS	NS	0.02	0.02	NS	NS	-0.09	-0.02	-0.01	-0.02	NS	NS
		P-value	0.07	0.2			0.5	<0.001			0.002	<0.001	0.6	<0.001		
	Retrolenticular part of internal capsule R	Correlation (r)	NS	NS	NS	NS	NS	NS	NS	NS	-0.07	-0.02	NS	NS	NS	NS
		P-value									0.01	<0.001				
	Retrolenticular part of internal capsule (L)	Correlation (r)	NS	NS	0.02	0.01	-0.02	0.008	0.04	0.01	-0.08	-0.02	NS	NS	NS	NS
		P-value			0.5	0.004	0.4	0.18	0.18	0.001	0.007	<0.001				
	Anterior corona radiata (R)	Correlation	-0.05	-0.02	0.11	0.02	0.08	0.01	0.11	0.02	-0.12	-0.02	NS	NS	NS	NS
		P-value	0.10	<0.001	<0.001	<0.001	0.005	0.01	<0.001	<0.001	<0.001	<0.001				
	Anterior corona radiata (L)	Correlation (r)	-0.09	-0.01	0.10	0.02	NS	NS	0.10	0.02	-0.10	-0.02	0.007	-0.001	NS	NS
		P-value	0.003	0.001	<0.001	<0.001			<0.001	<0.001	<0.001	<0.001	0.81	0.8		
	Superior corona radiata (R)	Correlation (r)	NS	NS	0.09	0.02	0.04	0.02	0.10	0.01	-0.10	-0.02	-0.001	-0.01	NS	NS
		P-value			0.001	<0.001	0.12	<0.001	<0.001	0.003	<0.001	<0.001	0.9	0.009		
	Superior corona radiata (L)	Correlation (r)	NS	NS	0.08	0.02	0.04	0.02	0.08	0.01	-0.09	-0.02	-0.004	-0.02	NS	NS
		P-value			0.008	<0.001	0.18	<0.001	0.006	0.003	0.001	<0.001	0.8	<0.001		
	Posterior corona radiata (R)	Correlation (r)	NS	NS	0.09	0.01	0.07	0.02	NS	NS	-0.09	-0.01	-0.02	-0.01	NS	NS
		P-value			0.004	<0.001	0.02	<0.001			0.002	<0.001	0.4	0.005		
	Posterior corona radiata (L)	Correlation (r)	NS	NS	0.06	0.01	0.05	0.01	0.06	0.01	-0.08	-0.01	NS	NS	NS	NS
		P-value			0.03	<0.001	0.06	0.07	0.03	0.001	0.005	0.013				
	Posterior thalamic radiation (R)	Correlation (r)	-0.08	-0.02	NS	NS	0.01	-0.008	0.09	0.02	-0.08	-0.01	-0.02	0.02	NS	NS
		P-value	0.005	<0.001			0.58	0.15	0.002	<0.001	0.005	0.002	0.45	<0.001		
	Posterior thalamic radiation (L)	Correlation (r)	-0.08	-0.03	NS	NS	-0.03	-0.01	0.07	0.02	-0.06	-0.02	0.08	0.03	NS	NS
		P-value	0.005	<0.001			0.28	0.07	0.01	<0.001	0.04	<0.001	0.01	<0.001		
	Sagittal stratum (R)	Correlation (r)	-0.08	-0.02	0.07	0.01	NS	NS	0.08	0.02	-0.07	-0.02	0.04	0.01	NS	NS
		P-value	0.01	<0.001	0.01	0.006			0.004	<0.001	0.01	<0.001	0.14	0.01		
	Sagittal stratum (L)	Correlation (r)	-0.05	-0.03	0.06	0.01	NS	NS	0.07	0.02	-0.07	-0.02	0.05	0.02	NS	NS
		P-value	0.08	<0.001	0.03	0.001			0.02	<0.001	0.01	<0.001	0.08	<0.001		
	External capsule (R)	Correlation (r)	-0.07	-0.01	0.07	0.01	0.06	-0.002	0.08	0.02	-0.14	-0.03	NS	NS	NS	NS
		P-value	0.01	<0.001	0.01	0.002	0.04	0.70	0.008	<0.001	<0.001	<0.001				
	External capsule (L)	Correlation (r)	-0.11	-0.01	0.08	0.01	0.03	-0.008	0.10	0.01	-0.14	-0.02	NS	NS	NS	NS
		P-value	<0.001	0.02	0.007	0.007	0.22	0.17	0.001	0.004	<0.001	<0.001				
	Cingulum cingulate gyrus R	Correlation (r)	-0.08	-0.01	NS	NS	NS	NS	0.09	0.01	-0.12	-0.02	0.04	0.007	NS	NS
		P-value	0.008	0.003					0.003	0.005	<0.001	<0.001	0.11	0.17		
	Cingulum cingulate gyrus (L)	Correlation (r)	-0.08	-0.01	NS	NS	NS	NS	0.08	0.01	-0.13	-0.01	0.03	0.01	NS	NS
		P-value	0.008	<0.001					0.004	0.02	<0.001	0.001	0.25	0.01		
	Cingulum hippocampus (R)	Correlation (r)	NS	NS	0.06	-0.002	NS	NS	NS	NS	NS	NS	NS	NS	NS	NS
		P-value			0.05	0.62										
	Cingulum hippocampus (L)	Correlation (r)	NS	NS	NS	NS	NS	NS	NS	NS	NS	NS	-0.03	0.01	0.02	0.02
		P-value											0.26	0.009	0.35	<0.001
	Fornix cresstria terminalis (R)	Correlation (r)	-0.08	-0.03	0.09	0.03	0.05	0.009	0.10	0.03	NS	NS	0.02	0.03	0.07	0.02
		P-value	0.005	<0.001	<0.001	<0.001	0.07	0.13	0.001	<0.001			0.4	<0.001	0.01	<0.001
	Fornix cresstria terminalis (L)	Correlation (r)	-0.06	-0.02	0.07	0.02	0.03	0.01	0.07	0.03	NS	NS	0.01	0.01	0.04	0.02
		P-value	0.03	<0.001	0.02	<0.001	0.27	0.04	0.01	<0.001			0.61	0.02	0.14	<0.001
	Superior longitudinal fasciculus (R)	Correlation (r)	-0.11	-0.02	NS	NS	NS	NS	0.09	0.02	-0.10	-0.02	NS	NS	NS	NS
		P-value	<0.001	<0.001					0.002	<0.001	<0.001	<0.001				
	Superior longitudinal fasciculus (L)	Correlation (r)	-0.08	-0.02	0.05	0.02	NS	NS	0.06	0.02	-0.09	-0.02	NS	NS	NS	NS
		P-value	0.01	<0.001	0.06	<0.001			0.02	<0.001	0.001	<0.001				
	Superior fronto-occipital fasciculus (R)	Correlation (r)	-0.09	-0.03	0.10	0.03	0.08	0.02	0.10	0.04	-0.13	-0.03	0.06	0.001	0.01	0.01
		P-value	<0.001	<0.001	<0.001	<0.001	0.009	<0.001	<0.001	<0.001	<0.001	<0.001	0.03	0.79	0.57	0.03

	Superior fronto-occipital fasciculus (L)	Correlation (r)	-0.07	-0.02	0.07	0.02	0.04	0.01	0.07	0.02	-0.11	-0.03	-0.01	0.007	0.02	0.005
		P-value	0.01	<0.001	0.02	<0.001	0.16	0.01	0.01	<0.001	<0.001	<0.001	0.53	0.17	0.48	0.35
	Uncinate fasciculus (R)	Correlation (r)	-0.04	-0.007	0.06	0.02	NS	NS	0.06	0.01	-0.11	-0.02	NS	NS	NS	NS
		P-value	0.14	0.23	0.04	<0.001			0.03	0.01	<0.001	<0.001				
	Uncinate fasciculus (L)	Correlation (r)	-0.03	-0.01	NS	NS	NS	NS	0.05	0.01	-0.08	-0.01	NS	NS	NS	NS
		P-value	0.24	0.02					0.06	0.03	0.005	0.002				
	Tapetum (R)	Correlation (r)	-0.10	-0.01	0.12	0.01	0.09	0.01	0.12	0.01	NS	NS	NS	NS	NS	NS
		P-value	<0.001	0.004	<0.001	<0.001	0.002	0.005	<0.001	0.001						
	Tapetum (L)	Correlation (r)	NS	NS	NS	NS	NS	NS	NS	NS	-0.10	-0.005	NS	NS	0.08	0.006
		P-value									<0.001	0.34			0.008	0.29

WM Tracts and Fibres	*FA*	*MD*	*AD*	*RD*	*ICVF*	*ODI*	*IsoVF*
Cerebellar peduncle (CP)	Middle CP --	Middle CP --	Middle CP ↑	Middle CP --	Middle CP --	Middle CP --	Middle CP --
	Bilateral CP Bilateral superior CP ↓ Bilateral inferior CP	Bilateral CP Bilateral superior CP ↑ Bilateral inferior CP	Bilateral CP ↓	Bilateral CP Bilateral superior CP ↑ Bilateral inferior CP	Bilateral CP --	Bilateral CP ↑	
			Bilateral Superior CP & Inferior CP --		Bilateral superior CP ↓	Bilateral superior CP ↑	Bilateral CP ↑
							Bilateral superior CP ↑
					Left inferior CP ↓	Left inferior CP ↑	Left inferior CP ↑
Pontine crossing tract (PCT)	--	--	--	--	↓	--	--
Genu of corpus callosum (gCC)	↓	↑	↑	↑	↓	↑	↑
Body of corpus callosum (bCC)	↓	↑	--	↑	↓	↑	↑
Splenium of corpus callosum (sCC)	↓	↑	--	↑	↓	--	--
Fornix (FX)	↓	↑	↑	↑	↓	↑	↑
Corticospinal tracts (CST)	--	--	Right ↓	--	--	--	Right ↑
Medial lemniscus (ML)	Bilateral ↓	--	--	Bilateral ↑	Right ↓	Bilateral ↑	--
Limbs of the internal capsule (IC)	Bilateral ALIC ↓	Right ALIC and PLIC ↑	Bilateral PLIC ↑	ALIC ↑	Bilateral PLIC ↓	Bilateral ALIC ↑	--
	Left PLIC ↑					Bilateral PLIC ↓	

Retrolenticular part of the internal capsule (RLIC)	--	Left ↑	Left ↑	Left ↑	Bilateral ↓	--	--
Anterior corona radiata (ACR)	Bilateral ↓	Bilateral ↑	Right ↑	Bilateral ↑	Bilateral ↓	Left ↑	--
Superior corona radiata (SCR)	--	Bilateral ↑	Bilateral ↑	Bilateral ↑	Bilateral ↓	Bilateral ↓	--
Posterior corona radiata (PCR)	--	Bilateral ↑	Bilateral ↑	Left ↑	Bilateral ↓	Right ↓	--
Posterior thalamic radiation (PTR)	Bilateral ↓	--	Bilateral ↓	Bilateral ↑	Bilateral ↓	Bilateral ↑	--
Sagittal stratums (SS)	Bilateral ↓	Bilateral ↑	--	Bilateral ↑	Bilateral ↓	Bilateral ↑	--
External capsule (EC)	Bilateral ↓	Bilateral ↑	Bilateral ↑	Bilateral ↑	Bilateral ↓	--	--
Cingulum cingulate gyrus (CgC)	Bilateral ↓	--	--	Bilateral ↑	Bilateral ↓	Bilateral ↑	--
Cingulum hippocampus (CgH)	--	Right ↓	--	--	--	Left ↑	Left ↑
Fornix cres+stria terminalis (FXCT)	Bilateral ↓	Bilateral ↑	Bilateral ↑	Bilateral ↑	--	Bilateral ↑	Bilateral ↑
Superior longitudinal fasciculus (SLF)	Bilateral ↓	Left ↑	--	Bilateral ↑	Bilateral ↓	--	--
Superior fronto-occipital fasciculus (SFOF)	Bilateral ↓	Bilateral ↑	Bilateral ↑	Bilateral ↑	Bilateral ↓	Bilateral ↑	Bilateral ↑
Uncinate fasciculus (UF)	Bilateral ↓	Right ↑	--	Bilateral ↑	Bilateral ↓	--	--
Tapetum	Right ↓	Right ↑	Right ↑	Right ↑	Left ↓	--	Right ↑

Table 4. Significant diffusion alterations in white matter tracts in T2DM participants based on the ROI statistical analysis ($p<0.05$, corrected). -- = not significant; arrow pointing up = increase; arrow pointing down = decrease.

Reviewers' Comments

The first published systematic review (Chapter 6)

- Response to Reviewer 1 Comments

Point 1: Page 2, line 46: please justify the text.

Response 1: Text is justified according to the comment and highlighted in yellow (autocorrect tracker) in the revised version of the systematic review.

Point 2: Figures are not sharp and do not make easy reading. Also, some figures (e.g. figures 2, 5, 6, 7, and 10) need a larger font size.

Response 2: All figures edited and presented with larger and sharp font.

Point 3: Page 12, line 352-352: please adjust the size of text.

Response 3: The size of the text is adjusted and highlighted in yellow (autocorrect tracker) in the revised version of the systematic review.

Point 4: Page 17, line 498: please correct the mistake in the sentence.

Response 4: The word "comorbidities" is corrected and highlighted in yellow (autocorrect tracker) in the revised version of the systematic review.

- Response to Reviewer 2 Comments

Point 1: For the diabetologist and any clinician, the authors might relate the DTI findings to known or suspected pathologies in the brain resulting from diabetes or its complications such as: Neuroinflammation, glucose transport at the BBB (cerebral insulin resistance), cerebral glucose metabolism, perfusion abnormalities. If such data are not available in the many articles, a theoretical discussion putting the DTI into a more familiar context would be welcome.

Response 1: Thank you for this suggestion, two small paragraphs are added to the discussion explaining the suspected pathologic (cerebral complications, neuroinflammation and glucose metabolism) relation with DTI findings. They are highlighted in green in the revised manuscripts.

#1: Hyperglycaemia could increase the risk of brain tissue damage or dysfunction by a metabolism-dependent cascade such as hyperglycaemia-induced oxidative stress. The DTI alterations presented in this review could alternatively be due to other glycolysis-independent biological factors that are changed simultaneously with severe hyperglycaemic episodes.

#2: Also, they showed that T2DM micro-vascular changes in the brain had been linked to cognitive deficits, supporting the hypothesis that neuroinflammation and microvascular pathology are involved in the cerebral complications/changes of diabetes, which DTI is sensitive to compared with other MRI conventional techniques.

Point 2: Diabetic brain is neither an accepted nor an acceptable term.

Response 2: The term “Diabetic brain” is replaced with “patients with diabetes” and highlighted in green in the revised manuscripts.
Here is the sentence: Diffusion Tensor Imaging (DTI) has been used as a sensitive MRI-based technique for quantifying and assessing brain microstructural abnormalities in “patients with diabetes”.

The second published systematic review & meta-analysis (Chapter 7)

- Response to Reviewer 1 Comments

Point 1: Since the authors mention a couple of significant loopholes in the present meta-analysis how and to what extent is this still relevant to the field?
Response 1: Two small paragraphs are added to the discussion explaining to what extent this meta-analysis can be relevant to the field. Responses are heighted comment in yellow and included in the text “response to first query”.

Point 2: Can the authors include some comparative images of NODDI from control and MS patients from the studies considered for this review to give a clearer idea of the concept behind it? It would make the review more comprehensive.
Response 2: Three images were added to the discussion from anther included study that show how NODDI metrics depict WM MS lesions. Response is highlighted in yellow “response to second query”.

Point 3: Since the authors didn't find any significant difference between ODI in MS lesions and NAWM compared to WM from healthy participants how reflective this meta-analysis is of the clinical settings/outcomes?
Response 3: One small paragraph was added to the discussion part to justify the reflection of ODI insignificance of the clinical settings and outcomes. Response is highlighted in yellow “response to third query”.

- Response to Reviewer 2 Comments

Point 1: What could be the possible reasons for more heterogeneity between the studies associated with the ODI in both WM and NAWM lesions compared to the NDI.
Response 1: Two small paragraphs are added to the discussion explaining the reasons of the heterogeneity of ODI between the included studies. Responses are heighted in red and included in the text “response to first query”.